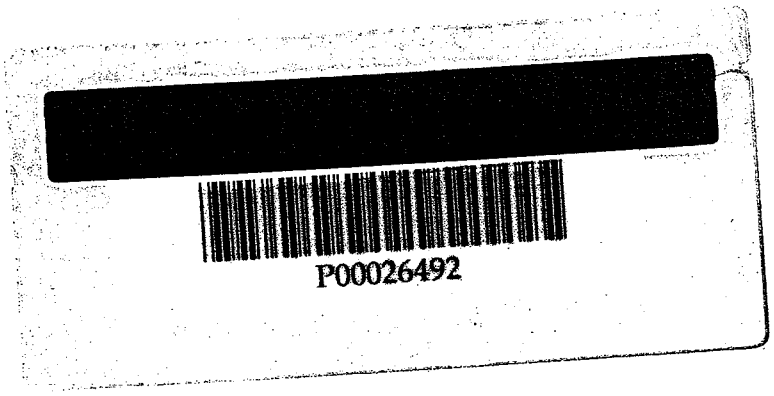

CERN 76-18
8 November 1976

ORGANISATION EUROPÉENNE POUR LA RECHERCHE NUCLÉAIRE
CERN EUROPEAN ORGANIZATION FOR NUCLEAR RESEARCH

PHYSICS WITH VERY HIGH ENERGY e^+e^- COLLIDING BEAMS

L. Camilleri, D. Cundy, P. Darriulat, J. Ellis, J. Field, H. Fischer, E. Gabathuler, M.K. Gaillard, H. Hoffmann, K. Johnsen, E. Keil, F. Palmonari, G. Preparata, B. Richter, C. Rubbia, J. Steinberger, B. Wiik, W. Willis and K. Winter

GENEVA
1976

CERN 76-18
8 November 1976

ORGANISATION EUROPÉENNE POUR LA RECHERCHE NUCLÉAIRE
CERN EUROPEAN ORGANIZATION FOR NUCLEAR RESEARCH

PHYSICS WITH VERY HIGH ENERGY e^+e^- COLLIDING BEAMS

L. Camilleri, D. Cundy, P. Darriulat, J. Ellis, J. Field, H. Fischer, E. Gabathuler*), M.K. Gaillard, H. Hoffmann, K. Johnsen, E. Keil, F. Palmonari, G. Preparata, B. Richter×), C. Rubbia, J. Steinberger, B. Wiik†), W. Willis and K. Winter

GENEVA
1976

---

*) Visitor from RHEL, Didcot, England.
×) Visitor from SLAC, Stanford, Calif., USA.
†) DESY, Hamburg, Germany.

ABSTRACT

This report consists of a collection of documents produced by a Study Group on Large Electron-Positron Storage Rings (LEP). The reactions of interest in the weak, electromagnetic and strong interactions are discussed. The technical feasibility of the relevant experiments is investigated by attempting, in each case, the design of an experimental set-up. Event rates are estimated using currently prevailing theoretical models and by extrapolation of results at present accelerators. A number of technical reports previously issued by members of the LEP Design Study Group are included as appendices.

CONTENTS

I - INTRODUCTION

A Study Group was set up at CERN in April 1976 to investigate the range and feasibility of experiments which could be done with very high energy e^+e^- storage rings starting from physics objectives with no limitation on considerations of site. The context was that of a European facility clearly going beyond PETRA in its physics potential. The present report is a summary of the work of this Study Group.

I - General considerations.

The primary motivation in considering such a machine is the unique opportunity it offers to study the weak interaction. The neutral weak current, recently discovered in neutrino interactions, couples directly to the electron-positron system. Little is known, so far, of its exact nature, but in the range of energies presently attainable, its behaviour is similar to that of the charged weak current. In particular, while cross sections for processes mediated via one photon annihilation decrease like s^{-1}, the weak neutral current should induce cross sections increasing like s at low energies and eventually overtaking the former at a total center of mass energy of, say, 50 to 100 GeV.

In gauge theories, which are successful at unifying weak and electromagnetic interactions, the weak interaction is mediated via a neutral boson Z^o and a doublet of charged bosons $W^\pm$ with masses between 50 and 100 GeV. In the simple formulation of the Weinberg-Salam model, when the Weinberg angle is taken in accord with present experimental results on neutral currents, the masses of these mesons are $m(Z^o) \simeq 80$ GeV and $m(W^\pm) \simeq 65$ GeV. The former would be produced

directly by annihilation of 40 GeV colliding $e^{\pm}$ beams, the latter in pairs by beams above 65 GeV. Between these energies the cross section for production of muon pairs via one-photon annihilation decreases from 15 to 5 picobarns. Although these simple considerations impose severe constraints on the parameters of the machine, the design study of a large electron-positron (LEP) ring being undertaken at CERN aims at demonstrating the feasibility of a 2x100 GeV colliding beam device with a luminosity of 10^{32} cm^{-2} s^{-1}. This is sufficient to perform a detailed study of the weak interaction and our considerations were therefore based upon the parameters of the LEP design.

A clear demonstration of some of the advantages of e^+e^- with respect to hadronic collisions was recently given at SPEAR and DORIS where a new chapter of physics, that of the J/ψ and related particles, is being efficiently and rapidly studied. This success is due in part to the absence of extraneous hadronic matter. In hadron machines instead, the new physics is hidden by a large hadronic background. In parton language, only one constituent of each colliding nucleon is used in each hard interaction. Thus only part of the center of mass energy is available, and the remaining partons produce a copious background of hadrons which complicates the analysis of the final state. At LEP, similarly to the J/ψ case, e^+e^- collisions can produce the Z^o and $W^{\pm}$ directly with no other particles in the final state.

The Z^o couplings can be deduced from the interference with one-photon processes, and from purely weak vector-axial vector interference. The cross section and angular distributions for W^+W^- production are good probes of weak couplings because of their sensitivity to interferences between different production mechanisms. The natural width of the Z^o is expected to be of the order of 1 GeV, one order of magnitude larger than the corresponding energy resolution of the

machine. This means a production rate of $\simeq$ 1500 Z^o's per hour, $\simeq$ 500 times higher than that of muon pairs via one-photon annihilation at the same energy. It is therefore possible to study rare decays of the Z^o particle in a similar manner so that of ψ mesons at SPEAR and DORIS.

What if intermediate vector bosons are not seen at LEP ? We would then expect weak cross sections to continue to rise with s, still providing a rich laboratory for the study of neutral currents, even if an unforeseen damping mechanism were to set in. This would be an important discovery in itself as it would contradict almost every present-day model of the weak interaction.

In addition to the study of the weak interaction, very high energy electron-positron rings offer the possibility of producing large mass quark-antiquark pairs and new hadrons with the same quantum numbers as a photon or a Z^o. Hadron jets already show up clearly at SPEAR energies, in contrast with the situation in hadron machines where they are partly hidden under the cumbersome background of the multiparticle final states.

The extension of the explored mass range far beyond that of the PEP/PETRA generation may reveal the existence of new quarks and would permit detailed studies of Z^o-quark couplings. The very large energy in the quark-antiquark centre of mass could be such that free quarks escape, in any case the nature of confinement will be explored in an entirely new domain.

II - Organization of the study

With the above considerations in mind, several specific topics which seemed of particular interest were studied and are presented in the subsequent sections of the present report. Many topics were left out, and those which were treated could not be

analysed in very great detail.

The next section gives a brief presentation of the LEP design, which was taken as a working basis in the present report. The machine is a large electron positron ring, 16 km in diameter, with eight zero angle intersection points. The energy range extends from 20+20 to 100+100 GeV. A wiggler magnet scheme makes it possible to maintain a constant luminosity of $10^{32} cm^{-2} s^{-1}$ from the top machine energy down to 50+50 GeV. It then decreases like s to $1.6\ 10^{31}\ cm^{-2}\ s^{-1}$ at the lowest energy, thereby offering a smooth connection to the PETRA-PEP domain while staying large in the important region of the expected Z^o pole. The relative energy spread of the beams is of the order of 1 $^o/_{oo}$, thereby excluding scans for very narrow resonances.

In section III we survey some important reactions and present a few cross sections and distributions.

Four sections are devoted to the study of specific experiments. They were selected as representative of the physics programme outlined in the introduction. The aim was to illustrate the feasibility of actual experimentation rather than producing detailed detector designs. With expected annihilation rates of a few events per hour (with the exception of resonance energies such as the Z^o pole) we consider it essential to detect as much as possible of each interaction, and we therefore discarded small coverage detectors. We assumed instead that each intersection would be equipped with a detector subtending a solid angle of nearly 4π , with as much momentum measurement and particle identification as possible, very much as is already the case at lower energy e^+e^- machines.

In section IV we consider the basic reactions $e^+e^- \rightarrow \mu^+\mu^-$ and $e^+e^- \rightarrow e^+e^-$. The detector is a magnetic spectrometer surrounded by total absorption counters for electron and photon detection and by a muon filter.

The beams are unlikely to be polarized, because of their large momentum spread. Nevertheless important information on the weak current is obtained from measurements of the charge asymmetry alone and of the polarization of forward muons.

In section V we consider the detection of hadron jets. To the extent that leading hadrons remember best the quantum numbers of their parent quarks it is important to resolve and identify particles within narrow jets. The angular distribution of the parent quarks thus deduced can be analysed in terms of charge asymmetry as in the case of $e^+e^- \rightarrow \mu^+\mu^-$ and the space time structure of their coupling to the neutral vector boson Z^o deduced. The proposed detector, of an unconventional design, provides simultaneous identification of hadrons, muons and electrons by combining imaging Cerenkov counters with a calorimeter. A small axial field coil permits momentum measurement of the soft collision products. The onset of thresholds for the production of new quarks may have little effect on the ratio $R = \frac{\sigma(e^+e^- \rightarrow \text{hadrons})}{\sigma(e^+e^- \rightarrow \mu^+\mu^-)}$. However measurements of the sphericity in the final state may be a good way to look for new quarks. Just above threshold the new channel should yield highly spherical events which can be separated from the other channels where a strong jet structure is expected. The same remark applies to the detection of resonances in the e^+e^- channel, which could be much narrower than the beam energy spread and therefore difficult to see directly.

In section VI we concentrate on reactions where charged leptons, hadrons and neutrinos are produced together. The detector consists of a total absorption calorimeter surrounded by a magnetic spectrometer which provides momentum analysis of the traversing muons. The total 4-momentum of the detected particles is measured with sufficient accuracy to reveal the presence of neutrinos. Missing energy would be the production signature and single and multi-

neutrino events could be distinguished by measuring the missing mass. The reaction $e^+e^- \rightarrow W^+W^-$, where one of the W mesons decays into hadrons, the other into muon and neutrino, is taken as an illustrative example.

Two-photon processes are considered in section VII. Although interesting in their own right because they provide even C final states, they are a dominant fraction of the total e^+e^- hadronic production. Thus they might be a dangerous background for e^+e^- annihilation studies. It is found that tagging of the scattered electron and positron in coincidence provides an almost pure sample of "2-photon" events. However the efficiency of tagging used in veto at the trigger level is too low to give any significant rejection of "2-photon" versus "1-photon" interactions. On the other hand off-line selection of events with at least one large transverse momentum particle in the final state reduces the "2-photon" background to a negligible level. The magnetic detector is designed to study hadron correlations in the "2-photon" process and concentrates on distinguishing hadrons in addition to tagging the scattered electrons. The possibility of measuring the structure function of the photon itself by taking one of the photons off the mass shell is investigated. Although cross sections are small, it is sufficient to make a crude measurement to differentiate between integral and fractional quark charges.

The last topic of our study is the influence of synchrotron radiation on the feasibility of experiments, and is treated in section VIII. The large power dissipated in synchrotron radiation and the high value of the critical energy make one worry about the operation of detectors close to the circulating beams. We present arguments demonstrating that this background can be reduced to an acceptable level by simply using low field magnets near intersections and properly designed absorbers. Also the interaction of one beam

with the synchrotron radiation of the other is shown to be small enough to not significantly disturb the operation of detectors.

For convenience, we have appended to the present report a set of relevant papers put out by the LEP design study group.

III - Some concluding remarks

The present report, even though incomplete, demonstrates clearly the feasibility of performing experiments to study certain aspects of weak interactions and answer some fundamental questions about their nature.

The preliminary parameters of the LEP design are adequate to perform such experiments, as shown by the examples presented in the next sections. They provide sufficient center of mass energy and event rate. The synchrotron radiation and the 2-photon processes are not expected to generate prohibitive background.

Most of the detectors considered in the report are compact and can be accomodated in the $\pm$ 10 m free space of the LEP design. This situation contrasts with that of proton colliding beams where the persistence of longitudinal phase space dominance and the extension of the rapidity plateau populate more and more the small angle region at higher energies. Here much less angular dependence is expected and the loss of a small solid angle in the vicinity of the beam pipes is likely to be unimportant. In addition the small spatial extension of the overlap region of the e^+e^- bunches facilitates compact detector geometries.

We have not yet commented on the desirability of chosing 100GeV as the top energy. This is a very important parameter to the extent that the size, and therefore the cost, of the machine critically depend upon its choice. While it is clear that the energy range must extend somewhat beyond the expected W^+W^- threshold, it

seems very difficult to evaluate the risk of missing interesting new phenomena just above top machine energy, whether it is chosen to be 75 or 100 GeV per beam.

Other machine parameters, such as the lateral free space in experimental areas, the number of intersections, have not been discussed and should be the subject of further investigations. We believe that the LEP design choice of 8 intersects is adequate to accommodate a sufficient variety of experimental set-ups.

Although many topics have been only superficially treated, or even ignored, in the present report, we feel that these considerations are very encouraging and that very high energy electron-positron rings are a most exciting option as a future european facility.

II- A MACHINE FOR e^+e^- PHYSICS UP TO 200 GeV c.m. ENERGY (LEP)

I - Introduction

The design of a large e^+e^- storage ring is being studied by a small group of machine physicists, the LEP working group (K. Johnsen, Chairman, R. Billinge, P. Bramham, E. Jones, E. Keil, B. Richter (SLAC), W. Schnell) with the technical advice of other people at CERN and elsewhere. The following requirements are imposed on the machine by physics considerations :

- a maximum energy E of 100 GeV,
- a luminosity $L = 10^{32}$ cm^{-2} s^{-1} in each intersection region at 100 GeV, and a good luminosity down to about 40 GeV. The luminosity variation adopted in the design is $L \geqslant 10^{32}$ cm^{-2} s^{-1} from 50 to 100 GeV and $L \propto E^2$ below 50 GeV.
- the free space around the interaction point is assumed to be $l_{int} = \pm 10$ m along the beam pipe.

The consequences of a reduction in E, or of a change in L and/or l_{int} will be discussed below. Several other machine parameters of a more technical nature will be introduced at appropriate points during the discussion.

At the time of writing, the machine study has reached roughly the halfway point. Therefore, what follows is essentially a status report on our present ideas. Unpleasant surprises might occur and oblige us to change the machine design in the future.

The machine description which follows is divided into 2 sections :

i) a cost optimisation procedure for choosing the basic machine parameters.

ii) description of LEP

A full report on the LEP design study is scheduled to appear in the middle of 1977.

II - A cost optimisation procedure for choosing the basic machine parameters.

The size of LEP becomes clear from two simple considerations. Firstly, the design involves an extrapolation from 15 GeV for e^+e^- storage rings under construction, i.e. PETRA or PEP, to 100 GeV. Secondly, the luminosity L in an optimized machine is related to the main parameters of the machine by the following expression :

$$L\ (cm^{-2}\ s^{-1}) = 1.23 \times 10^{33} \frac{\Delta Q\ P_B\ (MW)\ \rho\ (m)}{E^3\ (GeV)\ \beta_y^*\ (m)} \qquad (1)$$

Here, ΔQ is the maximum permissible beam-beam tune shift, P_B is the RF power delivered to both beams, ρ is the bending radius, and β_y^* is the vertical amplitude function at the crossing point. The units of these quantities are given in brackets. It is clear from (1) that at constant L, ΔQ, β_y^*, the product $P_B \rho$ scales as E^3. Assuming $\Delta Q = 0.06$ and $\beta_y^* = 0.1$m, $P_B \rho$ reaches a value of 136 GWm, a factor of 300 higher than in a 15 GeV machine.

Separate scaling laws for P_B and ρ can be obtained by the cost optimisation procedure shown in Appendix 1. Using unit costs obtained from the PEP cost estimate, and the present SPS power cost capitalized over 10 years at 5000 h/year, a power efficiency of 75% and a shunt impedance Z = 20 MΩ/m, an optimised 100 GeV machine has the following parameters :

machine radius	$R = 5.1$ km
dissipated power in RF cavities	$P_D = 87.5$ MW
beam power	$P_B = 26.7$ MW
total length of RF cavities	$L_c = 2.2$ km

With the unit cost of Appendix 1, the initial cost of this machine is 660 M$, and the annual power bill is 42 MsFr. The LEP machine has parameters in the neighbourhood of those shown above.

It is demonstrated in Appendix 1 that R, P_D, L_c and the cost of a machine optimized for an energy E are all nearly proportional to E^2, while P_B is nearly proportional to E. If a variable luminosity L in included in the optimization, it is found that the cost of the machine varies by less than 10% when L varies from 1/3 to 3 times the nominal value, while the annual power bill for the RF system alone changes from 37 to 54 MsFr. These figures should only be taken as an indication of the consequences of small changes in the design luminosity. It is likely that somewhere between $L = 10^{32}$ and 3×10^{32} cm^{-2} s^{-1} one has to change to a double ring design which will certainly be more expensive than a single ring design.

III- Description of LEP

A detailed machine design is under way. The present set of machine parameters is given in Appendix 2. Some of the reasoning behind our choice of parameters is explained below .

3.1 - Lattice concept and performance estimate.

The LEP lattice must have the following properties :

i) the amplitude functions must have low adjustable values β_x^* and β_y^* at the crossing points. This arises from (1) which shows that, for a given luminosity L, the beam power P_B is proportional to β_y^*. How small β_y^* can be depends on the bunch length, on the ability to correct chromatic effects which become worse when β_y^*

gets smaller, and on the beam-beam bremsstrahlung lifetime t_{bb} which is proportional to β_y^*. After trying several other values, a value $\beta_y^* = 0.1m$ has been adopted in order to obtain a reasonable value of t_{bb}. It is shown in Appendix 3 that the chromatic effects can be corrected at this value of β_y^* and at even smaller ones. The ratio β_y^*/β_x^* determines the amount of coupling K required to obtain the desirable axis ratio of the beams at the crossing point. This should be larger than the coupling present in the machine due to unavoidable skew fields. In LEP, they are expected to lead to almost complete coupling, $K \approx 1$. This would require $\beta_x^* = \beta_y^*$ to minimize the circulating current but may lead to excessive chromatic aberrations in the x-direction. Hopefully, this is avoided by choosing β_x^* so as to obtain about equal values for the maxima of β_x and β_y, and the current has been raised accordingly.

ii) the dispersion must vanish at the crossing points and also in the very long straight sections occupied by the RF system, in order to avoid the excitation of betatron-synchrotron coupling resonances.

iii) the dispersion in most of the lattice must be adjusted to obtain the beam size required at the maximum energy. This is done by fixing the number of cells and the phase advance/cell. For the latter, a value of about 60° has been chosen because it leads to a simple design for a dispersion suppressor and favourable conditions for the chromaticity correction.

iv) in order to obtain a weaker variation of the luminosity than E^4 the beam size at energies below 100 GeV must be artificially increased. Appendix 4 describes a scheme of wiggler magnets and lattice modifications which achieves constant luminosity from 50 to 100 GeV, and $L \sim E^2$ below 50 GeV. Extending the range of constant luminosity over more than a factor of two in energy could require

more complicated lattice modifications and even more aperture.

In the LEP lattice design, manipulating the dispersion by leaving out some bending magnets and modifying others allow to meet all these requirements. This leads to the regular behaviour of the amplitude functions β_x and β_y shown in figs. 1 and 2 of the Appendix 2. This behaviour stops at the 4th quadrupole from the crossing point, from where onwards one must let β_x and β_y increase, in order to achieve the very small values required at the crossing points. This operation needs 4 variable parameters, namely the gradients of 4 quadrupoles. The choice of the free space around the crossing point $l_{int} = \pm 10$m is closely related to the design of the machine lattice next to the crossing point and to the chromaticity correction scheme. At constant β_x^* and β_y^*, and hence constant luminosity L, chromaticity correction becomes more difficult when l_{int} is increased. If one is limited by chromaticity correction one must let β_x^* and β_y^* increase in proportion to l_{int}. Hence, in a machine in which l_{int} in some interaction regions is larger than the nominal value, those interaction regions invariably have a lower luminosity than the others, in proportion to $1/l_{int}$. If, on the other hand, one is not limited by chromaticity correction, then one is free to increase l_{int} at constant β_x^* and β_y^*, and hence constant luminosity. On the basis of the findings in Appendix 3 one might argue that l_{int} could be increased by a couple of meters should the need arise.

It is shown in Appendix 5 that no transverse polarisation is to be expected in LEP over most of its operating range. Consequently no provision has been made in the lattice to rotate the polarisation vector into the beam direction. The energy spread in each beam is $\sigma_e = 108$ MeV at 100 GeV, leading to a c.m. energy uncertainty $\sigma_{cm} \approx 150$ MeV. If turbulent bunch lengthening[1] occurs, σ_e and σ_{cm} might actually be bigger. However, this is believed to be unlikely. At fixed energy, $\sigma_e \sim \rho^{-\frac{1}{2}}$ where ρ is the magnetic

bending radius. In a machine with the size of LEP, it seems doubtful that one would reduce σ_e by increasing ρ. In principle, it is possible to reduce σ_{cm} at fixed σ_e by modifying the lattice such that the vertical beam size at the crossing points is mainly determined by the vertical dispersion η_y^* obtained by vertical electric deflection [2]. It seems doubtful whether such a scheme could be realised in LEP even if one were to accept the concomitant reduction in luminosity.

The machine aperture must be at least $A_x = \pm (10\ \sigma_{xmax} + 20mm)$ and $A_y = \pm (10\ \sigma_{ymax} + 10mm)$ where σ_{xmax} and σ_{ymax} have to be taken at the energy where they are largest. This occurs at 50 GeV because of the constant luminosity down to that energy. The remaining aperture allows for closed orbit distortions.

The lattice design is based on having 32 equidistant bunches in each beam. These bunches cross at 64 places around the circumference unless they are separated in those places where they should not cross.

Since the beam-beam tune shift from 64 crossings is clearly too large, the beams must be separated in 56 places around the machine. The electrostatic fields required to keep the deflection and tune shift of one beam due to the other one within reasonable limits are technically feasible. The reasons for choosing 32 bunches rather than 4 which would not require this separation are discussed below.

3.2 - RF system.

Some parameters of the RF system such as the voltage per turn and the power necessary to compensate the losses due to synchroton radiation are fixed once the lattice and performance of the machine are defined. The total length of the RF system is a result of the cost optimisation, and the shunt impedance per metre should be as high as possible.

The only RF parameter which appears to be reasonably free at the beginning is the RF frequency. Frequencies in the range from 200 MHz (the SPS frequency) to 500 MHz (the DESY-DORIS-PETRA frequency) have been considered. On one side, one prefers a high frequency in order to limit the physical size of the RF cavities, and the power dissipated per unit length of RF structure. Also the cost of RF power sources tends to decrease with increasing frequency. On the other hand, the number of synchrotron oscillation per revolution, Q_s, increases with the RF frequency. Q_s is of some importance in relation to betatron synchrotron coupling resonances, and should be less than 0.1. With the values of β_x^* and β_y^* as chosen the influence of the RF frequency on the bunch length is unimportant. None of these arguments is very strong and hence the average between the two limits has been adopted, 350 MHz, which also happens to be the SPEAR-PEP frequency.

The quantum lifetime t_q is the lifetime of the beam with respect to the emission of very energetic synchrotron radiation photons which cause the electron or positron to jump out of the energy acceptance of the RF system. It has been fixed at $t_q = 10$ h although it could be doubled by a very modest increase in the RF voltage, 4 MV, should the need arise.

In order to complete the parameter list of the RF system, the interaction between the RF system and the beam must be considered. The interaction between the beam and the driven fundamental mode in the RF cavities is usually called beam loading [3], while the interaction with other modes in the RF cavities and any mode in other boxes is called higher order mode losses.

One would naively expect that the RF power to be supplied by the RF power source is given by the sum of the power absorbed by the beam, and the power dissipated in the walls of the RF cavities. This holds as long as $t_o \ll 1$, where t_o is the ratio between the bunch spacing and the filling time of the RF cavities. For values $t_o \gtrsim 1$, the RF

power increases quite steeply. This is both costly and undesirable because of the increase in Q_s associated with it. A physically more transparent derivation is given in Appendix 6. At given beam power, the energy absorbed by a bunch during one revolution is proportional to the bunch spacing, and this energy must not exceed the energy stored in the RF system before the bunch passage. Hence, for bunch spacings above a certain value, the RF cavities must be prepared for the bunch passage by storing more energy in them than would be necessary if the same total current were stored in more bunches. It is this consideration which has led us to choose 32 bunches in each beam, resulting in $t_o \approx 0.2$.

The calculation of the higher-order mode losses in the RF cavities is quite straightforward [4], if the bunch length is known. We assume that the bunches are longer than their zero-current length due to bunch lengthening of the potential well distortion variety. The evaluation of the higher-order mode losses for the rest of the machine circumference is guesswork at the best. We assume that the impedance per unit length is better than that in SPEAR. This is not an unreasonable requirement bearing in mind that LEP cells are much longer than SPEAR cells, and that SPEAR was built before the importance of these losses was realised. Although the compensation of these losses needs RF voltage and power, which are costly, their most dangerous aspect is local heating of individual components. Altogether, we estimate the loss into higher modes to be 110 MeV/turn corresponding to a power of 1.3 MW/beam.

Since the bunch spacing corresponds to almost 2000 RF cycles, modulation of the RF system with the bunch frequency could save RF power. Appendix 7 describes a scheme in which the RF energy is transfered periodically between a low-loss storage cavity and the accelerating cavity.

3.3 - The magnet and vacuum system.

It is at present foreseen to inject electrons and positrons at 20 GeV. Since the magnetic field is only 0.0535 T at 100 GeV, it is as low as 0.0107 T (107 Gauss) at 20 GeV. This low guide field excludes it being used for distributed pumps at the same time. It is also rather low compared to the remanent field to be expected in magnets with iron pole pieces.

There are two alternatives for the design of the vacuum system, using distributed or lumped pumps both with their own magnetic field. At the moment the installation and operation of 50 km of distributed pumps would appear rather unattractive. The design studies are therefore concentrated on a lumped system with pumps only at regular intervals. Since the gas load due to synchrotron radiation is roughly uniformly distributed along the circumference, the whole machine must be connected to the pumps by pipes of sufficient conductance. There are two alternatives to reach this goal : either the diameter of the vacuum chamber is chosen large enough so that its conductance is adequate, or a vacuum chamber which fits tightly around the beam aperture is connected radially to a vacuum manifold of adequate conductance. With the beam aperture required for operation with full luminosity at 50 GeV the difference in the size of the vacuum chamber between these two alternatives is not all that large. Hence, we favour using the beam pipe as the vacuum manifold.

A circular beam pipe does not have the most favourable shape for designing a C or H type magnet with iron pole pieces around it. This fact together with the low injection field mentioned earlier has led us to consider a magnet design in which the field is created by shaped conductors fitting tightly around the beam pipe. Engineering studies on the problems involved with such magnets and on how to mass produce them cheaply are under way. The quadrupoles and sextupoles have considerably higher pole tip fields and will most

likely be of conventional design.

3.4 - Injection

The injector, a 50 Hz electron synchrotron with a maximum energy of 20 GeV is being studied at the Rutherford Laboratory. Its average radius is about 220m. Filling with positrons is expected to take place in two stages. The injector pulses consist of 32 e^+ bunches each, they are used to fill 32 bunch trains of 37 bunches in LEP until the required total e^+ current is reached. This is supposed to take a few minutes. Subsequently, all the e^+ in a bunch train of 37 bunches are transferred into a single bunch in a modified Tigner scheme [5], using the injector synchrotron as a delay line for the bunches. This operation takes a few seconds. The electrons are injected directly into the 32 bunches.

With the LEP lattice in its present from, the damping time in LEP at injection is too long to achieve the filling time quoted above. Apart from this problem -which concerns the details of the interface between LEP and its injector- there would not seem to be any significant problems with injection and filling.

3.5 - Open questions.

So far, the study of LEP has not revealed any unsurmountable problems, although the machine may not be as simple and straightforward as it seemed in the beginning. There are also several areas where open questions remain.

i) Consequences of full coupling.

We assume that the machine is fully coupled for luminosity calculations etc., but the lattice design, chromaticity correction etc. are all done for an uncoupled machine. This discrepancy should be resolved.

ii) Tracking and chromaticity correction.

The maximum stable beam emittances must be found by tracking

particle trajectories through the machine. They must be compared to the emittances required. More suitable sextupole schemes must be found if necessary.

iii) Optimisation of the low-β insertion.

Vary the length and separation of the quadrupole doublet next to the crossing point to minimize its strength ; study the consequences of changing l_{int}, investigate the effects of the linear part of the beam-beam force.

iv) Closed orbit correction schemes.

Find the optimum scheme for tunes in the vicinity of 100, calculate its capabilities, and define a suitable arrangement of pick up stations and correctors.

v) Beam separation schemes.

Design a scheme which separates the beams in 56 places, define tolerances on the residual beam displacements outside the bumps.

In addition to these outstanding problems which are all related to the beam dynamics and performance of LEP, there remain open questions in its engineering aspects. In the RF system, they are mainly concerned with the generation and distribution of the RF power. At this stage, the RF cavities are assumed to be copies of the DORIS or PEP cavities, depending on the frequency, only many more of them. The design of the magnet and vacuum system has not yet reached the stage where convincing engineering concepts for the component are available. They are required before one can affirm that a machine like LEP can be built, and at what price.

References

1 - P.J. Channell and A.M. Sessler, LBL-4613 (1975)

2 - A. Renieri, LNF-75/6 (R) (1975)

3 - P.B. Wilson, IXth Int. Conf. High Energy Accelerators, Stanford 1974, 57 (1974).

4 - E. Keil, C. Pellegrini, A. Turrin, A.M. Sessler, Nucl. Inst. and Methods 127, 475 (1975).

5 - M. Tigner, CNLS 299, Cornell U., Ithaca, N.Y.

III- THEORETICAL REMARKS

J. Ellis, M.K. Gaillard

Contents :

I - Introduction

As emphasized in the general introduction, the range of e^+e^- machine energies discussed in this report is very good for studying the weak interactions. Rising neutral weak current[1] cross-sections are expected to overtake falling electromagnetic annihilation cross-sections at centre of mass energies of the order of 100 GeV. Gauge theories[2] predict charged and neutral intermediate vector bosons with masses between 50 and 100 GeV. The fashionable Weinberg-Salam model[3] expects* $m(W^\pm)$ to be around 60 GeV, $m(Z^o)$ about 80 GeV.

Most of the theoretical discussion in this section centres on weak interactions, emphasizing how neutral current and Z^o properties can be established, charged $W^\pm$ bosons produced and studied, and searches made for Higgs particles and other weakly interacting exotics. The Z^o peak is expected to yield large cross-sections, enabling studies of its decay modes and properties which are inaccessible if the Z^o is produced in hadronic collisions.

High energy e^+e^- collisions are also uniquely suitable for many strong interaction studies. At the most naïve level, when quarks are given impulses of 100 GeV, either they will escape, or we should learn a great deal about the forces that confine them. For example, if quarks continue to be absent, the large hadronic cross-sections near the Z^o peak will facilitate studies of scaling violations and jet structures. Also, e^+e^- collisions may be the only hope for diagnosing new high-mass quark flavours.

The above can be regarded as the "bread and butter" physics of LEP. It is possible to imagine some types of "jam". We may hope that, by the time of this machine, the unification of strong with weak and electromagnetic interactions will be a dominant theme. The mass scale of such a unification is probably at least 200 GeV, and high energy e^+e^- collisions may be the most transparent window

* Similar estimates have recently been obtained for a wider class of models [4].

on it. More exotic possibilities include strongly interacting Higgs particles, which could have masses 0 (300) GeV, "leptoquark", bosons, monopoles... The existence of any of these objects is rank speculation, but it is clear that high energies are vital for probing them, and e^+e^- annihilations seem to exploit their centre of mass energy much more efficiently than hadronic collisions. Some students[4] of cosmic rays in fact believe that hadronic collisions may cross a dramatic new threshold at several hundred GeV in the centre of mass. If something bizarre exists, it is probably accessible at lower energies in e^+e^- collisions, and LEP may find it.

II - Weak interactions

2.1 - Neutral current effects

High energy e^+e^- colliding beams provide an ideal testing ground for the properties of weak neutral currents, because neutral weak interactions are expected to dominate in some energy range, whatever the mass of the intermediate vector boson or bosons. Interference with electromagnetic processes gives effects which are extremely sensitive to the weak couplings, particularly for energies near the intermediate boson mass. There are three types of effects to be studied[5]:

a) Interference effects in the shape of the total cross sections. These are particularly sensitive to the weak vector coupling.

b) Angular asymmetries, which require a non-vanishing axial coupling.

c) Polarization effects, which require an interplay of both axial and vector couplings and provide direct evidence of parity violation.

In the rest of this section we give general formulae governing these effects. In section 2.2 we discuss $e^+e^- \to \mu^+\mu^-$ in detail, and in section 2.3 we comment on the possibility of extracting the weak coupling parameters of hadrons, assuming them to be composed

of coloured spin $\frac{1}{2}$ quarks, u, d, s, c, etc... We shall sometimes specialize to the SU (2) x U (1) Weinberg-Salam model,[3] but always consider more general couplings and arbitrary Z^o masses. We define the Z^o couplings to a pair of fermions $f\bar{f}$ by :

$$L_z = -m_z \left(\frac{G_F}{\sqrt{2}} \right)^{\frac{1}{2}} \bar{f} \gamma_\mu \left(\frac{v_f - a_f \gamma_5}{\sqrt{2}} \right) f \qquad (2.1)$$

and write $v_e \equiv v$, $a_e \equiv a$. We define γ_5 so that

$\left(\begin{matrix} L \\ R \end{matrix} \right) = \frac{1}{2} (1 \mp \gamma_5)$ is a $\left(\begin{matrix} \text{left} \\ \text{right} \end{matrix} \right)$ projection operator,

i.e. $v_f = a_f$ for a (V-A) coupling. We also introduce a parameter g defined by

$$g = \frac{G_F}{8\sqrt{2}\,\pi\,\alpha} \approx 4.4 \times 10^{-5}\ \text{GeV}^{-2}. \qquad (2.2)$$

The couplings v_f and a_f are defined so that in the Weinberg-Salam model

$$a_f = 2\,(I_3^L - I_3^R)_f, \qquad v_f = 2\,(I_3^L + I_3^R)_f - 4Q_f \sin^2\theta_w \qquad (2.3)$$

where Q_f is the electric charge, and $I_{3_f}^L$ and $I_{3_f}^R$ are the weak isospins of the left and right-handed fermion fields $\frac{1}{2}(1 \mp \gamma_5)f$ respectively. For simplicity, we will specialize our discussions of the Weinberg-Salam model to include only left-handed isospin doublets and right-handed singlets.

We than have

$$\begin{aligned} &a = a_\mu = -1 \ , \quad v = v_\mu = -1 + 4 \sin^2 \theta_w \ , \\ &a_\nu = 1 \ , \quad v_\nu = 1 \ , \\ &a_u = a_c = \ldots = 1, \ v_u = v_c = \ldots = 1 - 8/3 \sin^2 \theta_w \ , \\ &a_d = a_s = \ldots = -1, \ v_d = v_s = \ldots = -1 + 4/3 \sin^2 \theta_w . \end{aligned} \qquad (2.4)$$

The shapes of cross sections

Normalizing to the point-like QED cross section

$$\sigma_{pt} = \sigma(e^+e^- \to \gamma \to \mu^+\mu^-) = \frac{4\pi\alpha^2}{3s} \simeq \frac{87}{s(\text{GeV}^2)} \text{ nb} \qquad (2.5)$$

we find

$$R^f = \frac{\sigma(e^+e^- \to \gamma, Z \to \mu^+\mu^-)}{\sigma_{pt}} = Q_f^2 - 2\, sQ_f\, v\, v_f\, g\, \left(\left(\frac{s}{m_z^2} - 1\right) + \frac{\Gamma_z^2}{s-m_z^2}\right)^{-1}$$
$$+ s^2 g^2 (v^2+a^2)(v_f^2+a_f^2) \left(\left(\frac{s}{m_z^2} - 1\right)^2 + \frac{\Gamma_z^2}{m_z^2}\right)^{-1} . \qquad (2.6)$$

If both v and v_f are non-zero, the Breit-Wigner shape of the resonance will be deformed.

The cross section at resonance is given by [6]

$$\sigma(e^+e^- \to Z \to f\bar{f})_{peak} = \frac{4\pi\alpha^2}{3} \frac{m_z^4}{\Gamma_z^2} g^2(v^2+a^2)(v_f^2+a_f^2) \qquad (2.7)$$

so that at the peak

$$\frac{\sigma(e^+e^- \to Z^o \to f\bar{f})}{\sigma_{pt}} = \frac{9}{\alpha^2} B(Z^o \to e^+e^-)\, B(Z^o \to f\bar{f})$$
$$\approx 1.7 \times 10^5\, B(Z^o \to e^+e^-)\, B(Z^o \to f\bar{f}) \qquad (2.8)$$

where branching ratios are indicated as $B(Z^o \to e^+e^-)$, etc...

The partial widths

$$\Gamma(Z \to f\bar{f}) = \frac{m_z^3}{24\sqrt{2}\pi} G_F (v_f^2 + a_f^2) \qquad (2.9)$$

will be O(50 to 100) MeV if $m_z \sim 80$ GeV and $(v_f^2+a_f^2) = 1$ to 2, as expected in some models. Combining lepton-antilepton and quark-antiquark decays of the Z^o, and assuming that each species of quark comes in three identical colours, we would expect

$$\Gamma_z = \Gamma(Z \to \text{all}) = 0\ (1)\ \text{GeV} . \qquad (2.10)$$

(A considerable uncertainty in the width commes from $Z \to \nu\bar{\nu}$ decays. High energy physics gives almost no restriction in the number of neutrinos. Cosmology requires neutral particles less massive than the electron to have masses 0 (1) eV, and allows no more than 7

such neutrinos.[7] We know of no restriction on the number of neutral leptons more massive than the electron). From equation (2.10), we see that the Z width is likely to be considerably larger than the machine resolution at the same energy.

To be more specific, we turn to the standard Weinberg-Salam model. In this case

$$m_W = \sqrt{\frac{\pi\alpha}{\sqrt{2}\,G_F}}\;\frac{1}{\sin\theta_W} \quad , \quad m_Z \geq \frac{m_W}{\cos\theta_W} \tag{2.11}$$

where the equality for m_Zo is realized when the usual doublet of Higgs fields is used. (The experimental magnitudes of neutral current cross-sections suggest that m_Zo may have this minimum value). If the model is specialized to include just left-handed (V-A) charged currents connecting members of weak SU(2) doublets, then we can use formula (2.7) ; we then see that

$$\Gamma(Z^o \to \text{all}) \approx \frac{G_F\, m_Z^3}{24\sqrt{2}\,\pi}\left\{ (1+(1-4\sin^2\theta_W)^2)\, N_{L^-} + 2N_\nu + 3(1+(1-\tfrac{8}{3}\sin^2\theta_W)^2)\, N_p + 3(1+(1-\tfrac{4}{3}\sin^2\theta_W)^2) N_n \right\} \tag{2.12}$$

where N_{L^-}, N_ν, N_p and N_n are the numbers of charged leptons, neutrinos, charge 2/3 and charge -1/3 quarks respectively which have masses appreciably less than m_Zo/2. Table 1 lists weak current and Z^o parameters in the Weinberg-Salam model for a few values of $\sin^2\theta_W$ consistent with present experiments and including the value $\sin^2\theta_W = 3/8$ favoured in some schemes unifying strong with weak and electromagnetic interactions. We see that counting rates on the Z^o peak could be quite substantial, permitting detailed studies of Z^o decays. But a word of warning is in order : the Z^o width can only be increased, and the peak height decreased, by decay modes we have omitted, for example if there were a proliferation of quark flavours or neutrinos.

Forward backward asymmetry.

Defining θ as the angle between the incident e^- and the outgoing f, the differential cross section is given by

$$\frac{d\sigma_f}{d\cos\theta} \simeq \frac{\pi\alpha^2}{2s} \left\{ Q_f^2 (1+\cos^2\theta) - 2Q_f \chi (vv_f(1+\cos^2\theta)+2aa_f\cos\theta) + \chi^2((v^2+a^2)(v_f^2+a_f^2)(1+\cos^2\theta)+8vav_fa_f\cos\theta) \right\} \quad (2.13)$$

where we have defined

$$\chi \equiv g \frac{s\, m_z^2}{s-m_z^2} \quad (2.14)$$

and neglected the decay width Γ_z assumed $\ll m_z$.

The integrated asymmetry, defined by

$$A_f = \frac{\int_0^1 d\cos\theta\, d\sigma_f - \int_{-1}^0 d\cos\theta\, d\sigma_f}{\int_{-1}^1 d\cos\theta\, d\sigma_f} = \frac{F-B}{F+B} \quad (2.15)$$

is given by the expression

$$A_f = \frac{3}{2} \chi (-Q_f a a_f + 2vav_f a_f \chi) / (Q_f^2 - 2Q_f \chi vv_f + \chi^2(v^2+a^2)(v_f^2+a_f^2)) \quad (2.16)$$

and is bounded by $|A_f| \leq 3/4$.

A non-vanishing effect requires $a, a_f \neq 0$.

Polarization effects

Assuming that the beams are unpolarized, the differential cross-section as a function of the final fermion helicity is of the form :

$$\frac{d\sigma_f}{d\cos\theta} = \sigma_1 + h_f \sigma_2 \quad (2.17)$$

where $\sigma_1 = \frac{1}{2} \frac{d\sigma_f}{d\cos\theta}$ (2.18)

is given in eq (2.13) and

$$\sigma_2 = \frac{\pi\alpha^2}{2s} \chi \left\{ Q_f(va_f(1+\cos^2\theta) + 2av_f\cos\theta) - \chi (v_f a_f(a^2+v^2)(1+\cos^2\theta) + 2av(a_f^2+v_f^2)\cos\theta) \right\} \quad (2.19)$$

which is non zero provided either a and v_f or a_f and v are non-zero. Note that, apart from the pure QED term,

$$\sigma_1 \stackrel{+}{-} \sigma_2 \propto (v_f \stackrel{-}{+} a_f)$$

i.e.a right (left) handed fermion decouples if $v_f = \stackrel{+}{-} a_f$

The polarization dependence for the anti fermion is

$$d\sigma_{\bar{f}} = \sigma_1 - h_f \sigma_2 \qquad (2.20)$$

and the average helicity is given by :

$$\langle h_f \rangle = - \langle h_{\bar{f}} \rangle = \frac{\sigma_2}{\sigma_1} = H_f(\theta, s) \quad . \qquad (2.21)$$

If the beams were longitudinally polarized, the differential cross section as a function of the beam helicities would be :

$$\frac{d\sigma_f(h^+, h^-)}{d\cos\theta} = (1-h^+h^-)\sigma_1 + (h^- - h^+)\bar{\sigma}_2$$

$$= \sigma_1((1-h^+h^-) + (h^- - h^+)\bar{H}^f(s, \cos\theta))$$

where $h^{\stackrel{+}{-}} = h_{e^{\stackrel{+}{-}}}$, and $\bar{\sigma}_2$ is obtained from σ_2 by the substitution

$$a_f, v_f \leftrightarrow a, v \; .$$

However, it is argued in Appendix 5 that the beams are unlikely to be polarized at LEP energies.

The integrated average fermion helicities from unpolarized beams are :

$$\frac{\int_{-1}^{1} \sigma_2}{\int_{-1}^{1} \sigma_1} = H^f(s) = -H^{\bar{f}}(s) = \frac{2\chi a_f (Q_f v - \chi v_f(a^2+v^2))}{Q_f^2 - 2Q_f \chi v v_f + \chi^2(a^2+v^2)(a_f^2+v_f^2)} \qquad (2.23)$$

and similarly for the integrated cross section for polarized beams :

$$\frac{\sigma_f(h^+, h^-)}{\sigma_f(0, 0)} = 1 - h^+h^- + (h^- - h^+)\bar{H}^f(s) \; ,$$

$$H^f(s) \rightarrow \bar{H}^f(s) \quad \text{for } a_f, v_f \leftrightarrow a, v \quad . \qquad (2.24)$$

2.2 - $e^+e^- \to \mu^+\mu^-$

The formulae above simplify considerably for the muon case if e-μ universality is assumed, and display various qualitative features which are model independent.

Shape of the cross section .

Eq. (2.6) takes the form (neglecting Γ_z)

$$R^\mu = 1 + 2v^2\chi + (v^2 + a^2)^2 \chi^2. \qquad (2.25)$$

Since

$$\chi \lesseqgtr 0 \qquad \text{for } Q^2 \lesseqgtr m_z^2$$

the interference term is always negative below the resonance. The cross section ratio will have a minimum before the peak at the value

$$\chi = \frac{-v^2}{(v^2+a^2)^2} \quad \text{or} \quad \frac{s}{m_z^2} = \frac{\delta}{1+\delta} \ , \ \delta = \frac{1}{m_z^2 g} \ \frac{v^2}{(v^2+a^2)^2} \ . \qquad (2.26)$$

The cross section ratio at the minimum takes the value

$$R^\mu_{min} = 1 - \frac{v^4}{(v^2+a^2)^2} \qquad (2.27)$$

and will vanish if there is no axial vector coupling.

The ratio R^μ is plotted in fig. 2.1 for a Z mass of 83 GeV and various values of the weak couplings.

Forward backward asymmetry.

The differential cross section (2.13) takes the form :

$$\frac{d\sigma^\mu}{d\cos\theta} = \frac{\pi\alpha^2}{2s} \left\{ (1+\cos^2\theta) + 2\chi\,(v^2(1+\cos^2\theta)+2a^2\cos\theta) + \chi^2\,((v^2+a^2)^2\,(1+\cos^2\theta) + 8v^2a^2\cos\theta) \right\} \qquad (2.28)$$

and the integrated asymmetry is

$$A_\mu = \frac{3}{2}\chi\ (a^2+2v^2a^2\chi)\ /\ (1+2\chi v^2 + \chi^2(v^2+a^2)^2)\ . \qquad (2.29)$$

The integrated asymmetry as a function of s and for several values of the weak couplings, with m_z = 83 GeV, is shown in fig. 2.2.

Whatever the coupling strengths (provided $a \neq 0$), the Z-photon interference gives a negative asymmetry below the peak which goes through a minimum at the energy

$$s/m_z^2\Big)_{A_{min}} \simeq \frac{\varepsilon}{\varepsilon+1} \quad , \quad \varepsilon = \frac{1}{gm_z^2\ (a^2+3v^2)} \quad , \qquad (2.30)$$

goes through zero at

$$s/m_z^2\Big)_{A=0} = \frac{\beta}{\beta+1} \quad , \quad \beta = \frac{1}{gm_z^2\ v^2} \qquad (2.31)$$

and remains positive beyond the resonance. The value of the asymmetry at minimum :

$$A_\mu(\text{min}) = -\frac{3}{4}\ (1+2v^2/a^2)^{-1} \qquad (2.32)$$

provides a test for the presence of a vector coupling ; the minimum negative asymmetry A_μ = -0.75 is attained only for v = 0.

Provided the parameter

$$\rho \equiv 1/gm_z^2\ (a^2-v^2)$$

is negative or > 1 (requiring $a^2-v^2 < 3.3$ if m_z = 83GeV), there will be a maximum positive asymmetry, A_μ = + 0.75, at an energy relative to the Z-mass determined by the sign of a^2-v^2 :

$$s/m_z^2\Big)_{A_{max}} = \rho/(\rho-1) \qquad (2.33)$$

$$\text{or } A_\mu(\max)=0.75 \text{ at } \begin{cases} s < m_z^2 \\ s = m_z^2 \\ s > m_z^2 \end{cases} \quad \text{for} \quad \begin{cases} v^2 > a^2 \\ v^2 = a^2 \\ v^2 < a^2 \end{cases} .$$

Polarization effects allow a determination of the sign of v/a. The muon helicity is given by eqs. (2.17) to (2.21) with

$$\sigma_2 = -\frac{\pi\alpha^2}{2s} \chi\, av(1+\cos\theta)^2 (1+\chi(a^2+v^2)) . \tag{2.34}$$

The average muon helicity as a function of angle is :

$$H^{\mu^-}(s,\cos\theta) = \frac{-2\chi av(1+\chi(a^2+v^2))}{A(1+\cos^2\theta) + B\cos\theta} (1+\cos\theta)^2 \tag{2.35}$$

with

$$A = 1+2\chi v^2 + \chi^2(v^2+a^2)^2,$$
$$B = 4a^2\chi + 8a^2v^2\chi^2 .$$

The helicity is maximum in the forward direction :

$$H^{\mu^-}(s, +1) = \frac{-4\chi av\,(1+\chi(a^2+v^2))}{(1+2\chi(v^2+a^2)+\chi^2((a^2+v^2)^2+4a^2v^2))} \tag{2.36}$$

which becomes on resonance ($\chi\to\infty$)

$$H^{\mu^-}(m_z^2, +1) = -4av(a^2+v^2)/((a^2+v^2)^2 + 4a^2v^2) \simeq 0.93 \tag{2.37}$$

in the Weinberg-Salam model if $\sin^2\theta_w=0.35$, so that v/a = -0.4.

The cross section dependence on the beam polarization is as given in eqs. (2.22- 2.24) with

$$H^\mu \equiv R^\mu$$

because of μ-e universality. The angular averaged helicity function is shown in fig. 2.3 for two values of v/a. Near and beyond the resonance the sign of H reflects the V $\pm$ A nature of the weak coupling :

$$H \lesseqgtr 0 \quad \text{for } v/a \gtreqless 0, \tag{2.38}$$

but below the resonance the Z-photon interference flips the sign.

Obviously the effects are optimal for $|v/a|$ near one, but even in the Weinberg-Salam model the effect is sizeable, particularly in the forward direction (eq. (2.37)), where measurements are apparently most feasible. (The helicity vanishes in the backward direction except for $B \simeq A$, as in the case of a pure $V \pm A$ coupling ; then the helicity is independent of angle ($H = \pm 1$ for $v = \pm a$))

In summary, the s-dependence of the $e^+e^- \to \mu^+\mu^-$ cross section is sensitive to the vector coupling and also provides information on the relative axial coupling strength, for example from the non-vanishing of the cross section at maximum negative interference. The angular asymmetry measures primarily the presence of an axial coupling, but also yields information on $|v/a|$ through the maximum value of the negative asymmetry and the position in s relative to the Z-mass of the maximum positive asymmetry. However with the favored value of v extracted from the Weinberg-Salam model, the presence of a vector coupling will be difficult to establish. Polarization effects, which are inherently of interest as they would directly establish a violation of parity, are also a much better probe of a small vector coupling, and allow a determination of the relative sign of the vector and axial couplings. The muon helicity is found to be nearly unity in the forward direction even in the Weinberg-Salam model.

2.3 - Hadronic neutral currents

In principle e^+e^- colliding rings have an advantage over ν experiments as a laboratory for studying quark neutral currents. The reason for this is that the neutrino is scattered from a fixed target, which -at present energies at least- is dominated by u and d quarks. Except for possible non diagonal neutral couplings, $u \to c, t, \ldots$, $d \to b, \ldots$, there is little sensitivity to heavy

quark neutral couplings. Electron-positron annihilation, on the other hand, is a more democratic source of quarks; all species are-given sufficient energy- produced with equal ease. To the extent that one can "measure" the quantum numbers of the produced quarks, tests of the underlying quark structure of weak and electromagnetic interactions become possible. For example the Weinberg-Salam SU(2)xU(1) left-handed doublet structure

$$\begin{pmatrix} u \\ d_c \end{pmatrix}_L \quad \begin{pmatrix} c \\ s_c \end{pmatrix}_L \quad \begin{pmatrix} t \\ b_c \end{pmatrix}_L \quad ? \ \ldots \ ? \tag{2.39}$$

predicts an exact symmetry of neutral couplings under the exchanges

$$\begin{aligned} u &\longleftrightarrow c \ (\longleftrightarrow t, \ \ldots) \\ d &\longleftrightarrow s \ (\longleftrightarrow b, \ \ldots) \end{aligned} \tag{2.40}$$

as shown in equation (2.4), and one would like to test this prediction.

The difficulty is of course in identifying the quark quantum numbers. Optimistically we can hope that jet structure will be prominent at high energies and that the average quantum numbers of a jet, or of its leading particles, will reflect the quark quantum numbers. Even so, rather clean particle identification is required.

γ- Z interference effects

Assuming the electron couplings are determined (up to an overall sign) by $ee \to \mu\mu$, the shape of the hadronic cross section determines the average quark couplings :

$$v \langle Q_q \, v_q \rangle \qquad \text{and} \qquad \langle v_q^2 + a_q^2 \rangle \ .$$

There have been conjectures that in the true unified theory there is only one independent coupling constant (so that $\sin^2 \Theta_w$ is not a free parameter). In this case there is a theorem [8] that in the sum over annihilation cross sections

$$\Sigma_f \, \sigma(e^+e^- \to \gamma, \ Z \to \bar{f}f) \tag{2.41}$$

the γ, Z interference term

$$\Sigma_f \ \sigma_{\gamma z}^{annih} = 0 \qquad (2.42)$$

because γ and Z are orthogonal states. This result is not exact but corrections are expected to be small if there are no excessively heavy intermediate bosons($m \gg 100$ GeV). It is a curious fact that the "observed" Weinberg angle is close to the value $\sin^2\theta_w = 3/8$ required for (2.42) to be satisfied if the left handed doublet structure (2.39) is correct. Since the annihilation contribution to Bhabha scattering is equal to σ^{μ}, this means that

$$\sigma_{\gamma z}\ (ee \to \text{"hadrons"}) = -2\ \sigma_{\gamma z}^{\mu}$$

where "hadrons" means everything but μ and e pairs.* Unfortunately, if the Weinberg-Salam model is correct, reference to fig. 2.1 tells us that this relation practically reduces to 0 = 0. In order to give content to the result one would want to isolate non-vanishing contributions to the sum.

Even these are predicted to be small, since v_f is always small and

$$\sigma_{\gamma z}^{f} / \sigma_{pt} \simeq -2sQ_f \ v\ v_f\ gm_z^2\ /\ (s-m_z^2)\ . \qquad (2.43)$$

However in contrast to the muon case illustrated in fig. 2.1, the interference term (2.43) is somewhat enhanced relative to single photon exchange, $\sigma_{\gamma}^{f}/\sigma_{pt} = Q_f^2$, for quarks because of their smaller charges :

$$\frac{v_f}{Q_f} = \begin{cases} -0.5 \\ 0 \\ +1.5 \end{cases} \left(\sin^2\theta_w = \frac{3}{8}\right) \text{ or } \begin{cases} -0.4 \\ +0.5 \\ +1.6 \end{cases} (\sin^2\theta_w = 0.35) \text{ for } f = \begin{cases} e,\mu \\ u,c \\ d,s\ . \end{cases} \qquad (2.44)$$

It is barely conceivable that the u+c contribution could be separated from the s+d contribution by measuring the interference as a function of the average hadronic squared charge. It is slightly more conceivable that one could isolate events with net strangeness (or a leading strange particle) in each jet, but presumably c and s quarks would both contribute to this sample. One could perhaps evade this problem

* and excluding possible charged Higgs mesons.

by cutting on the x-value of the strange particle : c jets may well have strange particles at lower values of x than s jets. Even if the separation of s and c were impossible one could still test the equality (eq. 2.4).

$$\sum_{s,c} \sigma_{z\gamma} \Big/ \sum_{s,c} \sigma = \sum_{u,d} \sigma_{z\gamma} \Big/ \sum_{u,d} \sigma \qquad (2.45)$$

but since each sum over the interference term is separately equal to $\simeq - \sigma^{\mu}_{z\gamma}$ in the Weinberg-Salam model, one is again getting $0 \simeq 0$. On the other hand, observation of a large interference would obviously be newsworthy.

Angular asymmetries.

To the extent that it is measurable, the quark differential cross section allows the determination of $\langle a_q^2 \rangle$ and $\langle v_q^2 \rangle$ and the relative sign of $\langle a_q \, v_q / av \rangle$. It is a property of the Weinberg-Salam doublet structure that

$$a_f = 2 \, I_3 \quad , \qquad Q_f \, a_f > 0 \qquad (2.46)$$

so that the sign of the Z-γ interference term is universal. One also expects $a_f^2 > v_f^2$ in all cases, but the sign of v_f is sensitive to the Weinberg angle ; for $\sin^2 \theta_w \simeq 0.35$, v/a is negative for leptons and positive for quarks. The angular dependence is more complicated than for muons and will generally not vanish in the backward direction.

Can one study quark asymmetry through jet asymmetry ? Defining $\cos \theta$ as the angle of a positively charged jet, for example, relative to the e^-, and

$$A = (F-B) \, / \, (F+B) \Big|_{Q_{jet} > 0} \qquad (2.47)$$

one measures (hopefully)

$$\frac{4}{5} \, (A_u + A_c) + \frac{1}{5} \, (A_{\bar{d}} + A_{\bar{s}}) + \ldots \qquad (2.48)$$

Since the vector axial interference term changes sign for $f \to \bar{f}$, the two terms in (2.48) have opposite signs. The cancellation is not complete however and varies with angle and energy.

If one could instead select a jet of given strangeness, the quantity

$$A_{S_{jet=-1}} = \frac{1}{4} A_s \overset{+}{\sim} \frac{4}{5} A_c \qquad (2.49)$$

would not have a cancellation. Even assuming maximal particle identification, this would be feasable only if multi kaon (i.e. multi K_L) events were not too abundant.

Another possibility is that leading particles sufficiently reflect the quark quantum numbers so that the angular asymmetry of a fast π^+ or K^+ -or even D^+- would provide probes of the appropriate quark couplings.

Polarization effects.

If it were possible to measure the helicity of a leading Λ, this might reflect the quark helicity (eq. (2.23)), it would at least demonstrate parity violation. Events with fast Λ's are presumably rare, but the quarks can be substantially polarized (see fig. 2.3). Longitudinally polarized beams would not add information on quark couplings ; the dependence of σ on the $e^{\pm}$ helicity reflects only the $V \pm A$ nature of the electron couplings.

In summary, there is considerable theoretical interest in determining the weak couplings of quarks of all flavors. High-mass flavors will be more abundant in high energy e^+e^- annihilation than elsewhere . Under the optimistic assumption that hadronic jets maximally resemble quarks, useful measurements require ideal particle identification. The exception is the shape of the total hadronic cross section, though in the Weinberg-Salam model this is expected to show only tiny interference effects.

2.4 - Charged intermediate boson production

It has emerged from the previous sections that LEP is an ideal machine for studying weak neutral currents, and the Z^o in particular. We now turn to the charged bosons $W^{\pm}$. There are two production processes of interest :[9)]

a) single W production :

$$e^+e^- \rightarrow W^-e^+\nu \,,\; W^-\mu^+\nu \quad \text{etc...}$$

b) W^+W^- pair production

$$e^+e^- \rightarrow W^+W^- \,.$$

The first of these is potentially important because its threshold is essentially half that of process (b). If the cross section for (a) were substantial, it would be the most cost-effective W source. Unfortunately, the cross section for single W production will turn out to be $0\ (10^{-37})\ cm^2$ even at the Z^o peak, so that it may indeed be necessary to go to energies $E \simeq 150\ GeV > 2m_W$, where $\sigma(e^+e^- \rightarrow W^+W^-) = 0\ (10^{-35})cm^2$, in order to see $W^{\pm}$ in e^+e^- collisions.

Single W production.

In figure 2.4 we present the lowest order diagrams which contribute to single W production in the Weinberg-Salam model. (While the numerical results may differ for other weak and electromagnetic gauge models, the qualitative conclusions of this section should be unaltered.) Only a few of these diagrams give appreciable contributions to the cross sections. Very important are diagrams 2,4d and 2.4e involving γ-exchange, which can be regarded as a simple weak generalization of the well-known two-photon processes which are well described in the literature [10)]. We use [11)] the Weizäcker-Williams approximation of quasi real photons, in which $\sigma\ (e^+e^- \rightarrow e^{\pm}\,\nu\,W^{\mp})$ is simply related to $\sigma\ (\gamma\, e^{\pm} \rightarrow \nu W^{\pm})$. The cross section coming from diagrams 2.4d and 2.4e is

$$\sigma_\gamma (e^+e^- \to e^+ \nu W^-) = \frac{\alpha^2 G_f}{2\pi\sqrt{2}} \ln\left(\frac{s}{m_e^2}\right) F(a) \qquad (2.50)$$

where $a = m_W^2/s$ and

$$F(a) = \ln\left(\frac{1}{a}\right)\left(2+\frac{3}{2}a-\frac{3}{4}a^2\right) - (1-a)\left(5-\frac{13}{4}a+a^2\right) + (\ln a)^2\left(a-\frac{3}{4}a^2\right) \qquad (2.51)$$

The function F(a) is plotted in fig. 2.5, and is seen to be O (1) for interesting ranges of m_W^2/s. If we take $\sin^2\theta_W = 3/8$ we find

$$\sigma_\gamma(e^+e^- \to W^-e^+\nu) \approx \begin{cases} 8\times10^{-38}\ \text{cm}^2 \\ 5\times10^{-37}\ \text{cm}^2 \end{cases} \quad \text{for} \quad \sqrt{s} = \begin{cases} 80\ \text{GeV} \\ 150\ \text{GeV}. \end{cases} \qquad (2.52)$$

The diagrams 2.4d and 2.4e were calculated for lower energies some time ago by many authors. Results obtained with and without the Weizäcker-Williams approximation were similar, and agree in order of magnitude with the results (2.52). Note, however, that previous calculations did not use γ-W couplings of the Yang Mills type [11].

Diagrams 2.4a and 2.4f can be estimated to be of order 10^{-41}cm^2 or smaller for 80 GeV $\lesssim \sqrt{s} \lesssim$ 180 GeV, and thus negligible. We are left with diagrams 2.4b and 2.4c with the Z^o in the s-channel, which should give an important contribution due to the enhancement through the Z propagator. The partial decay width $Z^o \to W^-e^+$ is found to be

$$\Gamma(Z^o \to W^-e^+\nu) \approx 3\times10^{-7}\ \text{GeV} \qquad (2.53)$$

for m_W = 62 GeV and m_Z = 80 GeV. The $Z^o \to W^-e^+\nu$ branching ratio is therefore

$$B(Z^o \to W^-e^+\nu) \simeq \begin{cases} 3\times10^{-7} \\ 2\times10^{-7} \end{cases} \quad \text{for} \quad \Gamma_z = \begin{cases} 1\ \text{GeV} \\ 1.5\ \text{GeV}. \end{cases} \qquad (2.54)$$

The $W^-e^+\nu$ cross section at the Z^o resonance peak is therefore

$$\sigma_{\text{peak}}(e^+e^- \to Z^o \to W^-e^+\nu) \simeq \begin{cases} 5\times10^{-38}\text{cm}^2 \\ 2\times10^{-38}\text{cm}^2 \end{cases} \quad \text{for} \quad \Gamma_z = \begin{cases} 1\ \text{GeV} \\ 1.5\ \text{GeV}. \end{cases} \qquad (2.55)$$

Thus even at resonance the cross sections from diagrams 2.4b and 2.4c are as small as those from 2.4d and 2.4e. Even disregarding

any possible negative interferences between different amplitudes, the single W production cross section is disappointingly small.

$\underline{e^+e^- \rightarrow W^+W^-}$

The lowest order diagrams contributing to this process are shown in fig. 2.6.(The electron mass, and hence the s-channel Higgs meson exchange graphs, have been ignored.)It is convenient to introduce quantities

$$\beta = \sqrt{1-4a} \qquad L = \ln\left|\frac{1+\beta}{1-\beta}\right| \qquad (2.56)$$
$$K^2 = m_w^2 - \frac{s}{2} + \frac{s}{2}\beta\cos\theta$$

where θ is the centre of mass scattering angle. The angular distribution of the W^+W^- pair in the Weinberg-Salam model is then

$$\frac{d\sigma(e^+e^- \rightarrow W^+W^-)}{d\Omega} = \frac{\alpha^2}{32\sin^4\theta_w}\,\frac{\beta}{s}\sum_{ij} M_{ij} \qquad (2.57)$$

where
$$M_{\nu\nu} = F_1(\theta,s), \qquad M_{\gamma\gamma} = \sin^4\theta_w F_2(\theta,s),$$
$$M_{zz} = (\sin^4\theta_w - \tfrac{1}{2}\sin^2\theta_w + \tfrac{1}{8})\,\frac{s^2}{(s-m_z^2)^2}F_2(\theta,s),$$
$$M_{z\gamma} = 2\sin^2\theta_w(\tfrac{1}{4} - \sin^2\theta_w)\,\frac{s}{s-m_z^2}F_2(\theta,s), \qquad (2.58)$$
$$M_{\nu z} = (\sin^2\theta_w - \tfrac{1}{2})\,\frac{s}{s-m_z^2}F_3(\theta,s),$$
$$M_{\gamma\nu} = -\sin^2\theta_w F_3(\theta,s),$$

and
$$F_1(\theta,s) = \frac{2}{a} + \frac{\sin^2\theta}{2}\left\{\left(\frac{s}{K^2}\right)^2 + \frac{1}{4a^2}\right\}\beta^2,$$
$$F_2(\theta,s) = \beta^2\left(\frac{16}{a} + \left(\frac{1}{a^2} - \frac{4}{a} + 12\right)\sin^2\theta\right), \qquad (2.59)$$
$$F_3(\theta,s) = 16\,(1 + m_w^2/K^2) + 8\beta^2/a + \beta^2\,\frac{\sin^2\theta}{2}\left(\frac{1}{a^2} - \frac{2}{a} + 4\,\frac{s}{K^2}\right).$$

Integrating (2.59) over Ω in order to get the total cross section we find

$$\sigma\,(e^+e^- \to W^+W^-) = \frac{\pi\alpha^2}{8\sin^4\theta_w}\,\frac{\beta}{s}\sum_{ij}\bar{\sigma}_{ij} \equiv \sum_{ij}\sigma_{ij} \qquad (2.60)$$

where

$$\begin{aligned}
\sigma_1 &= \frac{2}{a} + \frac{1}{12a^2}\,\beta^2 + 4\left\{(1-2a)\,\frac{L}{\beta} - 1\right\} \\
\sigma_2 &= \frac{16}{a}\,\beta^2 + \frac{2}{3}\,\beta^2\left(-\frac{1}{2} - \frac{4}{a} + 12\right) \qquad (2.61)\\
\sigma_3 &= 16 - 32\,\frac{La}{\beta} + 8\,\frac{\beta^2 a}{a} + \frac{\beta^2}{3a^2}\,(1-2a) + 4(1-2a) - 16\,\frac{La^2}{\beta}
\end{aligned}$$

and in turn

$$\begin{aligned}
\bar{\sigma}_{\nu\nu} &= \sigma_1 \\
\bar{\sigma}_{\gamma\gamma} &= \sin^4\theta_w\,\sigma_2 \\
\bar{\sigma}_{zz} &= \left(\sin^4\theta_w - \tfrac{1}{2}\sin^2\theta_w + \tfrac{1}{8}\right)\frac{s^2}{(s-m_z^2)^2}\,\sigma_2 \\
\bar{\sigma}_{z\gamma} &= 2\left(\frac{1}{4} - \sin^2\theta_w\right)\sin^2\theta_w\,\frac{s}{s-m_z^2}\,\sigma_2 \qquad (2.62)\\
\bar{\sigma}_{\nu z} &= \left(\sin^2\theta_w - \tfrac{1}{2}\right)\,\frac{s}{s-m_z^2}\,\sigma_3 \\
\bar{\sigma}_{\gamma\nu} &= -\sin^2\theta_w\,\sigma_3 \ .
\end{aligned}$$

Using (2.60, 2.61 and 2.62) the total cross section can be written as

$$\begin{aligned}
\sigma\,(e^+e^- \to W^+W^-) = \frac{\pi\alpha^2\beta}{2\sin^4\theta_w s}\Bigg\{&(1+2a+2a^2)\,\frac{L}{\beta} - \frac{5}{4} \\
&+ \frac{m_z^2\,(1-2\sin^2\theta_w)}{(s-m_z^2)}\left(2a^2\left(1+\frac{2}{a}\right)\frac{L}{\beta} - \frac{1}{12a} - \frac{5}{3} - a\right) \\
&+ \frac{m_z^4\,(8\sin^4\theta_w - 4\sin^2\theta_w + 1)}{48\,(s-m_z^2)^2}\,\frac{\beta^2}{a^2}\,(1+20a+12a^2)\Bigg\}\ . \qquad (2.63)
\end{aligned}$$

In fig. 2.7 we have plotted $\sigma(e^+e^- \to W^+W^-)$ from equation (2.63) for three values of $\sin^2\theta_w$, corresponding to M_w between 50 and 70 GeV. We see that in all three cases $\sigma(e^+e^- \to W^+W^-) \approx 10^{-35}\,\mathrm{cm}^2$ at its maximum value, attained about 30 to 40 GeV above threshold. In the region of this peak, the pair cross section is more than an order of magnitude larger than $\sigma(e^+e^- \to W^-e^+\nu)$.

The contributions (2.62) of different diagrams to $\sigma(e^+e^- \to W^+W^-)$ are plotted in fig. 2.8 as functions of $\sqrt{s}$ for $\sin^2\theta_w = 3/8$, together with the interference terms. We observe that in the range of s considered $\sigma_{\nu\nu} > \sigma_{\gamma\gamma} > \sigma_{zz}$ and all interference terms are large and negative, indicating strong cancellations between the various diagrams, as expected in a gauge theory.

The normalized angular distributions (2.57, 2.58, 2.59) $\frac{1}{\sigma}\,\frac{d\sigma}{d(\cos\theta)}$ are presented for $\sin^2\theta_w = 3/8$ and various values of s in fig. 2.9. Notice a strong asymmetry in $\cos\theta$, with strong peaking near $\cos\theta = 1$ which gets more pronounced at higher energies. It is evident from eq. (2.58) that the ν exchange diagram is responsible for this peaking.

In summary, the single W production cross section is $O(10^{-37}$ to $10^{-38})\ \mathrm{cm}^2$ for $80 \leq \sqrt{s} \leq 190$ GeV, and therefore probably difficult to measure experimentally.

The cross section for $e^+e^- \to W^+W^-$ is $O(10^{-35})\ \mathrm{cm}^2$ for $130 \leq \sqrt{s} \lesssim 180$ GeV and $50 \lesssim m_w \lesssim 70$ GeV, and thus probably large enough to be measured.

The angular distributions for $e^+e^- \to W^+W^-$ are very asymmetric with strong forward peaking.

There are strong cancellations between different diagrams contributing to $e^+e^- \to W^+W^-$ even just above threshold.

These points imply that the process $e^+e^- \to W^+W^-$ is well suited for a study of the delicate interferences which make gauge theories

of weak and electromagnetic interactions renormalizable.

2.5 - Higgs Boson production

Intermediate vector bosons for weak interactions were suggested long before the advent of gauge theories. Gauge theories [2] themselves existed for a long time before people discovered how to give the gauge bosons masses and retain renormalizability using the Higgs mechanism. This is still an essential ingredient of all unified gauge theories of weak and electromagnetic interactions. Higgs couplings are often the only things which violate μ-e universality. Every weak gauge theory has at least one physical neutral Higgs boson, and the above observations suggest that looking for such particles should be an integral part of any programme to study weak interactions at high energies. Most of the discussion of this section centres on the single neutral Higgs boson H expected in the simplest Weinberg-Salam model.[3] In this case the Higgs boson could be much less massive than the $W^{\pm}$ and Z^{o}, and relatively easily accessible. Other possibilities exist : for example if Higgs particles are much heavier than the intermediate vector bosons, then their self-interactions would be large and a whole new stratum of strong interactions could emerge at centre of mass energies $\geqslant$ (200-300 GeV). We will ignore this incalculable speculative possibility here, and now restrict ourselves to conservative Higgs sectors.

In the standard Weinberg-Salam model, the Higgs boson couples to other particles with strengths proportional to their masses. Thus as soon as one can produce very heavy particles, the production of Higgs bosons via bremsstrahlung processes such as that of fig. 2.10 becomes non negligible, provided that the Higgs bosons themselves are not exceedingly heavy. Assuming there are no quarks as massive as the intermediate bosons, the Higgs mass is required [12] to be

greater than about 7 GeV. For the following estimates we assume

$$m_z^2 \gg m_H^2 \gg \Gamma_z^2/4 \ . \qquad (2.65)$$

Then the Higgs production cross section is maximal for $\sqrt{s} = m_z + \sqrt{2}\, m_H$ and the cross section for fig. 2.10a [13] is

$$\left.\frac{\sigma(Z+H)}{\sigma_{pt}}\right|_{max} = \frac{3}{64}\left(\frac{m_z}{38\text{GeV}}\right)^4 \frac{m_z}{2\sqrt{2}m_H}\,(1+v^2/a^2) \simeq \frac{25\ \text{GeV}}{m_H} \qquad (2.66)$$

for $\sin^2\theta_w \simeq 0.35$, $m_z \simeq 80$ GeV and $v/a = -0.4$, where v and a are the vector and axial $Z\mu\mu$ couplings and σ_{pt} was defined in (2.5). If $m_H/m_z \simeq 1/10$, the Z contribution to $ee \to \mu\mu$ is about five times greater than the γ contribution, so

$$\left.\frac{\sigma(Z+H)}{\sigma(\mu\mu)_{total}}\right|_{max} \simeq 0.5 \qquad (2.67)$$

for $m_z \simeq 80$ GeV $\simeq 10\, m_H$. Again because of the mass dependence of its couplings, a Higgs mesons of 8 GeV is expected [13] to decay mostly into charmed particles and heavy leptons.

Presumably the most reasonable signal is

$$e^+e^- \to Z_{\hookrightarrow l^+l^-} + H_{\hookrightarrow \text{hadrons}} \ . \qquad (2.68)$$

If the Z leptonic branching ratio is 0 (5) percent, this will be a few percent of the $\mu\mu$ signal at the optimal energy.

At higher energies the cross section is

$$\frac{\sigma(Z+H)}{\sigma_{QED(\mu\mu)}} = \frac{3}{64}\left(\frac{m_z}{38}\right)^4 \frac{m_z^2}{s-m_z^2}\,(1+v^2/a^2) \simeq 0.2 \qquad (2.69)$$

for $\sqrt{s} \simeq 200$ GeV, $m_z = 80$ GeV.

Below threshold for Z+H production the Higgs can be made via bremsstrahlung from a virtual Z, for example

$$e^+e^- \to H + \mu\mu \qquad (2.70)$$

as illustrated in fig. 2.10b. The cross section is

$$\frac{\sigma(H\mu\mu)}{\sigma(e^+e^-\to Z^0\to\mu^+\mu^-)} \simeq \frac{\alpha}{4\pi}\left(\frac{m_z}{38\text{GeV}}\right)^2 \frac{m_z^2}{s} \left\{\frac{(2m_z^2-s)}{s}\ln\left(\frac{m_z^2}{m_z^2-s'}\right) - \left(\frac{m_z^2-s}{m_z^2-s'}\right) - 1\right\}, \tag{2.71}$$

$$\sqrt{s'} = \sqrt{s} - m_H .$$

At resonance this becomes

$$\left.\frac{\sigma(H\mu\mu)}{\sigma(e^+e^-\to Z^0\to\mu^+\mu^-)}\right|_{\text{peak}} \simeq \frac{\alpha}{4\pi}\left(\frac{m_z}{38\text{GeV}}\right)^2 \left\{\ln\left(\frac{m_z}{2m_H}\right) - 1\right\} \simeq 1.5\times10^{-3} \tag{2.72}$$

for $m_z \simeq 80\text{GeV} \simeq 10m_H$. The total fraction of Higgs production at resonance should be similar :

$$\frac{\Gamma(Z\to H + \text{anything})}{\Gamma(Z\to\text{anything})} \simeq \frac{\Gamma(Z\to H\mu\mu)}{\Gamma(Z\to\mu\mu)} \simeq 10^{-3} \tag{2.73}$$

but presumably the $H\mu\mu$ channel is the most accessible experimentally. If the $Z^0\to\mu^+\mu^-$ branching ratio is O(10%) we get

$$\left.\frac{\sigma(e^+e^-\to H\mu^+\mu^-)}{\sigma(e^+e^-\to Z^0\to\text{all})}\right|_{\text{peak}} \simeq 0\ (10^{-4}). \tag{2.74}$$

Below the resonance, $m_H \ll s \ll m_z^2$, the cross section becomes

$$\frac{(e^+e^-\to H\mu^+\mu^-)}{\sigma_{pt}} \simeq \frac{\alpha}{24\pi}\ \frac{1}{(16)^2}\ \frac{s^3}{(38\text{GeV})^6} . \tag{2.75}$$

For models beyond the minimal Weinberg-Salam one, predictions may vary, but one might expect that because of the Higgs role in providing masses a correlation between mass and coupling may persist, at least for some of the Higgs scalars. There may also be charged Higgs scalars which would be produced electromagnetically (fig. 2.11) ; they might also identify themselves through a violation of μ-e universality

$$\Gamma(H^{\pm} \to \mu \nu) \overset{?}{>>} \Gamma(H^{\pm} \to e \nu) \qquad (2.76)$$

or by generally preferring to decay into heavy particles.

In summary, looking for Higgs bosons may be an important aspect of studying weak interactions at high energies.

If their masses are considerably less than m_{Z^o}, Higgs particles can probably be found in the debris of Z^o decay, and possibly at higher centre of mass energies in more background free conditions.

2.6 - Other weak processes

In this subsection we discuss a few more lowest order processes which may be important at high energy e^+e^- machines.

Charged lepton production

There is an extensive literature [14] on the production and decays of charged leptons $L^{\pm}$, and we do not discuss these questions in detail here. It is well known that the annihilation cross section $e^+e^- \to L^+L^-$ rises very rapidly above the threshold $s = 4m_L^2$. As soon as $\sqrt{s}/m_L \gtrsim 2.5$, the annihilation cross section will be well approximated by that given for $e^+e^- \to \mu^+\mu^-$ in equ. (2.6). In fact, at LEP energies the dominant mechanism for $L^{\pm}$ production is expected to be the two-photon process $e^+e^- \to e^+L^+L^-e^-$ illustrated in fig. (2.12), with a cross section [15]

$$\sigma(e^+e^- \to e^+L^+L^-e^-) \approx \frac{112\alpha^4}{9\pi} \frac{1}{m_L^2} \left(\ln\left(\frac{E_{beam}}{m_e}\right)\right)^2 \ln\left(\frac{E_{beam}}{m_L}\right). \qquad (2.77)$$

The probable decay modes of different types of charged heavy leptons have also been extensively studied. For a charged lepton with its own neutrino the principal decay modes are expected to be $L^+ \to e^+ \nu_e \bar{\nu}_L$, $\mu^+ \nu_\mu \bar{\nu}_L$, $h^+ \bar{\nu}_L$, where h^+ denotes a hadronic system with charge +1. For such a sequential lepton these decay modes are expected to occur in the ratio

$$B\,(L^+ \to e^+ \nu_e \bar{\nu}_L) : B\,(L^+ \to \mu^+ \nu_\mu \bar{\nu}_L) : B\,(L^+ \to h^+ \bar{\nu}_L) = 1 : 1 : 3N_D \qquad (2.78)$$

where 3 is the number of quark colours, and N_D is the number of weak doublets of quarks : $\binom{u}{d'}_L$, $\binom{c}{s'}_L$ etc...

Hadronic decay modes are expected to be mainly multiparticle, probably appearing in jets if m_L is sufficiently high. Low multiplicity decay modes such as $L^+ \to \pi^+ \bar{\nu}_L$ are expected to have small branching ratios for m_L much bigger than the range already explored at SPEAR and DORIS. Signatures of $e^+e^- \to L^+L^-$ would still include $(e\mu)$ events, and (ee) or $(\mu\mu)$ events with missing (neutrinos) energy or transverse momentum. Events with e^+ or μ^+ + hadrons + missing energy/momentum, or two pairs of hadron jets + missing energy/momentum, could also be produced by heavy leptons. Such events could also be produced by $e^+e^- \to W^+W^-$. A crucial distinction between this process and $e^+e^- \to L^+L^-$ may come from the $e^\pm$ and $\mu^\pm$ decay spectra, which have the characteristic two-body form from $W^\pm \to e^\pm \nu$, $\mu^\pm \nu$, whereas heavy lepton decays would have a softer three body spectrum from $L^\pm \to e^\pm \nu \bar{\nu}$. The leptonic decays of heavy leptons can also serve to analyze the heavy lepton's helicity, which may allow probes of the neutral current couplings of $L^\pm$ similar to the polarization effects discussed for muons in subsection 2.2.

Neutral lepton production[16)]

Massive neutral leptons L^o are expected in many gauge theories of weak and electromagnetic interactions. They cannot be produced by γ annihilation in lowest order, but can be produced by the Z^o in the direct channel. Taking this process alone would yield

$$R^{L^o} = \frac{\sigma(e^+e^- \to Z^o \to L^o\bar{L^o})}{\sigma_{pt}} \approx s^2 g^2 \frac{(v^2+a^2)(v_{L^o}^2 + a_{L^o}^2)}{\left(\left(\frac{s}{m_z^2} - 1\right)^2 + \frac{\Gamma_z^2}{m_z^2}\right)} \qquad (2.79)$$

where $\sigma_{pt} = \sigma(e^+e^- \to \gamma \to \mu^+\mu^-) = \frac{4\pi\alpha^2}{3s}$ as before. If we take

the Weinberg-Salam model with $v^2_{L^o} = a^2_{L^o} = 1$ and $\sin^2\theta_w = 3/8$, then we find $R^{L^o} > 1$ between $\sqrt{s} \simeq 60$ and 90 GeV. From table 1 we see that the branching ratio $Z^o \to L^o\bar{L}^o$ would be $O(20/N)\%$. Neutral lepton pairs could therefore be produced quite copiously, even if they cannot be produced by crossed-channel exchange diagrams.

Decay modes of L^o, $\bar{L}^o$ might include

$$L^o \to e^+\mu^-\nu,\quad e^+e^-\nu,\quad \mu^+\mu^-\nu,\quad \bar{\nu}\nu\nu,$$
$$e^+h^-,\quad \mu^+h^-,\quad \nu h^o \quad (h^{+-o} \text{ are hadron systems}) \tag{2.80}$$

in some model dependent combination. In certain models there is also $L^o \leftrightarrow \bar{L}^o$ mixing, so that processes such as $e^+e^- \to L^o\bar{L}^o$, $L^o \to \mu^+h^-$, $\bar{L}^o \to \mu^+h^-$ are possible. A final state $(\mu^+\pi^-)$ $(\mu^+\pi^-)$ would certainly be spectacular !

Crossed channel exchanges

In all the processes considered so far, except for $e^+e^- \to W^+W^-$, we have only considered direct channel annihilation graphs via γ or Z^o. An obvious process we have not considered is Bhabha scattering $e^+e^- \to e^+e^-$ with crossed channel γ and Z^o exchanges. Formulae for this process exist in the literature *, and we will not go into them here. We are interested now in more exotic crossed channel exchange processes.

The cross section from the annihilation graph of fig. 2.13a with B a vector meson can be written as

$$\sigma_s = \frac{G^2}{3}\,\frac{s}{(s-m_B^2)^2} \tag{2.81}$$

The crossed channel exchange of fig. 2.13b can be written as

$$\sigma_t = G'^2\left\{\frac{(s+2m_{B'}^2)}{sm_{B'}^2} - \frac{2(m_{B'}^2+s)}{s^2}\ln\left(1+\frac{s}{m_{B'}^2}\right)\right\} \tag{2.82}$$

where we have assumed a $V\pm A$ coupling, neglected fermion masses, and the normalization has been chosen so that $G' = G$ for equal couplings.

* see R. Budny, ref. 5.

Asymptotically,

$$\sigma_t/\sigma_s \rightarrow \left(\frac{3s}{2m_{B'}}\right)\frac{G'^2}{G^2}\ , \qquad (2.83)$$

so that at high energies processes of the type of fig. 2.13b dominate. At $\sqrt{s}$ = 200 GeV they are already enhanced :

$$s/m_W^2 \approx 11 \quad , \quad s/m_Z^2 \approx 6\ ,$$

for typical values $m_W \approx 60$, $m_Z \approx 83$ GeV. Explicit evaluation of (2.82) gives

$$\frac{\sigma_t(Z)}{\sigma_s(Z)} \approx 15 \quad , \frac{\sigma_t(W)}{\sigma_s(Z)} \approx 22(G_W/G_Z)^2\ , \qquad (2.84)$$

where with the standard couplings $(G_W/G_Z)^2 \approx 2.5$. Unfortunately the only process of type (2.82) occuring in the simplest Weinberg-Salam theory, aside from elastic e^+e^- scattering, is the experimentally unappetizing $e^+e^- \rightarrow \bar{\nu}_e\ \nu_e$. On the other hand, if there are any heavy unstable leptons, either charged or neutral, which couple to the electron they should be abundantly produced at high $\sqrt{s}$. This would probably be the case for any neutral lepton L^o with substantial decays into $\mu e \nu$ or e + hadrons, for example. Also, any exotic μ e coupling such as a non-diagonal neutral current or a $\Delta Q = 2$ current (mediated by an exotic boson W^{++} which could decay into μ^+e^+!) would give a significant deviation from the annihilation cross section for $e^+e^- \rightarrow \mu^+\mu^-$, provided G'/m_B is not too small.

2.7 - Higher order weak effects[14)]

One of the outstanding theoretical achievements of recent years has been the construction of renormalizable theories of weak interactions, allowing the calculation of higher order weak effects. Unfortunately, aside from a few notable exceptions such as the K_L-K_S mass difference, where hadrons are involved and confrontation of the theory is clouded by our ignorance of strong interaction effects, higher order W/Z exchange is essentially indetectable at low energies. However, at energies comparable to or larger than the masses of intermediate bosons where W/Z exchange becomes competitive with photon exchange, one might also expect observable higher order "weak" effects - i.e. those involving the exchange of more than one heavy vector meson.

In the existing renormalizable gauge theories which marry weak and electromagnetic interactions, their effects cannot be treated separately. A complete fourth order calculation of, say, $e^+e^- \to \mu^+\mu^-$ involves a large number of diagrams (some of which are illustrated in fig. 2.14) and evaluating them would be a long term project. Here we shall :

a) make some general remarks based on conventional wisdom, which may well be wrong, and

b) give some quantitative results for the imaginary forward amplitude for $ee \to \mu\mu$. Hopefully these are representative of the general order of magnitude of such effects.

General remarks

As a consequence of the construction of a well behaved finite theory uniting weak and electromagnetic interactions, higher order "weak" (an extra heavy boson exchanged) and "electromagnetic" (an extra photon) effects are of comparable order ; they may be somewhat

enhanced by logarithms : a $2n^{th}$ order contribution to a given amplitude may be

$$(\alpha \ln (s/m))^n.$$

For photon exchange m is necessarily small - m=a fermion mass or a photon energy cut off- and considerable enhancement may occur for moderate energies. For heavy boson exchange, no singularity occurs for massless fermions, so that $m = m_{W,Z}$, and the factor is order 1 for $\sqrt{s} \lesssim 200$ GeV. More intuitively, a relativistic fermion (fig. 2.15) can emit a quasi real photon ($k^2 \lesssim 0$), but emission of a quasi real W/Z requires energies such that the W/Z mass is itself negligible.

Thus we expect that at energies $\sqrt{s} \lesssim 200$ GeV multi-heavy boson exchange will give corrections $O(\alpha)$ to the $e^+e^- \to \mu^+\mu^-$ amplitude. An exception might occur in a theory where electron and muon number are not conserved, an example being the SU(3) model of Fritzsch and Minkowski [18] where the e^- and μ^+ belong to a common multiplet and the process of fig. 2.16 is allowed. Since generally annihilation processes behave asymptotically like 1/s, whereas an exchange process is asymptotically constant (2.82), we might expect the amplitude arising from fig. 2.16 to be (for $m_L^2 << m_W^2$)

$$\simeq \alpha \frac{s}{m_B^2} \ln (s/m_B^2)$$

relative to the lowest order annihilation term.

Imaginary forward amplitude

To partially substantiate the above remarks we have calculated some fourth order corrections to the forward imaginary amplitude. We invoke the optical theorem to make use of the calculations of section 2.4.

Higher order "weak" amplitudes -as opposed to purely electro-

magnetic amplitudes- are characterized by their helicity dependence (i.e. parity violation). Neglecting lepton masses, all the processes we are considering conserve helicity at the electron and muon vertices, so there are four independent amplitudes

$$A = A_{RR} + A_{LL} + A_{LR} + A_{RL} \cdot$$

The helicity flip amplitudes vanish in the forward direction, and purely electromagnetic processes are characterized by $A_{RR} = A_{LL}$. The lowest order contributions to the helicity dependent forward imaginary amplitude are illustrated in fig. 2.17 and 2.18, those of fig. 2.17 being "second order weak" in the sense defined above. Unitarity determines the imaginary part of the forward amplitude to be :

$$2\mathrm{Im}\ \langle \mu^+\mu^- | T | e^+e^- \rangle = \sum_n \langle \mu^+\mu^- | T | n \rangle \langle n | T^+ | e^+e^- \rangle \qquad (2.85)$$

and from μ-e universality

$$\langle \mu^+\mu^- | T | n \rangle \langle n | T^+ | e^+e^- \rangle \Big|_{\theta=0} = | \langle n | T | e^+e^- \rangle |^2 = 8s\, \sigma (e^+e^- \to n)$$

for $n \neq e^+e^-,\ \mu^+\mu^-,\ \bar{\nu}_e \nu_e,\ \bar{\nu}_\mu \nu_\mu$. (2.86)

To evaluate the WW intermediate state contribution (fig. 2.17a) we use the results of sections 2.4 for the $e^+e^- \to W^+W^-$ cross section, which we separate into left and right helicity contributions :

$$\sigma = \sigma_L + \sigma_R \cdot$$

Neutrino exchange contributes only to σ_L, photon exchange contributes equally to σ_L and σ_R and the decomposition of the Z-exchange contribution depends on the Weinberg angle. In the notation of section 2.4 :

$$\sigma_L(e^+e^- \to W^+W^-) = \sigma_{\nu\nu} + \sigma_{\nu\gamma} + \sigma_{\nu z} + \tfrac{1}{2}\sigma_{\gamma\gamma} + \frac{(1-2x)^2}{1-4x+8x^2}\sigma_{zz} + \frac{1-2x}{1-4x}\sigma_{z\gamma},$$

$$\sigma_R\,(e^+e^- \to W^+W^-) = \tfrac{1}{2}\,\sigma_{\gamma\gamma} + \frac{4x^2}{1-4x+8x^2}\,\sigma_{zz} - \frac{2x}{1-4x}\,\sigma_{z\gamma}\,, \tag{2.87}$$

where $x = \sin^2\theta_w$. The contribution of fig. 2.17a to the imaginary forward amplitude is

$$\mathrm{Im}\,A^{17a}_{L,R} = 4s\,\sigma_{L,R}\,(e^+e^- \to W^+W^-)\,. \tag{2.88}$$

The calculation of the contribution of figs 2.17b-d to the forward amplitude is straightforward. The bubble diagram of fig. 2.17b, summed over fermion states f, gives :

$$\mathrm{Im}\,A^{17b}_L = \frac{s^2}{(s-m_z^2)^2}\,\frac{4\pi\alpha^2}{3\sin^4 2\theta_w}\,(1-2x)^2\,(2-4x+\tfrac{16}{3}x^2)\,N_F$$

$$= \frac{(1-2x)^2}{4x^2}\,\mathrm{Im}\,A^{17b}_R \tag{2.89}$$

where N_F is the number of quark flavours (=number of lepton types). For comparison, the purely QED contribution of fig. 2.19 is

$$\mathrm{Im}\,A^{19}_L = \mathrm{Im}\,A^{19}_R = \frac{32\pi\alpha^2 N_F}{9} \tag{2.90}$$

The contributions of figs 2.17e and 2.17d are of the form

$$\mathrm{Im}\,A^{17c,d}_h = \tfrac{1}{2}\Big\{\frac{1}{4\pi}\,\frac{s}{s-m_1^2}\,\Big(2\Big(1+\frac{m_2^2}{s}\Big)\ln\Big(\frac{s+m_2^2}{m_2^2}\Big) - 3 - \frac{2m_2^2}{s}\Big)$$

$$g^h_{1ee}\,g^h_{1ff}\,(g^h_{2f\mu})^2 + e \leftrightarrow \mu\Big\} \tag{2.91}$$

where $h = L,R$; m_1 and m_2 are the masses of the vector mesons exchanged in the s and t channels, respectively, and the relevant couplings are

$$g^L_{z11} = -\frac{(1-2x)e}{\sin 2\theta_w} = \frac{(1-2x)}{-2x}\,g^R_{z11}\,,$$

$$g^L_{z\nu_1\nu_1} = \frac{e}{\sin 2\theta_w}\,, \quad g^R_{z\nu_1\nu_1} = 0\,, \tag{2.92}$$

$$g^L_{w1\nu_1} = \frac{e}{\sqrt{2}\sin\theta_w}\,, \quad g^R_{w1\nu_1} = 0\,,$$

$$1 = \mu, e\,.$$

We have not calculated the contribution of fig. 2.17e, but we expect that it should be similar to the WW contribution, except that the Z coupling to charged leptons is predominantly right handed ($g^L_{zl}/g^R_{zl} \simeq 0.32$). Logarithm terms arise when there is a t-channel exchange so only the neutrino exchange (left handed) contribution to the WW intermediate state is asymptotically enhanced. The different contributions of fig 2.17, relative to the lowest order QED forward amplitude

$$A^R_{QED}\ (\theta = 0) = A^L_{QED}\ (\theta = 0) = -2\ e^2 \qquad (2.93)$$

are evaluated in table 2 for $\sqrt{s}$ = 200 GeV and $\sin^2\theta_w = 0.38$, the asymptotic behavior is also indicated.

For comparison consider the contribution of the L^+L^- intermediate state to the imaginary backward ($\theta_{\mu^+e^-} = 0$) amplitude. Assuming (this does not correspond to any specific model, but is illustrative of the high energy dependence) a V-A amplitude and that $A\ (L^+L^- \to e^+e^-) = A\ (L^+L^- \to \mu^+\mu^-)$, we may use unitarity and the cross section of eq (2.82) to write

$$\text{Im}\ A^{16}_{L\ \text{or}\ R} \equiv 4s\,\sigma^t = 4G'^2 \left\{ \frac{s+2m_B^2}{m_B^2} - \frac{2(m_B^2+s)}{s}\ \ln\left(1+\frac{s}{m_B^2}\right) \right\}$$

$$\xrightarrow[s\to\infty]{} 4\,G'^2\,\frac{s}{m_B^2} \qquad . \qquad (2.94)$$

If the couplings are those of the usual charged W,

$$4G_w^2 / 2\,e^2 = m_w^4\ G_F^2/\pi\,e^2 \simeq 4.5\times10^{-3}$$

and the second order effect could become appreciable for $s >> m_B^2$ but for $\sqrt{s} \simeq 200$ GeV, $m_B \simeq 60$ GeV, it is still only 3 or 4 per cent.

As anticipated the higher order weak effects are of the same order as electromagnetic corrections. They can induce an apparent T-violation which is in principle distinguishable from pure QED effects by its helicity dependence, i.e. parity violation, (but not

from interference of 2γ with single Z exchange). Such effects are extremely hard to measure ; for a two-body final state a double spin correlation is necessary : $\langle (\vec{\sigma}_1 \times \vec{\sigma}_2).\vec{p} \rangle$.

III - Strong interactions

3.1 - Looking for new quark thresholds

It is generally believed that e^+e^- annihilation is a very egalitarian source of quarks. Above threshold, the annihilation production rate is just given by the quark charges in the low energy regime where electromagnetism is dominant, or by the weak current couplings which are dominant near the Z^o pole. This situation contrasts with electroproduction, where the valence quarks dominant at presently accessible energies have no exotic quark flavours. At very high energies in electroproduction, the sea of quark-antiquark pairs may be relatively more important and flavour symmetric at very large Q^2. But for new quark flavours with masses $\geqslant 20$ GeV the cross sections and signal to background ratio in electroproduction do not seem likely to compete with e^+e^- annihilation, at least in the Z^o peak. The future possibilities for new flavour production in neutrino production are unclear, depending crucially on the existence of new charged (e.g. a right handed $\binom{u}{b}_R$ coupling) or non diagonal neutral currents which can use valence quark flavours to produce new high mass flavours. In any case a new generation of fixed target machines is probably necessary for obtaining neutrino beams capable of generating new quarks with masses $\geqslant 20$ GeV, which is the range of interest to LEP.

It is not clear that new flavour production will still be interesting at LEP energies, but e^+e^- annihilation may be the best machine to do it. To say that is not to say that analyzing a new

flavour threshold will be easy. We cannot expect a repetition of the charm experience of SPEAR and DORIS. We now analyze in turn some possible ways of diagnosing a new quark threshold at LEP.

Threshold in hadron production

This was historically [19] the first indication of a new threshold in e^+e^- annihilation. It has not yet been elucidated, but the rise in $R \equiv \frac{\sigma(e^+e^- \to \text{"hadrons"})}{\sigma(e^+e^- \to \mu^+\mu^-)}$ is now commonly attributed to a coincidence between charm and heavy lepton thresholds. Any future rises in R would be less dramatic, according to conventional ideas. We can distinguish two limiting physical situations, where R is dominated by annihilation by a photon ($R = R_\gamma$), and by a Z^o boson (R_z) respectively. The fractional increases in R are

$$\frac{\Delta R_\gamma}{R_\gamma} = \frac{4\Delta N_p + \Delta N_n + 3\Delta N_{HL}}{4\,N_p + N_n + 3\,N_{HL}}$$

$$\frac{\Delta R_z}{R_z} = \frac{\left\{ \begin{array}{l} 3(2-\frac{16}{3}\sin^2\theta_w+\frac{64}{9}\sin^4\theta_w)\Delta N_p+3(2-\frac{8}{3}\sin^2\theta_w+\frac{16}{9}\sin^4\theta_w)\Delta N_n \\ +\,(2-8\sin^2\theta_w+16\sin^4\theta_w)\Delta N_{HL} \end{array} \right\}}{\left\{ \begin{array}{l} 3(2-\frac{16}{3}\sin^2\theta_w+\frac{64}{9}\sin^4\theta_w)N_p+3(2-\frac{8}{3}\sin^2\theta_w+\frac{16}{9}\sin^4\theta_w)N_n \\ +\,(2-8\sin^2\theta_w+16\sin^4\theta_w)N_{HL} \end{array} \right\}} \qquad (3.1)$$

where N_p and N_n are the numbers of charge 2/3 and charge -1/3 quark colour triplets, and N_{HL} the number of heavy leptons, below threshold. The Δ quantities are the increases in these numbers at the new threshold. Assuming that $N_p = N_n = 3$ and $N_{HL} = 1$, which is as good an estimate as any other of the PETRA/PEP contribution to our knowledge, we find

$$R_\gamma = 6\,, \quad \frac{\Delta R_\gamma}{R_\gamma} = 22\%\ ,\ 5\%\ ,\ 17\% \qquad (3.2)$$

for a ΔN_p, ΔN_n, $\Delta N_{HL} = 1$ respectively. Bearing in mind the uncertainties in present day measurements of R, and the lower data

rate expected at LEP outside the Z^o peak, it is questionable whether any of the increases (3.2) would be easy to detect. Assuming $\sin^2 \theta_w = 3/8$ we find for the same numbers of quarks and leptons

$$R_z = 17.2 \qquad \frac{\Delta R_z}{R_z} = 14\%,\ 17\%,\ 5\% \tag{3.3}$$

and the same remarks about detection difficulties apply, possibly unless a new threshold were very close to the Z^o peak. It is clear that looking for a new threshold by looking at a change in the total hadron production rate is not an attractive proposition. It will probably be nessary to look for thresholds in classes of special events, possibly including the following (we discard out of hand the possibility of looking for peaks in invariant mass plots).

Threshold in lepton production

A signature of the threshold in e^+e^- annihilation at 4 GeV is the appearance of two classes of events containing prompt leptons : (μe) events [20] commonly assigned to heavy lepton decays, and (eK)[21] events commonly associated with charmed particles. We expect naive quark and lepton counting to be a reasonable estimate of semileptonic branching ratios of future "supercharmed" hadrons, or heavy leptons. Thus

$$\begin{aligned} &B(\text{supercharm} \to e + \nu + X) \approx B(\text{supercharm} \to \mu + \nu + X) \\ &\approx B(\text{heavy lepton} \to e + \nu + \nu) \approx B(\text{heavylepton} \to \mu + \nu + \nu) \\ &\approx \frac{1}{3N_D + N_{HL} + 2} \approx (5 \text{ to } 10)\ \% \end{aligned} \tag{3.4}$$

where we have used N_D = the number of weak doublets of quarks such as $\begin{pmatrix} u \\ d_c \end{pmatrix}_L$, $\begin{pmatrix} c \\ s_c \end{pmatrix}_L$ etc. with masses appreciably below the decaying particle mass. Signatures of a new threshold in e^+e^- annihilation might therefore include:

- A jump in the single lepton rate, and the rate of opposite sign two lepton events, of around 25% : this low number because the branching ratio (3.4) is smaller than experimental indications

of (10-20) % for both charmed particle and heavy lepton decays. Probematic because of low statistics ?

- A threshold in "same-sign" dileptons, or in events with more than two prompt leptons. These could result from sequences of decays like

$$e^+e^- \rightarrow \begin{cases} \underline{\text{supercharm}} \rightarrow \mu^- + \nu + \text{ ordinary hadrons} \\ \text{supercharm} \rightarrow \text{charm} + \text{ordinary hadrons} \\ \qquad\qquad\qquad\quad \hookrightarrow \mu^- + \nu + \text{ordinary hadrons} \end{cases}$$

and so on. If PEP and PETRA find more quarks, the threshold for such events may already be passed before LEP energies.

New narrow resonances

Searches for these are hampered by the fact that the integral under a narrow vector resonance peak V

$$\int dE_{cm} \quad \sigma(e^+e^- \rightarrow V \rightarrow \text{all}) = \frac{6\pi^2}{m_V^2} \Gamma(V \rightarrow e^+e^-) \qquad (3.5)$$

is expected to decrease roughly as m_V^{-2} for high mass vector mesons, since $\Gamma(V \rightarrow e^+e^-)$ is not expected to increase much as m_V increases (Phenomenologically $\Gamma(V \rightarrow \gamma \rightarrow e^+e^-) \propto Q_q^2$, with the appropriate modifications to take mixing into account, seems a good approximation for vector mesons containing quarks with charge Q_q).

Problems may also arise from the energy resolution of the beams : if $\Delta E/E \sim 10^{-3}$ as projected, then any narrow peak will be smeared over a larger spread in nominal energy than at lower energy e^+e^- machines. If this spread becomes comparable with the separation between successive radial excitations (recall $m(\psi') - m(J/\psi) < m(\rho'(1600)) - m(\rho(770))$), then the splayed-out "hidden supercharm" peak will probably be no higher than the rise in R due to the subsequent "naked supercharm" threshold, as illustrated in fig. 3.1. In the worst case, the narrow resonances could even get smeared indistinguishably with each other and the "naked supercharm" thresholds.

It has often been remarked that the strong decays of the J/ψ are so suppressed relative to that already observed for the ϕ (Zweig rule ?), that the dominant decays of "hidden supercharmed" vector mesons might be via an intermediate photon, as indicated in fig. 3.2a. Close to the Z^o pole, the dominant decays of such vector mesons might actually be via the Z^o (Axial vector mesons could also be produced by the Z^o, but their couplings are suppressed in the model discussed later in this section) as indicated in fig. 3.2b

$$\frac{\Gamma(V\to\gamma\to e^+e^-)}{\Gamma(V\to Z^o\to e^+e^-)} = \frac{Q_q^2\,(m_v^2 - m_z^2)^2}{g^2\, m_z^4\, m_v^4 (1+(1-4\sin^2\theta_w)^2)(1-4|Q_q|\sin^2\theta_w)^2} \qquad (3.6)$$

where g was defined in equation (2.2). The ratio (3.6) would fall below 1 for a bound state of charge -1/3 quarks with $|m_v - m_z| \lesssim 15$ GeV. The larger electronic decay width would not necessarily imply great visibility for V : the total hadronic cross section would be enhanced by the Z^o in a similar way.

Competitive with the above decay modes could be the weak decay of one of the component supercharmed quarks shown in fig. 3.2c, perhaps

$$\Gamma\,(q\to q'\,e\,\nu) \approx \frac{1}{192\pi^3}\; G_F^2\;\; m_q^5 \qquad (3.7)$$

for $m_q \gg m'_q$. With all the quarks at our disposal, the total weak decay width $\approx 10\times\Gamma(q\to q'e\nu)$ could well overtake $\Gamma(V\to\gamma\to e^+e^-)$ = O(1) keV for $m_q > 20$ GeV ($m_v > 40$ GeV). This would further confuse the location of a new quark threshold. With sufficient malice, one could imagine a vector meson V with

$$\Gamma(\text{neutral weak current}) > \Gamma(\text{charged weak current}) > \Gamma(\text{electromagnetic}) > \Gamma(\text{strong})\ . \qquad (3.8)$$

May be this apparent paradox should teach us something profound.

In the above qualitative remarks we have avoided using any specific model for "hidden supercharmed"mesons, as none is generally accepted. To go quantitative, we use a <u>very specific, controversial and unproven</u> model, the " charmonium " one of Appelquist and

Politzer [22]. Using it (fig. 3.2d) we can calculate

$$\Gamma(V \to \gamma \to e^+e^-) = \tfrac{1}{2}\,(Q_q \alpha)^2\,(\tfrac{4}{3}\,\alpha_s)^3\,m_q\ ,$$

$$\frac{\Gamma(V \to \text{hadrons})}{\Gamma(V \to \gamma \to e^+e^-)} = \frac{(\pi^2 - 9)\ \frac{5}{18}\ \alpha_s^3}{\frac{9}{4}\,\pi\,(Q_q\,\alpha)^2}\ , \qquad (3.9)$$

$$m_V = 2\,m_q - (\tfrac{4}{3}\,\alpha_s)^2\ \frac{m_q}{4}\ ,$$

where $$\alpha_s \approx \frac{1}{4 + \frac{25}{12\pi}\ \ln\,(m_V^2\,/10\ \text{GeV}^2)} \qquad (3.10)$$

is the asymptotically free quark- gluon coupling constant (the form (3.10) for α_s has the correct asymptotic form for an SU(3) colour gauge theory with 4 flavours of quark, and $\alpha_s = 1/4$ for $V = J/\Psi$ (3100), consistent with the e^+e^- branching ratio of this state), m_q and Q_q are the heavy quark mass and charge respectively.

The results of (3.9) and (3.10) are given in Table 3, for different choices of the heavy quark mass. We see that <u>in this model</u> the peak integral (3.5) does indeed fall rapidly as the mass increases, that the lowest lying narrow resonance does not get blurred into the "naked supercharm" threshold, while the spectacular inversion (3.8) of decay widths is not inconceivable.

<u>No-jet events</u>

One other possibility for detecting a new threshold that we have considered involves looking for events which are not jet-like. Suppose that high energy hadronic final states due to light quarks have a predominantly two-jet structure, as suggested by SPEAR data[23] and naive parton ideas. Near threshold, events due to decays of new "naked supercharmed" mesons or heavy leptons may be rather spherically symmetric. Monte Carlo programs based on the SPEAR data suggest that the sphericity distribution from two-jet events will be drastically different from such isotropic events. It may be much easier to

isolate this special class than look for small changes in the totality of hadronic events.

In summary:- Diagnosing a new quark threshold at LEP by a rise in hadron or prompt lepton production looks rather difficult.

- Finding new narrow resonances also looks very difficult. The states probably have intriguing properties, but a repeat of the $J/\psi/\psi'/P_c/\chi/X$ drama seems unlikely at LEP energies.

- The best bet for locating a new threshold may be the onset of a new class of almost isotropic hadronic events, and their disappearance at higher energies.

3.2 - The hadronic contiuum

If quarks do not escape from their confining "bag" when given a centre of mass energy of 100 GeV, we may learn a lot about the confinement mechanism by looking at the hadronic continuum. We may learn things about the strong interactions which cannot be learnt with any other machine, except possibly electron-proton colliding rings. It may be that one of the naive parton or bag models is correct with perfect scaling and the high energy cross section always appearing as two thin jets. Alternatively...

Scaling violations

There are indications of scaling violations in deep inelastic scattering. These resemble qualitatively the predictions of renomalizable field theories[24], which suggest that deep inelastic structure functions $F(x, q^2)$: $x = -q^2/2\nu$ should shift towards $x = 0$ as $q^2 \to -\infty$ (see fig. 3.3). The present experimental situation with regard to scaling violations in e^+e^- annihilation is confused by the existence of new particle thresholds. There are suggestions that in renormalizable field theories single particle distributions $\bar{F}(\xi, s)$: $\xi = s/2p.q$ in e^+e^- annihilation should shift towards

$\xi = \infty$ as $s = q^2 \to +\infty$ (see fig.3.3). Unlike the case in electroproduction, we know of no unimpeachable calculation of these scaling violations. To guess them, we recall that in many naive parton models if $F(x,q^2) \simeq A(1-x)^n$ as $x \to 1^-$, then also $\bar{F}(\xi,q^2) \simeq \bar{A}(\xi-1)^n$ as $\xi \to 1^+$, albeit with $\bar{A} \neq A$ in general.

It may be that scaling violations in $F(x,q^2)$ as $x \to 1^-$ also give indications of the magnitudes of scaling violations in $\bar{F}(\xi,q^2)$ as $\xi \to 1^+$. If that is so, reference to calculations for deep inelastic electroproduction suggest that the energies of LEP may not be required for seeing scaling violations in e^+e^- annihilation [24]. On the other hand, electroproduction calculations suggest that $q^2 = O(10^4)$ GeV^2 may be necessary to discriminate between the scaling violations predicted by different field theoretic possibilities, such as asymptotically free gauge theories and fixed point theories. Hadronic decays of the Z^o would give a much higher event rate at high time-like q^2 in e^+e^- annihilation than is available in electroproduction where high space-like q^2 events are suppressed by propagator factors.

Thus we think that scaling violations in e^+e^- annihilation may be a source of information about field theories of the strong interactions as rich as the corresponding effects in electroproduction. Electron-positron annihilation might even be superior from this point of view, but the theory of inclusive distributions in e^+e^- annihilation is relatively underdeveloped by comparison with electroproduction.

Jets

One of the most beautiful recent discoveries[23] in e^+e^- annihilation has been the predominance of two-jet hadronic events at $E_{cm} \gtrsim 6$GeV. These are widely believed to reflect a fundamental process $e^+e^- \to \gamma \to q\bar{q}$, the angular distribution $\propto (1+\cos^2\theta)$ reflecting fundamental spin $\frac{1}{2}$ parton constituents as shown in fig. 3.4. What

may happen to jets at higher energies ?

Two jets with hadron transverse momenta fixed ? This is predicted by the sort of naive parton model that gives exact scaling. It would give highly collimated beams of hadrons, whose identification might be difficult. The orientations of the jets could give useful information about quark neutral current couplings, as discussed in section 2. For this purpose, fast K/π separation would be useful for separating out events due to strange quarks assuming that quantum numbers (I_3, S, C) are indeed reflected in the jets as sometimes believed. The production of heavier quarks may be expected to yield final states with no apparent jet structure close to threshold. They probably yield final state hadrons at low momenta—c.f. the pattern of scaling violations around the 4 GeV threshold in e^+e^- annihilation, where almost all the increase is found at low momenta.

Two jets with growing transverse momenta ? It has been suggested[15] on the basis of some field theories that $\langle p_t \rangle \sim E_{cm}$ at high energies. Jets would still carry quark quantum numbers, but there would be no "collimation catastrophe".

Multi-jet events ? Field theories have also been used to suggest[26] such events, reflecting fundamental processes with more than two quark-antiquark constituents, as indicated in fig. 3.5. These events could be connected with scaling violations in inclusive hadron distributions. The more fundamental constituents in a given event, the smaller the energy fraction each one of them possesses on average, and so the smaller the possible energy of a final state hadron. In a fixed point field theory, such multi-constituent, multi-jet events might dominate at high energies. In asymptotically free theories, the interconstituent coupling $\alpha_s \to 0$ as $q^2 \to \infty$, and we might expect two-jet $e^+e^- \to q\bar{q}$ events to be dominant, with the most important corrections three-jet events reflecting $e^+e^- \to q\bar{q}$ + gluon[27] as illustrated in fig. 3.6.

No-jet events ? As mentioned above, these could be a signature for a new heavy particle threshold. More generally, all the above remarks about jets are speculations since the transformation of constituents into final state hadrons is an infra-red problem not understood at present. Perhaps $e^+e^- \rightarrow q\bar{q}$ two-jet events are an accidental phenomenon which disappears at higher energies. Maybe three or more-jet events blur into a quasi-isotropic blob at higher energies.

In summary: Scaling violations and jet structures in high energy e^+e^- collisions could be important discriminators between different parton and field theory models of strong interactions.

3.3 - Unifying strong, weak and electromagnetic interactions

Many people believe such a grand unification will be made at some time, though there is no consensus as to how to achieve it. Grand unification may be the most pressing physical problem when LEP is operating. Within the gauge theory framework, most schemes[28] involve new interactions, weaker than the weak and mediated by heavier intermediate vector bosons. These interactions may either change flavours as shown in fig. 3.7a, or change leptons into quarks as shown in fig. 3.7b. Estimates of the masses of the new flavour changing or leptoquark bosons vary between 200 and 10^{19} GeV. Such models also predict $\sin^2\theta_w$, common values obtained being 3/8 and 3/4. However these predictions apply to the ratio of weak SU(2) and U(1) coupling constants at the mass scale of the next stage of unifying bosons. Since coupling constants are energy dependent according to the renomalization group, the value of $\sin^2\theta_w$ at mass scales $O(m_W, m_Z)$ will in general differ from the prediction of 3/8 or 3/4. Experimentally, $\sin^2\theta_w$ is close to 3/8, and a precision measurement of it may help fix the next intermediate boson mass scale.

More interesting would be the direct search for new interactions in either $e^+e^- \rightarrow \mu^+\mu^-$ or $e^+e^- \rightarrow$ hadrons. It follows from equations (2.81) and (2.82) that the ratio of the crossed channel exchange cross section to the direct channel Z^o contribution is :

$$\frac{\sigma_t\,(B)}{\sigma_s\,(Z)} \approx \frac{(s-m_z^2)^2}{m_B^4} \qquad \text{for } m_B^2 \geqslant s \,. \tag{3.11}$$

The ratio (3.11) could be significant if m_B is close to the lower limit of 200 GeV mentioned above. Once again, centre of mass energy is clearly at a premium in looking for such an effect.

Table 1

$\sin^2\theta_W$	0.30	0.375	0.45
$m_{W^\pm}$ (GeV)	68	61	56
m_{Z^0} [a] (GeV)	81	77	75
Γ_{Z^0} [b] (GeV)	0.60N	0.50N	0.47N
$B(Z^0 \to e^+e^-)$	$\frac{0.10}{N}$	$\frac{1}{8N}$	$\frac{0.16}{N}$
$\Sigma_\nu B(Z^0 \to \nu\bar{\nu})$	0.20	0.20	0.20
$B(Z^0 \to u\bar{u}) = B(Z^0 \to c\bar{c})$	$\frac{0.31}{N}$	$\frac{0.31}{N}$	$\frac{0.31}{N}$
$B(Z^0 \to d\bar{d}) = B(Z^0 \to s\bar{s})$	$\frac{0.40}{N}$	$\frac{0.38}{N}$	$\frac{0.34}{N}$
$\left[\frac{\sigma(e^+e^- \to Z^0 \to all)}{\sigma_{pt}}\right]_{peak}$	$\frac{17000}{N}$	$\frac{21000}{N}$	$\frac{27000}{N}$
$\left[\frac{\sigma(e^+e^- \to Z^0 \to \mu^+\mu^-)}{\sigma_{pt}}\right]_{peak}$	$\frac{1700}{N^2}$	$\frac{2600}{N^2}$	$\frac{4400}{N^2}$
$[\sigma(e^+e^- \to Z^0 \to all)]_{peak}$ (nb)	$\frac{230}{N}$	$\frac{310}{N}$	$\frac{420}{N}$
$[\sigma(e^+e^- \to Z^0 \to \mu^+\mu^-)]_{peak}$ (nb)	$\frac{23}{N^2}$	$\frac{38}{N^2}$	$\frac{66}{N^2}$

a) These values are the minimal ones corresponding to a Higgs doublet.

b) These and subsequent numbers assume equal numbers N of $L^\pm$, ν, charge $^2/_3$ and charge $-^1/_3$ quarks, which need not necessarily be the case (there may be more neutrinos kinematically accessible, for example).

Table 2

Contributions of the diagrams of Fig. 2.17 to the forward imaginary amplitude for $e^+e^- \to \mu^+\mu^-$ in the Weinberg-Salam model with $\sin^2\theta_W = 0.38$. The contributions are normalized to the forward amplitude for $e^+e^- \to \gamma \to \mu^+\mu^-$: $r_h = (\mathrm{Im}\, A_h / A_h^{QED})_{\theta=0}$, and N_F is the number of quark flavours.

Graph	B = 200 GeV		$s \to \infty$	
	r_L	r_R	r_L	r_R
a)	2×10^{-2}	$\sim 10^{-4}$	$1.2 \times 10^{-2} \ln\left(\frac{s}{m_W^2}\right)$	1.7×10^{-3}
b)	$10^{-1}\, r_R$	$\frac{N_F}{4} \times 10^{-3}$	$10^{-1}\, r_R$	$0.18 \times 10^{-3}\, N_F$
c)	-3×10^{-3}	0	$-2.5 \times 10^{-3} \ln\left(\frac{s}{m_W^2}\right)$	0
d)	$10^{-2}\, r_R$	1.7×10^{-3}	$10^{-2}\, r_R$	$2.7 \times 10^{-3} \ln\left(\frac{s}{m_Z^2}\right)$
e)	$10^{-2}\, r_R$	$\sim (10^{-3} - 10^{-2})$	$10^{-2}\, r_R$	$\sim \alpha \ln \frac{s}{m_Z^2}$

Table 3

m_q (GeV)	20	30	50
$2m_q - m_V$ (GeV)	0.2	0.2	0.3
$\Gamma(V \to \gamma \to e^+e^-)$ (keV)	0.4	0.4	0.6
$\frac{\Gamma(V \to Z^0 \to e^+e^-)}{\Gamma(V \to \gamma \to e^+e^-)}$	0.03	0.5	1
$\frac{\Gamma(V \to \text{hadrons})}{\Gamma(V \to \gamma \to e^+e^-)}$	14	12	9
$\Gamma(V \to$ charged current decay) (keV)	~0.6	~ 5	~60

The above numbers are calculated with $\sin^2 \theta_W = 3/8$ and $Q_q = -1/3$. For $Q_q = +2/3$ $\Gamma(V \to Z^0 \to e^+e^-)/\Gamma(V \to \gamma \to e^+e^-) \approx 0$ in this approximation.

Figure captions

Fig. 2.1 - The ratio of $\sigma(e^+e^- \to \gamma, Z \to \mu^+\mu^-)$ to the reference cross section $\sigma_{pt} \equiv \sigma(e^+e^- \to \gamma \to \mu^+\mu^-) = 4\pi\alpha^2/3s$.

Fig. 2.2 - The forward-backward asymmetry for $e^+e^- \to \mu^+\mu^-$.

Fig. 2.3 - The average helicity of the μ^- in $e^+e^- \to \mu^+\mu^-$.

Fig. 2.4 - Lowest order diagrams for single W production in the Weinberg Salam model.

Fig. 2.5 - The function F(a) appearing in the $e^+e^- \to e^+\nu W^-$ cross section formula (2.50).

Fig. 2.6 - Lowest order diagrams for $e^+e^- \to W^+W^-$ in the Weinberg-Salam model.

Fig. 2.7 - $\sigma(e^+e^- \to W^+W^-)$ in the Weinberg-Salam model for three values of $\sin^2\theta_W$.

Fig. 2.8 - The contributions of the different diagrams of fig. (2.6) to the cross section of fig (2.7), with $\sin^2\theta_W = 3/8$.

Fig. 2.9 - Normalized angular distributions for $e^+e^- \to W^+W^-$, for different values of s and $\sin^2\theta_W = 3/8$.

Fig. 2.10- Higgs boson production by bremsstrahlung from a) a virtual Z boson, b) a real Z boson.

Fig. 2.11- The process $e^+e^- \to H^+H^-$

Fig. 2.12- The two-photon process $e^+e^- \to e^+L^+L^-e^-$.

Fig. 2.13- a) Direct and b) crossed channel contributions to $e^+e^- \to \bar{f}f$.

Fig. 2.14- Fourth order contributions to the process $e^+e^- \to \mu^+\mu^-$.

Fig. 2.15- A relativistic fermion emitting a boson.

Fig. 2.16- An interesting fourth order contribution to $e^+e^- \to \mu^+\mu^-$.

Fig. 2.17- Some contributions to the imaginary part of the forward amplitude for $e^+e^- \to \mu^+\mu^-$.

Fig. 2.18 - Some more contributions to the imaginary part of the forward amplitude for $e^+e^- \to \mu^+\mu^-$.

Fig. 2.19 - A purely electromagnetic contribution to the imaginary part.

Fig. 3.1 - A new quark threshold, with narrow "hidden supercharm" mesons being smeared out by the machine energy resolution.

Fig. 3.2 - a) Electromagnetic, b) neutral weak current, c) charged weak current, and d) hadronic decays of a "hidden supercharm" meson.

Fig. 3.3 - Patterns of scaling violation expected in deep inelastic structure functions $F(x, q^2)$ and e^+e^- inclusive hadron distributions $\bar{F}(\xi, q^2)$.

Fig. 3.4 - A two-jet hadronic event resulting from $e^+e^- \to \gamma \to q\bar{q}$.

Fig. 3.5 - A multiconstituent state giving multiple jets.

Fig. 3.6 - A three jet event.

Fig. 3.7 - Exotic new interactions.

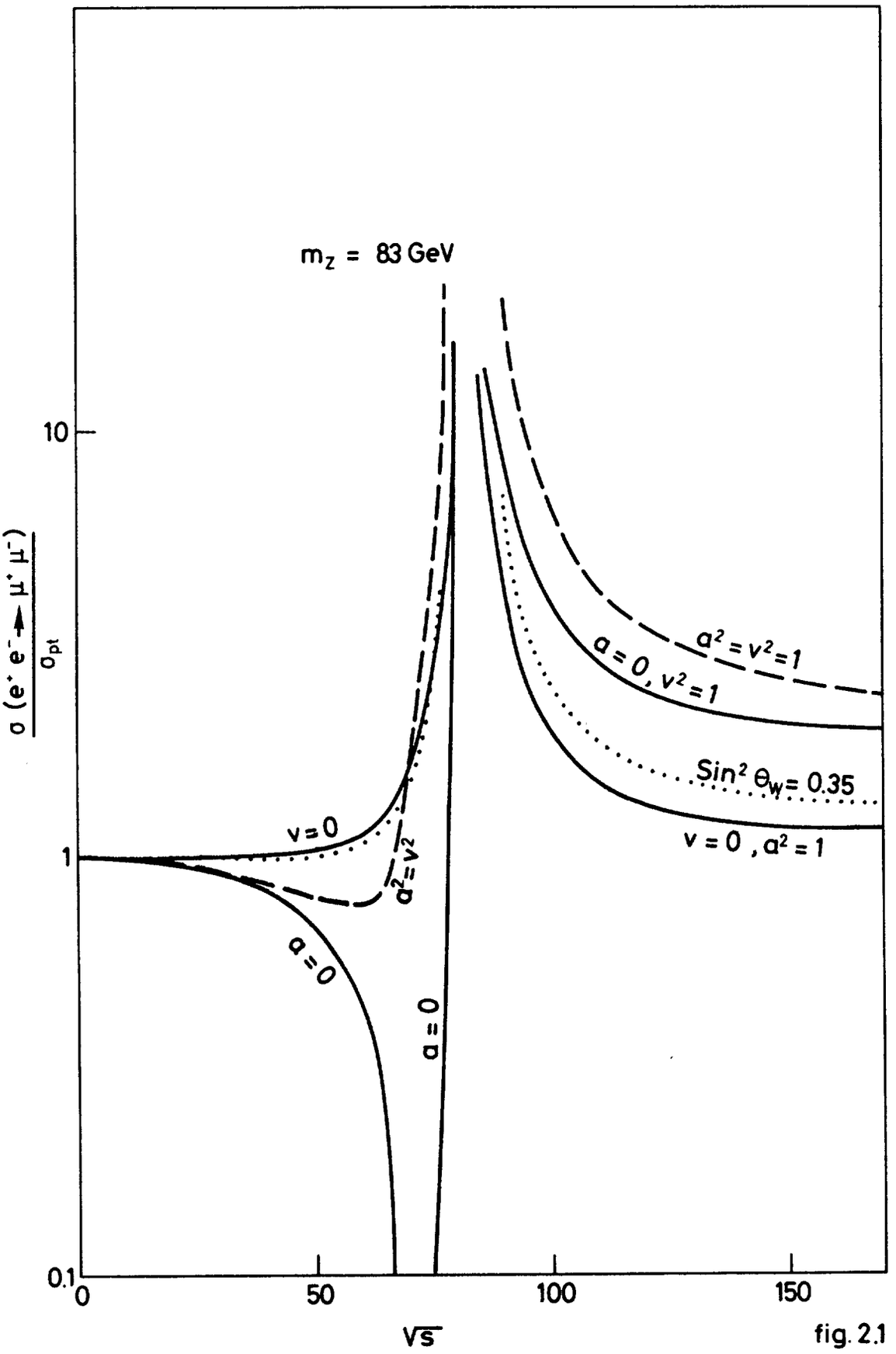
m_Z = 83 GeV
10
1
0.1
$\frac{\sigma(e^+e^- \to \mu^+\mu^-)}{\sigma_{pt}}$
v=0
$a^2=v^2$
a=0
a=0
$a^2=v^2=1$
a=0, $v^2=1$
$\sin^2\theta_W$= 0.35
v = 0 , a^2 = 1
0
50
100
150
$\sqrt{s}$

fig. 2.1

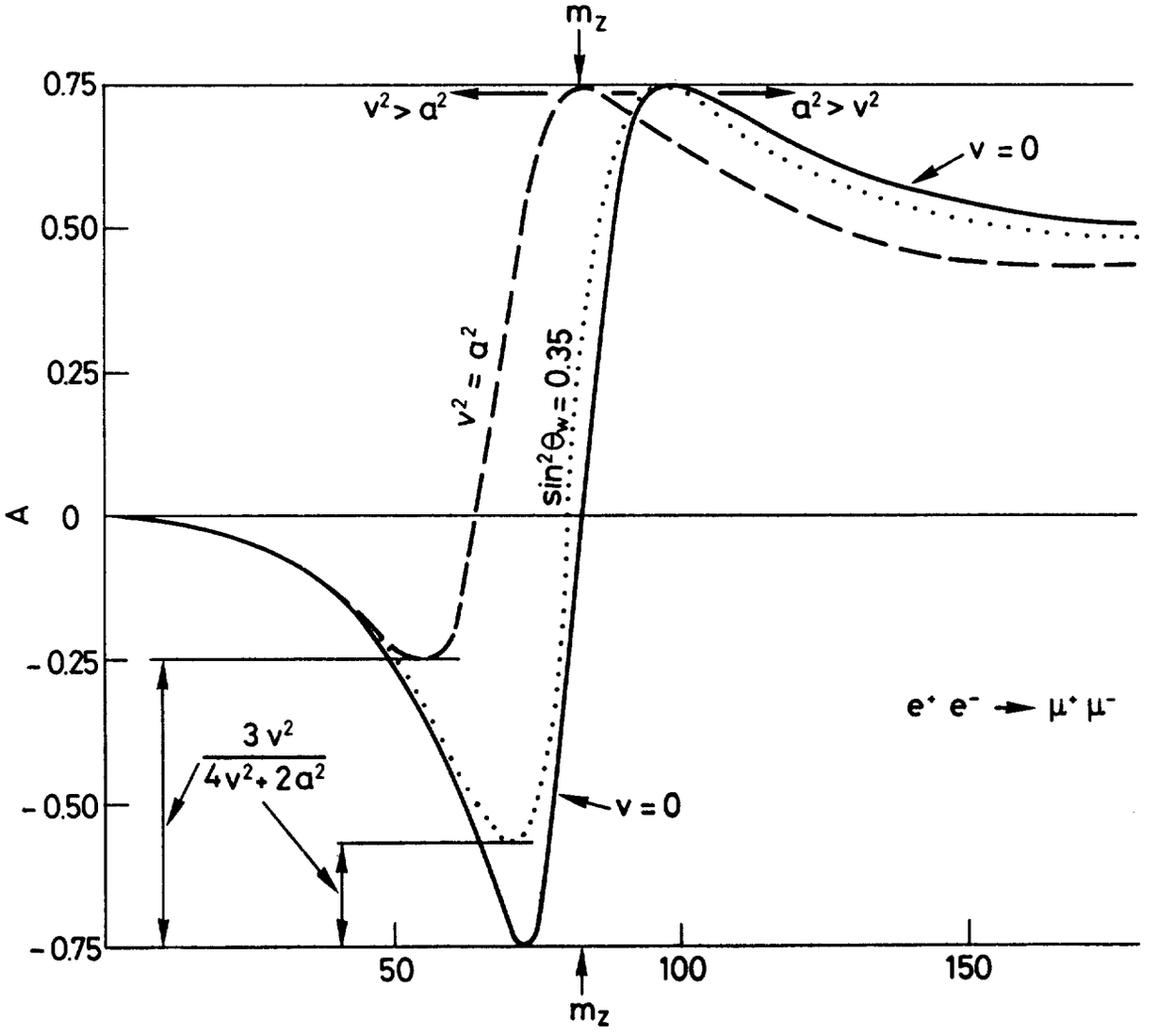
m_z
0.75
0.50
0.25
0
-0.25
-0.50
-0.75
A
v² > a²
a² > v²
v = 0
v² = a²
sin²θ_w = 0.35
e⁺ e⁻ → μ⁺ μ⁻
3 v² / 4v² + 2a²
v = 0
50
100
150
m_z
√s

fig. 2.2

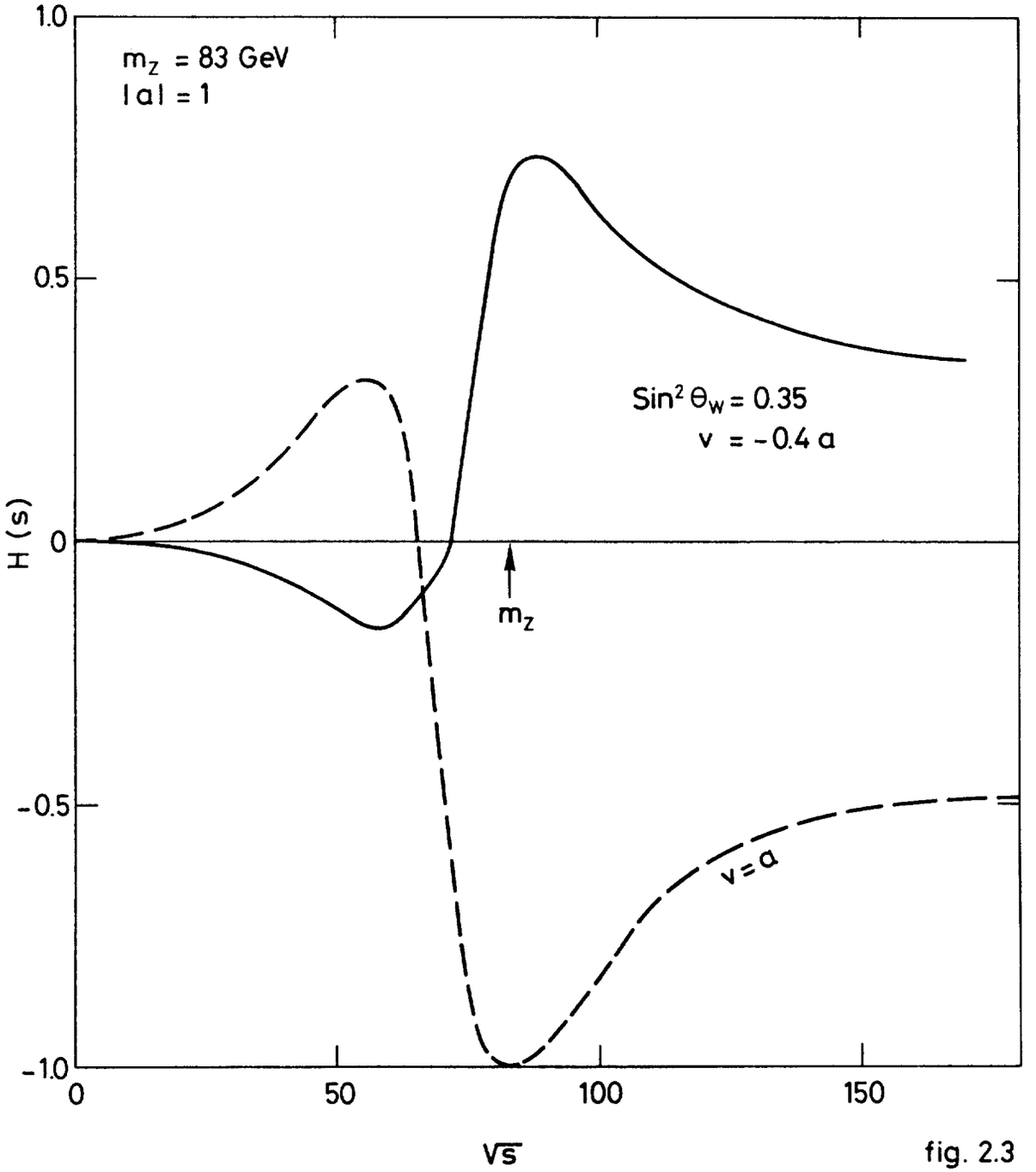
1.0
0.5
0
-0.5
-1.0
H (s)
m_Z = 83 GeV
|a| = 1
$\sin^2\theta_W = 0.35$
v = -0.4 a
m_Z
v=a
0
50
100
150
$\sqrt{s}$

fig. 2.3

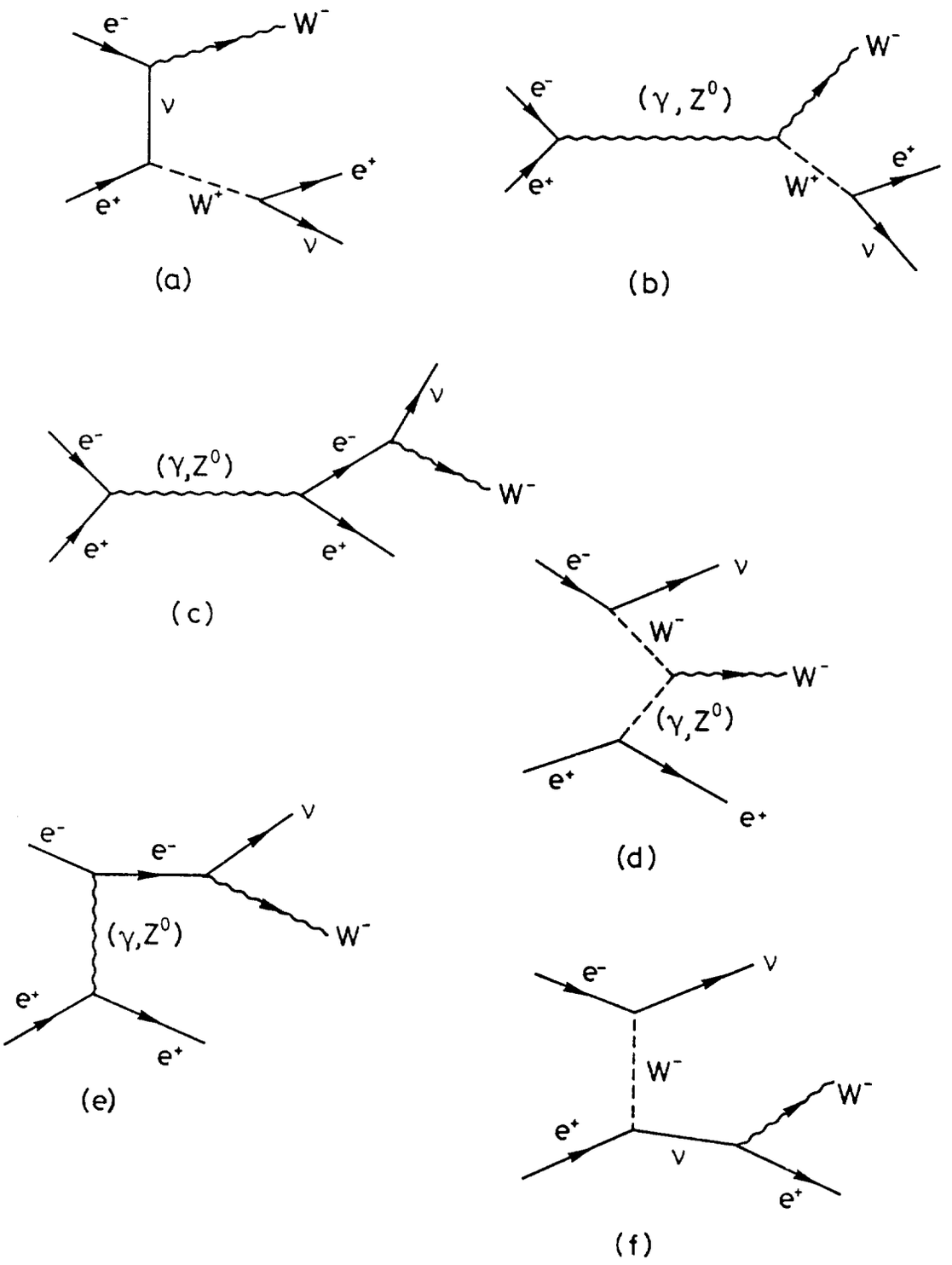
e⁻
W⁻
ν
e⁺
W⁺
e⁺
ν
(a)
W⁻
e⁻
(γ, Z⁰)
e⁺
W⁺
e⁺
ν
(b)
ν
e⁻
e⁻
(γ,Z⁰)
W⁻
e⁺
e⁺
(c)
e⁻
ν
W⁻
W⁻
(γ,Z⁰)
e⁺
e⁺
(d)
ν
e⁻
e⁻
(γ,Z⁰)
W⁻
e⁺
e⁺
(e)
e⁻
ν
W⁻
e⁺
W⁻
ν
e⁺
(f)

FIG. 2.4

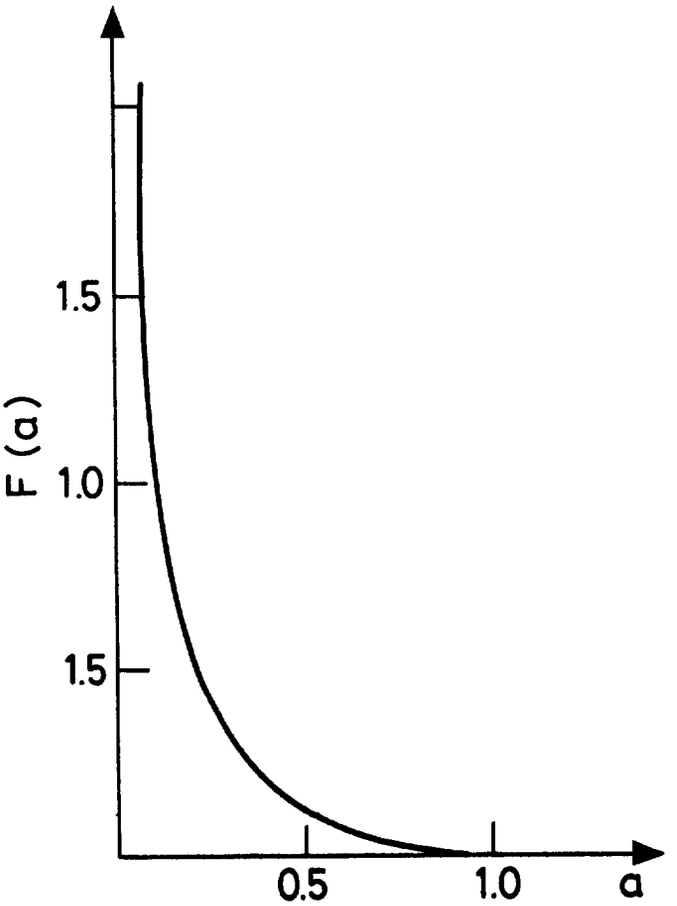

fig. 2.5

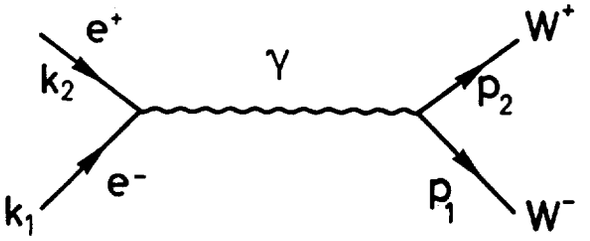

(a)

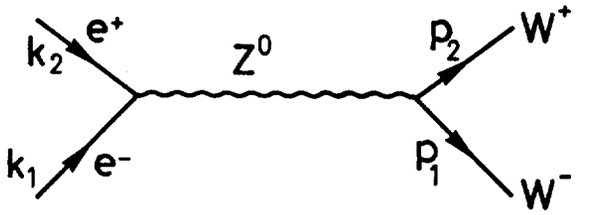

(b)

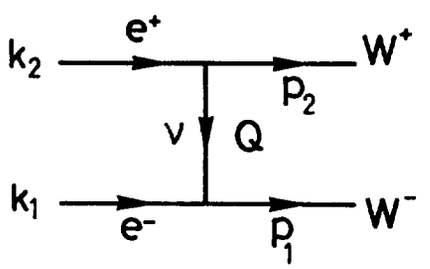

(c)

FIG. 2.6

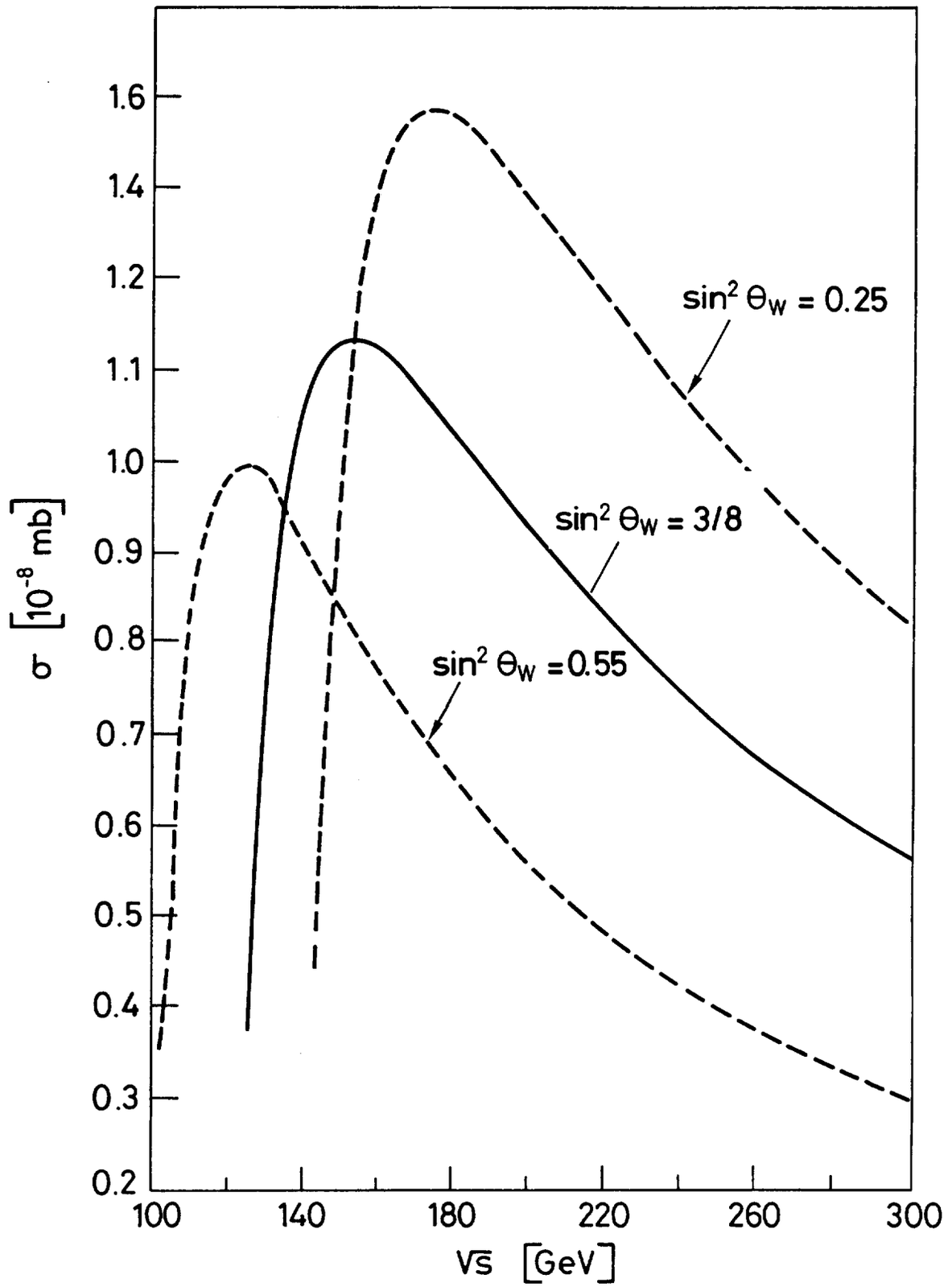
1.6
1.4
1.2
1.1
1.0
0.9
0.8
0.7
0.6
0.5
0.4
0.3
0.2
σ [10⁻⁸ mb]
sin² θW = 0.25
sin² θW = 3/8
sin² θW = 0.55
100
140
180
220
260
300
√s [GeV]

FIG. 2.7

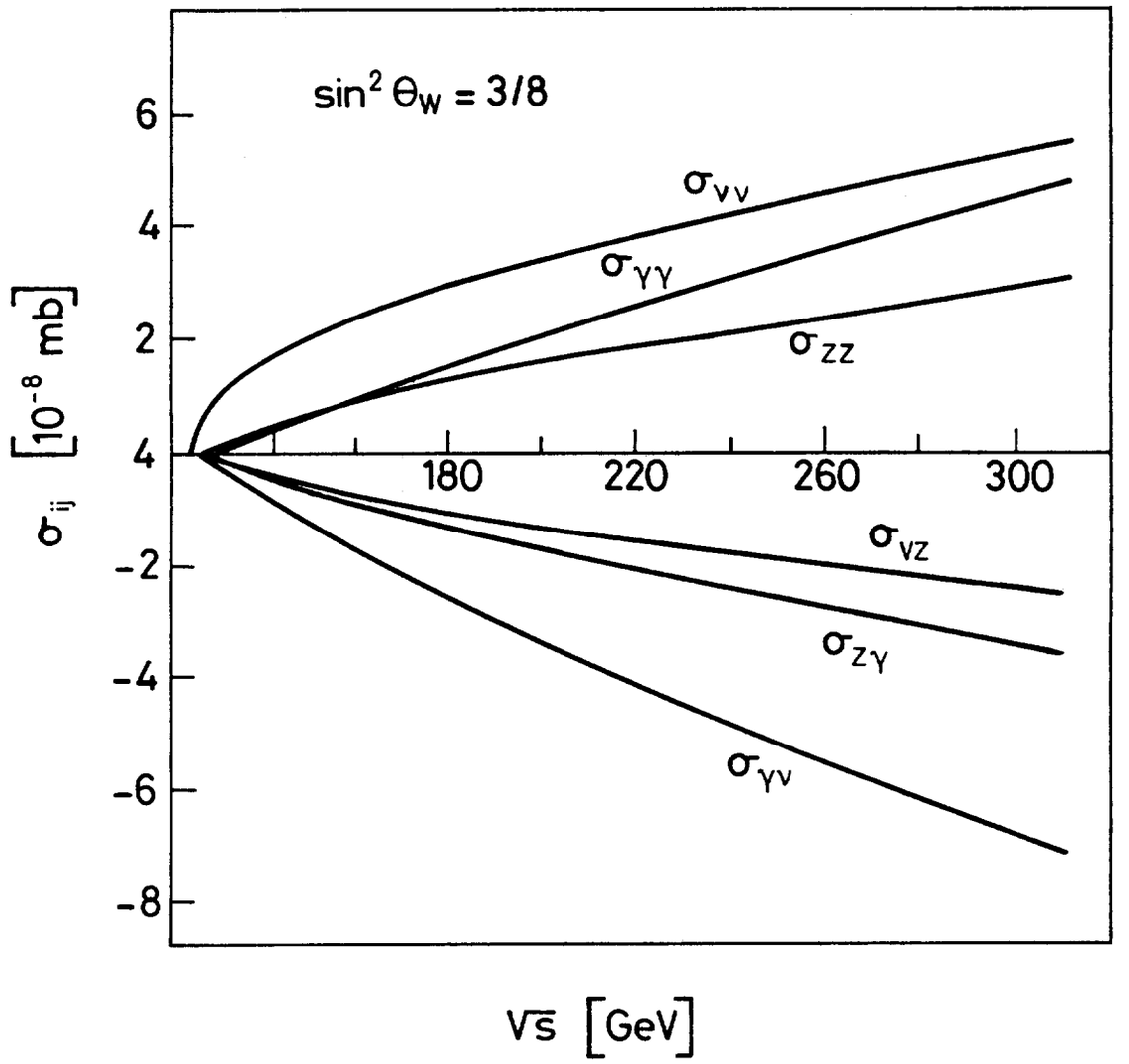
sin² θW = 3/8
σνν
σγγ
σZZ
σνZ
σZγ
σγν
6
4
2
4
-2
-4
-6
-8
180
220
260
300
σij [10⁻⁸ mb]
√s [GeV]

FIG. 2.8

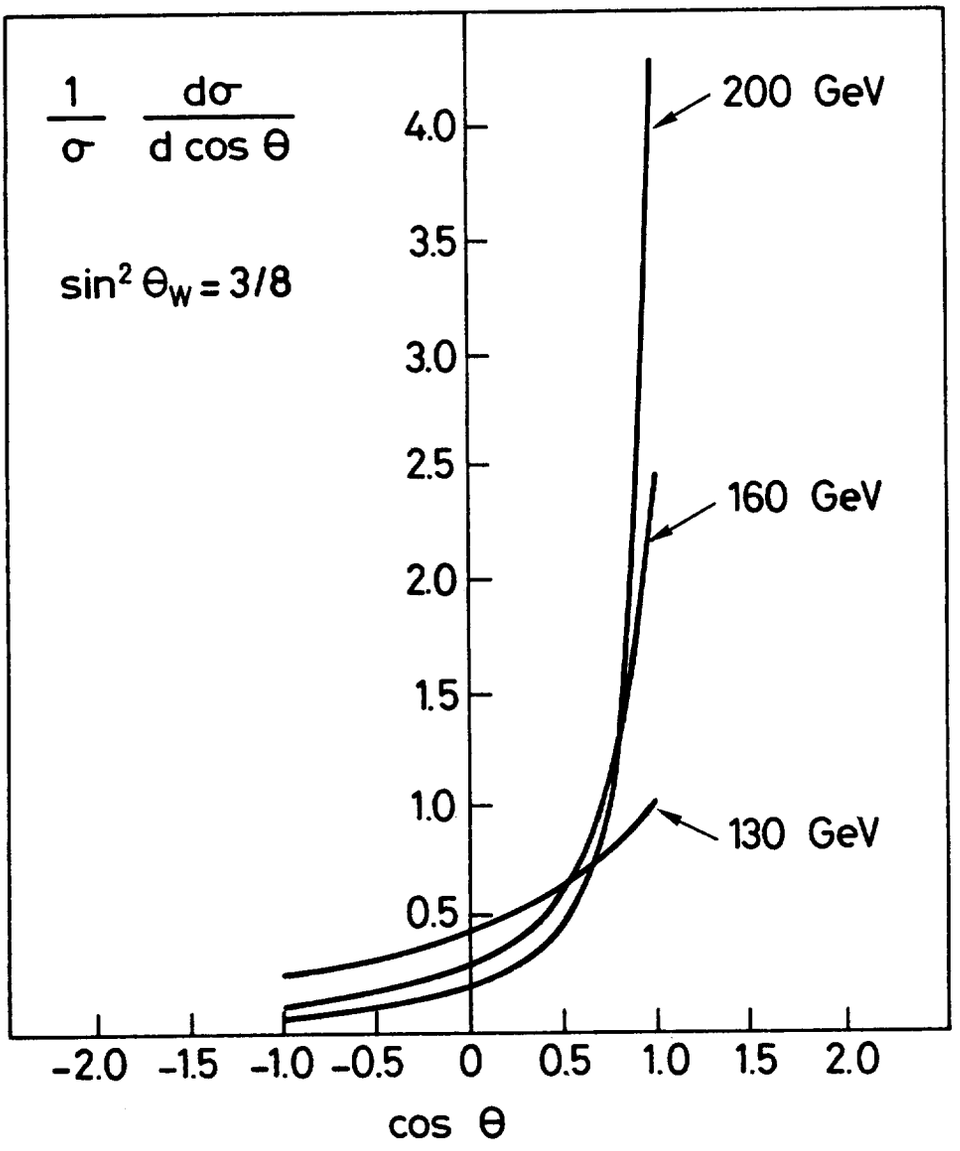
1/σ dσ/d cos θ
sin² θW = 3/8
200 GeV
160 GeV
130 GeV
4.0
3.5
3.0
2.5
2.0
1.5
1.0
0.5
-2.0 -1.5 -1.0 -0.5 0 0.5 1.0 1.5 2.0
cos θ

FIG. 2.9

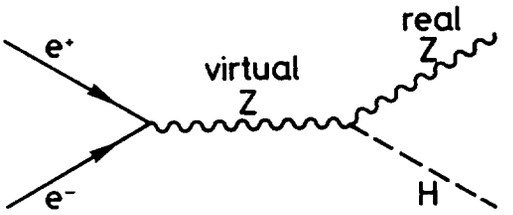

fig. 2.10 (a)

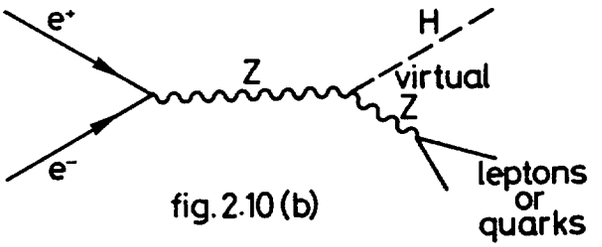

fig. 2.10 (b)

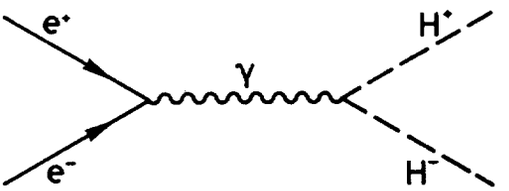

fig. 2.11

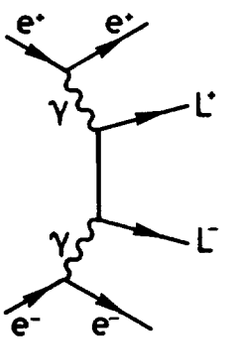

fig. 2.12

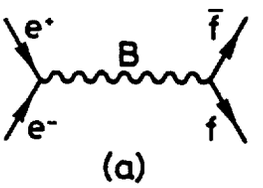

(a)

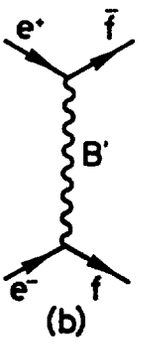

(b)

fig. 2.13

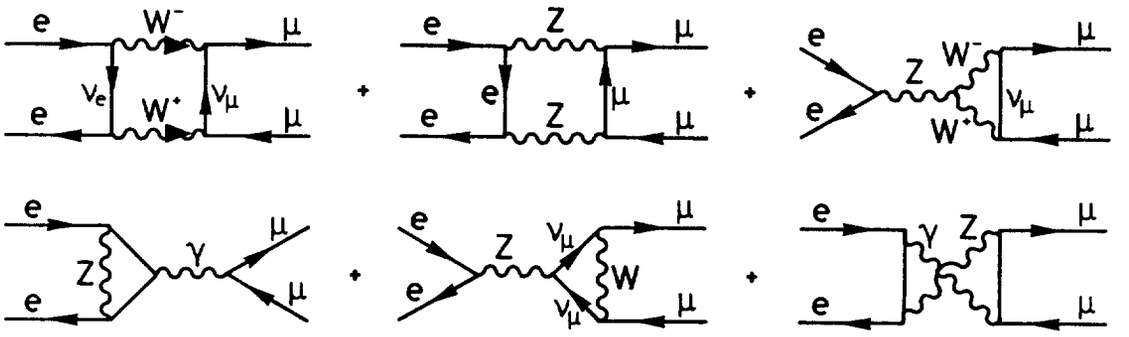

fig. 2.14

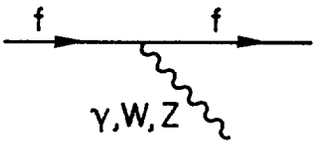

fig. 2.15

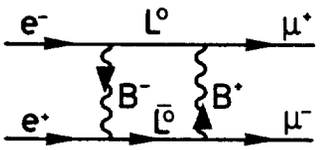

fig. 2.16

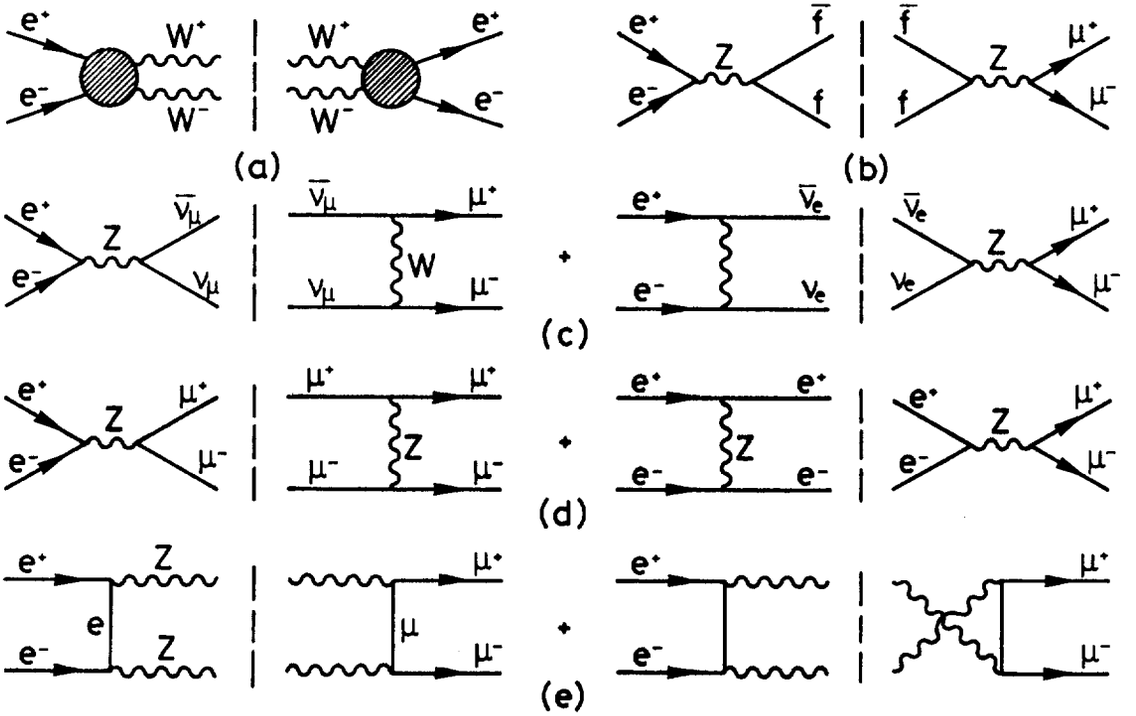

fig. 2.17

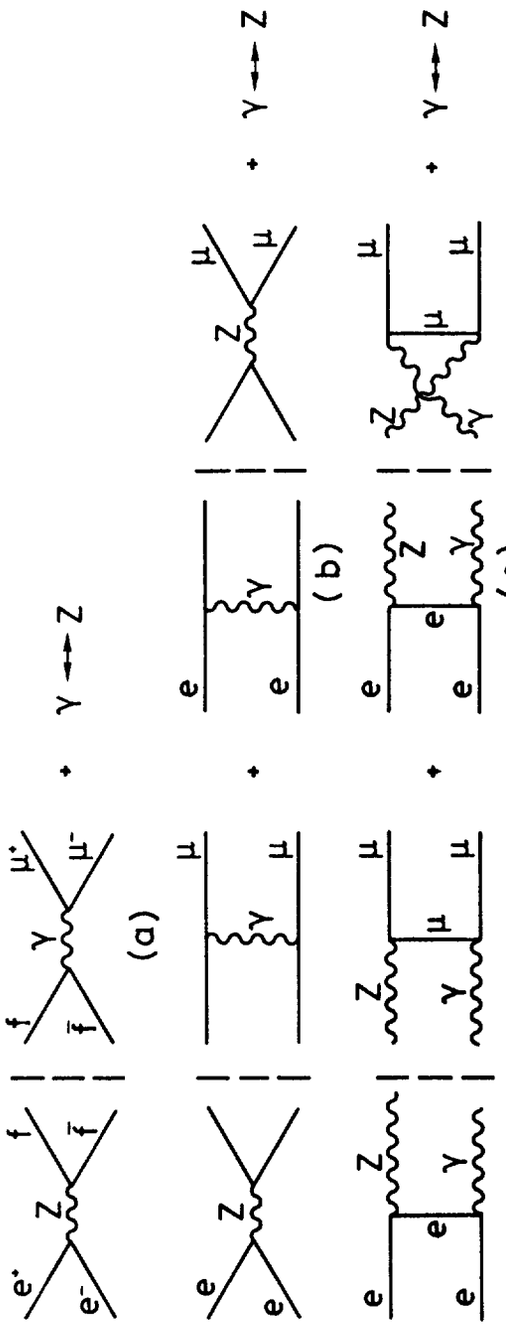

fig. 2.18

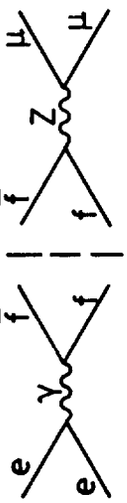

fig.2.19

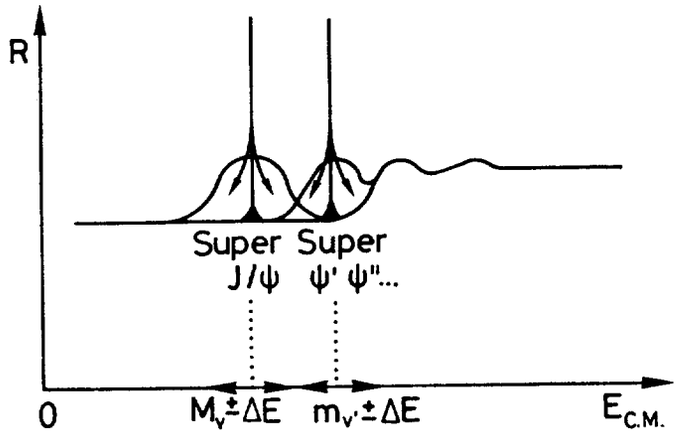

fig. 3.1

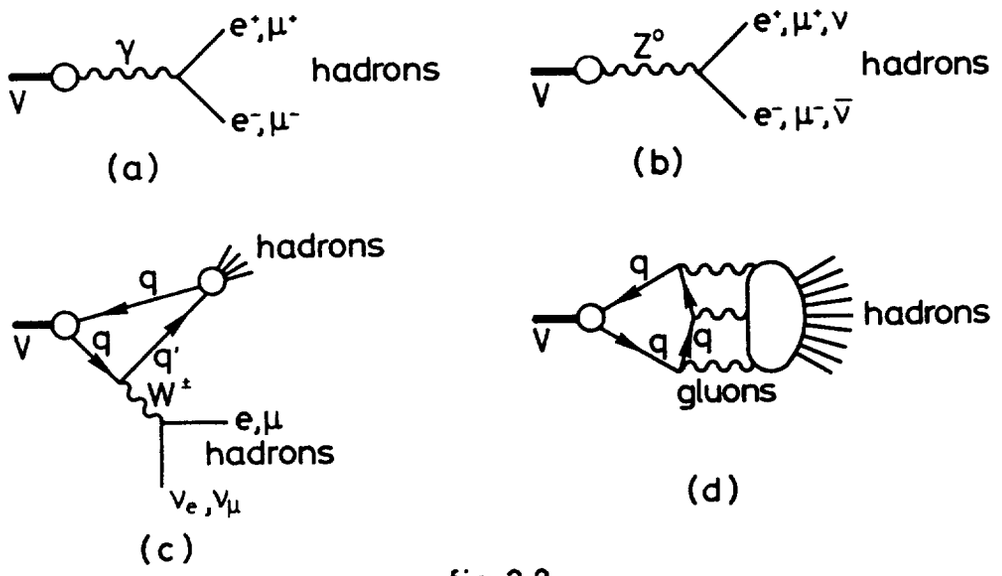

fig. 3.2

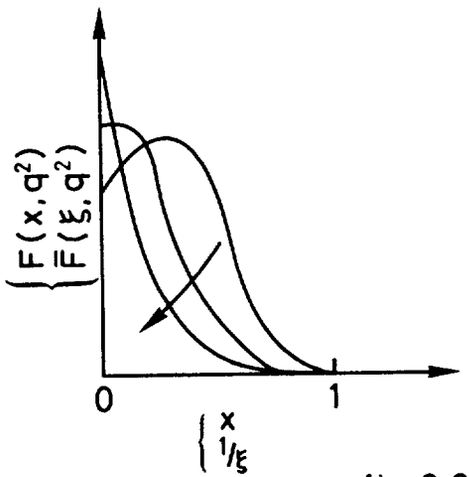

fig. 3.3

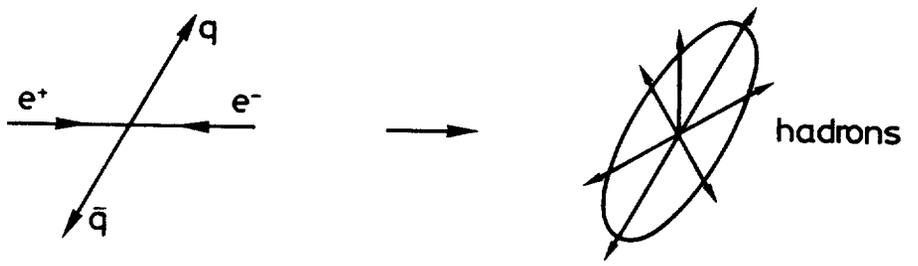

fig. 3.4

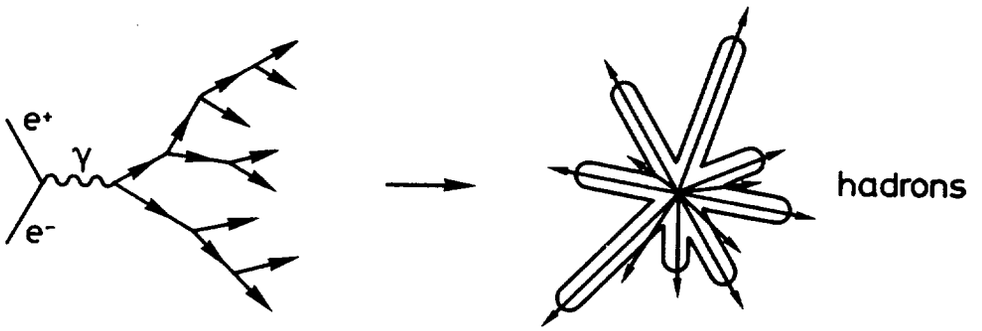

fig. 3.5

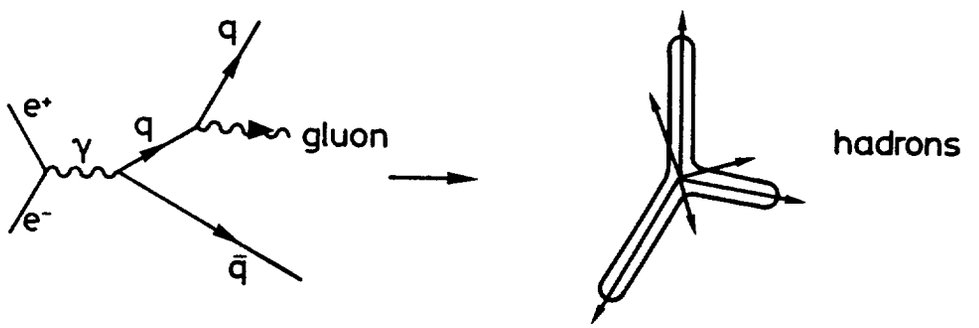

fig. 3.6

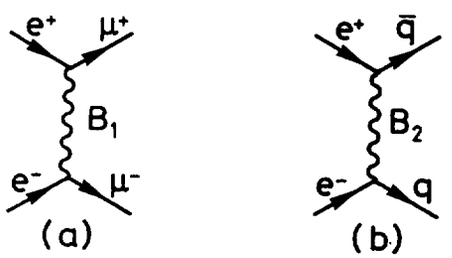

fig. 3.7

Appendix

Comparison of e^+e^- annihilation with hadron collisions for the production of heavy mass objects.

In this appendix we compare the efficiency of the Drell-Yan mechanism for quark antiquark annihilation into high mass objects with e^+e^- annihilation, taking the specific example of Z^o production which should be illustrative. Other cases would include the production of very heavy leptons or even quarks. (According to folklore, strong, weak and electromagnetic couplings may become similar at high energies, and strong production, requiring the exchange of more than one couloured gluon, may become less important than single photon or W, Z exchange- see sect 3.2).

We may express the hadronic cross section for Z^o production in terms of the Drell-Yan cross section for lepton pair production :

$$(pp \to Z^o + x) = \frac{3}{8\alpha^2} \frac{\langle G_q^2 \rangle}{\langle Q_q^2 \rangle} m_z \left. \frac{d\sigma_{em}}{dm} \right|_{m=m_z} \qquad (A.1)$$

where $\sigma_{em} = \sigma(pp \to l^+l^- + X)$, and $\langle Q_q^2 \rangle$ and $\langle G_q^2 \rangle$ are the average squared charge and Z-coupling of the quarks in the proton wave function. The Z-production cross section in e^+e^- annihilation is

$$\sigma(e^+e^- \to Z)_{peak} = G_e^2 / m_z \Gamma_z \qquad (A.2)$$

for Γ_z large compared with the energy resolution. Then the cross section ratio is

$$\frac{\sigma(ee \to Z^o)}{\sigma(pp \to Z^o + X)} = \frac{G_e^2}{\langle G_q^2 \rangle} \frac{8\alpha^2}{3} \langle Q_q^2 \rangle \frac{1}{m_z^2 \Gamma_z} \left[\left. \frac{d\sigma_{em}}{dm} \right|_{m=m_z} \right]^{-1} . \qquad (A.3)$$

In the parton model the electromagnetic cross section in expressed in terms of a scaling function

$$\frac{d\sigma_{em}}{dm} = \frac{1}{m^3} f(m^2/s) . \qquad (A.4)$$

The scaling variable $\tau = m^2/s$ is the product of the momentum fractions carried by the annihilation quarks. Eq (A.3) may be written

$$\frac{\sigma(ee \to Z^o)}{\sigma(pp \to Z^o + X)} = \frac{G_e^2}{\langle G_q^2 \rangle} \quad \frac{8\alpha^2}{3} \langle Q_q^2 \rangle \quad \frac{m_z}{\Gamma_z} \quad \frac{1}{f(m_z^2/s)} . \qquad (A.5)$$

(For production of a pair of objects with invariant mass $m_p \pm \frac{\Delta m_p}{2}$, $m_z \to m_p$ and $\Gamma_z \to \Delta m_p$). Neglecting the relatively small vector coupling of the Z in the Weinberg-Salam model,

$$G_e^2 \simeq \langle G_q^2 \rangle = \frac{e^2}{4\sin^2 2\theta_w} = 0.025 , \quad \sin^2 \theta_w = .35 . \qquad (A.6)$$

For a valence quark model (relevant for τ near 1), $\langle Q^2 \rangle = 1/3$; for an SU(3) (SU(4)) symmetric sea (relevant for τ near 0), $\langle Q^2 \rangle = 2/9$ (5/18). According to ideas borrowed from asymptotic freedom, the sea contribution should increase and become more SU(n) symmetric at high energies. To simplify notation we define the dimensionless function

$$g(\tau) = 10^{32} \text{ (cm GeV)}^{-2} f(\tau) \simeq O(1), \quad \tau \lesssim 10^{-2},$$

$$f(\tau) = 2.5 \times 10^{-5} g(\tau) \qquad (A.7)$$

Then eq. (A.5) becomes

$$\frac{\sigma(ee \to Z^o)}{\sigma(pp \to Z^o + X)} = \frac{m_z}{\Gamma_z} \quad \frac{1}{g(m_z^2/s)} \times (1 \text{ to } 2) \qquad (A.8)$$

In fig. A.1 we show some data points for the function $g(\tau)$ (or $f(\tau)$)and parton model predictions [29, 30]. For two parametrizations (NP) which apparently accomodate the data we show the analogous function for $p\bar{p} \to l^+l^- + X$. At large values of τ , where

valence quarks dominate, $p\bar{p}$ is clearly more efficient (and is less subject to uncertainty since the parton distribution functions are well measured for $x \gtrsim 0.1$). However at energies sufficiently high so that $\tau \lesssim 0.01$ and the sea contribution dominates, pp and $p\bar{p}$ are about equally efficient. These qualitative features are supported by the experimental comparison of $\pi^- p$, $\pi^+ p$ and pp production of lepton pairs, where $\pi^- p$ is found to enhance production for high invariant masses [31].

For $\tau \lesssim 0.01$, $g(\tau) \simeq 1$ or 2, and the cross section ratios are

$$\frac{\sigma(ee \to Z^o)}{\sigma(pp \to Z^o+X)} \simeq \frac{\sigma(ee \to Z^o)}{\sigma(p\bar{p} \to Z^o+X)} \simeq \frac{m_z}{\Gamma_z} \simeq 50 \text{ to } 80 \qquad (A.9)$$

for $m_z \simeq 80$ GeV, $\Gamma_z = (1 \text{ to } 1.5)$ GeV. The relatively low efficiency for hadronic production is due to the fact that the annihilating quarks carry only a small fraction of the incident energy.

The absolute cross section for Z^o production is

$$\sigma(pp \to Z^o+X) = \frac{3}{8\alpha^2} \frac{\langle G_q^2 \rangle}{\langle Q_q^2 \rangle} \frac{g(m_z^2/s)}{m_z^2} \times 10^{-32} \text{cm}^2\text{GeV}^2 \simeq 3\times 10^{-34} \text{cm}^2 \qquad (A.10)$$

for $\sin^2\theta_w = .35$, $m_z \simeq 80$ GeV and $\sqrt{s} \gtrsim 800$ GeV. The leptonic branching ratio may be roughly (see sect. 2.1)

$$B(Z^o \to e^+e^-) = B(Z^o \to \mu^+\mu^-) \simeq 1/8\ N \qquad (A.11)$$

where N is the number of quark or lepton doublets, assumed equal,

$$\sigma(pp \to Z^o+X) \simeq 10^{-35} \text{ cm}^2 \qquad N \sim 2 \text{ to } 3\ . \qquad (A.12)$$
$$\hookrightarrow l^+l^-$$

For $W^\pm$ production, hadronic collisions have an apparent advantage since a single $W^\pm$ may be produced via quark-antiquark annihilation. Both the production cross section and leptonic branching ratio are somewhat higher for the $W^\pm$:

$$\langle G^2_{Wq} \rangle \simeq G^2_{We\nu} = \frac{e^2}{4\sin^2\theta_w} \simeq 0.06 \qquad \text{(A.13)}$$

$$B(W \to e\ \nu_e) = B(W \to \mu\ \nu_\mu) = \frac{1}{4N}$$

and

$$\sigma(pp \to W^\pm + X) \simeq 7\times10^{-34}\ \text{cm}^2$$
$$\sigma(pp \to W^\pm + X) \simeq 10^{-34}\ \text{cm}^2 \quad . \qquad \text{(A.14)}$$
$$\hookrightarrow l^\pm\nu$$

This is roughly two orders of magnitude higher than the maximum cross section for $e^+e^- \to W^+W^-$ given in section 2.4. However one has to cope with the problem of identifying W production in multihadron final states. In fig. A.2 we show p_t distributions for leptons and in fig. A.3 for hadron jets from $W^\pm$ production and decay estimated [32] in a parton model calculation where the transverse momentum of the $W^\pm$ is neglected. Measured p_t distributions in dilepton production are actually found to be surprisingly broad.

$$\langle p_t\ (\mu^+\mu^-) \rangle \simeq 0.7\ (m_{\mu^+\mu^-})^{0.4}, \quad \sqrt{s} \simeq 20, \quad m_{\mu^+\mu^-} \gtrsim 1\text{GeV} \qquad \text{(A.15)}$$

being a reasonable parametrization, so the peak at $p_t = m_W/2$ may be smeared over a few GeV. The lepton distribution is compared with that from Drell-Yan dilepton production, and the hadron jet distribution using p_t^{-4} and p_t^{-8} extrapolations of the measured hadron distributions. Identification of $W^\pm$ production via its hadronic decay modes does not appear promising.

A detailed study of Drell-Yan production of heavy vector bosons is given in ref. 33.

Figure captions

Fig. A.1 - Drell-Yan cross sections : theory and experiment.

Fig. A.2 - Distributions in p_t for leptons from W decay.

Fig. A.3 - Distribution in p_t for hadron jets from W decay, composed with extrapolated hadronic backgrounds.

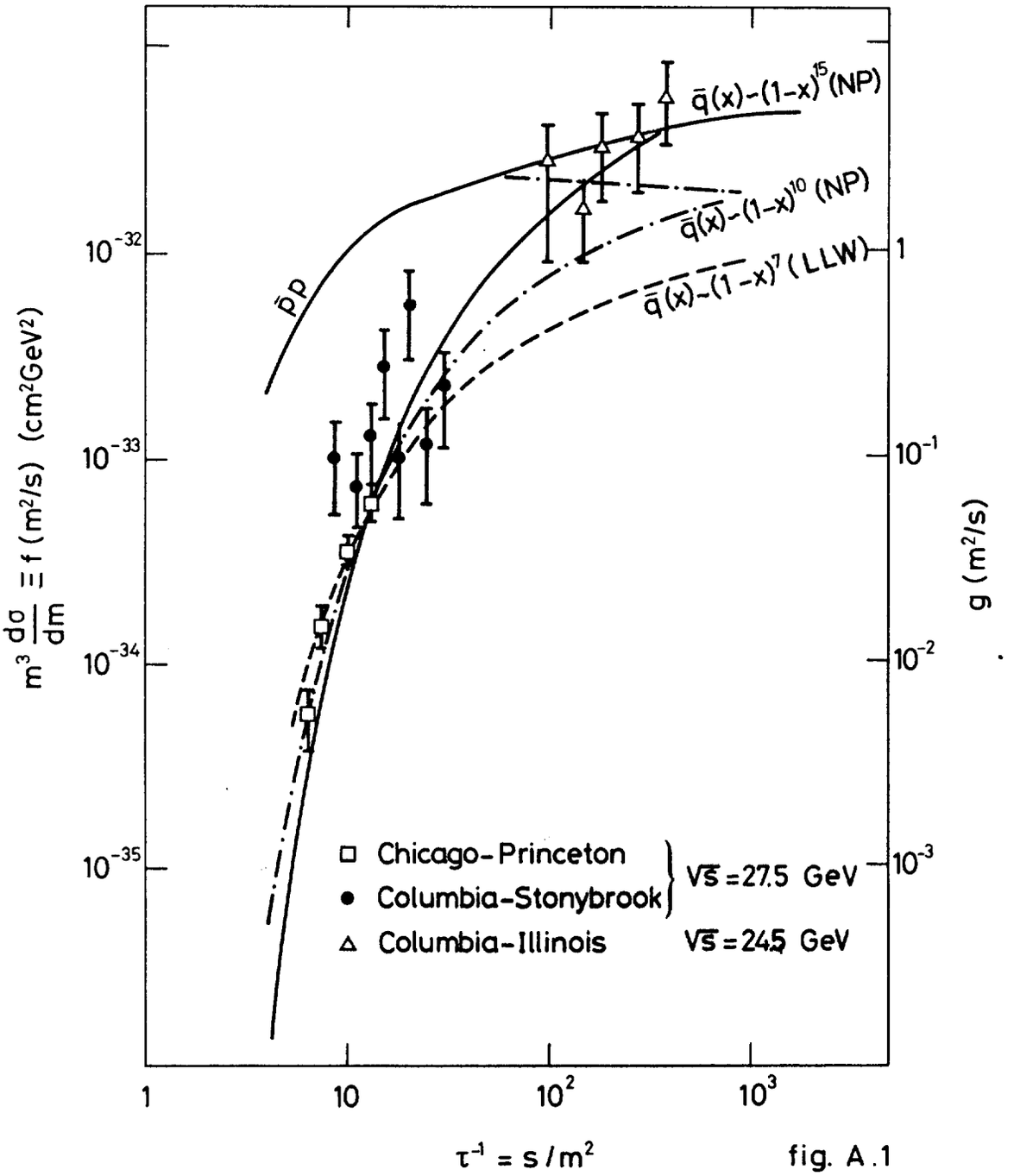
$m^3 \frac{d\sigma}{dm} \equiv f\ (m^2/s)\ (cm^2GeV^2)$
10^{-32}
10^{-33}
10^{-34}
10^{-35}
1
10^{-1}
10^{-2}
10^{-3}
g (m^2/s)
$\bar{q}(x)-(1-x)^{15}$ (NP)
$\bar{q}(x)-(1-x)^{10}$ (NP)
$\bar{q}(x)-(1-x)^{7}$ (LLW)
$\bar{p}p$
□ Chicago-Princeton
● Columbia-Stonybrook
△ Columbia-Illinois
$\sqrt{s}$ = 27.5 GeV
$\sqrt{s}$ = 24.5 GeV
1
10
10^2
10^3
$\tau^{-1} = s/m^2$

fig. A.1

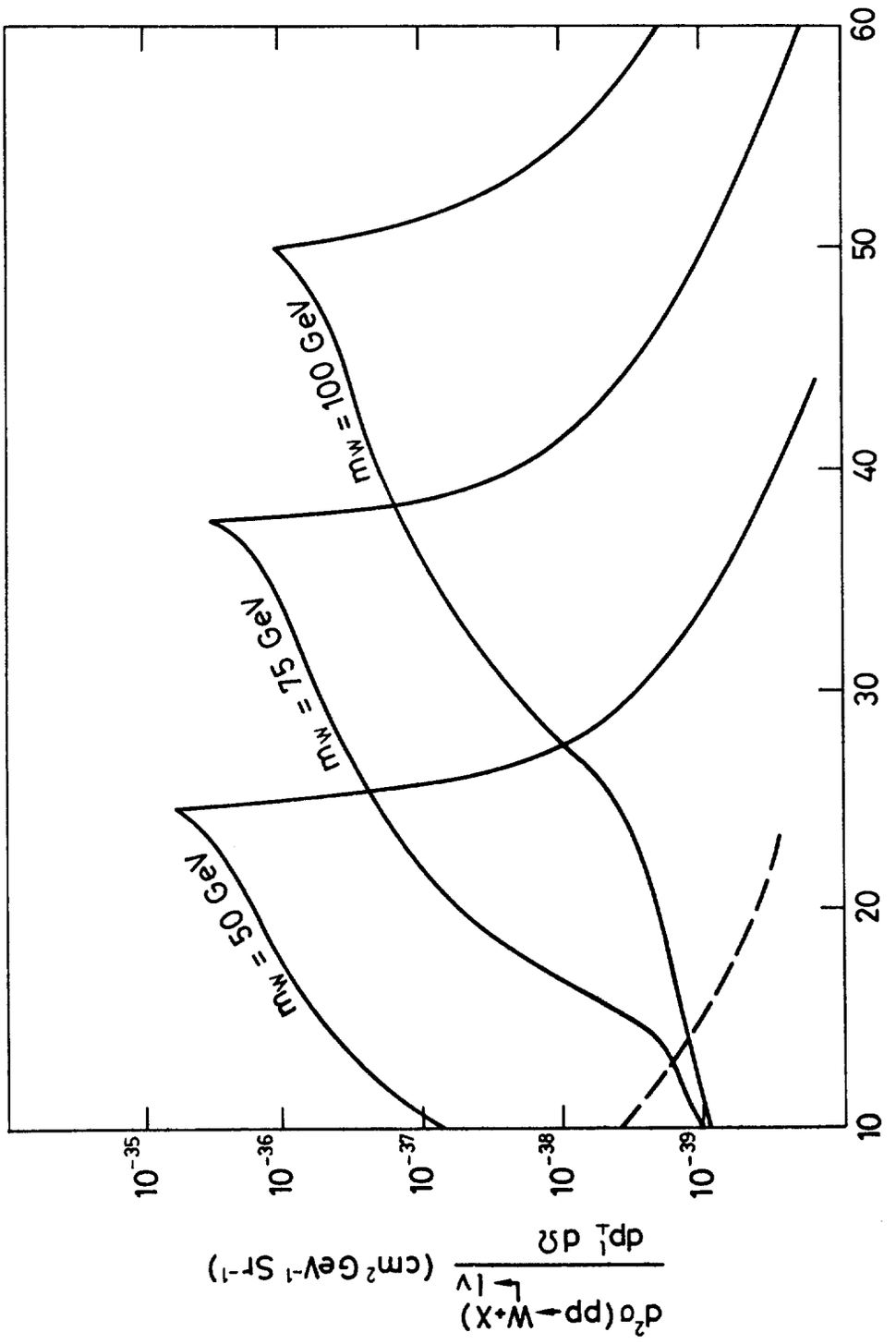
$m_W = 50$ GeV
$m_W = 75$ GeV
$m_W = 100$ GeV
10^{-35}
10^{-36}
10^{-37}
10^{-38}
10^{-39}
10
20
30
40
50
60
$P_\perp^l$ (GeV/c)
$\frac{d^2\sigma(pp \to W^+ X)}{dp_\perp^l \, d\Omega}$ $\downarrow l\nu$ (cm^2 GeV^{-1} Sr^{-1})

fig. A.2

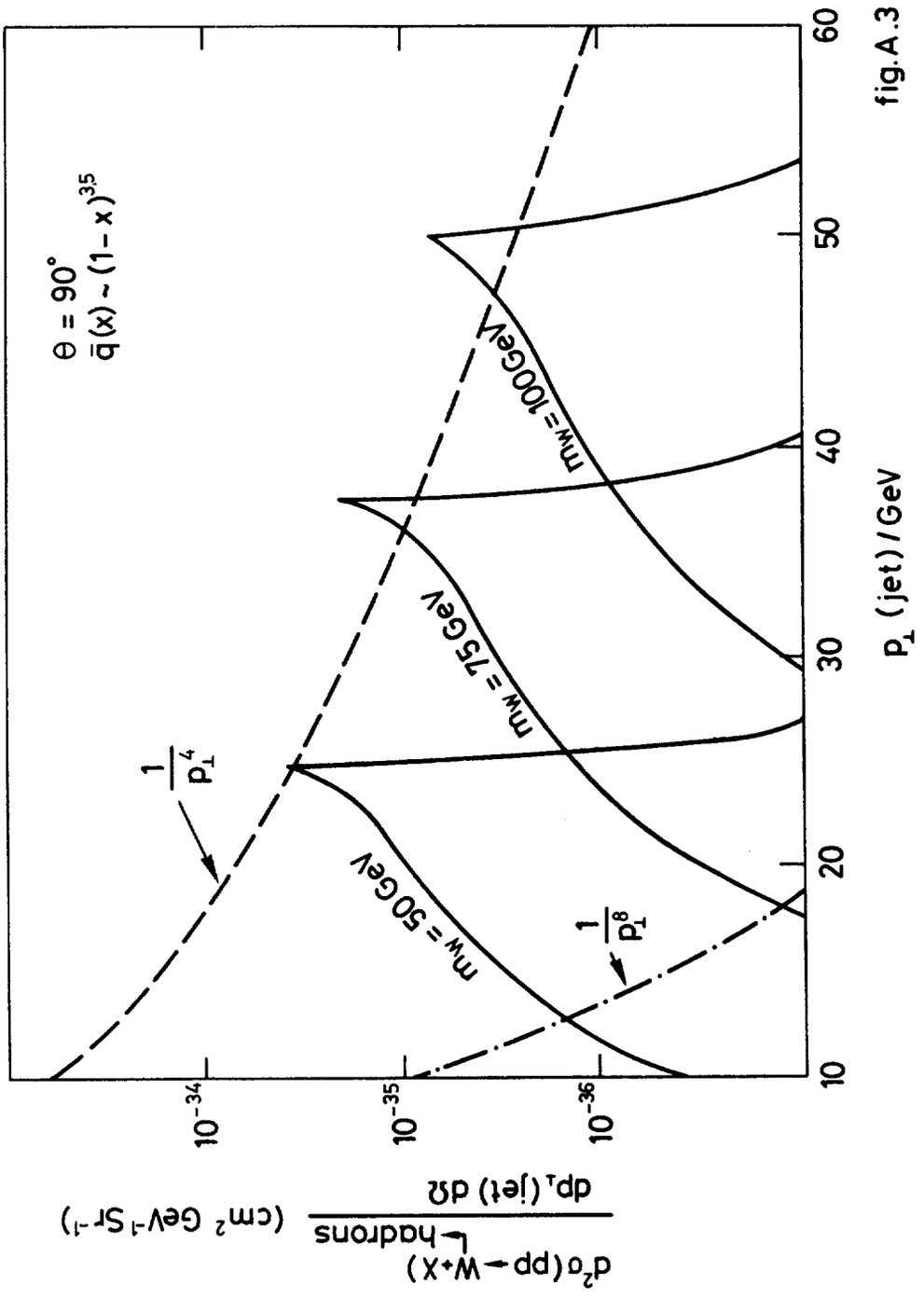
$\frac{d^2\sigma(pp \to W^+X)}{dp_\perp(jet)\,d\Omega}$ (cm^2 GeV^{-1} Sr^{-1})
$\hookrightarrow$ hadrons
10^{-34}
10^{-35}
10^{-36}
10
20
30
40
50
60
$p_\perp$ (jet) / GeV
$\theta = 90°$
$\bar{q}(x) \sim (1-x)^{3.5}$
$\frac{1}{p_\perp^4}$
$\frac{1}{p_\perp^8}$
$m_W = 50$ GeV
$m_W = 75$ GeV
$m_W = 100$ GeV

fig. A.3

References

1 - F.J. Hasert et al., Phys. Lett. 46B, 121 and 138 (1973).

2 - E.S. Abers and B.W. Lee, Phys. Reports 9, 1 (1973).

3 - S. Weinberg, Phys. Rev. Lett. 19, 1264 (1967).
A. Salam, Proc. 8th Nobel Symp, Stockholm 1968, ed. N. Svartholm(Almquist and Wiksells, Stockholm, 1968) p.367.

4 - J.D. Bjorken, "Physics issues and the VBA", paper presented to the International study group on future accelerators and high energy physics, Serpukhov, May 1976 (1976), and lectures delivered at SLAC Summer Institute (1976).
F. Halzen, "Hadron collisions above 10 TeV or Guessing particle physics at new accelerators" invited talk presented at the VIIth Int. Colloq. on multi-particle reactions, Tutzing, Germany, June 1976 (1976).

5 - Most studies in the literature are relevant to lower energies where only the (Z, γ) interference term is important. Exceptions include :
R. Budny, Phys. Lett 45B, 340 (1973)
A. McDonald, Nucl. Phys. B75, 343 (1974)
R. Budny, Phys. Lett. 55B, 227 (1975)
M. Gourdin, "Leptonic currents", Proc. Aachen Neutrino Conf., to be published (1976).

6 - Calculations of the Z^o peak were made by C. Jarlskog and F.J. Yndurain.

7 - G. Steigman, private communication

8 - C. Jarlskog and F.J. Yndurain, Phys. Lett. 63B, 215 (1976)

9 - Most of the material in this section is based on the work of W.Alles, Ch. Boyer and A.J. Buras, "W Boson production in e^+e^- collisions in the Weinberg Salam Model", CERN preprint TH 2220 (1976). This paper contains an extensive list of references to earlier work.

10 - See for example R. Gatto and G. Preparata, Rivista del Nuovo Cimento 4, 445 (1974).

11 - This calculation is due to J. Prentki and G. Preparata. For other calculations see references in W. Alles et al., ref. 8. We thank F.A. Berends for giving us his numerical results recalculated for high energies, and a comparative compilation of existing calculations

12 - A.D. Linde, JETP Letters 23, 73 (1976)
S. Weinberg, Phys. Rev. Letters 36, 294 (1976)

13 - J. Ellis, M.K. Gaillard and D.V. Nanopoulos, Nucl. Phys. B106 292 (1976).

14 - A recent study of $e^+e^- \rightarrow L^+L^-$ containing references to earlier work is K. Fujikawa and N. Kawamoto, "A study of heavy lepton production in e^+e^- annihilation" DESY preprint 76/01 (1976). For a recent review, see C.H. LLewellyn Smith "Heavy leptons" Oxford preprint OUTP 76-33 (1976)

15 - H. Terazawa, Rev. Mod. Phys. 45, 615 (1974) and R. Gatto and G. Preparata, ref. 10.

16 - H. Fritzsch is making a more detailed investigation of this process.

17 - The results in this section are due to M.K. Gaillard, and the irresistable insistence of B. Richter.

18 - H. Fritzsch and P. Minkowski, CERN preprint TH 2165 (1976) For a classification of similar models see : H. Fritzsch "Vector like interactions of leptons and quarks", CERN preprint TH 2198, to be published in Proc. Aachen Neutrino Conf. (1976).

19 - K. Strauch, Proc. VIth Int. Symp. on electron and photon interactions at high energies, Bonn 1973 (North Holland publishing Co., Amsterdam, 1974), p.1.

20 - M.L. Perl et al., Phys. Rev. Lett. 35, 1489 (1975), Phys. Lett. 63B, 466 (1976).

21 - W. Braunschweig et al., Phys. Lett. 63B, 471 (1976)
J. Burmester et al. , DESY preprint 76/50 (1976).

22 - T. Appelquist and H.D. Politzer, Phys. Rev. D12, 1404 (1975)

23 - G. Hanson et al., Phys. Rev. Lett. 35, 1609 (1975)

24 - For a review with references see :
C.H. Llewellyn Smith, Proc 1975 Int. Symp. on lepton and photon interactions at high energies, Stanford 1975, ed. by W.T. Kirk (SLAC, Stanford, 1975) p.709.

25 - J. Kogut and L. Susskind, Phys. Rev. D9, 697 and 3391 (1974)

26 - A.M. Polyakov, JETP 32, 296 and 33, 850 (1971), and Proc. 1975 Int. Symp. on lepton and photon interactions at high energies, Stanford 1975, ed. by W.T. Kirk (SLAC, Stanford, 1975) p. 855.

27 - J. Ellis, M.K. Gaillard and G.G. Ross, Nucl. Phys. B111, 253(1976).

28 - H. Georgi and S.L. Glashow, Phys. Rev. Lett. 32, 438 (1974)
H. Fritzsch and P. Minkowski, Ann. Phys. (NY) 93, 193 (1975)
and references therein.

29 - N. Phinney, private communication. These curves (NP) are obtained from fits to low energy (SLAC and Gargamelle) electro-and neutrino-production data.

30 - L.L. Wang, private communication. This curve (LLW) is from a fit including more recent high energy leptoproduction data, but with an antiproton distribution not sufficiently peaked at low x to fit the low τ dilepton data.

31 - K.J. Anderson et al. "Production of continuum muon pairs at 225 GeV by pions and protons", paper submitted to the XVIIIth Int. Conf. on high energy physics, Tbilisi, USSR (1976)

32 - L.L. Wang, private communication. We have rescaled the curves provided to us to account for colour and charm.

33 - L.B. Okun and M.B. Voloshin. "Production of intermediate bosons in pp and $\bar{p}p$ collisions" Moscow preprint HEP-111 (1976).
See also E.A. Paschos and L.L. Wang, Comments on Nuclear and particle phys. 6, 115 (1976) and references cited by W. Alles et al., ref. 8.

IV- EXPERIMENTAL STUDY OF THE REACTIONS $e^+e^- \rightarrow \mu^+\mu^-$, e^+e^- NEAR THE Z^o POLE

J.H. Field, B. Richter

I - Introduction

The physics contained in the e^+e^- → lepton pair channel is one of the most important motivations for contemplating the construction of an e^+e^- storage ring of the scale of LEP [1].

If our present ideas on the weak interaction are correct, in particular if the weak interaction is described by a gauge field theory, as is electromagnetism, then the simplest theory, that of Weinberg [2] and Salam [3] when combined with existing measurements [4] on neutrino interactions leads us to expect the existence of neutral and charged heavy bosons Z^o, $W^{\pm}$ of masses $\sim$ 80 GeV, 64 GeV. The energy of LEP is such that a Z^o of this mass may be formed directly, at rest in the laboratory, by e^+e^- annihilation. The process is then dominated by the weak interaction, and in the case when the Z^o decays into lepton pairs precision tests (comparable to classical tests of QED) can be made of any theory of the weak interaction. In the Weinberg-Salam (W-S) model all observable quantities (angular distributions and polarisation effects) are completely defined in terms of the position (M_z) of the Z^o pole and the decay width (Γ) of the Z^o. The sensitivity of such a test of the (W-S) model is considered in some detail below. A possible solenoidal magnetic detector is outlined which could

perform both the $\mu^+\mu^-$ and e^+e^- experiments. Suitable dimensions and detector resolutions are given. The method of triggering and background rates due to both annihilation (1γ) and 2γ hadron production are considered. It is found that, even at the trigger level, there should be little difficulty in obtaining clean samples of $\mu^+\mu^-$, e^+e^- events.

Finally brief mention is made of a possible second generation experiment to measure the polarization of the final state muons.

II - Possible experiments

Four different types of experiment can be made :

1) cross section : $\sigma(w)$ $w = \sqrt{s}$ = 2 x beam energy

2) charge asymmetry $A(w) = \dfrac{N_f - N_b}{N_f + N_b}$

N_f = number of events with μ^+, e^+ in forward hemisphere relative to incoming e^+.

N_b = number of events with μ^+, e^+ in backward hemisphere relative to incoming e^+.

3) beam polarization experiments

4) μ polarization experiments

Experiment 1) which discovers the Z^o and determines M_z and Γ, can be carried out with apparatus of limited angular acceptance, detecting any final state from Z^o decay. For reasons of counting rate it will be more efficient to find these parameters from the rate of wide angle multi-hadron events as a function of machine energy, rather than triggering specifically on the $\mu^+\mu^-$, e^+e^- channels.

The function A(w) is completely specified in the W-S model once M_z and Γ are known. The model is tested by comparing the observed and predicted A(w) distributions. The sensitivity which may be reached in this comparison is given in section 3 below.

The constant spacing in energy of the relevant spin resonances, together with a beam energy spread proportional to the beam energy, makes any possibility of achieving transverse beam polarization by the synchotron radiation mechanism [5] extremely unlikely[6] in LEP. For this reason experiments of type 3) are not considered further here.

μ - polarization experiments, type 4) may be possible if the Z^o pole exists in the energy range of LEP. However the apparatus required is extremely massive, and because of limited acceptance counting rates are low. A possible approach to such an experiment is given in section 5.

III - Measurement of total cross section, $\sigma(w)$ and backward-forward charge asymmetry A(w)

In the absence of beam polarization and measurement of final state helicities the differential cross section for $e^+e^- \to \mu^+\mu^-$ (e^+e^-) is in lowest order in the weak and electromagnetic interactions

$$\frac{8s}{\alpha^2}\frac{d\sigma^{ll}}{d\Omega} = 4B_1 + (B_2+B_3)(1+\cos^2\theta) + 2(B_3-B_2)\cos\theta \qquad l = e,\mu \qquad (1)$$

We follow here the notation of Budny.[7] B_1, B_2, B_3 are defined in terms of g_a, g_v and kinematic variables in the Appendix (Eqns A2). Eqn (1) results from summing the graphs shown in fig.1. Only the annihilation graphs a), b) contribute to $e^+e^- \to \mu^+\mu^-$, whereas both annihilation c), d) and exchange e), f) graphs contribute to $e^+e^- \to e^+e^-$. From μ-e universality (which can be tested by comparing the rate for the e^+e^- and $\mu^+\mu^-$ final states) the graphs a), c) give equal contributions to the cross section as do b), d). The $\mu^+\mu^-$ cross section is then obtained from that of e^+e^- by setting to zero all terms arising from graphs e), f). The $\mu^+\mu^-$ differential cross section then takes the simpler form :

$$\frac{4s}{\alpha^2}\ \frac{d\sigma^{\mu\mu}}{d\Omega} = F_1(w)\,(1+\cos^2\theta) + 2F_3(w)\cos\theta \qquad (2)$$

F_1, F_3 are functions only of g_a, g_v and $w = \sqrt{s}$ which are defined in the Appendix (Eqns A2, A3, A4). From 2) the backward-forward asymmetry for $\mu^+\mu^-$, $A^{\mu\mu}(w)$ is :

$$A^{\mu\mu}(w) = \frac{N_f - N_b}{N_f + N_b} = \frac{3}{4}\ \frac{F_3}{F_1} \qquad (3)$$

Here, the full angular range of θ, the angle between the incoming e^+ and out-going μ^+ is taken. Fig. 2 shows curves of $A^{\mu\mu}(w)$ for various values of g_a, g_v. Also shown are the positions of the Z^o pole in the W-S model. In this model, the coupling constants g_a/e, g_v/e of Eqns A2 are related to the Weinberg angle θ_w by :

$$\frac{g_v}{e} = \frac{4\sin^2\theta_w - 1}{2\sin 2\theta_w}$$

$$\frac{g_a}{e} = \frac{1}{2\sin 2\theta_w} \qquad (4)$$

and the Z^o mass is given in terms of θ_w by :

$$M_z^2 = \frac{\pi\alpha}{\sqrt{2}\,G_F \sin^2\theta_w \cos^2\theta_w} \qquad (5)$$

For $\sin^2\theta_w = \frac{1}{2}$, $(g_a = g_v)$ the maximum allowed asymmetry, 0.75 occurs on the Z^o pole. For $\sin^2\theta_w = \frac{1}{4}$ $(g_v = 0)$ the asymmetry vanishes on the pole. The curve labelled $\sin^2\theta_w = 0.35$ corresponds to the value of θ_w favoured by neutrino experiments [4] at present. It is clear from fig. 1 that $A^{\mu\mu}(w)$ is extremely sensitive to the ratio g_a/g_v.

A simple expression like Eqn (3) cannot be given for $A^{ee}(w)$ the charge asymmetry in $e^+e^- \to e^+e^-$, as the space like graphs e), f) give complicated angular dependences. All angular integrations can however be done analytically, and the result for $A^{ee}(w)$

for arbitrary angular cuts is given in the Appendix.

The result with an angular cut $30^\circ < \theta < 150^\circ$, (corresponding to the acceptance of the solenoidal magnetic detector proposed below) is shown in fig.3. Curves are plotted for the same 3 values, of g_a/g_v as in fig.2. Away from the pole, propagator effects associated with the space-like graphs give a large positive asymmetry. The effect of the pole is to"punch a hole", in this asymmetry, the depth of the "hole" depending on g_a/g_v. Again the charge asymmetry clearly has good sensitivity to g_a/g_v.

The e^+e^- channel differs from $\mu^+\mu^-$ in that the A(w) curve is much more sensitive to the value of Γ. The curves in fig.2 have Γ = 1 GeV, but Γ = 100 eV (i.e. $\simeq 0$) and 5 GeV give essentially identical curves. For e^+e^- the depth of the asymmetry dip is quite sensitive to the width Γ, particularly in the region 1 GeV $< \Gamma <$ 5 GeV. This is shown in fig. 4, where $A^{ee}(w)$ curves for $\sin^2\theta_w = 0.35$ ($g_v = 0.4\ g_a$) for different Γ values are plotted.

Figs.5, 6 show the counting rates per hour for $\mu^+\mu^-$, e^+e^- respectively in the region of the Z^0 pole. The curves shown assume :
i) a detector with angular acceptances :

$$30^\circ < \theta < 150^\circ$$
$$0^\circ < \varphi < 360^\circ$$

ii) a luminosity $\mathcal{L} = 10^{32}\ (E/100\ \text{GeV})^2 \text{cm}^{-2}\ \text{sec}^{-1}$
iii) $\sin^2\theta_w = 0.35$
The counting rate at the peak is about 400 h^{-1} for both $\mu^+\mu^-$ and e^+e^- for a width Γ of 1 GeV. For Γ = 5 GeV this figure drops to 17 h^{-1} for $\mu^+\mu^-$ and 40 h^{-1} for e^+e^-. As is indicated in fig.5, the error in W due to the natural energy spread of the beams is much less than the width of the Z^0 peak.

Figs.7, 8 show the accuracy with which $A^{\mu\mu}(w)$ may be measured in the case where Γ = 1, 5GeV respectively. The error bars shown

are statistical errors corresponding to 100 hrs running at each W value. The input assumptions are the same as in figs.5, 6. As can be seen by comparing the points with errors bars with the neighbouring curves where $\sin^2 \theta_w = 0.33$, 0.37 respectively, the sensitivity of this experiment ($\sim$1000 hrs total running time) to the predictions of the W-S theory is high, even for the Γ = 5 GeV case where the peak counting rate is much lower. Fig. 9 shows the accuracy with which $A^{ee}(w)$ may be determined. Γ = 1 GeV, the error bars correspond to 100 hrs per point, and other conditions are as in fig 6. Good sensitivity to the predictions of the W-S model is again obtained.

IV - Backgrounds and trigger requirements

For $\mu^+\mu^-$ events the most important sources of background are :

1) cosmic ray muons
2) π and K decays
3) hadron punch through

For e^+e^- events the only serious source is misidentification of π as e in the shower detectors.

(1) is reduced to a negligible level by T.O.F. techniques [8].

To gain an idea of the possible importance of (2) and (3) and also the π misidentification problem for e^+e^-, which is directly comparable to (3), an estimate has been made of the relative fluxes of particles in the region $80^\circ < \theta < 100^\circ$ due to :

i) $e^+e^- \rightarrow$ hadrons (1γ)
ii) $e^+e^- \rightarrow e^+e^-$ + hadrons (2γ)
iii) $e^+e^- \rightarrow \mu^+\mu^-$

The comparison is done for beam energy E = 100 GeV, increasing the importance of ii) relative to the E = 40 GeV region where the Z^0 pole is expected to lie. Further more the Q.E.D cross section only is taken for iii). At the Z^0 pole the rates of both i) and iii)

will increase. However the ratio $R = \frac{Z^o \to \text{hadrons}}{Z^o \to \mu^+\mu^-}$ is not expected to be greater than 10-20 [9] compared with an R value of ~ 5 for the highest energy SPEAR points so far measured. To estimate i) the $s\,\frac{d\sigma}{dx}$ ($x = 2p/w$) single particle inclusive distribution found at the highest SPEAR energy $\sqrt{s} = 7.4$ GeV at present available is scaled. By using an R of 5 we may be optimistic by a factor of 2-4 relative to the probable situation at the Z^o pole [10].

The pion flux due to ii) has been calculated from the following set of assumptions [11]

a) γ- flux from the equivalent-photon (Weizacker-Williams) approximation.

b) $\sigma_{\gamma\gamma}^{tot} = 2.5 \times 10^{-31}$ cm^2 [12]

c) p_t distribution for $p_t > 2.0$ GeV/c from a fit to ISR data [13]

$$E_\pi \frac{d^3\sigma}{dp^3} = K\, p^{-7.5}\, e^{-\frac{30.8}{\sqrt{s}}p} \qquad p \sim p_t \ (\theta \simeq 90^o)$$

Taking E = 100 GeV and integrating over the range $0.01 < \frac{W_{\gamma\gamma}}{2E} < 0.99$ of $\gamma\gamma$ effective mass $W_{\gamma\gamma}$, the resulting p_t distribution for pions from $\gamma\gamma$ collisions is found to be well represented in the range 2.0 GeV/c $< p_t <$ 20 GeV/c by :

$$\frac{E_\pi}{\pi}\frac{d^2\sigma}{dp_L\, dp_t^2} = 4.33 \times 10^{-34} \times p_t^{-9} \times e^{-0.17 p_t} \text{ cm}^2 \text{ GeV}^{-2}$$

Integrating this distribution over the angular region :

$$80^o < \theta < 100^o$$
$$0^o < \varphi < 360^o$$

gives the curve labelled $\sigma > p_t$ (2γ) in fig. 10. This is the cross section for all particles of momentum $> p_t$ in the given angular region. The line labelled $\sigma_{\mu\mu}^{QED}$ is the cross section for a muon from reaction iii) above to be in the region ; while the

curve $\sigma > p_t$ (1γ) gives the contribution from (i) given by scaling the SPEAR data, as mentioned above, assuming an istotropic angular distribution to apply the θ cut. The ratio $\sigma > 0(1\gamma)/\sigma_{\mu\mu}(QED)$ is simply R times the mean multiplicity in the 1 photon hadron production reaction. The hadron flux is dominated by reaction (ii) for $p_t < 2.0$ GeV/c and (i) for $p_t > 2.0$ GeV. The characteristic feature of a μ pair event is two and only two coplanar particles of high transverse momentum. Any detection system with particle tracking and crude momentum analysis will have no trouble with hadronic background from both 1γ and 2γ processes at the event reconstruction stage. Below we consider some simple requirements which can reject background events at the trigger level. An Fe absorber of thickness $\sim$ 2m will range out hadrons of less than 2 GeV/c momentum so the 2γ processes will not contribute significantly. The flux of pions from 1γ hadrons events is then from 1-2 orders of magnitude higher than the flux of muons from process (iii) (see fig. 10).

The trigger arrangement proposed is to require co-planarity, with one track in the angular region $0 < \theta < \frac{\pi}{2}$(forward) and the other in $\frac{\pi}{2} < \theta < \pi$ (backward), see fig. 11. If each of the hodoscope elements outside the hadron absorber subtends an azimuthal angle of 10^o, the probability of triggering on a hadron event with multiplicity 10 (typical for W = 200 GeV) will be :

$$\text{Trig. prob} \simeq \frac{1}{7}\left(p_{pt}^2 + p_{dec}^2 + p_{pt} \cdot p_{dec}\right)$$

Where p_{pt}, p_{dec} are the punch-through and decay probabilities of a track. The geometrical rejection of 1/7 assumes no azimuthal correlation between tracks. If 2 jet structure is important this number will be larger. Table 1 shows p_{pt} as a function of momentum for pions, for hadrons absorbers of thickness 1m, 2m of Fe. Also shown in table 1 are p_{dec} as a function of momentum for π, K assuming 1m of decay path.

TABLE 1

Punch through^{+} and decay probabilities* for different momenta p

p (GeV/c)	2	4	6	8	10	15	20	40	60	80	100
$p_{p.t.}^{(\pi)}$ 1m Fe	.008	.044	.106	.161	.207	.296	.376	.475	.562	.632	.685
$p_{p.t.}^{(\pi)}$ 2m Fe	10^{-5}	3.10^{-4}	$1.6.10^{-3}$	.003	.005	.008	.012	.023	.029	.035	.040
p_{dec} (π)	.009	.005	.003	.0023	$1.8.10^{-3}$	$1.2.10^{-3}$	$9.0.10^{-4}$	$4.5.10^{-4}$	$3.0.10^{-4}$	$2.3.10^{-4}$	$1.8.10^{-4}$
p_{dec} (K)	0.065	.033	.022	.017	.013	.009	$6.5.10^{-3}$	$3.3.10^{-3}$	$2.2.10^{-3}$	$1.7.10^{-3}$	$1.3.10^{-3}$

+ integrated over full lateral extent of shower

* for 1m decay path

For the 2m Fe absorber p_{pt}^2 varies from 10^{-10} to 1.6×10^{-3} as p varies from 2 to 100 GeV while p_{dec} (π) varies from 10^{-4} to 3×10^{-8}. If the K flux is $\sim 1/10$ of the π flux the π and K decay background trigger rates should be roughly equal. In any case the trigger probability is never higher than 2×10^{-4} for any momentum, so ever this relativly simple trigger, should have a background level which is nowhere worse than 2×10^{-2} using the raw pion fluxes given in fig. 10.

For the e^+e^- trigger it is proposed to use a set of hodoscope counters shadowing those outside the hadron absorber but placed before the shower counters inside the solenoid (see fig.12). The coplanarity requirement is as before, and the e^+e^- events have the further fast trigger requirement of a large energy deposition in the corresponding shower counters. Pb/scintillator sandwich counters should be adequate for this purpose.

A further trigger requirement, which may be imposed on both $\mu^+\mu^-$ and e^+e^- events is a "2 and only 2" multiplicity requirement in the inner cylinder of hodoscope counters. For W = 200 GeV, the mean charged multiplicity is $\bar{n} \simeq \ln s = 10.6$. The probability that a hadron event will have charge multiplicity 2 is then 1.4×10^{-3}, assuming a poissonian distribution of multiplicities. This rejection factor may be used to relax the punch- through probability requirement, reducing the thickness of the hadron absorber from 2m to say 1m at a considerable saving of cost.

A further background rejection factor may be achieved at the trigger level by using an "end cap veto". Scintillation counters are placed over the end caps, and all events having a track with ϑ from 30^o to as close to the beam direction as is practicable, are vetoed. This should be particularly effective in suppressing 2 γ hadronic events.

In summary, it seems possible to obtain $\mu^+\mu^-$, e^+e^- event samples with background levels much below 1%, purely at the trigger level without using the more stringent collinearity cuts which may be applied in the off-line analysis. This additional rejection can be quantitatively discussed only when a full calculation of the radiative corrections to $e^+e^- \rightarrow \mu^+\mu^-$ (e^+e^-) in the region of the Z^o pole is available.

V - Solenoidal magnetic detector

As requirements on momentum resolution are modest (it is essential only that the charge of the outgoing leptons be unambigously determined) very large dimensions and/or very high field strengths are not required. A suitable set of parameters for the magnet would be :

radius = 1.4 m

length = 4.0 m

field = 10 kg

Using 4 planes of drift chambers over 1m, with spacial resolution $\sigma = 100\mu$, the momentum resolution at p = 100 GeV/c is $\sigma_p/p = 0.27$, sufficient to give 7.4 standard deviations discrimination between positive and negative tracks. The arrangement of drift chambers, trigger hodoscopes, and shower detectors is shown in fig.12. Because of low particle fluxes and modest resolution requirements spark chambers are adequate to define the muon trajectory after the hadron absorber. The detector is shown with a 1m thick Fe hadron absorber. In this case the "2 and only 2" multiplicity requirement in the inner hodoscope counters is needed to give acceptable background suppression (see section 4 above).

VI - μ polarization experiment

The charge asymmetries for both the $\mu\mu$ and ee channels are invariant if the relative sign of g_a and g_v is changed. The sign of g_a/g_v can be found only in polarisation experiments. As it is of interest in verifing models to know this sign (e.g. in the W-S model, with the sign conventions given in the Appendix,it is positive if $\sin^2\theta_w = .35$) and beam polarisation is unlikely to be available [6], the only possibility is to measure the polarisation of the final state muons in $e^+e^- \rightarrow \mu^+\mu^-$. The longitudinal polarisation of a μ^+ emitted at angle θ is given by

$$P_L(\mu^+) = \frac{-F_4 (1 + \cos\theta)^2}{(F_1(1 + \cos^2\theta) + 2F_3 \cos\theta)} \qquad (6)$$

where F_1, F_3, F_4 are defined in the Appendix (Eqns A_3, A_4, A_{10}). Integrating over the full range of θ, the mean polarisation $\bar{P}_L(\mu^+)$ is :

$$\bar{P}_L(\mu^+) = -F_4/F_1 \qquad (7)$$

In fig. 13 $\bar{P}_L(\mu^+)$ is plotted, as a function of W for the W-S model with $\sin^2\theta_w = 0.33, 0.35, 0.37$.

Because $\sim$33m of Fe are needed to stop a 40 GeV/c muon it is only practical to detect the muons in the near forward or backward directions. A possible experimental set-up is sketched in fig.14. A "μtrap" of magnetised iron with a toroidal field configuration [15] bends muons of the correct sign back towards the beam axis. The length is chosen so that μ from near the Z^o pole are ranged into a polarimeter, where they stop. The longitudinal polarisation is measured by the forward/backward asymmetry of the decay electrons [16]. If the length of the trap is $\sim$30m only a small correction is necessary to account for the g-2 rotation of the muon spin in the $\sim$20kg field of the magnetised iron.

The angular acceptance is roughly related to the initial

radius of curvature of the μ in the Fe ρ_o, and the radius R of the iron toroid by the relation :

$$\theta_{max} = \sqrt{\frac{2R}{\rho_o}} \qquad (8)$$

This gives a conservative estimate of the acceptance, as the radius of curvature ρ will decrease linearly with distance due to energy loss in the Fe, causing the μ trajectory to bend closer to the beam axis, than if ρ is constant as is assumed in the derivation of Eqn 8). Taking :

$$B = 20 \text{ kg (in Fe)}$$
$$\rho = 66.7\text{m } (p_\mu = 40 \text{ GeV/c})$$
$$R = 3.0 \text{ m}$$

gives $\theta_{max} = 0.30$ radians.

The counting rate in the angular region $0 < \theta < 0.30$ radians, N_F, is related to the total counting rate in $0 < \theta < \pi$, N_{tot} by :

$$\frac{N_F}{N_{tot}} = 0.033 \ (1 + (4/3) A^{\mu\mu}(w)) \qquad (9)$$

Where $A^{\mu\mu}(w)$ the forward backward asymmetry is defined in Eqn (3). Fig. 15a shows curves of P_L (μ^+) as a function of W for $\sin^2\theta_w$ = 0.33, .35, .37 and θ = 0.2 rad. (curves for θ = 0.1, 0.3 rad. have essentially the same shape). For these near forward angles the sensitivity to the precise value of θ_w is not great, however the sign of g_a/g_v can be unambiguously determined in a quite short period of running time, as shown in fig. 15b. The errors bars on P_L (μ^+) shown here are for 100 hrs at each W value with the same luminosity as in Figs. 5,6. The number of events N_F, given by Eqn 9) at each W value are indicated in the figure. The formula used to calculate the errors is :

$$\sigma_{P_L} = \frac{6}{1+R}\sqrt{\frac{R}{N_F}}, \quad R = \frac{1 - \bar{A}_e P_L}{1 + \bar{A}_e P_L} \qquad (8)$$

$\bar{A}_e$ is the mean asymmetry in $\mu \rightarrow e\,\nu\bar{\nu}$ decay, taken as 1/3, and P_L (μ^+) is the longitudinal polarisation, given by Eqn 6) with $\theta = 0.2$. At the peak of the cross section curve, P_L is measured with a fractional error of $\sim$10% in 100 hrs running.

Note added in proof.

The LEP machine design was evolving during the preparation of this report. All rates given here are based on the "Version 1" parameters where the luminosity varies with energy as $\mathcal{L} = 10^{32} \left(\frac{E}{100}\right) cm^{-2}s^{-1}$. Using the "Version 3" parameters, as presented in Appendix 2, the luminosity at the Z^o pole - $E \simeq 40$ GeV - is four times higher. This has the effect of scaling down all error bars shown in the figures by a factor 2, for the same period of running time.

References and footnotes.

1 - B. Richter, Nucl. Inst. and Methods 136 (1976) 47.
C. Rubbia CERN EP Internal Report 76-2 (1976)

2 - S. Weinberg Phys. Rev. Letters 19, 1264 (1967), 27, 1688 (1971).

3 - A. Salam Proceedings of the Eighth Nobel Symposium, John Wiley and Sons, New York 1968.

4 - See, for example, J.G.Morfin, Proceedings of the 1975 International Symposium on Lepton and Photon Interactions at High Energy S.L.A.C. P 537.

5 - V.N. Baier in Proceedings of the International School of Physics Enrico Fermi 1971, Academic Press p. 1.

6 - D. Möhl and B.W. Montagne CERN/ISR-LTD/76-21, submitted to Nuclear Instruments and Methods.

7 - R. Budny, Phys. Letters 55B , 227 (1975).

8 - S. Ting Proceedings of discussion meeting on Petra experiments Frascati March 1976, p.E103.

9 - M.K. Gaillard, private communication.

10 - This assumes similar multiplicity distributions for hadrons from $Z^{o} \rightarrow$ hadrons and background events at neighbouring W values.

11 - See section VII.

12 - R. Gatto and G. Preparata Rivista del Nuovo Cimento Vol 4, 445 (1974).

13 - L. Camilleri, private communication.

14 - A. Grant, Nuclear Instruments and Methods 131, 167 (1975)
J. Ranft, Nuclear Instruments and Methods 48, 261 (1966).

15 - A muon spectrometer of this type has been proposed for a μ - scattering experiment at the CERN SPS. Proposal CERN SPSC/74-79/P19.

16 - A polarimeter of this type intended to measure the polarisation of μ produced in ν interactions at the CERN SPS is described in the proposal SPSC/75-59/P49.

Lowest order Weak and $\mathcal{EM}$
Contributions to $e^+e^- \rightarrow \mu^+\mu^-(e^+e^-)$

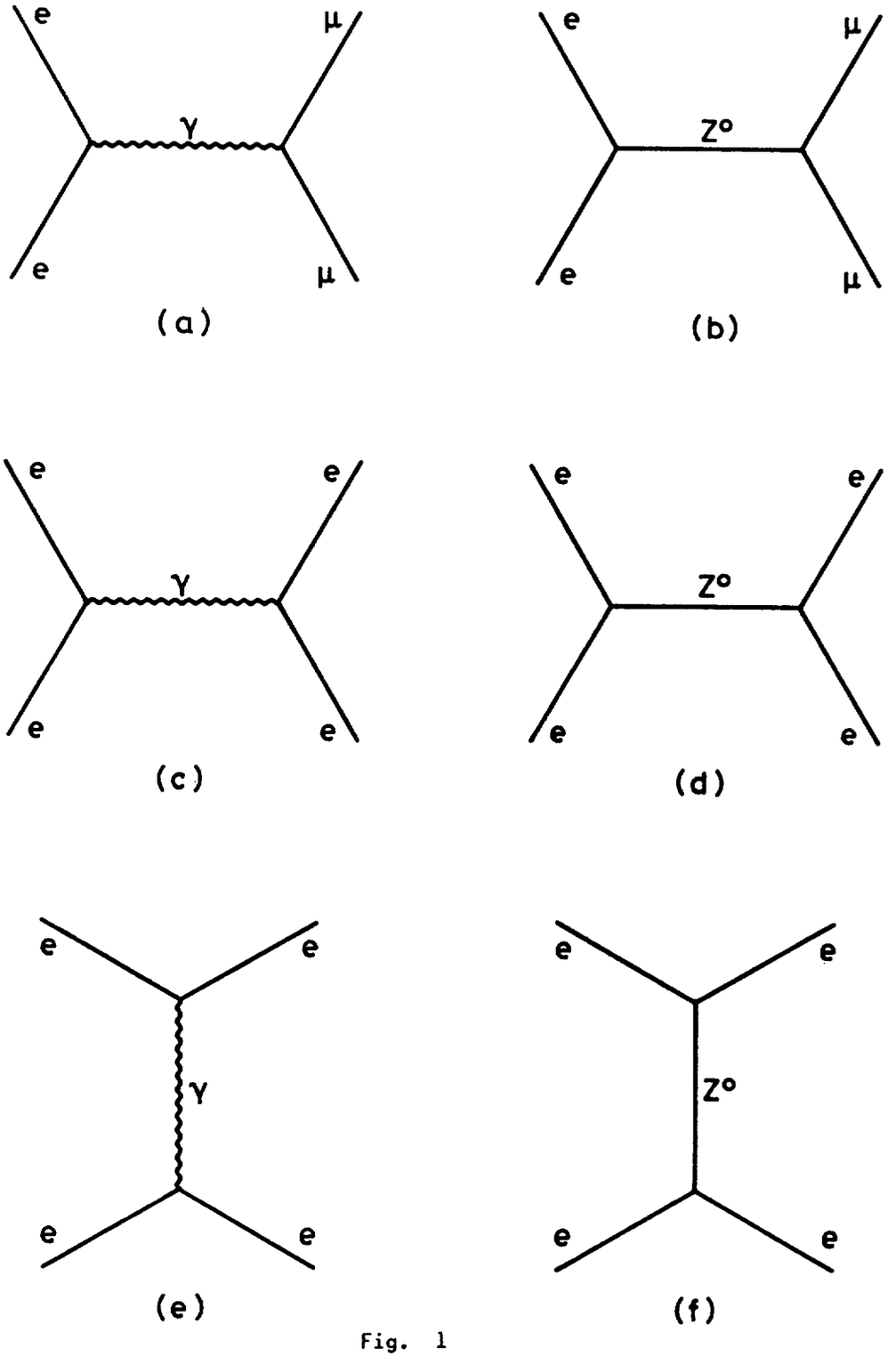

Fig. 1

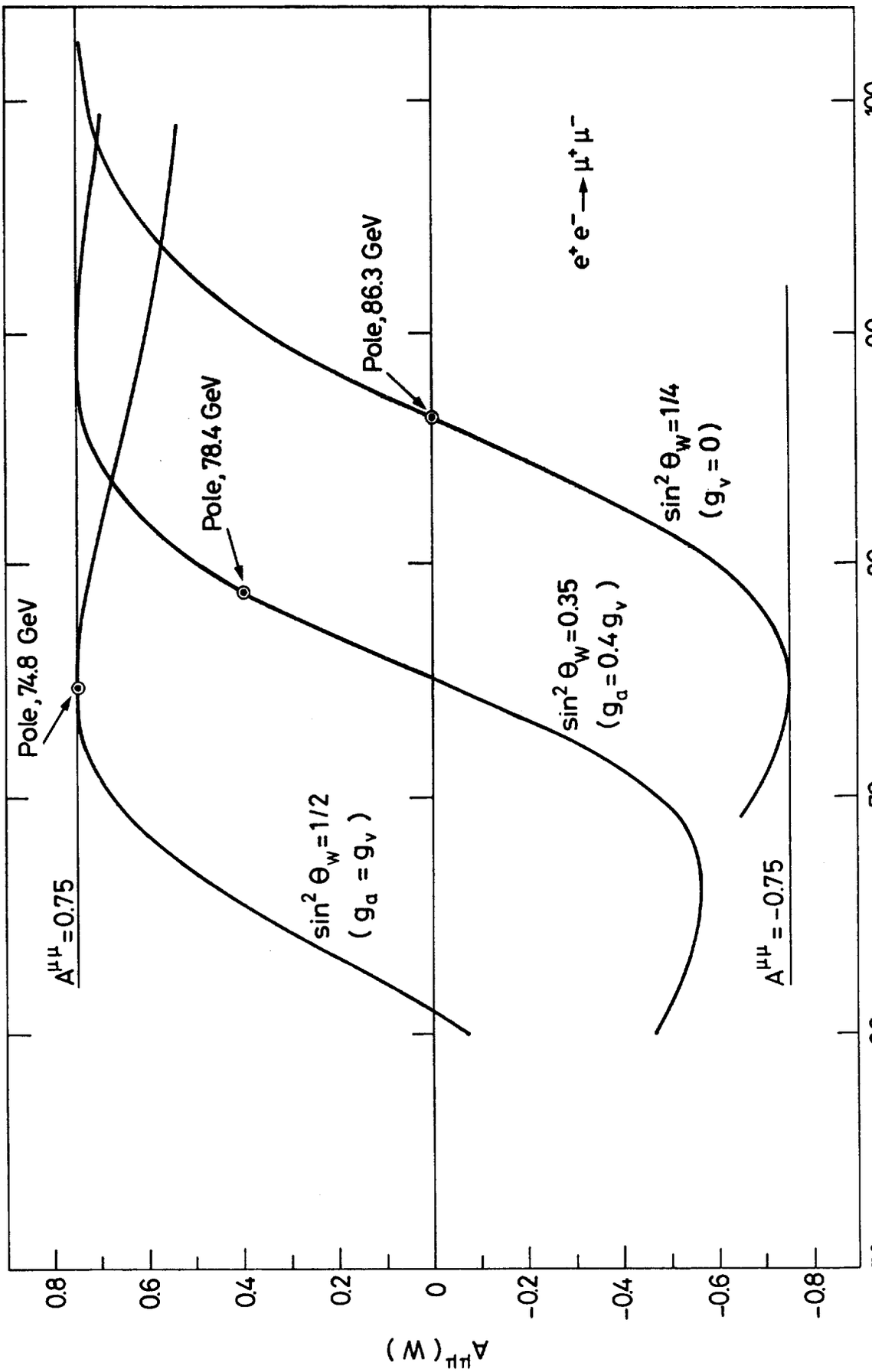
$e^+e^- \rightarrow \mu^+\mu^-$
Pole, 74.8 GeV
Pole, 78.4 GeV
Pole, 86.3 GeV
$A^{\mu\mu}=0.75$
$A^{\mu\mu}=-0.75$
$\sin^2\theta_W=1/2$ ($g_a=g_v$)
$\sin^2\theta_W=0.35$ ($g_a=0.4\,g_v$)
$\sin^2\theta_W=1/4$ ($g_v=0$)
$A^{\mu\mu}(W)$
$W=\sqrt{s}$ GeV
0.8
0.6
0.4
0.2
0
-0.2
-0.4
-0.6
-0.8
50
60
70
80
90
100

Fig. 2

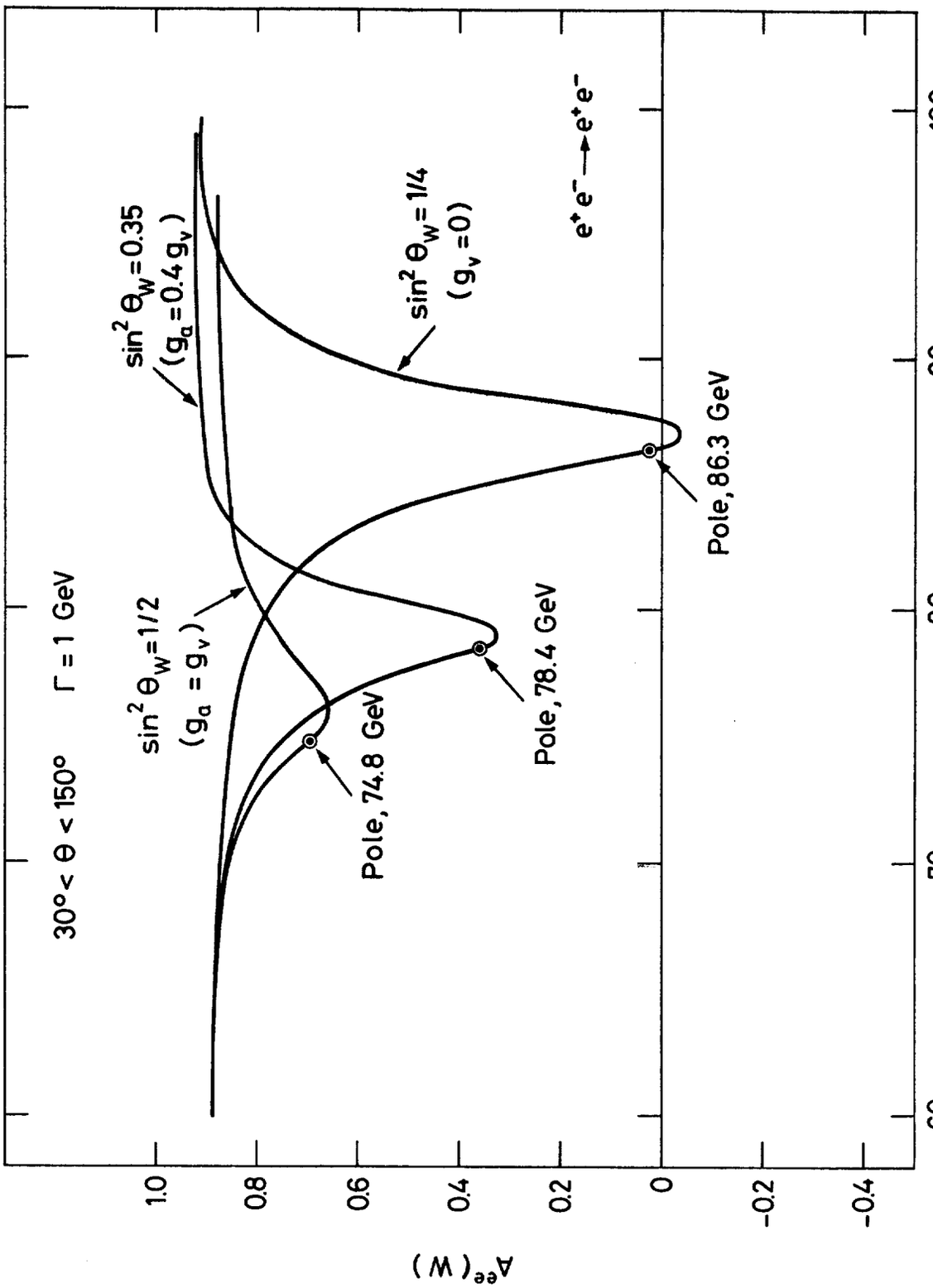
$e^+e^- \rightarrow e^+e^-$
$30° < \Theta < 150°$ $\Gamma = 1$ GeV
$\sin^2\theta_W = 0.35$
$(g_a = 0.4\, g_v)$
$\sin^2\theta_W = 1/4$
$(g_v = 0)$
$\sin^2\theta_W = 1/2$
$(g_a = g_v)$
Pole, 74.8 GeV
Pole, 78.4 GeV
Pole, 86.3 GeV
$A^{ee}(W)$
$W = \sqrt{s}$ GeV
1.0
0.8
0.6
0.4
0.2
0
-0.2
-0.4
60
70
80
90
100

Fig. 3

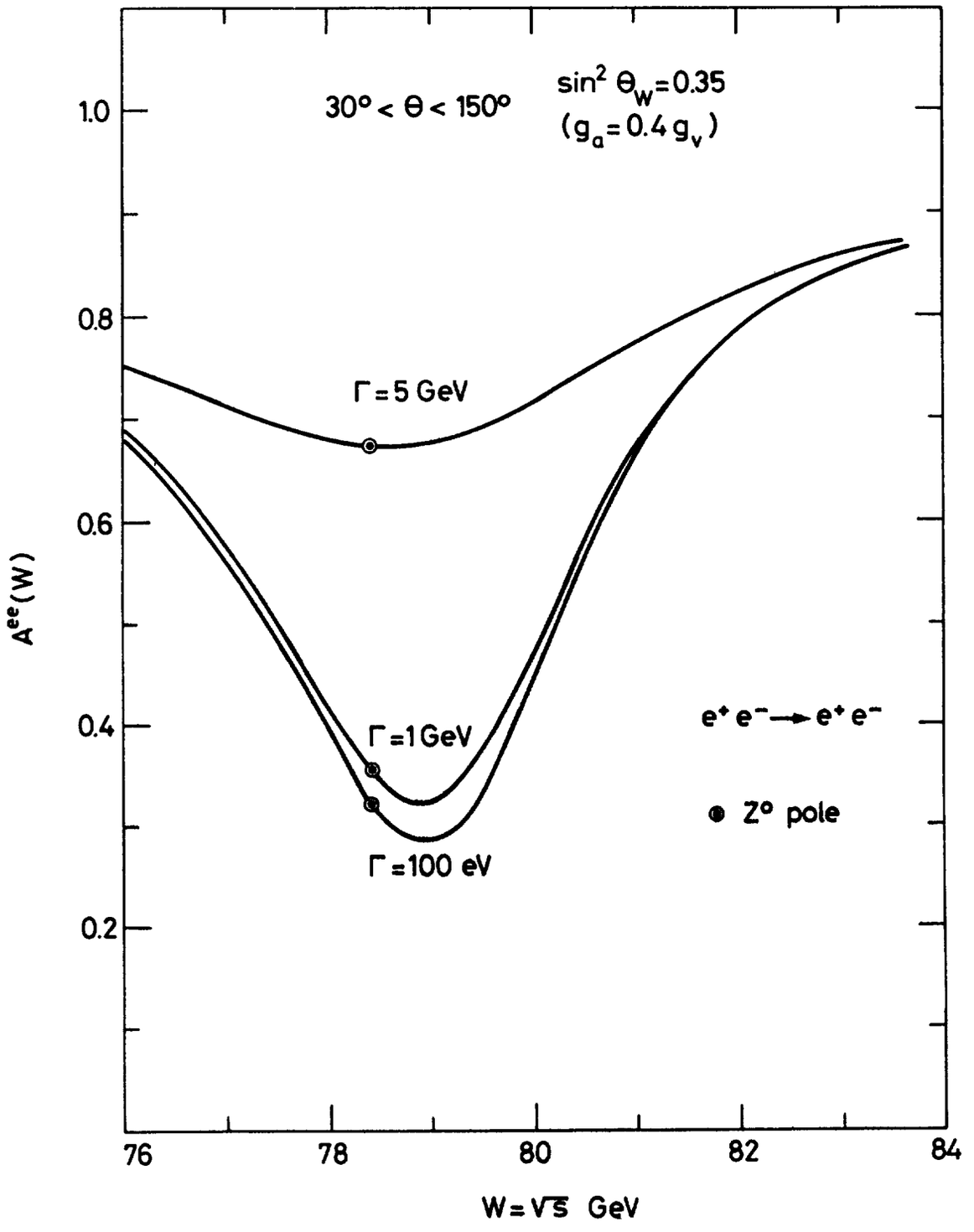
30° < Θ < 150°
sin² Θ_W = 0.35
(g_a = 0.4 g_v)
Γ = 5 GeV
Γ = 1 GeV
Γ = 100 eV
e⁺e⁻ → e⁺e⁻
Z° pole
A^ee(W)
W = √s GeV
1.0
0.8
0.6
0.4
0.2
76
78
80
82
84

Fig. 4

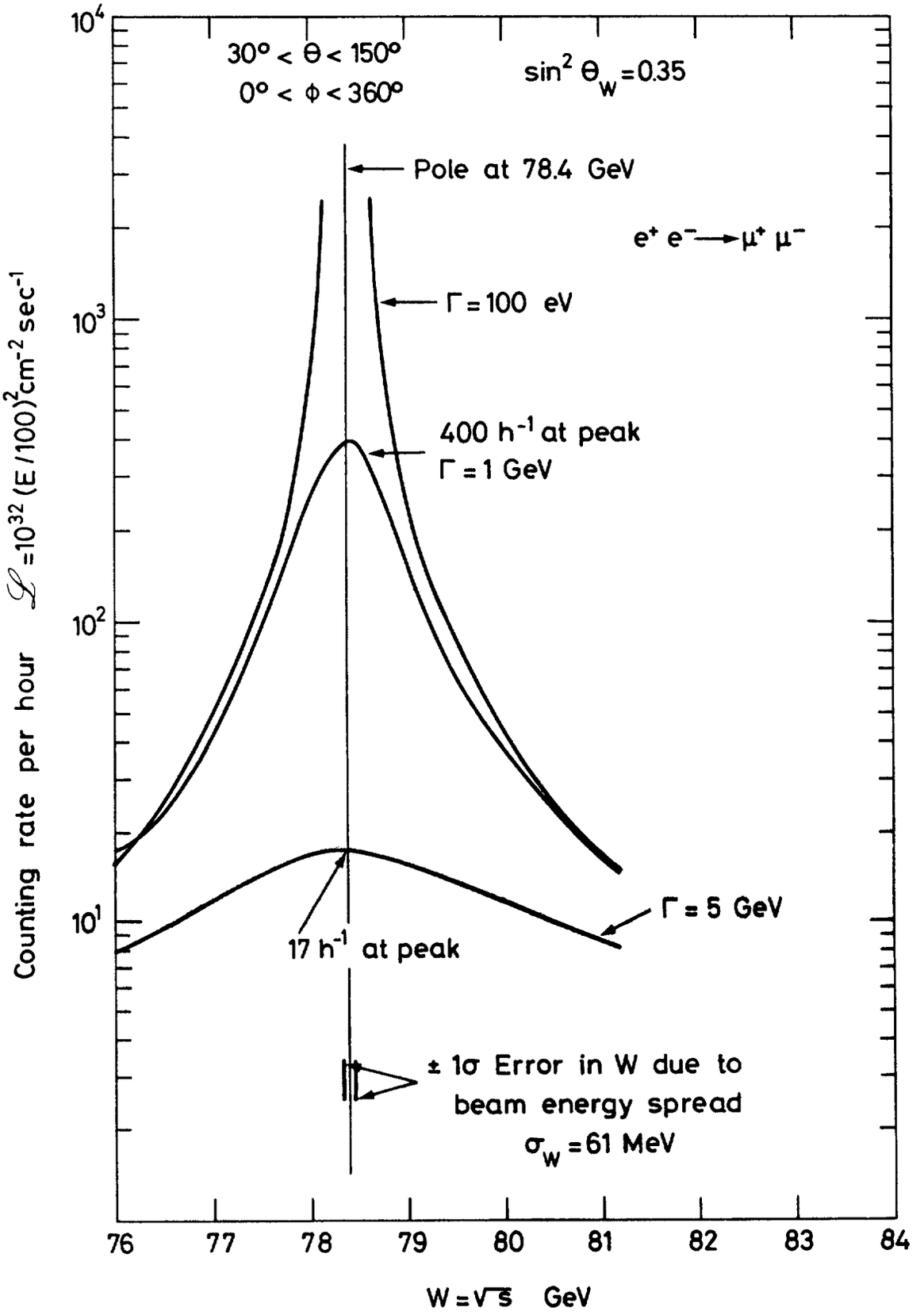
10^4
10^3
10^2
10^1
$30° < \Theta < 150°$
$0° < \phi < 360°$
$\sin^2 \Theta_W = 0.35$
Pole at 78.4 GeV
$e^+ e^- \rightarrow \mu^+ \mu^-$
$\Gamma = 100$ eV
400 h^{-1} at peak
$\Gamma = 1$ GeV
$\Gamma = 5$ GeV
17 h^{-1} at peak
$\pm 1\sigma$ Error in W due to
beam energy spread
$\sigma_W = 61$ MeV
Counting rate per hour $\mathscr{L} = 10^{32} (E/100)^2 cm^{-2} sec^{-1}$
76
77
78
79
80
81
82
83
84
$W = \sqrt{s}$ GeV

Fig. 5

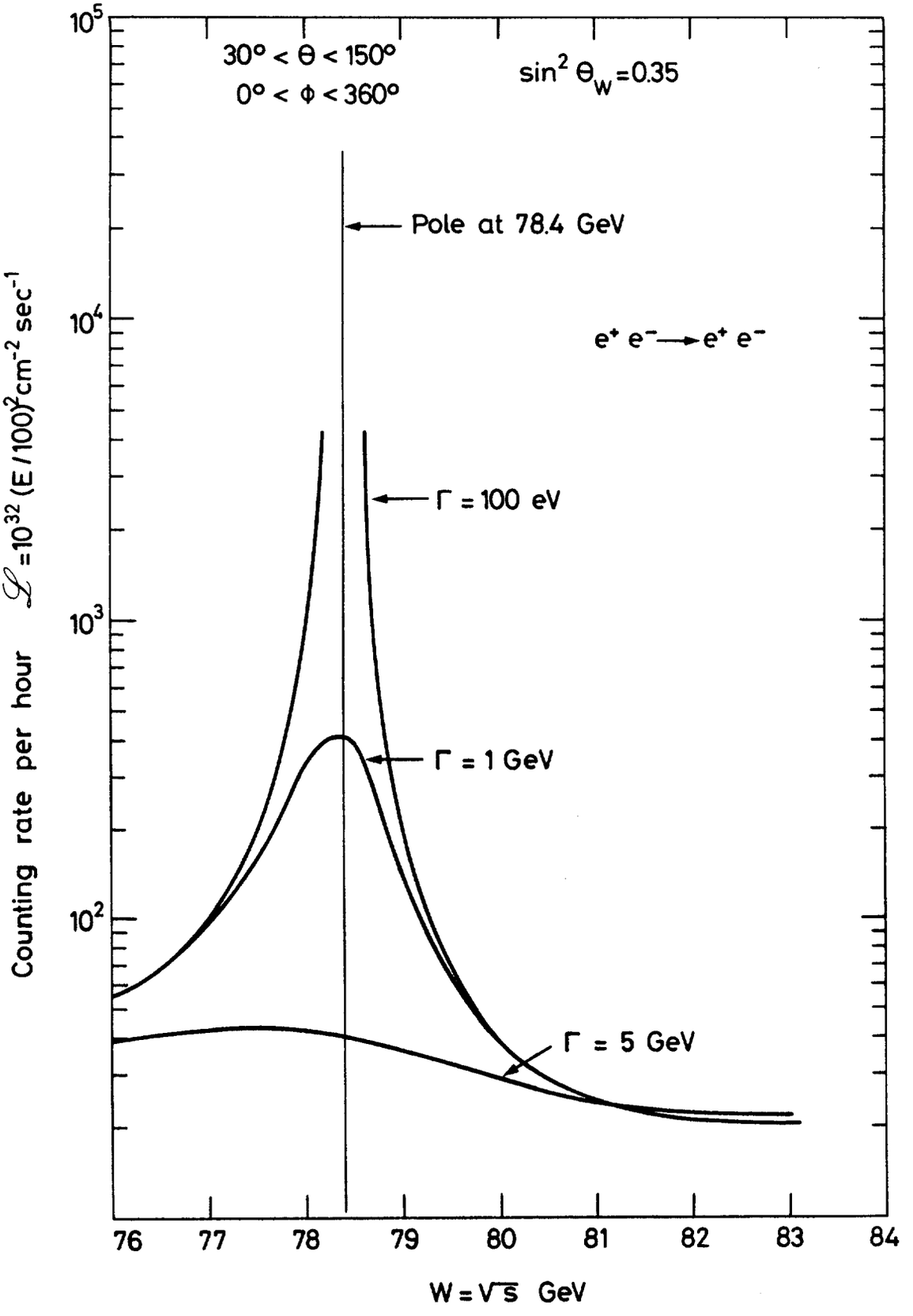
30° < Θ < 150°
0° < Φ < 360°
sin² Θ_W = 0.35
Pole at 78.4 GeV
e⁺ e⁻ → e⁺ e⁻
Γ = 100 eV
Γ = 1 GeV
Γ = 5 GeV
Counting rate per hour ℒ = 10³² (E/100)² cm⁻² sec⁻¹
10⁵
10⁴
10³
10²
76
77
78
79
80
81
82
83
84
W = √s GeV

Fig. 6

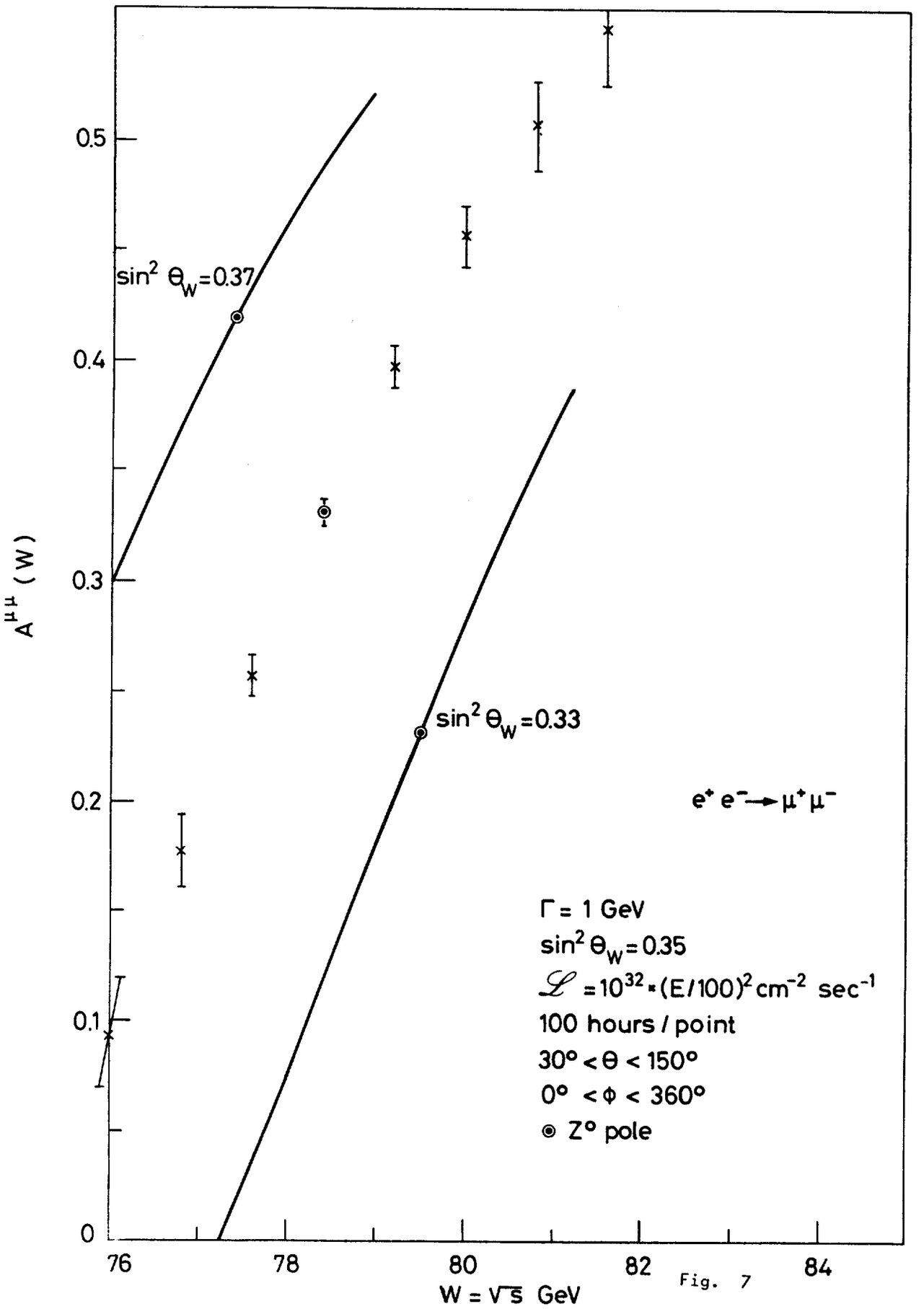
0.5
0.4
0.3
0.2
0.1
0
$A^{\mu\mu}(W)$
$\sin^2\theta_W=0.37$
$\sin^2\theta_W=0.33$
$e^+e^- \rightarrow \mu^+\mu^-$
$\Gamma = 1$ GeV
$\sin^2\theta_W=0.35$
$\mathscr{L} = 10^{32} * (E/100)^2 cm^{-2}\ sec^{-1}$
100 hours / point
$30° < \theta < 150°$
$0° < \phi < 360°$
⊙ Z° pole
76
78
80
82
84
$W = \sqrt{s}$ GeV

Fig. 7

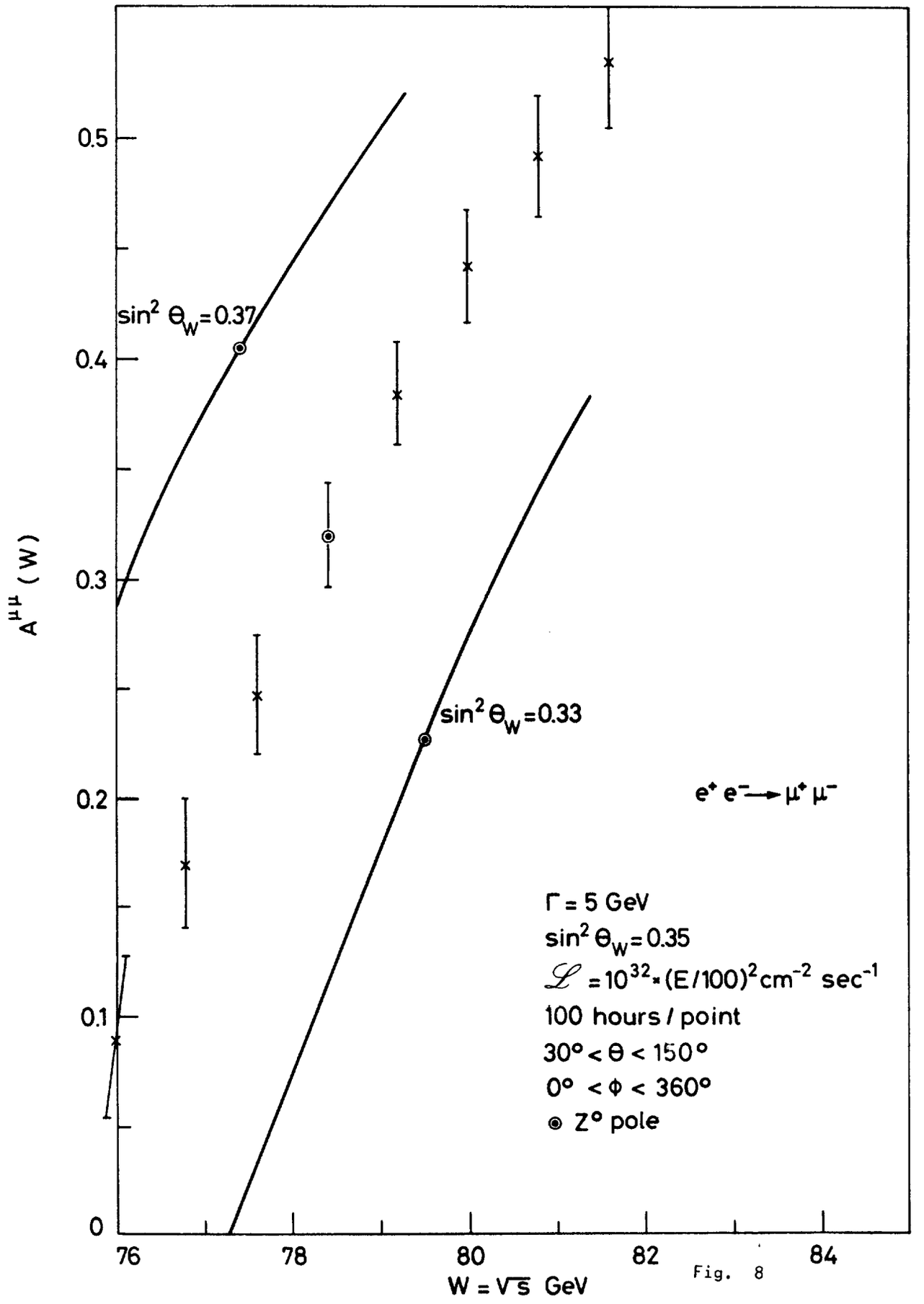
0.5
0.4
0.3
0.2
0.1
0
$A^{\mu\mu}(W)$
$\sin^2\theta_W = 0.37$
$\sin^2\theta_W = 0.33$
$e^+e^- \rightarrow \mu^+\mu^-$
$\Gamma = 5$ GeV
$\sin^2\theta_W = 0.35$
$\mathscr{L} = 10^{32} * (E/100)^2 cm^{-2} sec^{-1}$
100 hours / point
$30° < \theta < 150°$
$0° < \phi < 360°$
◉ Z° pole
76
78
80
82
84
$W = \sqrt{s}$ GeV

Fig. 8

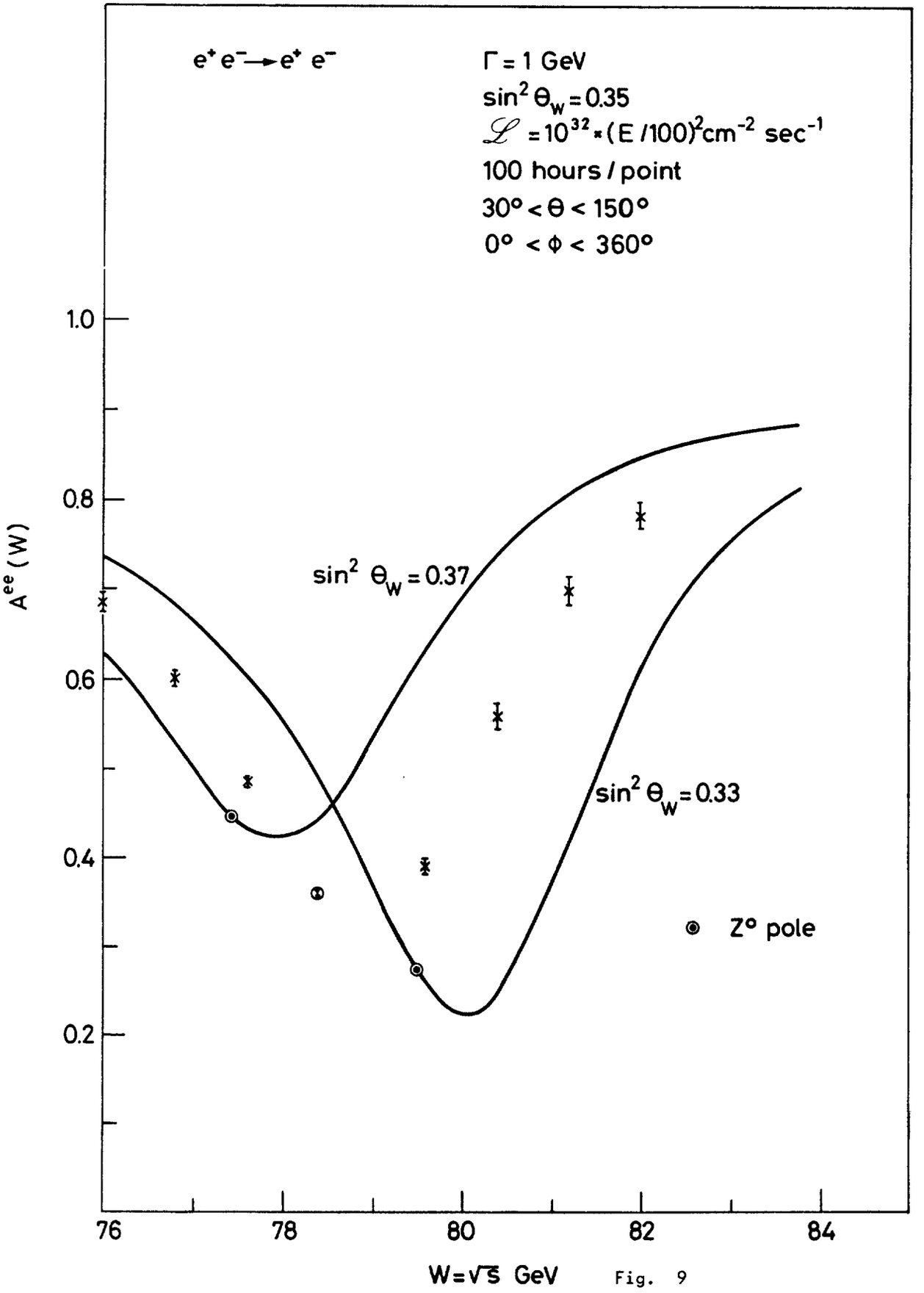
e⁺ e⁻ → e⁺ e⁻
Γ = 1 GeV
sin² θ_W = 0.35
ℒ = 10³² * (E /100)² cm⁻² sec⁻¹
100 hours / point
30° < θ < 150°
0° < φ < 360°
1.0
0.8
0.6
0.4
0.2
A^ee (W)
sin² θ_W = 0.37
sin² θ_W = 0.33
Z° pole
76
78
80
82
84
W = √s GeV

Fig. 9

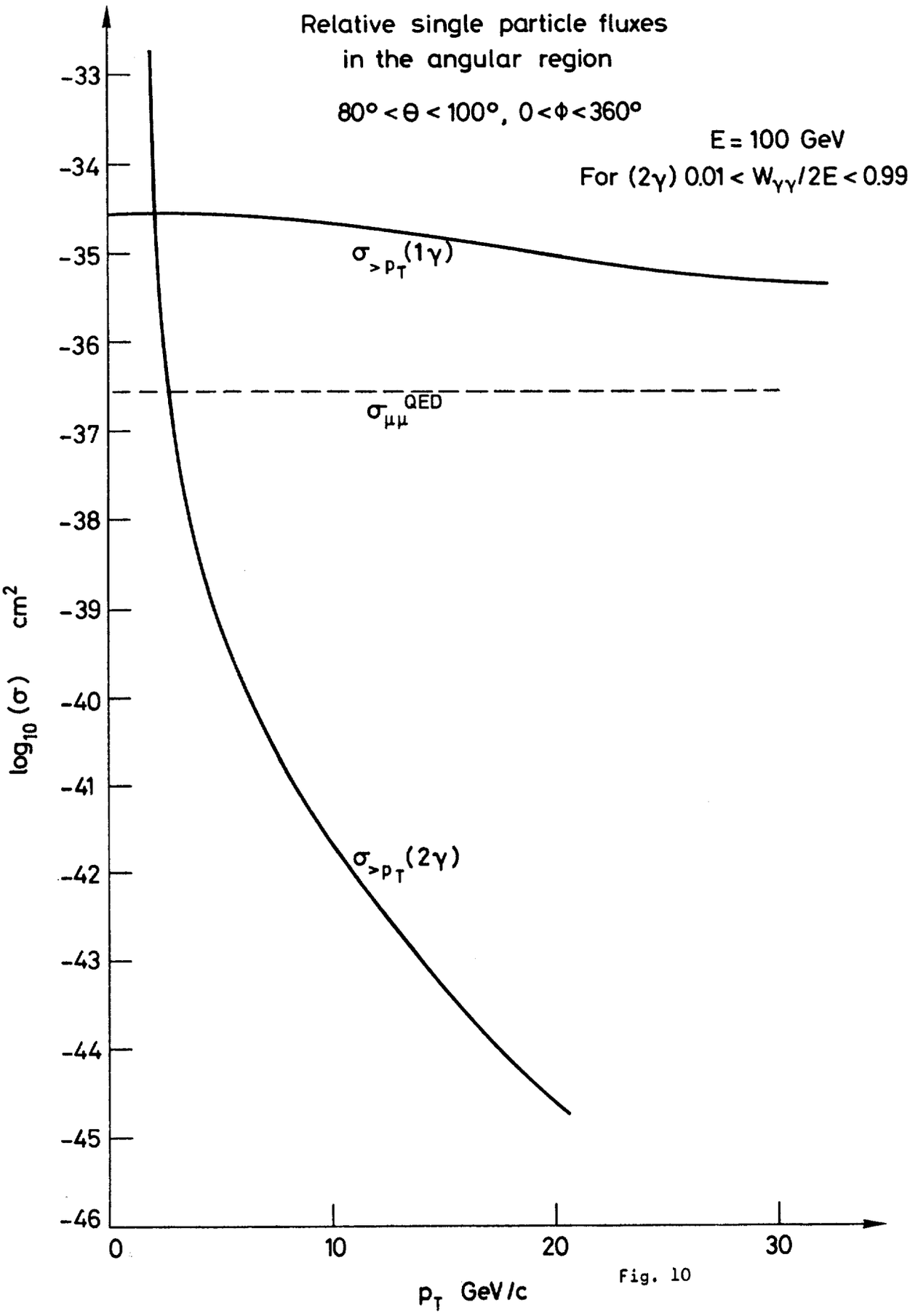
Relative single particle fluxes
in the angular region
80° < Θ < 100°, 0 < Φ < 360°
E = 100 GeV
For (2γ) 0.01 < W_γγ/2E < 0.99
σ_>pT(1γ)
σ_μμ^QED
σ_>pT(2γ)
log10 (σ) cm²
-33
-34
-35
-36
-37
-38
-39
-40
-41
-42
-43
-44
-45
-46
0
10
20
30
pT GeV/c

Fig. 10

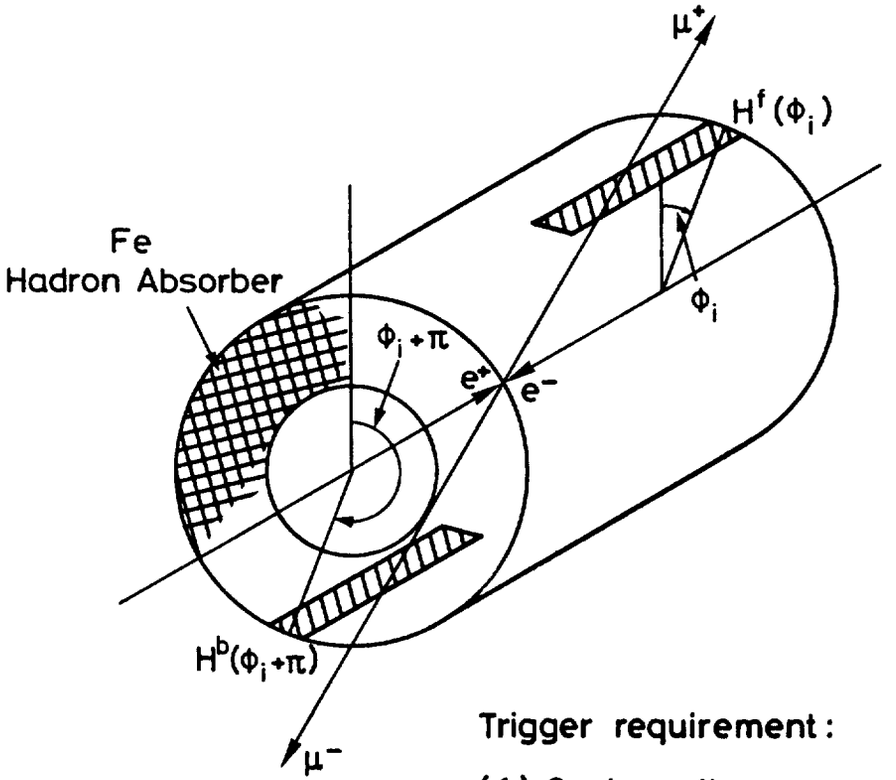

Trigger requirement:

(1) Coplanarity

(2) 1 Track Forward
1 Track Backward

$$\sum_i H^f(\phi_i) \cdot H^b(\pi+\phi_i)$$

Fig. 11

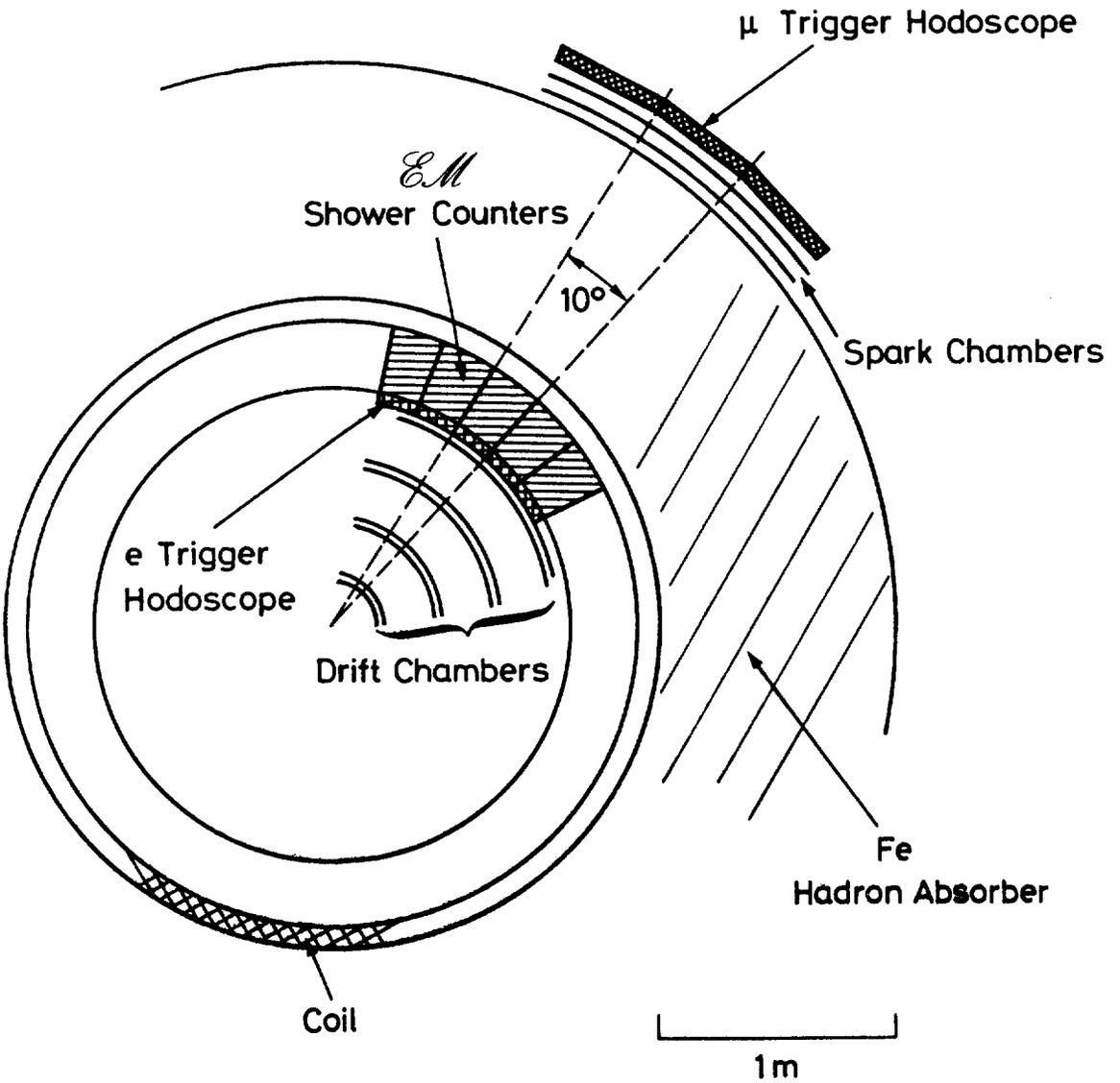
μ Trigger Hodoscope
EM
Shower Counters
10°
Spark Chambers
e Trigger
Hodoscope
Drift Chambers
Fe
Hadron Absorber
Coil
1m

Fig. 12

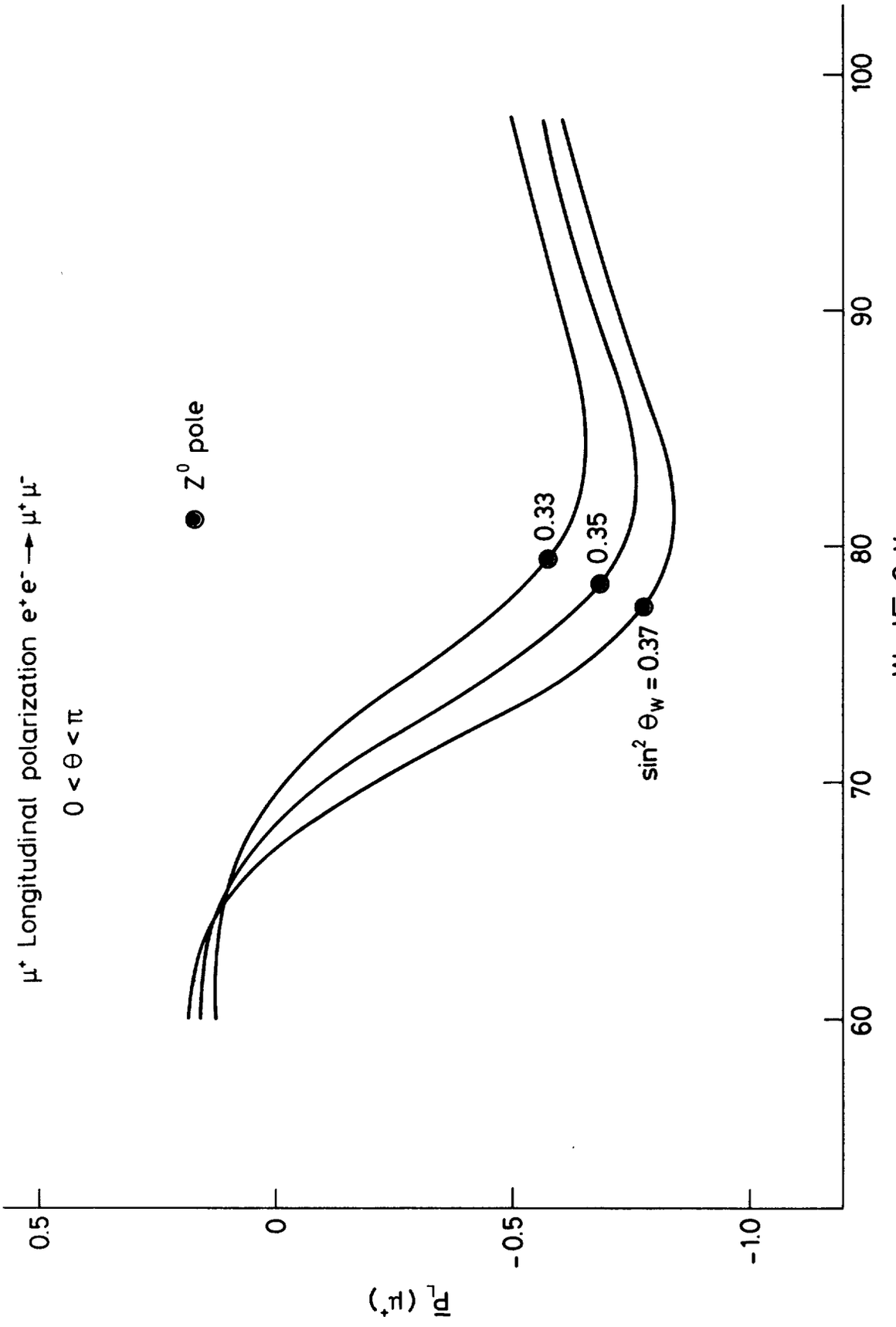
μ⁺ Longitudinal polarization e⁺e⁻ → μ⁺μ⁻
0 < θ < π
Z⁰ pole
0.33
0.35
sin² θw = 0.37
P_L (μ⁺)
0.5
0
-0.5
-1.0
60
70
80
90
100
W = √s GeV

Fig. 13

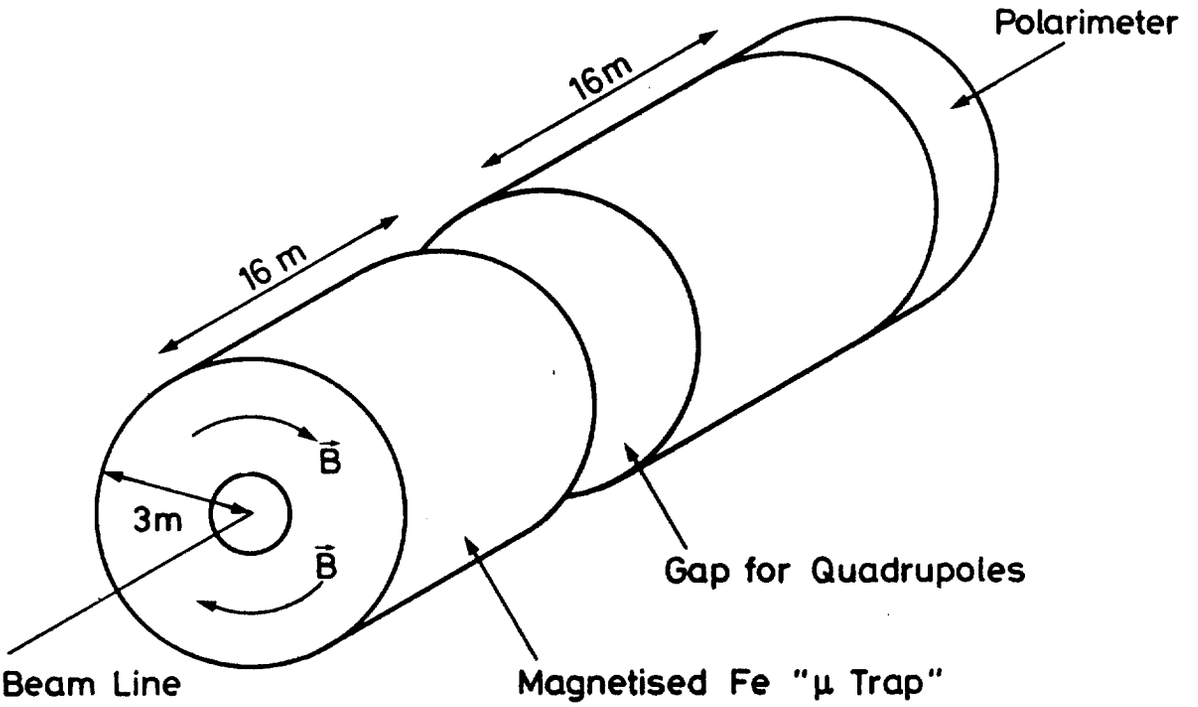
Polarimeter
16m
16 m
$\vec{B}$
3m
$\vec{B}$
Gap for Quadrupoles
Beam Line
Magnetised Fe "μ Trap"

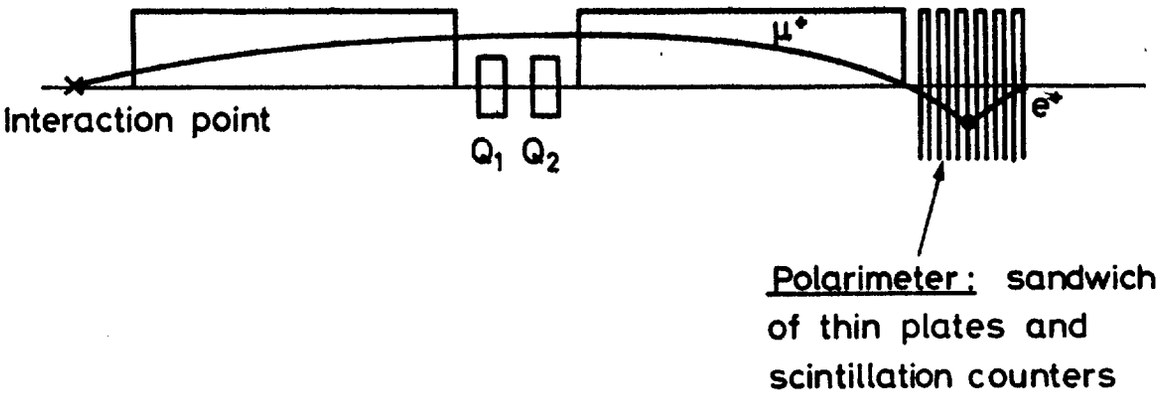
μ*
Interaction point
Q_1 Q_2
e*
Polarimeter: sandwich
of thin plates and
scintillation counters

Fig. 14

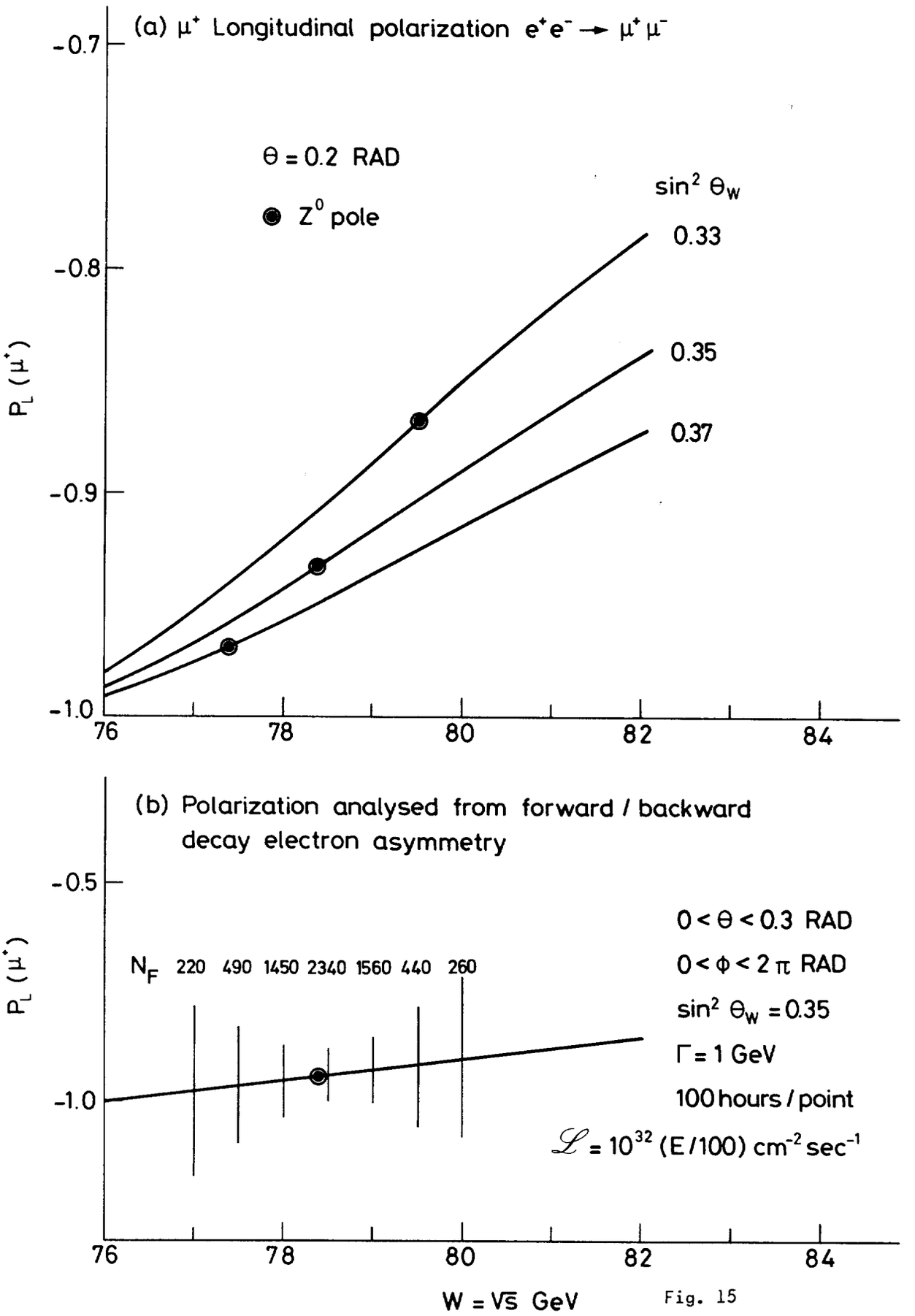
(a) μ⁺ Longitudinal polarization e⁺e⁻ → μ⁺μ⁻
-0.7
-0.8
-0.9
-1.0
P_L (μ⁺)
Θ = 0.2 RAD
Z⁰ pole
sin² θ_W
0.33
0.35
0.37
76
78
80
82
84
(b) Polarization analysed from forward / backward
decay electron asymmetry
-0.5
-1.0
P_L (μ⁺)
N_F 220 490 1450 2340 1560 440 260
0 < Θ < 0.3 RAD
0 < φ < 2π RAD
sin² θ_W = 0.35
Γ = 1 GeV
100 hours / point
ℒ = 10³² (E/100) cm⁻² sec⁻¹
76
78
80
82
84
W = √s GeV

Fig. 15

Appendix

The differential cross section for $e^+e^- \rightarrow e^+e^-$ in the absence of beam polarisation and averaged over final state helicities is given by the relation 7) :

$$\frac{8s}{\alpha^2}\frac{d\sigma^{ee}}{d\Omega} = 4B_1 + (B_2+B_3)(1+\cos^2\theta) + 2(B_3-B_2)\cos\theta \qquad (A1)$$

θ = angle between incoming and outgoing e^+.

$s = 4E^2$ (E= beam energy)

$t = -2E^2(1-\cos\theta)$

B_1, B_2, B_3 are defined by the relations :

$$B_1 = \left(\frac{s}{t}\right)^2 \left| (1 + (g_v-g_a)^2 Q) \right|^2$$

$$B_2 = \left| (1 + (g_v^2 - g_a^2) R) \right|^2 \qquad (A2)$$

$$B_3 = \tfrac{1}{2}\left\{ \left| \frac{s}{t}(1+(g_v+g_a)^2 Q)+1+(g_v+g_a)^2 R \right|^2 + \left| \frac{s}{t}(1+(g_v-g_a)^2 Q)+1+(g_v-g_a)^2 R \right|^2 \right\}$$

$$R = \frac{s}{e^2(s-M_z^2 + iM_z\Gamma)}$$

$$Q = \frac{t}{e^2(t-M_z^2)}$$

where M_z, Γ are the mass and width of the Z^o. Terms in Γ^2 are neglected, as well as terms in Γ in Q . Γ has a significant effect only near the pole in R.

Eqns (A1), (A2) give the differential cross section for $e^+e^- \rightarrow e^+e^-$. The equations for $e^+e^- \rightarrow \mu^+\mu^-$ are given by setting $\frac{s}{t}$ to zero throughout. B_1 is then zero, B_2 and B_3 depend only on s :

$$B_2 = 1 + 2(g_v^2-g_a^2)\,\mathrm{Re}(R) + (g_v^2-g_a^2)^2 |R|^2$$

$$B_3 = 1 + 2(g_v^2+g_a^2)\,\mathrm{Re}(R) + (g_v^4 + 6g_v^2 g_a^2 + g_a^4) |R|^2 \qquad (A3)$$

setting $B_2 + B_3 = 2F_1$

$B_3 - B_2 = 2F_3$ (A4)

the $\mu\mu$ differential cross section becomes :

$$\frac{4s}{\alpha 2}\ \frac{d\sigma^{\mu\mu}}{d\Omega} = F_1(w)\ (1+\cos^2\theta) + 2F_3(w)\cos\theta \qquad (A5)$$

$(w = \sqrt{s})$

From Eqn (A5) the backward-forward asymmetry $A^{\mu\mu}$ is readily found to be

$$A^{\mu\mu}(w) = \frac{N_f - N_b}{N_f + N_b} = \frac{3}{4}\ \frac{F_3(w)}{F_1(w)} \leqslant \frac{3}{4} \qquad (A6)$$

From the positivity of the cross section in Eqn A5 $F_3 \leqslant F_1$.

In the W-S model where g_a, g_v are related to the Weinberg angle by Eqns (4), F_1, F_3 are given explicity in terms of $S_w = \sin\theta_w$, M_z, Γ and s by the relations :

$$F_1 = 1 + \frac{s(s-M_z^2)}{8((s-M_z^2)^2+\Gamma^2M_z^2)}\ \frac{(4S_w^2-1)^2}{S_w^2(1-S_w^2)} + \frac{s^2}{16((s-M_z^2)^2+\Gamma^2M_z^2)}\left[\frac{1+(4S_w^2-1)^2}{4S_w^2(1-S_w^2)}\right]^2$$

$$F_3 = \frac{s(s-M_z^2)}{8((s-M_z^2)^2+\Gamma^2M_z^2)\ S_w^2(1-S_w^2)} + \frac{1}{4}\ \frac{s^2}{4((s-M_z^2)^2+\Gamma^2M_z^2)}\left[\frac{4S_w^2-1}{4S_w^2(1-S_w^2)}\right]^2 \qquad (A7)$$

The counting rate curves in fig.5 are proportional to F_1. $A^{\mu\mu}$ in fig. 2 is given by Eqns (A6), (A7). $A^{\mu\mu}$ in fig. 7, 8 are given by (A6) with the replacement $\frac{3}{4} \rightarrow \frac{2\sqrt{3}}{5}$, and (A7).

The backward forward asymmetry for the ee channel $A^{ee}(w)$ involves much more complicated formulae than Eqn(A6) due to the t (or $\cos\theta$) dependence of B_1 and B_3. It is convenient to change variables from $\cos\theta$ to t in Eqn (A1). Integrating over the azimuthal angle gives :

$$\frac{d\sigma^{ee}}{dt} = \frac{2\pi\alpha^2}{s^2}\ (B_1+B_3+\frac{2B_3t}{s} + (B_2+B_3)\ \frac{t^2}{s^2}) \qquad (A8)$$

$A^{ee}(w)$ can be found from the general integral, $\int \frac{d\tilde{\sigma}^{ee}}{dt}\,dt$ which in turn is given from (A8) by the 5 integrals :

$$\int B_1\,dt,\quad \int B_3\,dt,\quad \frac{2}{s}\int B_3 t\,dt,\quad \frac{1}{s^2}\int B_2 t^2\,dt,\quad \frac{1}{s^2}\int B_3 t^2\,dt$$

These are found to depend on the integrals $I_1 - I_{12}$ of 12 different functions of t and M_z^2 according to the equations :

$$\int B_1\,dt = s^2\,(I_1 + 2c\,I_7 + c^2\,I_5)$$

$$\int B_3\,dt = \tfrac{1}{2}\Big\{s^2(2I_1+2(a_+{+}a_-)I_7 + (a_+^2{+}a_-^2)I_5) + 2s\,((b_+{+}b_-)I_2 + (a_+b_+{+}a_-b_-)I_6) + (b'_+{+}b'_-)I_3\Big\}$$

$$\int \frac{2B_3 t}{s}\,dt = s\,(2I_2+2(a_+{+}a_-)I_6 + (a_+^2{+}a_-^2)I_{10}) + 2((b_+{+}b_-)I_3 + (a_+b_+{+}a_-b_-)I_8) + \frac{1}{s}\,(b'_+{+}b'_-)I_4$$

$$\int \frac{t^2}{s^2} B_3\,dt = \tfrac{1}{2}\Big\{(2I_3+2(a_+{+}a_-)I_8 + (a_+^2{+}a_-^2)I_{11}) + \frac{2}{s}\,((b_+{+}b_-)I_4 + (a_+b_+{+}a_-b_-)I_9) + \frac{1}{s^2}\,(b'_+{+}b'_-)I_{12}\Big\}$$

$$\int \frac{B_2 t^2}{s^2}\,dt = \frac{B_2}{s^2}\,I_{12}$$

here : $a_\pm = \frac{1}{e^2}\,(g_v \pm g_a)^2$, $b_\pm = 1 + a_\pm \frac{s(s-M_z^2)}{(s-M_z^2)^2 + \Gamma^2 M_z^2}$

$$b'_\pm = 1 + \frac{a_\pm^2\; s(s-M_z^2)}{(s-M_z^2)^2 + \Gamma^2 M_z^2} + \frac{a_\pm^2\; s^2}{(s-M_z^2)^2 + \Gamma^2 M_z^2}$$

$$c = \frac{1}{e^2}\,(g_v^2 - g_a^2)$$

It turns out that $I_1 - I_{12}$ can all evaluated analytically, with the results : $\quad \alpha \equiv M_z^2 \qquad \beta \equiv t - M_z^2$

$$I_1 = -\frac{1}{t} \qquad I_2 = \ln t$$

$$I_3 = t \qquad I_4 = \frac{t^2}{2}$$

$$I_5 = -\frac{1}{\beta} \qquad I_6 = \ln \beta$$

$$I_7 = \frac{1}{\alpha}(\ln\beta - \ln t) \qquad I_8 = t + \alpha \ln\beta$$

$$I_9 = \frac{t^2}{2} + \alpha t + \alpha^2 \ln\beta \qquad I_{10} = \ln\beta - \frac{\alpha}{\beta}$$

$$I_{11} = t + 2\alpha \ln\beta - \frac{\alpha^2}{\beta} \qquad I_{12} = \frac{t^3}{3}$$

This rather cumbersome set of equations then gives $A^{ee}(w) = \frac{N_f - N_b}{N_f + N_b}$

$$N_f = \int_{-2E^2}^{-2E^2(1 - \cos 30^\circ)} \frac{d\sigma^{ee}}{dt}\, dt \qquad N_b = \int_{-4E^2(1+\cos 30^\circ)}^{-2E^2} \frac{d\sigma^{ee}}{dt}\, dt$$

$A^{ee}(w)$ is plotted in figs. 3, 4, 9, while the counting rate curves in fig.6 are proportional to $N_f + N_b$.

For unpolarised initial beams the differential cross section for production of $\mu^+\mu^-$ with $\mu^\pm$ helicity $h_\pm$ is :

$$\frac{32s}{\alpha^2}\frac{d\sigma}{d\Omega} = 2F_1(1+\cos^2\theta) + 4F_3\cos\theta - h_+h_-(1-\cos\theta)^2(F_1 - F_3) + (h_- - h_+)(1+\cos\theta)^2 F_4 \qquad \text{(A9)}$$

F_1, F_3 are defined in Eqns (A3, A4) while F_4 is given, in terms of g_v/e, g_a/e, s, Γ and M_z^2, by the relation :

$$F_4 = 2g_v g_a \left[\frac{s(s-M_z^2)}{e^2((s-M_z^2)^2 + \Gamma^2 M_z^2)} + \frac{(g_v^2 + g_a^2)\, s^2}{e^4((s-M_z^2)^2 + \Gamma^2 M_z^2)}\right] \qquad \text{(A10)}$$

Averaging over the helicity of the μ^-, the μ^+ helicity $P_L(\mu^+)$ is defined by

$$\frac{d\sigma(h_+ = 1) - d\sigma(h_+ = -1)}{d\sigma(h_+ = 1) + d\sigma(h_+ = -1)} = P_L(\mu^+) \qquad \text{(A11)}$$

Substituting from Eqn A9 (after setting $h_- = 0$) in Eqn A11 gives Eqn 6 of the main text.

V- HADRON JETS IN e^+e^- ANNIHILATIONS AT $\sqrt{s}$ = 200 GeV

W. Willis and K. Winter

1. Evidence for hadron jets at Spear

Two different pieces of information can be interpreted as evidence for hadron jets[1]:

- A deviation from isotropy of the angular distribution of energy in the final state, $dE/d\Omega$.

Searching for a preferred direction with respect to which the transverse momenta of charged secondaries are minimized, a quantity called sphericity can be defined as

$$S = \frac{3(\Sigma P_{Ti}^2)\min}{2\Sigma P_i}$$

Figure 1 shows the observed mean sphericity as a function of the total energy. The data support a decreasing mean sphericity with increasing energy equivalent to a constant mean transverse momentum, relative to the preferred (jet) direction, of $\bar{P}_T$ = 315 MeV/c. In assessing this evidence one should bear in mind, however, that only 70% of the solid angle has been covered by the detector, and that the remaining fraction has been inferred from a simulation.

- A deviation from isotropy of the azimuthal angle (of jet axis) distribution when using polarized e^+e^- beams (see figure 2).

The jet axis is defined as before, in practice, however, by the leading particle. We expect an angular distribution as

$$\frac{d\sigma}{d\Omega} \alpha\ 1 + \alpha \cos^2\theta + P^2\alpha \sin^2\theta \cos 2\psi$$

where P is the degree of polarization of each beam, and α = +1 if the helicity along the jet axis is ±1. This beautiful experiment also shows how strongly a leading particle with $X = P/(E_{cm}/2)$ is correlated with the jet axis; figure 3 shows the asymmetry parameter

$$\alpha = \frac{\sigma_T - \sigma_L}{\sigma_T + \sigma_L}$$

as a function of X for data at $E_{cm} = 7.4$ GeV. The data points are compatible with the asymmetry expected for the beam polarization and for $X > 0.3$ they are in agreement with $\alpha \sim +1$: hadron jets with a leading particle $X > 0.3$ have the same angular distribution as the $\mu^+\mu^-$ final state.

We now interpret this as evidence for annihilation into a pair of quarks, and suppose that

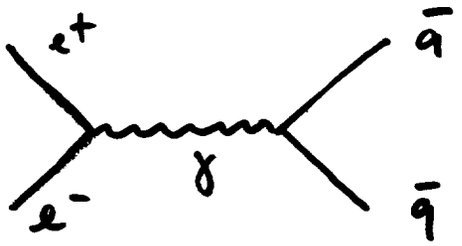

the leading particle gives information on the direction of the quark. It is under this premise that we have studied the interest and feasibility of experiments on hadron jets at LEP.

2. Hadron jets at LEP

We shall discuss[2] how to infer the jet axis and the quark flavour from the hadron final state.

(1) u, d, s jets. Leading particles with $X > 0.3$ are expected to remember the quark flavour and charge, since the dressing of quarks involves a 1-stage process only. At LEP energies we have to include weak interactions, mediated by the neutral weak boson.

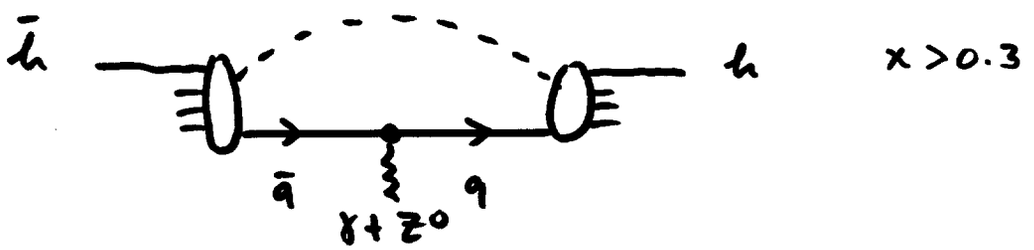

There exist many relations concerning the relative production of η, K^0_s, K^+ and π^+ which allow to verify whether the quark flavour assignment is correct.

(2) Charm jets. Due to the charm quantum number, purely hadronic final states involve a two-stage process, giving first a charmed boson or baryon via process (1) and then a weak decay to hadrons with X < 0.3, e.g. kaons.

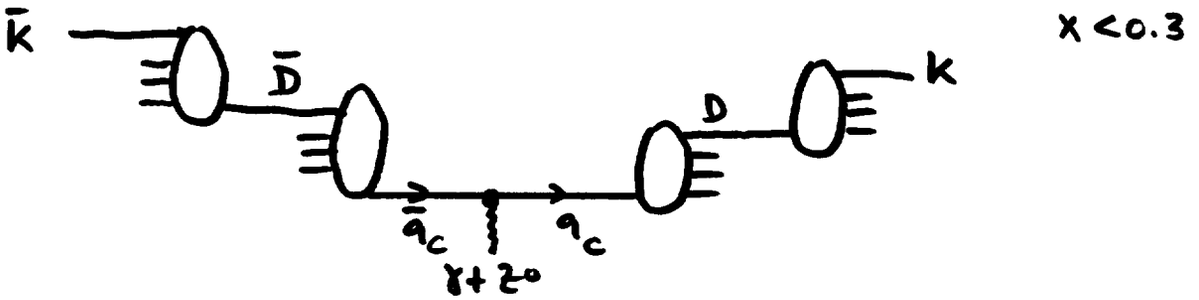

A more specific signature of the quark direction and flavour may be obtained in semi-leptonic decays. The lepton would give the quark direction and the mean X value of the kaon its flavour.

(3) Supercharm jets. Final states involving a new, supercharm quark may occur at LEP energies. Hadrons are then produced via three stages, involving both process (1) and (2) and giving leading hadrons with X < 0.1.

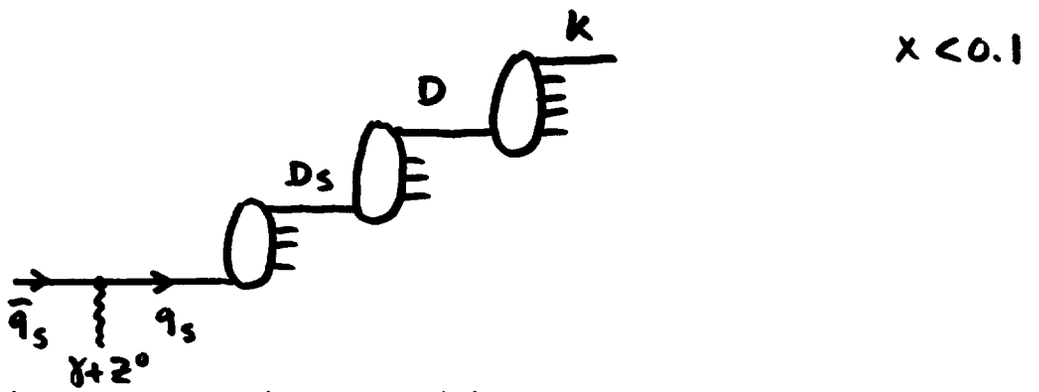

Again, a more practical proposition consists in detecting semi-leptonic decays of D-meson and inferring the flavour of the quark from the mean X-value of both the lepton and the kaon.

We thus expect three regions in X to be related to quarks of different flavour.

Hence, identifying the quark flavour means identifying all hadrons produced.

The difficulties of this task will be rewarded by the ultimate goal: a study of the charge asymmetry and its s-dependence of the various quark final states to deduce, in analogy to $e^+e^- \to \mu^+\mu^-$, the interference terms of weak and electromagnetic interactions, and to infer the weak lagrangian in terms of quarks.

3. Experiments at LEP

We have studied two different detectors, each being appropriate for a class of experiments.

(1) Calorimetric detector for $dE/d\Omega$

This detector would allow an accurate measurement of the angular distribution of hadron energy. Hence, it can be used to search for thresholds due to new quark flavours at LEP energies. While the "old" physics, involving u, d, s and c quarks, is expected to be dominated by jets of very small sphericity (being far from threshold), the "new" physics, e.g. due to supercharm, would display highly spherical events near threshold. A small step in $R = \sigma(e^+e^- \to \text{hadrons})/\sigma(e^+e^- \to \mu^+\mu^-)$, e.g. by 0.5 for a new quark of charge 1/3 or by 1.5 for a new quark of charge 2/3, can thus be detected with high sensitivity, because the sphericity distributions of "old" and "new" physics would not overlap at all, as shown in figure 4.

Multi-jet events may also be searched for, e.g. the famous "splash of glue", due to large angle gluon bremsstrahlung, as proposed by J. Ellis, M.K. Gaillard and G.G. Ross.

(2) Jet particle detector

This detector should allow measurements of momenta, charges and masses of all final state hadrons and leptons in view of charge asymmetry measurements, in analogy to the beautiful games with $\mu^+\mu^-$ final states discussed in Chapter III.

4. Hadron final state at $\sqrt{s}$ = 200 GeV

At LEP energy $\sqrt{s}$ = 200 GeV we expect[3] a mean number of produced hadrons of $\langle n \rangle = 25$, a mean momentum of $\langle p \rangle = 12.3$ GeV/c and a mean transverse momentum with respect to the jet axis of $\langle P_T \rangle = 310$ MeV/c. Hence, a jet would have a mean opening angle of

$$\Delta\theta_{jet} \sim \langle P_T \rangle / \langle P \rangle \sim 0.025 \text{ rad}$$

The main experimental problem is to design a detector with small enough cell size to make the overlap probability negligible or small. Figure 5 shows the result of a simulation[3] of hadron jets at $\sqrt{s}$ = 200 GeV; the probability that more than 1 particle per event enters a cell of solid angle $\Delta\Omega$ has been evaluated. Aiming for less than 10% of the events having two particles overlap in a cell, e.g. in a detector designed to measure momentum, charge and mass of each particle, we require $\Delta\Omega \leq 100$ μsterad.

The natural size of a shower in a calorimeter covers a solid angle[4] of $\Delta\Omega = 10^{-2}$ sterad, a factor 100 larger than the detector cell size required for small overlap. Hence, calorimetric measurements can yield $dE/d\Omega$ only and not the details of the jets.

5. Calorimetric jet detector, $dE/d\Omega$

The energy of a jet can be measured, using a sampling calorimeter composed of iron plates and detectors, e.g. proportional counters, with a variance of

$$\sigma_E = \tfrac{1}{2}\sqrt{E_{beam}/\text{GeV}}$$

The direction of the jet can be determined by connecting the beam vertex and the centre of gravity of the shower, as described in reference 3). Using detector elements of 1 cm width one expects an angular resolution of

$$\sigma_\theta = \frac{0.1}{\sqrt{E/\text{GeV}}} \text{ rad}$$

Hence, the energy and direction of a 100 GeV jet can be measured with good resolution,

$$\sigma_\theta = 10 \text{ mrad}$$

$$\sigma_E = 5 \text{ GeV}$$

The background of γ-γ events can be kept below 1% by requiring $E_h > 180$ GeV (for $\sqrt{s} = 200$ GeV); the remaining background has small sphericity and does not obscure, therefore, the search for small steps in the ratio R.

This detector is insensitive to heavy background from synchrotron radiation.

6. Jet particle detector

The traditional way of particle identification by Cerenkov counter hodoscopes cannot be pushed further to reach a cell size of $\Delta\Omega = 100$ μsterad. A new approach is required.

Due to the small size of the interaction region, the problem can be solved by imaging Cerenkov counters, in particular by applying ideas recently put forward by T. Ypsilantis.

A schematic layout is given in figure 6. The detector consists of three main components:

1. a small axial field coil for momentum measurements below 5 GeV/c and charge measurement up to 20 GeV/c
2. imaging Cerenkov counters
3. calorimeter.

1. Axial field coils produce a bending power of $\sim$ 0.2 Tm, or about 60 MeV/c transverse momentum. If the beam positions are known to $\sim$ 100μ and the error in the cylindrical chambers is the same, while the error in the centre of the $\check{C}$ image in the liquid Neon is 300μ, the momentum resolution is $\Delta p/p \sim 3\%$ for $p \leq 1$ GeV/c and there is a $\sim$ 3 standard deviations sign measurement for 20 GeV/c.

2. The imaging Cerenkov counter follows the work of T. Ypsilantis. The photons, with about 8 eV, are detected with photoionisation proportional counters, with 1 mm resolution in the first counter and 3 mm in the second. There are three radiators:

- the LiF window, effective threshold $\gamma_t = 1.35$
- 2.5 cm of liquid Neon, $\gamma_t = 2.39$
- krypton with 1 atm $\gamma_t = 28$

K/π/p separation can be maintained up to $\sim$ 60 GeV/c, where $\Delta\gamma/\gamma$ for a K is $\sim$ 0.2. π/μ separation can be made up to momenta of $\sim$ 10 GeV/c. π/e separation is obtained for momenta below 15 GeV/c.

3. The calorimeter must measure energy well enough to separate K and p of the same γ from 5 GeV up. It is the most accurate measurement of energy for γ above 80. It gives, then, the only measurement for electrons above 10 GeV, and of course the only measurement for neutrals. It identifies μ's of energy larger than 10 GeV. The forward cones are covered by special sections of calorimeter. Events due to two-photon interactions can be vetoed by the energy measurement at the trigger level, if no search for missing momentum and energy due to neutrinos is intended.

It should be stressed that simultaneous identification of hadrons, muons and electrons is a unique feature of this type of detector. All previous attempts, e.g. at PETRA and PEP, failed to achieve this goal or had to take compromises.

References

1) R.F. Schwitters et al., Phys. Rev. Letters 35, 1320 (1975).
G.H. Hanson et al., Phys. Rev. Letters 35, 1609 (1975).

2) See for instance T. Walsh, Discussion Meeting on PETRA Experiments, Frascati, 1976 (DESY, Hamburg, 1976), p. B1-B17.

3) Using simulation as described in PEP Summer Study, 1975.

4) B. Friend et al., Nucl. Instrum. Methods (in print).

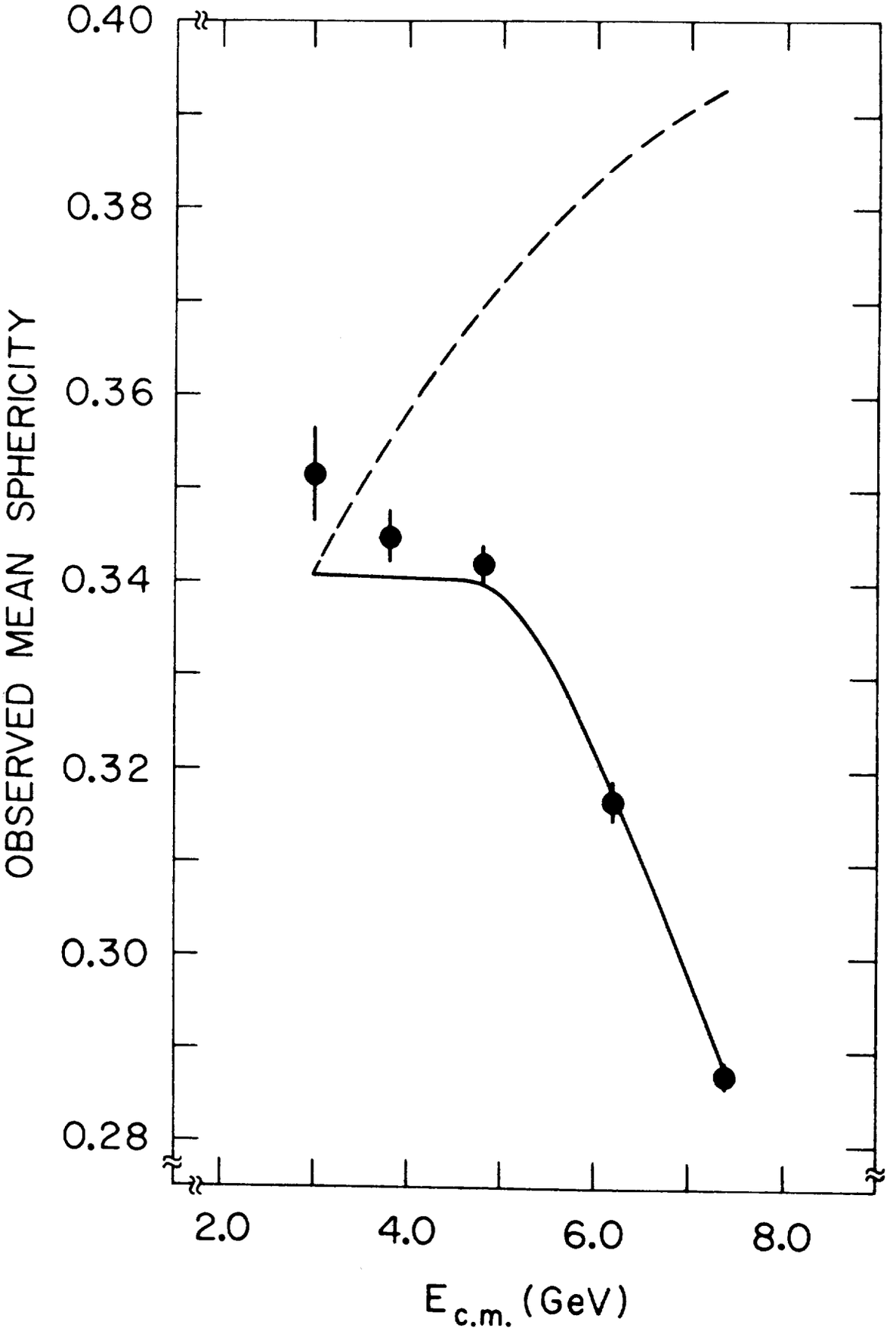
0.40
0.38
0.36
0.34
0.32
0.30
0.28
OBSERVED MEAN SPHERICITY
2.0
4.0
6.0
8.0
E c.m. (GeV)

Fig. 1

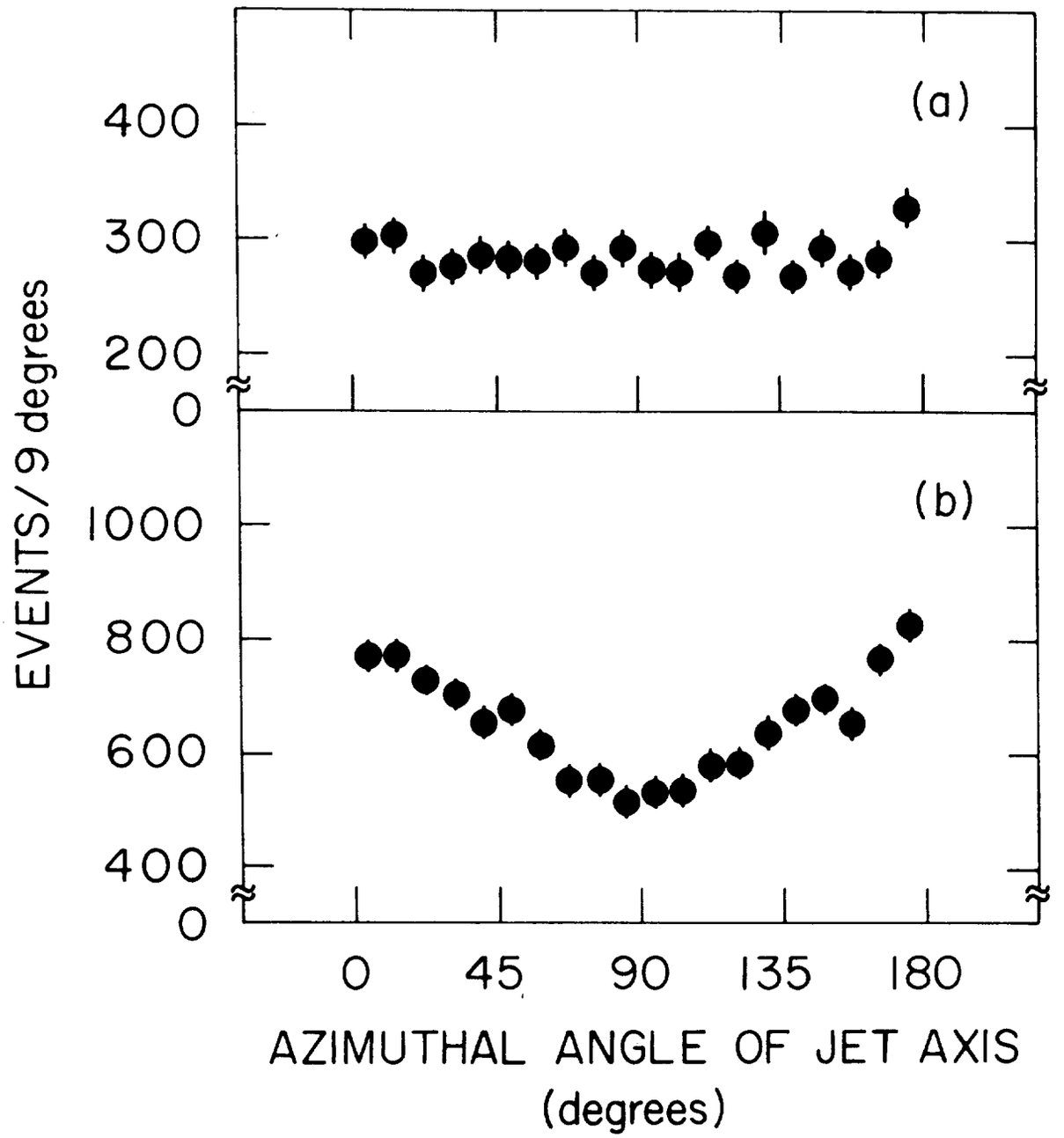
(a)
(b)
400
300
200
0
1000
800
600
400
0
EVENTS/9 degrees
0
45
90
135
180
AZIMUTHAL ANGLE OF JET AXIS
(degrees)

Fig. 2

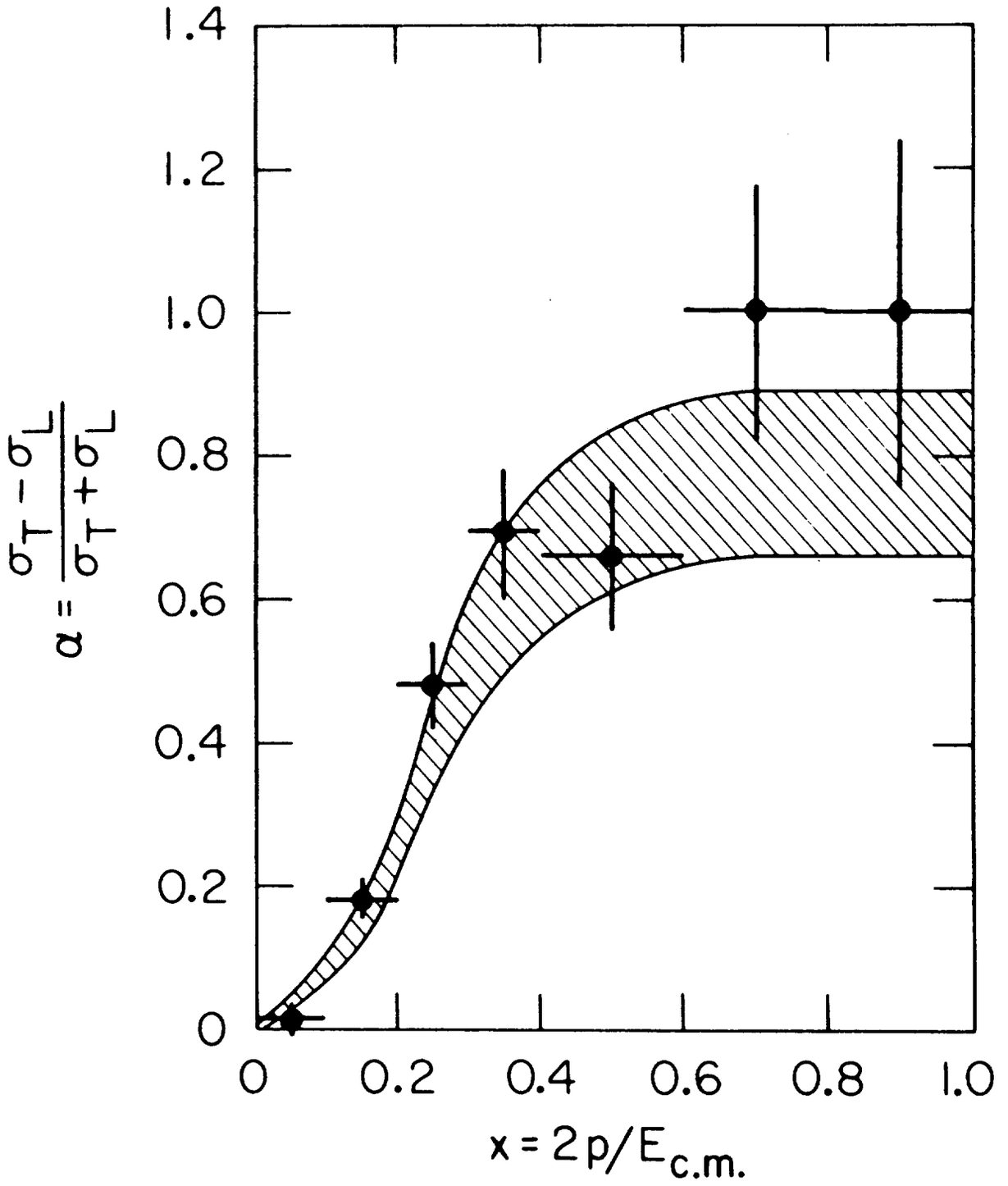
1.4
1.2
1.0
0.8
0.6
0.4
0.2
0
0
0.2
0.4
0.6
0.8
1.0
$\alpha = \frac{\sigma_T - \sigma_L}{\sigma_T + \sigma_L}$
$x = 2p/E_{c.m.}$

Fig. 3

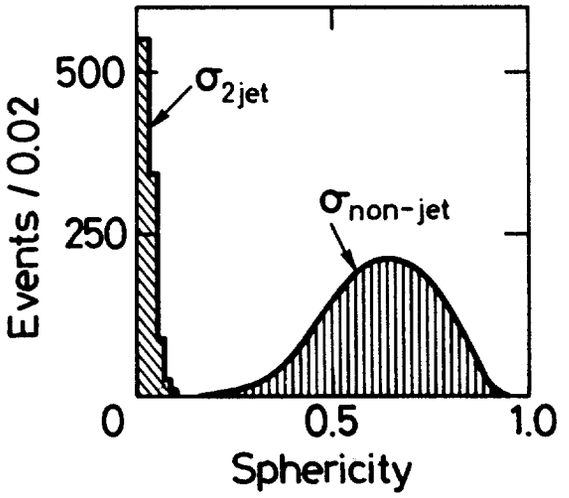
500
250
0
Events / 0.02
σ_{2jet}
$\sigma_{non-jet}$
0.5
1.0
Sphericity

FIG. 4

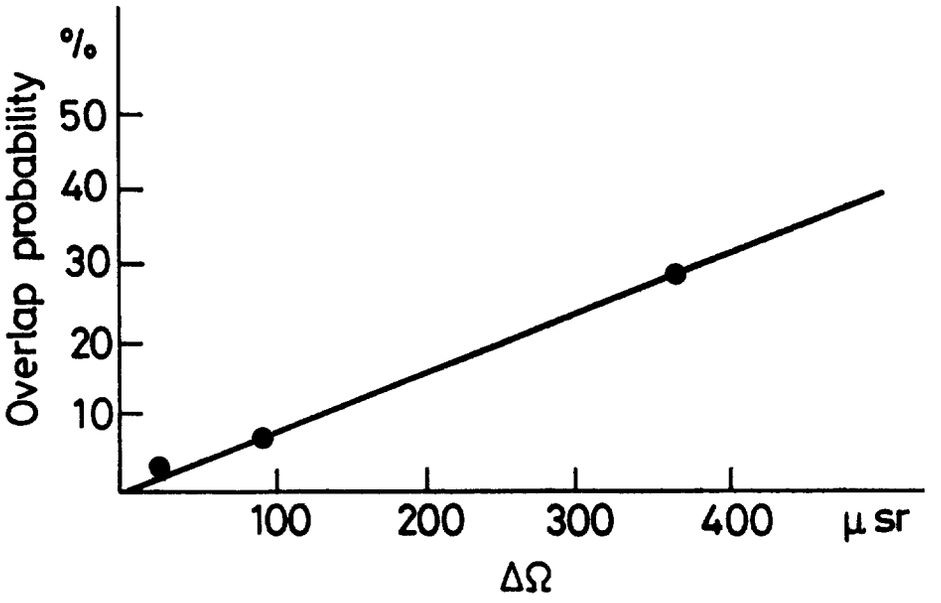
%
50
40
30
20
10
Overlap probability
100
200
300
400
μ sr
ΔΩ

FIG. 5

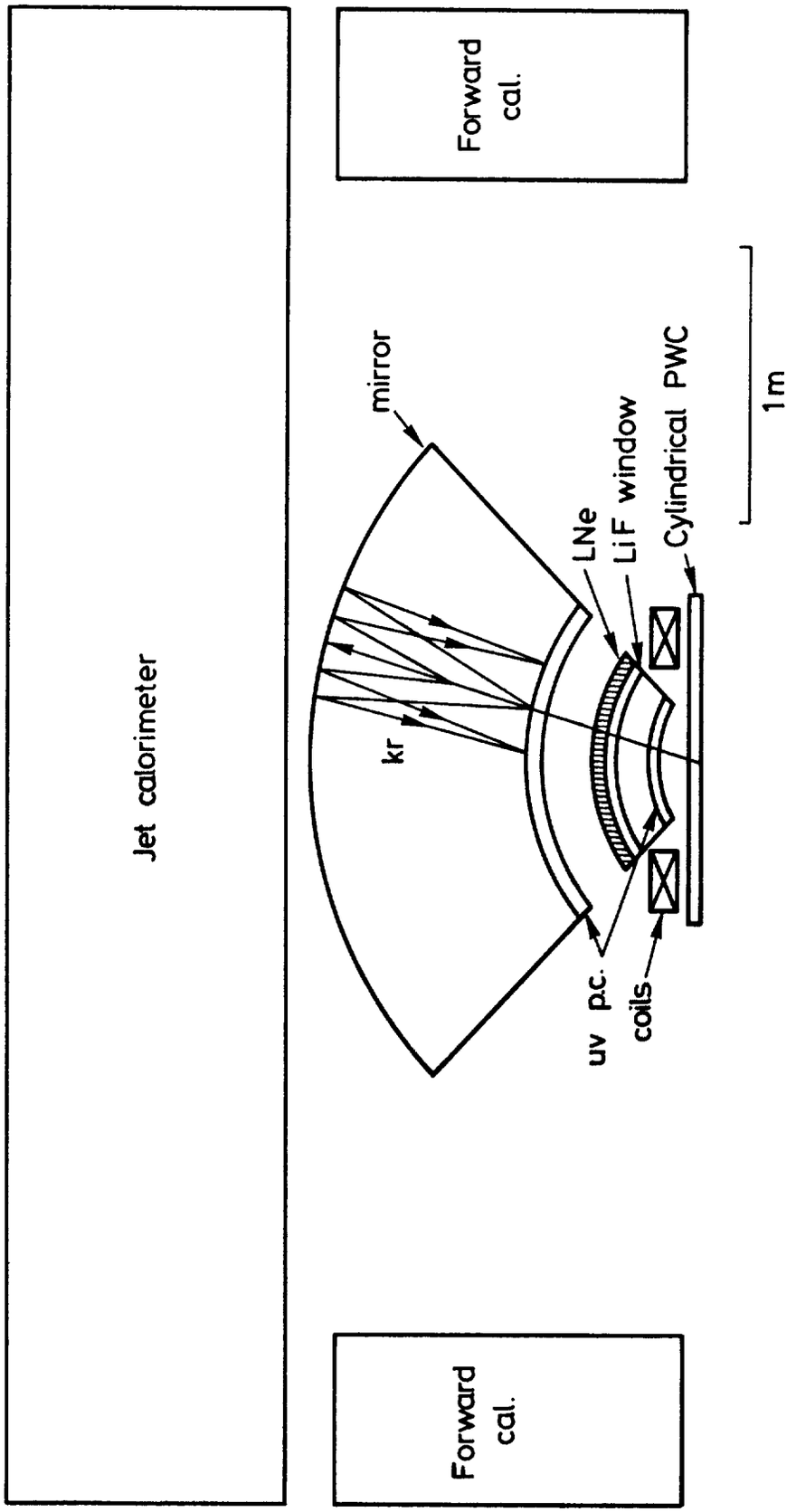

Jet detector + particle identifier : Axial field 0.2 T.m
Imaging Č detectors (needle bed)
Calorimeters

FIG. 6

VI- MEASUREMENT OF REACTIONS PRODUCING NEUTRINOS

D. Cundy, P. Darriulat, F. Palmonari and W. Willis

Many of the most interesting reactions produced by LEP have one or more neutrinos in the final state. In order to analyse these reactions it is necessary to measure all the directly detectable particles, neutral as well as charged hadrons, photons, and charged leptons. The presence of neutrinos can then be detected by energy and momentum conservation. In many cases, reactions producing more than one neutrino will be distinguished by a mass of the unobserved particles significantly different from zero.

The only way to detect the neutral hadrons and photons is by the total absorbtion counter, or calorimeter, technique. This also measures the charged hadrons and the electrons. The momentum of the muons must be measured by deflection in a magnetic field. Even in events which do not contain a neutrino, it is useful to make a calorimetric measurement of the hadrons, to allow a complete measurement of jets, for example.

To illustrate the problem of sorting out the different reactions producing neutrinos, we give in Table I the list of decay modes of the four new kinds of particles we might hope to encounter, and in Table II the production mechanisms. Following through the production and decay reactions, we arrive at the description in terms of the number of neutrinos produced, the numbers and types of charged leptons, and the presence or absence of hadrons, as shown in Table III,

with the present estimates of the relative cross section times branching ratios, using the formulae tabulated in Appendix III. Since the number of events is likely to be small, except when the energy is near a resonance peak, the different reactions may be hard to separate. However, we shall show that with proper detectors, certain crucial reactions can be cleanly identified.

In Appendix I, the measurement of energy and angle of the interacting particles is discussed. It is shown that for a jet model for the distribution of the hadrons, the errors on the momentum vector of the missing neutrino is determined by the energy resolution of the calorimeter rather than by the angular accuracy, even if the distance from the beam pipe is small. This allows the most compact possible calorimeter, which minimizes the false muon candidates arising from pi-mu decays. If the errors from the muon momentum measurement do not contribute excessively, the neutrino momentum can be measured to a few per cent. The calorimeter measures the electron momentum accurately, but a consequence of the compact calorimeter configuration is that it is not possible to measure the sign of the electron.

In Appendix II, the measurement of the muon is described. Unfortunately, the use of magnetised iron does not give a sufficient accuracy. Adequately small errors are achieved using an air core magnet. The calorimeter material which precedes this magnet provides adequate attenuation of hadrons, but the magnet is rather large.

A view of the whole apparatus is shown in fig. 1 and 2. The beam pipe is of the full 20cm diameter to avoid synchroton radiation. It is surrounded by three layers of non-ambiguous PWC to detect charged tracks, which is needed most for the measurement of charged leptons, and therefore not much troubled by the high density of tracks in the jet cores. There follows a high density uranium calori-

meter, described in Appendix I.

Outside the calorimeter is a set of drift chambers for muon measurements, the air core magnet, and another set of drift chambers, described in Appendix II.

A study of costs might determine that it is less expensive to have a larger calorimeter outside a smaller magnet, but we have chosen the present alternative because the performance is much better in terms of rejection of pi-mu decays.

To illustrate the performance of this detector, we consider a search for the $W^{\pm}$, by production of a pair of $W^{+}W^{-}$, one of which decays into n-hadrons, and the other decays into a lepton-neutrino pair (reaction 13 in Table III) The charged lepton can be either an electron or a muon. We assume that the total $e^{+}e^{-}$ energy is not near a resonance such as the Z^{o}, so that the relative rates in Table III apply, and this reaction constitutes about 5% of the total cross section. However, it represents as much as 50% of the cross section for events containing neutrinos.

A Monte Carlo routine has been run to investigate the performance of the detectors for this reaction, using the calculations of Alles, Boyer and Buras (CERN TH-2220) for the distributions of W production and decay. For the hadronic decay of the W, we assume a two jet structure with pions distributed uniformly in rapidity. The jet axis is given the production angular distribution calculated by Alles et al. followed by isotropic decay. The detectors are as specified in Appendices I and II, with the appropriate acceptances and errors, which are different from hadrons, electrons and photons, and muons.

The results are shown in fig. 3 and 4. The test of momentum balance allows the presence of the neutrino to be demonstrated in a large fraction of the events, thereby eliminating the most common background reactions. The events are then further selected by requiring :

$$M_{nh} = M_{\ell\nu}$$

$$M^2_{\nu} = 0$$

To evaluate the effectiveness of the M^2_{ν} cut, we show in fig.4 the distribution for the wanted reaction, together with the distribution for the most serious background reaction, heavy lepton pair production. There, the two neutrinos are interpreted as one missing particle which gives a distribution at higher masses.

After these kinematic cuts are made, each event gives one value of the W mass which can be used for further discrimination against background. Note that the event rate is one or two per day, which requires that the detectors have a large acceptance. Since most background is eliminated, modest statistics should allow a convincing demonstration of the existence of this reaction.

The reactions with a still smaller rate are practically out of reach. For example, reaction 17, double leptonic decay of the W pair, is in some ways the most characteristic W reaction, but with a rate of 1/100 of the mu pair rate, or ideally one in five days. This is particularly difficult for a reaction which must be analysed statistically, rather than kinematically. Thus there are only about twelve reactions in Table III with acceptable rates.

One of the most interesting possibilities is to find the Higgs meson among the Z^o decays. The crucial reaction is probably nr. 9 in Table III. The analysis will depend on seeing a narrow peak in the mass recoiling opposite the lepton pair in the final state. This is one reason for pressing for good momentum resolution for muons as discussed in Appendix II. Note that the rate is a few per day when running near the Z^o peak, which means that there are large numbers of possible background events to be eliminated. It is probably necessary to have the best possible measurement of the hadrons in the Higgs decay as well as the missing mass measurement.

The conclusion is that one can foresee successful analysis of the reactions with a rate of one a day, but that the complexity

of final states is such as to require powerful detectors with large acceptance.

We note that this detector can also be used with advantage in the measurement of $\sigma_{tot}(1\gamma)$. The accuracy for the total energy measurement in the calorimeter is about 4%, as shown in Appendix I. This allows the two-photon events to be eliminated by requiring the visible energy to be consistent with the beam energy within that accuracy. The analog nature of the calorimeter response ensures that this measurement is proof against any reasonable amount of synchrotron radiation.

Table I - Decays

Name	Reaction	B branching ratio
$L_{\ell\nu\nu}$	$L^{\pm} \rightarrow \begin{pmatrix} e \\ \mu \end{pmatrix} + \nu + \bar{\nu}$	$1/10$
$L_{h\nu}$	$L^{\pm} \rightarrow nh + \nu$	1
$W_{\ell\nu}$	$W^{\pm} \rightarrow \ell + \nu$	$1/10$
W_{nh}	$W^{\pm} \rightarrow nh$	1
$Z_{\ell\bar{\ell}}$	$Z^0 \rightarrow \begin{pmatrix} e \\ \mu \end{pmatrix} + \overline{\begin{pmatrix} e \\ \mu \end{pmatrix}}$	$1/10$
Z_{nh}	$Z^0 \rightarrow nh$	1
$H_{\ell\bar{\ell}}$	$H \rightarrow \begin{pmatrix} e \\ \mu \end{pmatrix} + \overline{\begin{pmatrix} e \\ \mu \end{pmatrix}}$	$< 10^{-3}$
H_{nh}	$H \rightarrow nh$	1
$H_{L\bar{L}}$	$H \rightarrow L + \bar{L}$	$< 1/6$

L: heavy lepton

W: charged intermediate boson

Z: neutral intermediate boson

H: Higgs meson

Table II - Production reactions

Reactions		Approximate cross-section*)
$ee \to L\bar{L}$	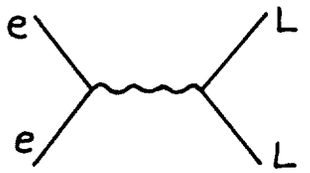	1
$ee \to W\bar{W}$	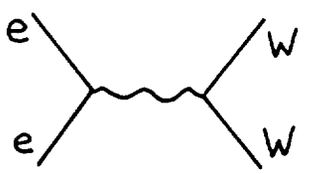	1
$ee \to W\nu(e)$	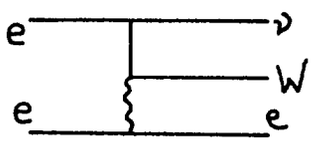	$1/100$
$ee \to Z$	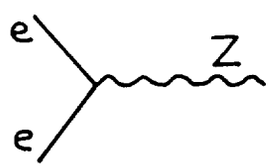	10^3
$ee \to Wh$	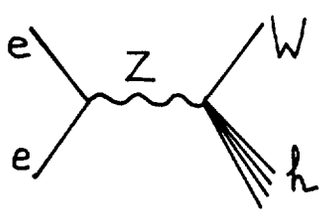	$1/10 \propto m_Z^5$
$ee \to ZH$	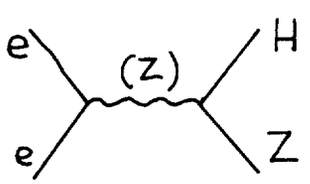	1

*) Normalized to $\sigma_{\mu\mu} = 1$.

Table III - Particle configurations

Number	Configuration[a]	Relative[b] σB	Reaction	Comments
1	nh	∿ 10	Jets	
2		1	$W_{nh}\ W_{nh}$	Makes 4-jet events W-mass determined
3		$^1/_{10}$	$W_{nh}\ h$	σB relative to Z, on Z peak, very sensitive to W-Z mass difference
4		(10^3)	Z_{nh}	At peak
5		(1)	$Z_{nh}\ H_{nh}$	At Z^0 peak
6	nh 1ν (e)	$^1/_{100}$	$W_{nh}\ \nu(e)$	
7	$2\binom{e}{\nu}$	1	$\mu\bar{\mu}$	
8		$(^1/_{10})$	$Z_{\ell\bar{\ell}}$	At peak
9	nh $2\binom{e}{\nu}$	$(^1/_{10})$	$Z_{\ell\bar{\ell}}\ H_{nh}$	At Z^0 peak
10	$4\binom{e}{\mu}$	(10^{-3})	$Z_{\ell\bar{\ell}}\ H_{\ell\bar{\ell}}$	At Z^0 peak
11	2μ + 2e	(10^{-3})	$Z_{\ell\bar{\ell}}\ H_{\ell\bar{\ell}}$	At Z^0 peak
12	nh 1ν $\binom{e}{\mu}$	$(^1/_{100})$	$W_{\ell\nu}\ h$	At Z^0 peak
13		$^1/_{10}$	$W_{\ell\nu}\ W_{nh}$	Detailed analysis in text
14	nh 2ν	1	$L_{h\nu}\ L_{h\nu}$	
15		$< {}^1/_6$	$Z_{nh}\ H_{L\bar{L}}$	$L_{h\nu} + L_{h\nu}$
16	2ν $\binom{e}{\mu}$	$^1/_{1000}$	$W_{\ell\nu}\ \nu(e)$	
17	2ν e + μ	$^1/_{100}$	$W_{\ell\nu}\ W_{\ell\nu}$	

Table III - cont.

Number	Configuration[a]	Relative σB[b]	Reaction	Comments
18	$2\nu \quad 2\binom{e}{\mu}$	$1/100$	$W_{\ell\nu}\ W_{\ell\nu}$	
19	$nh\ 2\nu \quad 2\binom{e}{\mu}$	$< 1/60$	$Z_{\ell\bar{\ell}}\ H_{L\bar{L}}$	
20	$nh\ 3\nu \quad \binom{e}{\mu}$	$1/10$	$L_{\ell\ell}\ L_{h\nu}$	
21		$< 1/60$	$Z_{nh}\ H_{L\bar{L}}$	$L_{h\nu} + L_{\ell\nu\nu}$
22	$nh\ 3\nu \quad 3\binom{e}{\mu}$	$< 1/600$	$Z_{\ell\bar{\ell}}\ H_{L\bar{L}}$	$L_{h\nu} + L_{\ell\nu\nu}$
23	$2\binom{e}{\mu}\ \binom{\mu}{e}$			
24	$4\nu \quad 2\binom{e}{\mu}$	$1/100$	$L_{\ell\nu\nu}\ L_{\ell\nu\nu}$	
25	$4\nu \quad e + \mu$	$1/100$	$L_{\ell\nu\nu}\ L_{\ell\nu\nu}$	
26	$4\nu \quad 4\binom{e}{\mu}$	$< 1/6000$	$Z_{\ell\bar{\ell}}\ H_{L\bar{L}}$	
27	$4\nu\ 2_\mu + 2_e$	$< 1/6000$	$Z_{\ell\bar{\ell}}\ H_{L\bar{L}}$	$L_{\ell\nu\nu} + L_{\nu\nu}$
28	$4\nu\ 3\binom{e}{\mu}\ \binom{\mu}{e}$	$< 1/6000$	$Z_{\ell\bar{\ell}}\ H_{L\bar{L}}$	
29	$nh\ 4\nu \quad 2\binom{e}{\mu}$	$< 1/600$	$Z_{nh}\ H_{L\bar{L}}$	
30	$nh\ 4\nu \quad e + \mu$	$< 1/600$	$Z_{nh}\ H_{L\bar{L}}$	

a) eμ reactions are shown separately because they are characteristic.

b) σB normalized to $ee \to \mu\mu$ except as noted

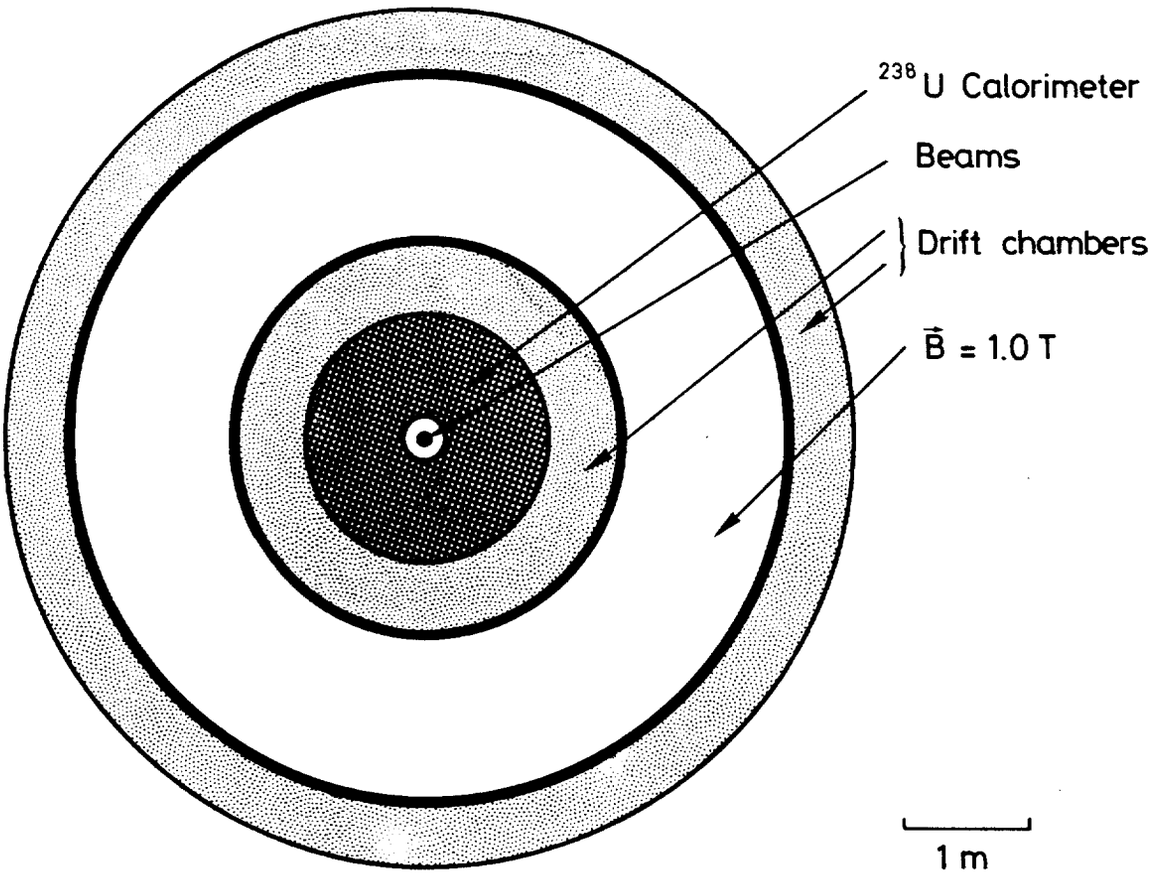

FIG. 1

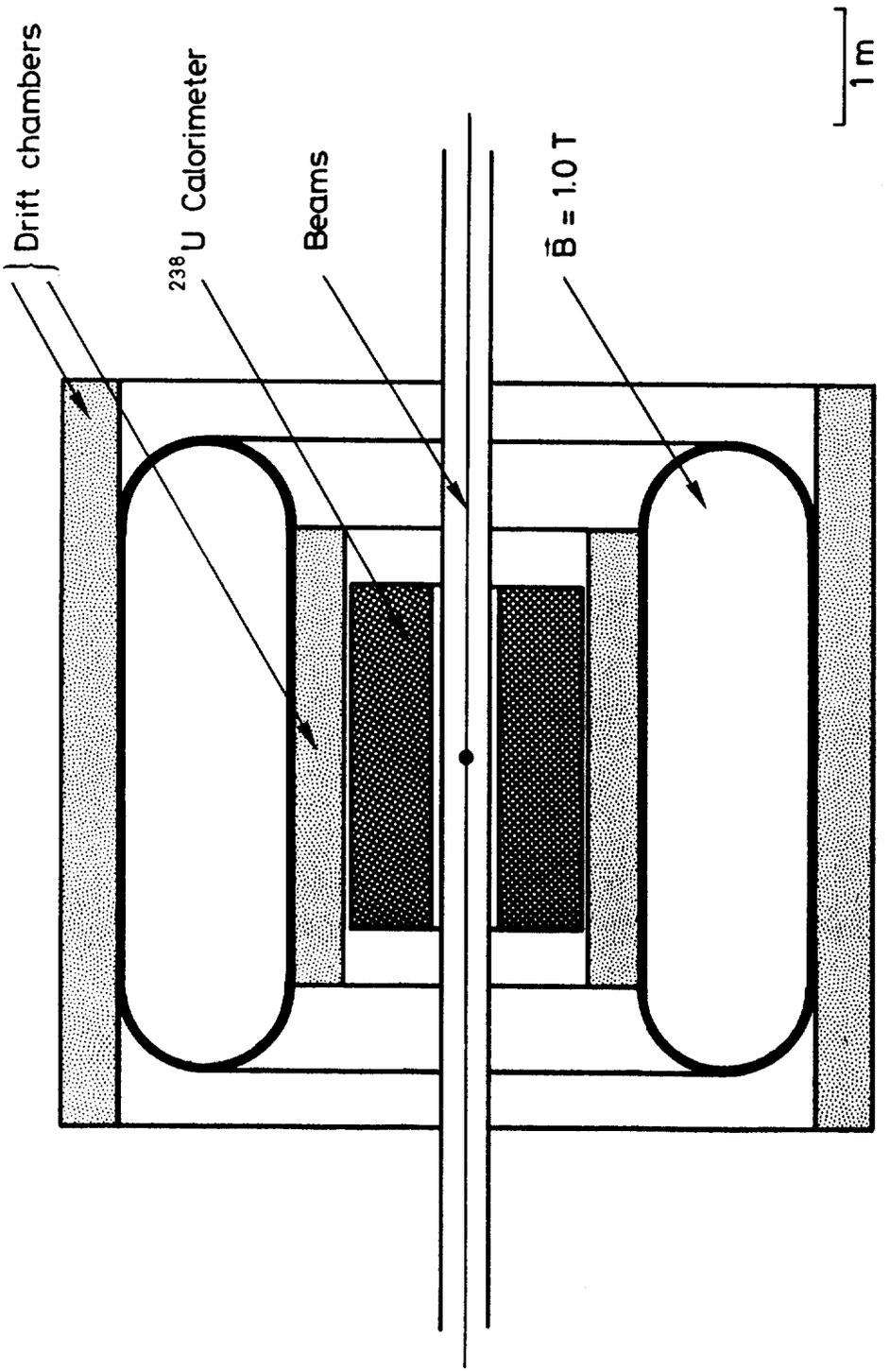

FIG. 2

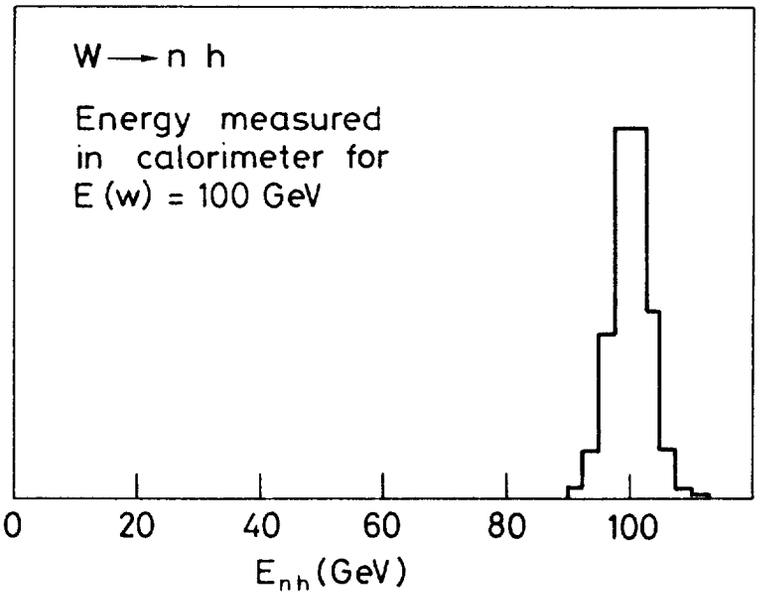
W → n h
Energy measured
in calorimeter for
E (w) = 100 GeV
0
20
40
60
80
100
E_{nh} (GeV)

Fig. 3 a

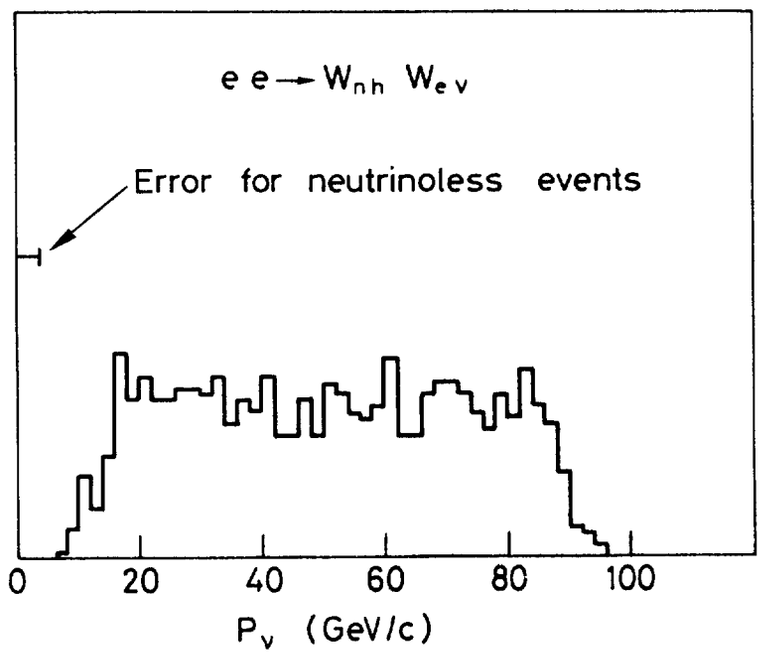
e e → W_{nh} $W_{e\nu}$
Error for neutrinoless events
0
20
40
60
80
100
P_ν (GeV/c)

Fig. 3 b

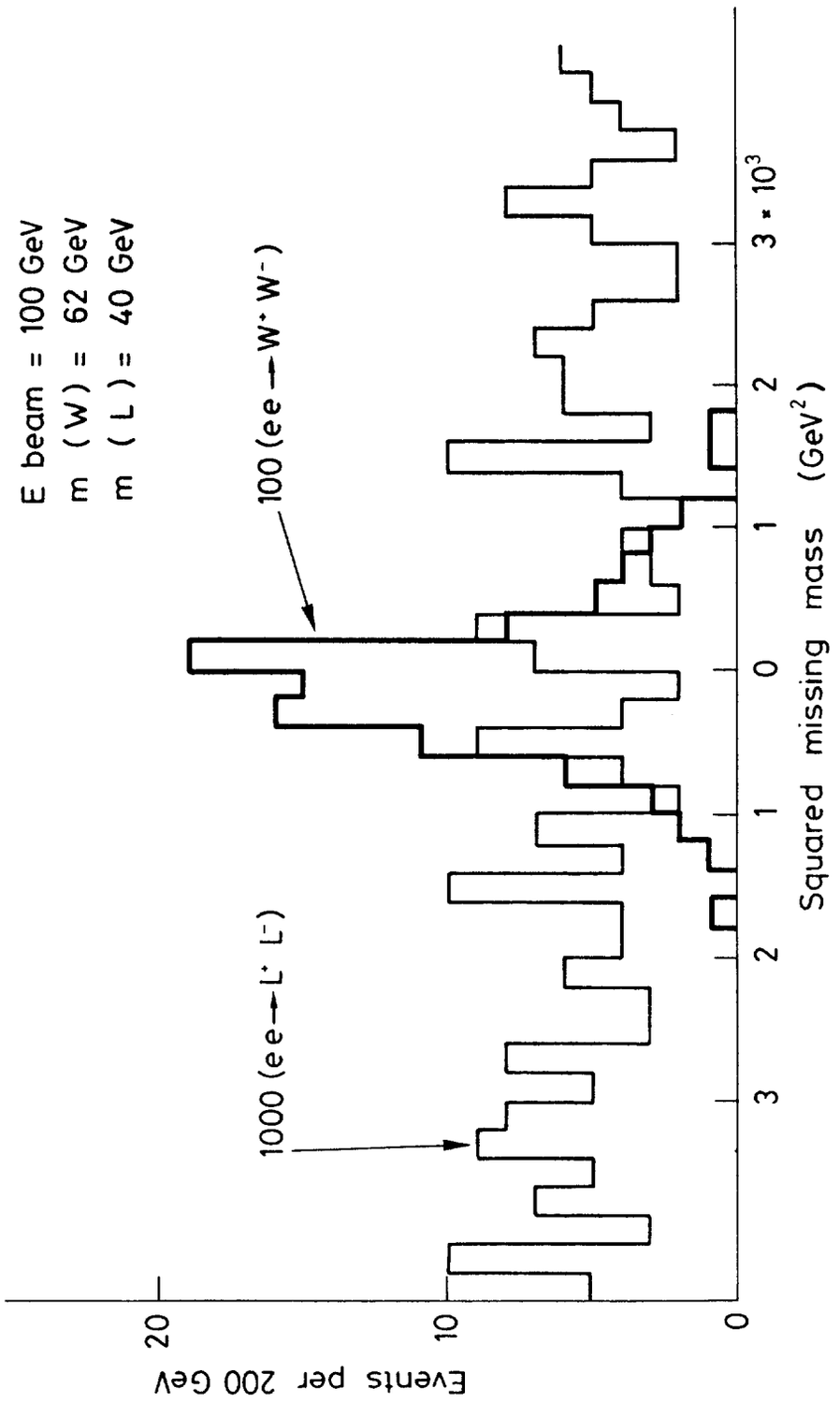
E beam = 100 GeV
m (W) = 62 GeV
m (L) = 40 GeV
100 (e e → W⁺ W⁻)
1000 (e e → L⁺ L⁻)
Events per 200 GeV
0
10
20
0
1
2
3
1
2
3 × 10³
Squared missing mass (GeV²)

FIG. 4

APPENDIX I

CALORIMETER FOR MISSING NEUTRINO DETECTION IN CONJUNCTION WITH MUON MEASUREMENT

***

For this purpose the calorimeter should be as compact as possible in order to minimize the size of the surrounding muon detector, while maintaining the best feasible accuracy on the missing momentum. Under these circumstances, the use of uranium can be economical as well as giving improved performance. (A price of 25 DM/kg for uranium plates was recently quoted, much less if the material is leased on a fixed term).

The most important quantity to be determined is the vector momentum due to the hadrons and electromagnetically interacting particles, $\vec{p}_{vis}$. It is combined with the measured momentum of the muon(s) to give $\vec{p}_{\nu} = -\vec{p}_{vis} - \vec{p}_{\mu}$.

The errors on $\vec{p}_{vis}$ come primarily from four sources :
1 - the approximation for determining $|\vec{p}_{vis}|$ for a given shower in the calorimeter, which is to take p_{vis} equal to the apparent energy, the quantity measured in the calorimeter. In an ideal calorimeter this is equal to the kinetic energy T, for protons, electrons and photons ; the total energy for mesons ; and the total energy plus one nucleon mass for antibaryons. In a practical calorimeter the hadron apparent energy deposit is reduced by the nuclear binding energy and related effects, about 30% in iron, where this effect dominates the other sources of error. In uranium, the net binding energy is close to zero (PL 60B, 105 (1975)), and this error is much reduced. In this case, the errors of this kind may be dominated by the baryon-antibaryon apparent energy difference.

As indicated above, when a proton-antiproton pair is created, for relativistic protons

$$|\vec{p}| = T + m_p = E_{apparent} + m_p$$

while for antiprotons

$$|\vec{p}| = E_{apparent} - m_p$$

Since it is $\vec{p}_{vis} = \sum \vec{p}$ which is of most interest, the error is very dependent on the distribution of the angle between the proton and the antiproton. If the pair is produced in a jet, correlated within about one unit of rapidity, the average angle between the two will be small, and this error will be negligible, 0.1 GeV, due to the cancellation of the two mass terms. The only serious contribution to the error comes from baryon-antibaryon pairs of large angles, which give rise to $\Delta \vec{p}_{vis} \lesssim 2$ GeV.

2 - energy error due to shower fluctuations and calorimeter imperfections, and

3 - angular errors. These must be considered together because their effect on the net momentum is dependent on the configuration of the event.

The nuclear binding energy effects mentioned before increase the errors on the energy and angle of individual particles, as well as leading to the systematic differences between photons and hadrons which were discussed. Again, the situation is improved by the use of uranium, where the energy error for a practical calorimeter (with, say, 2mm plates) may be represented by

$$\sigma_E = .3 \sqrt{E} \text{ in GeV}$$

From the measurements of Friend et al. (to appear in Nucl. Instr. Methods), the error on the position of the center of gravity of the shower in iron is

$$\sigma_x = \frac{18}{\sqrt{E}} \text{ gm/cm}^2 .$$

The reduced binding energy fluctuations in uranium should lead to a decreased error, but this has not been measured. A density of 10 gm/cm^2 should be achieved in the calorimeter. It must be subdivided into strips of width 2 cm.

If the calorimeter begins at the minimum radial distance from the beam, R, and the angle of the particle with respect to the beam is θ, the angle error is

$$\sigma_\theta = \sin\theta \frac{\sigma_x}{R + 10cm}$$

For R = 20 cm, the error at 90° is

$$\sigma_\theta = \frac{0.06}{\sqrt{E}}$$

The error on $\vec{p}_{vis}$ depends on the nature of the event. If the particles are distributed isotropically, we may measure the angle θ with respect to an arbitrary axis, say perpendicular to the beam. We ignore the fact that the angular error are smaller for particles near the beam, because of the longer lever arms in our cylindrical detector geometry. Then

$$\sigma_\odot^2 = \left\langle \sum_i \sigma_{E_i}^2 \cos\theta_i^2 + \sum_i \sigma_\theta^2 E_i^2 \sin^2\theta_i \right\rangle$$

$$= \left\langle \sum_i s^2 E_i \cos^2\theta_i + \sum_i a^2 E_i \sin^2\theta_i \right\rangle$$

where the sum is over the particles in an event and the average is over the distributions, and

$$\sigma_{E_i}^2 = s^2 E_i , \qquad s = 0.3$$

$$\sigma_\theta^2 = a^2/E_i , \qquad a^2 = 3.6\times10^{-3}$$

For isotropic distributions and these errors, the energy distribution need not be specified and

$$\sigma_\odot^2 = (\tfrac{1}{2}s^2 + \tfrac{1}{2}a^2) E_{beam}$$

$$\sigma_\odot = 0.22 \sqrt{E}_{beam}$$

dominated by the energy errors.

For a jet, we take for the longitudinal distributions the rough approximation

$$\frac{d\sigma}{dx} = \frac{1}{N}\,\frac{1}{x}\,, \qquad x = \frac{p_i}{E_{beam}}$$

and we assume p_t is uncorrelated with x.

Then we take a jet with $\theta = 0$, and evaluate the error on the component of $\overrightarrow{p_{vis}}$ which is along the jet axis.

$$\begin{aligned}
\sigma_{//}^2 &= \langle \Sigma \sigma_E^2 \cos^2\theta_i + \Sigma \sigma_\theta E_i^2 \sin^2\theta_i \rangle \\
&= \langle \Sigma s^2 E_{beam} \times \left(1 - \left(\frac{p_t}{E_{beam}\, x}\right)^2\right) \\
&\qquad + \Sigma a^2 E_{beam} \times \left(\frac{p_t}{E_{beam} x}\right)^2 \rangle \\
&\cong 2s^2 E_{beam} + \frac{a^2}{E_{beam}} \left\langle p_t^2 \frac{1}{x} \right\rangle \\
&= 2s^2 E_{beam} + a^2 \frac{\langle p_t^2 \rangle}{m_\pi}
\end{aligned}$$

$$\sigma_{//} = 0.3 \sqrt{2E_{beam}}$$

dominated by the energy error.

For an axis perpendicular to the jet

$$\begin{aligned}
\sigma_t^2 &= \langle \Sigma \sigma_E^2 \sin^2\theta_i + \Sigma \sigma_\theta^2 E_i^2 \cos^2\theta_i \rangle \\
&= s^2 \frac{\langle p_t^2 \rangle}{m_\pi} + 2 a^2 E_{beam} \\
&= .1 \times .6 + 0.36 \times 10^{-4} \times 2 E_{beam}
\end{aligned}$$

$$\sigma_t \simeq 0.06 \sqrt{2E_{beam}}\,, \quad E_{beam} > 100 \text{ GeV}$$

This is dominated by angle errors, for sufficiently large beam energies. Consequently, the error could be reduced as far as $\sigma_t = 0.025 \sqrt{2E_{beam}}$ by increasing R by a factor of about three. This may not be worthwhile, since the most interesting events are closer

to the isotropic case.

4 - the energy going down the beam pipes is lost. Given the prominence of two photon events, we suspect that any event with lots of energy disappearing in this fashion would not be considered as decent neutrino candidates in any case, and that it is acceptable to require a large transverse component in $\vec{p}_{\nu}$. In this case the beam pipe correction should be smaller than the fractional solid angle of the beam pipes, and therefore negligible.

In summary, the errors on momentum components of $\vec{p}_{vis}$ along a given axis, for E_{beam} = 100 GeV, are

$$\sigma_{\odot} = 3.1 \text{ GeV}$$
$$\sigma_{//} = 4.2 \text{ GeV}$$
$$\sigma_{t} = 0.85 \text{GeV}$$

For electrons, or for photons occuring outside the cores of jets, the energy resolution is better, about one or two percent. This is better than can be achieved with muons. Another question is the hadron rejection which can be achieved when studying electrons or photons, using just a shower identification. The radial and longitudinal shower distribution can be measured for this purpose. The data for these high energies are not available, but we may anticipate hadron rejections of the order of 10^3. This rejection is probably adequate, if, as expected, a large fraction of energetic hadrons occur in jets, while most electrons are well separated from the jets.

APPENDIX II

The conventional design for a muon detector at a storage ring is an iron toroid. The multiple scattering in the iron then generates an error

$$\frac{\Delta p}{p} = \frac{0.22}{\sqrt{L}}$$

Then, to achieve an accuracy of 5%, in order to match the calorimeter accuracy, a length of 20m would be needed, which is clearly out of the question.

Noting that muon filtering is already provided by the calorimeter material, an air core magnet may be used to measure the muon momentum. The design we have chosen is a continuous toroid, 1.5m in radial depth, with an average field of 1.0 T. We assume that the coil thicknesses will total two radiation lengths. This device is shown in fig. 1 and 2. The muon angle is measured before and after the magnet by drift chamber arrays with a depth of 0.5m. The accuracy is limited by multiple scattering, and is $\Delta p/p = 4.7\%$. Improved resolution could be achieved at the lower momenta by measuring the position of the muon inside the magnet, but we avoid this to maintain full accessibility to the detectors.

The angle measurement of the muon is limited by the multiple scattering in the calorimeter. The rms scattering angle of a muon at the exit of the calorimeter is 180mr/p (GeV). However, there is a correlation between the exit angle, which is measured with high precision in the drift chambers, and the angle of the chord between the source point, which is known because of the small size of the electron bunch, and the chambers inside the calorimeter. Use of this angular correlation reduces the error to $\sigma_\theta = 90$ mr/p as shown by

W.T. Scott, Phys. Rev. 76, 212 (1949). It is not desirable to try to improve this by providing more lever arm inside the calorimeter, for reasons of cost and pi-mu decay background. In any case, one of the advantages of a storage ring experiment on muon pairs is that the angle between the two muons is very large, so that the effective mass error is limited by the momentum errors, and the accuracy required on the muon angles is not very great.

APPENDIX III *

Table I - Decay Modes

Notation :

e = electron

μ = muon

h = hadrons

$L^{\pm}$ = charged heavy lepton

L^{o} = neutral heavy lepton

$W^{\pm}$ = charged intermediate boson

Z^{o} = neutral intermediate boson

H = neutral Higgs meson

$$R = \frac{\sigma(e^+e^- \rightarrow \text{hadrons})}{\sigma(e^+e^- \rightarrow \mu^+\mu^-)}$$

N_H = number of hadron doublets
e.g. $\binom{u}{d}$, $\binom{c}{s}$...

N_L = number of lepton doublets
e.g. $\binom{\nu_e}{e}$, $\binom{\nu_\mu}{\mu}$...

$M_{Q(L)}$ = mass of heaviest kinematical accessible quark (lepton)

* from the Working Party Theory Group.

Branching ratios

	Ball-park estimates [b]	Weinberg-Salam model [a] [c]
$L^- \to e\,\nu\nu\,, \mu\nu\nu$	$\frac{1}{2R+2}$ to $\frac{1}{R+2}$ each	$\frac{1}{3N_H + N_L}$
$L^- \to h\,\nu$	$\frac{2R}{2R+2}$ to $\frac{R}{R+2}$ each	$\frac{3N_H}{3N_H + N_L}$
$L^o \to \begin{cases} ee\,\nu \\ \mu e\,\nu \\ \mu\mu\,\nu \end{cases}$	$O(\frac{1}{R})$ in total	[d]
$L^o \to \begin{cases} eh \\ \mu h \\ \nu h \end{cases}$	$1-O(\frac{1}{R})$ in total	
$W^- \to e\,\nu, \mu\,\nu$	$\frac{1}{2R+2}$ to $\frac{1}{R+2}$ each [e]	$\frac{1}{3N_H + N_L}$
$W^- \to h$	$\frac{2R}{2R+2}$ to $\frac{R}{R+2}$ each	$\frac{3N_H}{3N_H + N_L}$
$Z \to ee, \mu\mu$	$O(\frac{1}{R+2+N_\nu})$ each [e][f]	$\frac{5}{5N_L + 8N_\nu + 27N_H}$ [f]
$Z \to \nu\nu$	$O(\frac{N}{R+2+N_\nu})$ in total	$\frac{8N_\nu}{5N_L + 8N_\nu + 27N_H}$
$Z \to h$	$O(\frac{R}{R+2+N_\nu})$	$\frac{27N_H}{5N_L + 8N_\nu + 27N_H}$
$H \to \nu\nu$	0	
$H \to ee$	$\leqslant \frac{1}{5}$	$\frac{M_e^{2\,0}}{3M_Q^2 + M_L^2} \leqslant 2 \times 10^{-8}$
$H \to \mu\mu$	$< \frac{1}{5}$	$\frac{M_\mu^2}{3M_Q^2 + M_L^2} \leqslant 10^{-3}$
$H \to L^+L^-$	$\leqslant \frac{1}{6}$	$\frac{M_L^2}{3M_Q^2 + M_L^2}$
$H \to L^o\bar{L}^o$	$\leqslant \frac{1}{6}$	[d]
$H \to h$	$\geqslant \frac{1}{2}$	≈ 1

Notes :

a) We use the model with only left-handed doublets and right-handed singlets, and take $\sin^2 \theta_w = 3/8$.

b) R is $O(\frac{5}{3} N_H)$ when cross sections are mainly electromagnetic at low energies, and is expected to be in this ball-park, at higher energies also, probably $\geqslant 4$. The lower branching ratios would apply for example in models with equal numbers of left- and right-handed doublets. R should be evaluated at momenta characteristic of decay : $Q \leqslant M_L$.

c) Only doublets less massive than the decaying particle should be included in N_H, N_L.

d) An L^o would not exist in this model, as long as "neutrinos" continue to be massless.

e) R should be evaluated at m_w (m_z).

f) Note that Z decays into all the world's neutrinos, even if they are associated with very massive charged leptons : N_ν could be much larger than N_L.

Table II - Production reactions

	Graphs	Cross-section
$e^+e^- \to L^+L^-$	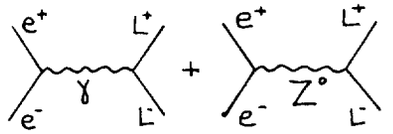	$\frac{4\pi\alpha^2}{3s}\left\{1 + 2sv_e v_L - g\left[\left(\frac{s}{m_Z^2} - 1\right) + \frac{\Gamma_Z^2}{s - m_Z^2}\right]^{-1} + \right.$ $\left. + s^2g^2(v_e^2 + a_e^2)(v_L^2 + a_L^2)\left[\left(\frac{s}{m_Z^2} - 1\right)^2 + \frac{\Gamma_Z^2}{m_Z^2}\right]\right\}$
$e^+e^- \to L^0\bar{L}^0$	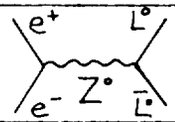	$\frac{4\pi\alpha^2}{3} sg^2(v_e^2 + a_e^2)(v_L^2 + a_L^2)\left[\left(\frac{s}{m_Z^2 - 1}\right)^2 + \frac{\Gamma_Z^2}{m_Z^2}\right]$
$e^+e^- \to W^+W^-$	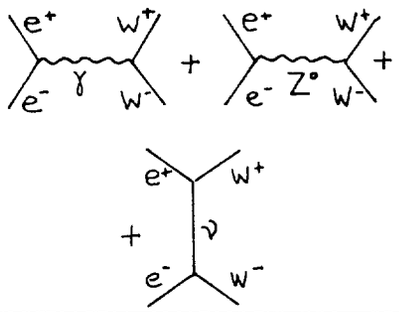	$\frac{\pi\alpha^2\beta}{2\sin^4\theta_W s}\left\{\left(1 + \frac{2}{y} + \frac{2}{y^2}\right)\frac{L}{\beta} - \frac{5}{4} + \right.$ $+ \frac{m_Z^2(1 - 2\sin^2\theta_W)}{s - m_Z^2}\left[\frac{2}{y^2}(1 + 2y)\frac{L}{\beta} - \frac{y}{12} - \frac{5}{3} - \frac{1}{y}\right] +$ $\left. + \frac{m_Z^2(8\sin^4\theta_W - 4\sin^2\theta_W + 1)\beta^2}{48(s - m_Z^2)^2}(y^2 + 20y + 12)\right\}$
$e^+e^- \to Z^0$	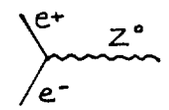	near peak $\approx 12\pi \frac{\Gamma(Z \to e^+e^-)\Gamma(Z \to \text{all})}{(s - m_Z^2)^2 + m_Z^2\Gamma^2}$
$e^+e^- \to Wh$	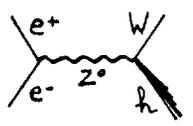	as above $\times \frac{\Gamma(Z \to Wh)}{\Gamma(Z \to \text{all})} \approx (10^{-7}$ to $10^{-5})$ $\sigma = \mathcal{O}(10^{-38}$ to $10^{-37})\text{cm}^2$ at top
$e^+e^- \to HZ^0$	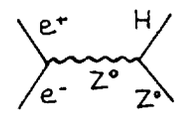	$\sigma(Z + H) \approx \sigma_{pt}\frac{3\sqrt{2}}{8} \cdot \frac{G_F^2}{e^4} \cdot \frac{m_Z^5}{m_H} \approx \sigma_{pt} \cdot \frac{19\text{ GeV}}{m_H}$ at maximum ($\sqrt{s} = m_Z + \sqrt{2}\, m_H$), assumming $\frac{\Gamma_Z^2}{4} \ll m_H^2 \ll m_Z^2$.
$e^+e^- \to W\nu e$	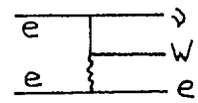	$\sigma \approx \frac{\alpha^2 G_F}{2\pi\sqrt{2}} \ln\left(\frac{s}{m_W^2}\right) F\left(\frac{s}{m_W^2}\right)$ $F \approx 1$ for $s \gg m_W^2$

Notation:

$\sigma_{pt} = \frac{4\pi\alpha^2}{3s}$; $g = \frac{G_F}{8\sqrt{2}\pi\alpha} \approx \frac{1}{16}(38\text{ GeV})^{-2}$; $\beta = \sqrt{1 - \frac{4m_W^2}{s}}$; $L = \ln\left|\frac{1 + \beta}{1 - \beta}\right|$; $y = \frac{s}{m_W^2}$.

VII- PHOTON-PHOTON INTERACTIONS

by

L. Camilleri, J.H. Field, E. Gabathuler and G. Preparata

1 - Introduction

The experimental research programme in e^+e^- collisions has concentrated mainly on the study of hadrons produced by the one photon annihilation process leading to states of well defined quantum numbers ($J^{PC} = 1^{--}$). At present, it is assumed on simple quark parton concepts that this cross-section divided by the Q.E.D. muon pair cross-section will approach a value $\geqslant 2$ depending on the type and number of quarks involved in the interaction. The Q.E.D. cross-section is given by $21.7/E^2$ nanobarns and is therefore ~ 2 picobarns at 100 GeV electron beam energy.

The two-photon non-annihilation process becomes an important process at high energies since the cross-section increases with energy and is ~ 250 nanobarns at a machine energy of 100 GeV. If the one-photon hadronic cross-section is several times the muon pair cross-section, then there is approximately 4 decades between the one-photon and two-photon process total cross-sections. This large cross-section enables hadrons from C = +1 states to be studied in their own right. In the simple vector dominance picture the 2-photon collisions

can be considered as having occurred in an ISR containing ρ-type mesons of energy ranging from zero to 100 GeV/c. This large difference in total cross-section means that some method must be found of separating the two processes.

This report considers the kinematics of the two-photon process, the separation of the one-photon and two-photon processes, the possibility of deep inelastic scattering off the photon and a detector to measure the two-photon process. Previous information on this topic can be obtained from the PEP Summer Study Report (1).

2 - Kinematics of Tagging

The two-photon process (notation for kinematics given in Fig. 1 and Appendix A) can be considered as a two-step process where the two particles radiate off two almost real photons and these two photons then collide to form C = +1 states, e.g. l^+l^-, h^+h^-, π^0, η^0 ... etc. This is analogous to the treatment in electroproduction where the 'equivalent radiator' defines the flux of photons interacting on a nucleon target. Each of the Q.E.D. vertices in Fig. 1 is very similar to ordinary bremsstrahlung where it is possible to "tag" each photon by measuring the energies of the incident and scattered electrons. Single tagging corresponds to tagging of either of the scattered electrons, double tagging to a coincidence of the two outgoing electrons.

The spectrum of equivalent photons generated at either electron vertex from an electron of energy E, fractional energy loss y and scattered angle θ between 0 and θ_{MAX} is given by:

$$\frac{1}{y}\int_0^{\theta_{MAX}} N(E,y,\theta)\,d\theta = \frac{\alpha}{\pi}\frac{1}{y}\left\{\left[1+(1-y)^2\right]\left[\ln\frac{E\theta_{MAX}}{2m_e}-\frac{1}{2}\right]+\frac{y^2}{2}\left[\ln\frac{2(1-y)}{y}+1\right]+\left(\frac{2-y}{2}\right)^2\ln\frac{2(1-y)}{\left[y^2+(1-y)\theta_{MAX}^2\right]^{\frac{1}{2}}}\right\} \quad \text{-----} \quad (1)$$

The spectrum is illustrated in Fig. 2 as a function of y. The yield of photons is essentially independent of incident energy and peaks at small values of y, i.e. for low energy photons. Approximately 50% of the photon flux has a scattered electron produced at angles $\lesssim$2 mrad which corresponds to a physical separation between the scattered electron and the circulating beam of 20mm at the end of the 10 metre straight-section. In a study of one-photon events, this clearly rules out any possibility of vetoing all the two-photon events by tagging them with any realistic detector.

Using the Weizsäcker-Williams approximation (2), the production of a state $X_{\gamma\gamma}$ of normalised mass $z = \sqrt{S_{\gamma\gamma}}/2E$ can be written as:

$$\frac{d^4\sigma(e^+e^- \to e^+e^-X)}{dy_1 dy_2\, d(\cos\theta_1)d(\cos\theta_2)} = f_1 f_2 \sigma(\gamma\gamma\to X) \quad ----(2)$$

where the expressions for the flux f_1 and f_2 are obtained from equation (1) and are given in the appendix A (EqnA2). By performing an integration over the full angular range of θ_1, θ_2 and y_1, y_2 the above cross-section can be written as:

$$\frac{1}{\sigma_{\gamma\gamma}(z)}\frac{d\sigma}{dz} = \left(\frac{\alpha}{\pi}\right)^2 2\left(\ln\frac{E}{m_e}\right)^2 \frac{1}{z}\left[(2+z^2)^2 \ln y - 2(2+z^2)\, y + y^2 + \frac{2z^2(2+z^2)}{y} - \frac{z^4}{y^2}\right]_{y_{lower}}^{y_{upper}}$$

where $y \equiv y_1$

$z^2 = y_1 y_2$ ------ (3)

It is now convenient to introduce the concept of the differential $\gamma\gamma$ luminosity $\frac{d\mathcal{L}_{\gamma\gamma}}{dz}$ as defined by the relation:

$$\sigma_{\gamma\gamma}(z)\,\frac{d\mathcal{L}_{\gamma\gamma}}{dz} = \mathcal{L}_{ee}\,\frac{d\sigma}{dz} \quad ------(4)$$

$\frac{d\mathcal{L}_{\gamma\gamma}}{dz}$ is then given by $\mathcal{L}_{ee}$ x RHS of equation (3) and involves only flux factors. Figures (3) and (4) illustrate the efficiency

for single tagging and double tagging within various angular intervals as a function of the mass of the hadronic system $X_{\gamma\gamma}$. In the case of either single or double tagging in either of the two symmetrical detection systems, it is evident that efficiency for a given tagging range is almost independent of z, changing by only a factor of $\sim$5 when the minimum angle is reduced fron 0.1 to 10 millirad. It is therefore our conclusion that it is unnecessary to attempt to reach very small angles of <10 millirad in order to study photon-photon interactions.

The variation with z of the differential luminosity for photon-photon interactions is given in Fig. 5, and emphasises the fact that the majority of the interactions are produced by photons of lower energy. From this picture it is also apparent that one way to suppress two-photon events is to constrain the observed hadron energy to be greater than some minimum energy E_{min}. As an example, changing E_{min} from 25% to 75% of the total available energy reduces the yield of 2γ events by two orders of magnitude.

3 - Single Particle Inclusive Cross-sections

In order to determine the possibility of separating one-photon and two-photon processes, we calculated the inclusive single photon annihilation cross-section using the formula (3)

$$\frac{E_\pi}{\pi}\frac{d^2\sigma}{dp_L\,dp_T^2} = \frac{k}{S^2}\,(1+\cos^2\theta)\,\left(\frac{1-x}{x}\right)^2 \quad \text{------ (5)}$$

where $x = p/E$. This formula gives a good fit to the highest energy ($\sqrt{S}$ = 7.4GeV) SPEAR data for $x > 0.1$

Since no data exists on the two-photon inclusive hadron distributions, it was decided to use as input inclusive hadron distributions from the ISR. The single particle invariant cross-section in the 2-photon interaction can be written

as:

$$E_\pi^* \frac{d^3\sigma}{dp^{*3}} = \sigma_{\gamma\gamma}(S_{\gamma\gamma})\ f(x^*,p^*) \qquad \text{------ (6)}$$

where $x^* = 2p_L^* / \sqrt{S_{\gamma\gamma}}$ (starred quantities are defined in the $\gamma\gamma$ barycentric frame). By assuming factorisation we can write

$$f(x^*,p_T^*) = \lambda(1-x^*)\ F(S_{\gamma\gamma},p_T^*) \qquad \text{------ (7)}$$

and the function $F(S_{\gamma\gamma},p_T^*)$ is then taken directly from a fit to π^0 production at the ISR as given in Appendix B. The observed single particle invariant cross-sections for a given range of y and z are then obtained by multiplying by the flux factor and integrating over the appropriate range of y and z. The results of these calculations are presented in Figures (6) and (7). From Fig. 6, it is possible to conclude that by taking any single hadronic event and requiring that at least one hadron have $p_T > 5\text{GeV/c}$, $\theta > 70^0$, the one-photon and two-photon processes can be separated to the level of 1% or better. For any given event, there will most probably be two or more particles of large p_T and therefore further separation is possible. In addition, as stated earlier the two-photon cross-section is peaked at low values of z and therefore further separation is possible by making cuts on the total observed hadronic energy. From Fig. 7, it is evident that particles from the two-photon hadronic events are produced preferentially along the beam direction and therefore any detection system should be capable of covering a large part of the forward cone.

4 - Deep Inelastic Scattering

The physics processes which have been discussed so far deal with the interaction of two photons which are almost real. However, it is worth considering the possibility of performing an experiment where one of the photons is taken

well off its mass shell to study inelastic scattering off the photon and hence study the hadronic structure of the photon.[4]

The experience of inelastic scattering off the proton suggests that even at moderate $q^2 \simeq 1$ GeV/c^2, the quark-parton picture works reasonably well and therefore inelastic scattering off the photon at similar q^2 should yield interesting information about the photon structure functions. Since the photon structure function measures the sum of the fourth powers of the quark charges, just as the total single photon cross-section measures the sum of the squares of the quark charges, it may be possible by a crude measurement to distinguish a fractionally charged quark model from an integrally charged one. Estimates of this cross-section have been made for various values of Q_0^2 the minimum momentum transfer to the 'off shell' photon and $\sqrt{S_{\gamma\gamma}^0}$ the minimum mass of the produced hadron system X. These estimates are given in Table 1. Three coloured quarks were assumed. The addition of a fourth charmed quark will increase these cross-sections by about 50%.

5 - Electron Tagging Detector

The electron tagging detector has to operate close to the beam, withstand high rates of soft electromagnetic background and be able to operate as a fast coincidence detector to enable us to carry out missing mass scans in the production cross-section of the $X_{\gamma\gamma}$ state. A lead glass detector is favoured for the small angle detector since it can be simply triggered and provides good photon detection efficiency and resolution.

The largest source of background which can activate the detector is the bremsstrahlung processes $e^+ + e^- \rightarrow e^+ + e^- + \gamma$ and $e^+ + e^- + 2\gamma$. The cross-section for single bremsstrahlung (see Appendix C) has a characteristic

$1/\theta^4$ dependence compared with $(1/\theta^2)$ for the $\gamma\gamma$ collisions. This eeγ process dominates the single electron tagging rate by several orders of magnitude over most of the physical ranges of interest, as seen in Fig. 8. This rules out any possibility of using single tagging for studying 2-photon interactions and emphasises the need to ensure that the tagging range is not pushed into too small angles. We therefore propose to tag in the region 150mrad > θ > 15mrad.

The integrated cross-section for single bremsstrahlung electrons in our angular range over all energies is $\sim 1.0 \times 10^{-31} cm^2$, which corresponds to a singles rate in the tagging system of $\sim 6 \times 10^{-5}$/bunch-bunch collision. The rate of accidental coincidences of two such events simulating a 2γ event is $\sim 3.7 \times 10^{-9}$/bunch-bunch collision, compared with $\sim 8 \times 10^{-8}$/bunch-bunch collision for the two-photon process. It will therefore be desirable to impose some further restriction on the trigger, for example the requirement that at least one hadron is observed. The double bremsstrahlung total cross-section (see Appendix C) is smaller than that for single bremsstrahlung by a factor of 10^3. However over the kinematic range of interest, the coincidence rate (6×10^{-8}/b-b collision) is comparable to that for the real 2-γ events. The singles rates in the tagging counters are low for all these processes, but clearly there will be a large background of soft radiation around such a machine.

6 - Detection Apparatus

The apparatus was considered to be used predominantly for photon-photon interactions and therefore the following criteria were imposed:

1. A region of 2 metres on either side of the interaction region should be left free for a 'standard' one-photon annihi-

lation solenoid or calorimeter detector, which should be available to study large angle events produced in $\gamma\gamma$ interactions. (At these energies rho-rho interactions should produce interesting large p_T phenomena).

2. The electrons should be detected and used in the trigger with a minimum energy response from 1 GeV upwards. The minimum angular range should be around 15 mrad.

3. The detector should be able to record and separate hadrons both charged and neutral, produced over a wide region of the forward cone. Assuming that the multiplicity grows as log $S_{\gamma\gamma}$, then we expect 2-10 charged particles in the range from 5 GeV - 100 GeV.

The apparatus is illustrated in Fig.(9), (only one half is shown, identical detectors are installed on the other side of the intersection point) and has been designed to meet the previous requirements as far as possible. It is based on the use of two superconducting magnets, a dipole of 2.5 metres length ($\sim$4Tm) to enable electrons down to 15 mrad to be detected and a large toroidal magnet to cover the angular range 150mrad - 800mrad. The toroidal magnet is 2m in length containing 8 vanes and provides a mean $\int$Bdl of 3Tm.

Electrons within the angular range 15-150mrad are detected by an annular array of lead glass detectors of resolution $\sigma_E/E = (\frac{5}{\sqrt{E}} + 2)\%$. The effect of this resolution on z is illustrated in Fig. (10). As expected, the resolution in z decreases at low z. Also shown is the resolution achieved using the magnet together with drift and proportional chambers assuming $\sigma_p/p = 4\times10^{-4}p(\text{GeV/c})$. The minimum angle of 15mrad is defined by a superconducting tube which extends through the dipole magnet.

For the toroidal magnet, a figure of $\sigma_p/p = 5\times10^{-3}$ p(GeV/c) should be possible using the position of the intersection region to define the starting point of tracks.

Cerenkov counters, 2m in length, can be inserted

into the gap of the dipole magnet and similarly 8 Cerenkov counters can be inserted between the vanes of the toroidal magnet. Using RCA Quantacon tubes, it is possible to achieve a figure for $N_o = 120cm^{-1}$ ($N_{PE} = N_o L \sin^2\theta_c$). By using CO_2 and N_2 gas at 1 Atmosphere π, K and P can be separated using pulse-height (6 photo-electrons min.) in the energy range 5-30 GeV/c.

Photon detection is achieved using the lead glass behind the dipole magnet and a large lead-plexipop scintillator hodoscope can be inserted behind the toroid.

The detector can be used to measure the mass of the 2γ system in a missing mass technique by measuring the energy and direction of the two scattered electrons. This missing mass can then be plotted for various combinations of hadrons observed in the dipole and toroid. These hadrons need only be measured well enough to be identified, as the mass of the 2γ system they originate from is accurately obtained from the 2 scattered electrons.

7 - Conclusions

Using an electron-positron storage ring of 100GeV in each beam will open up new physics in the properties of the C = +1 final states as well as the C = -1 final states. Since the two-photon physics process provides a large hadronic cross-section with well defined initial quantum numbers and it is possible to trigger selectively on a given missing mass object, then it is our opinion that at least one of the interaction regions should have a well designed apparatus capable of studying two-photon physics.

TABLE I

Cross-sections in cm^2 for deep inelastic scattering on the photon.

Q_o^2 = (minimum momentum transfer)^2 to the 'off shell' photon.

$\sqrt{s^o_{\gamma\gamma}}$ = minimum mass of produced hadron system. E = 100 GeV

$\sqrt{Q_o^2}$ GeV/c \ $\sqrt{s^o_{\gamma\gamma}}$ GeV	10	20	50	100
1	1.0×10^{-34}	1.1×10^{-34}	4.8×10^{-35}	6.0×10^{-36}
5	6.5×10^{-36}	4.5×10^{-36}	1.9×10^{-36}	2.4×10^{-37}
10	1.6×10^{-36}	1.1×10^{-36}	4.8×10^{-37}	6.0×10^{-38}
50	6.5×10^{-38}	4.5×10^{-38}	1.9×10^{-38}	2.4×10^{-39}

Appendix A

Tagging Kinematics and Photon Flux Factors in the Equivalent Photon Approximation

Three diagrams [(i), (ii), (iii) in Fig. 11] can contribute to the process

$$e^+e^- \to e^+e^- + \text{ hadrons}$$

(i) and (ii) lead to C = +1 hadronic states, while (iii) gives C = -1 states. When the outgoing e^+, e^- make small angles to the incident e^+, e^- directions, photon propagator effects result in the complete dominance of diagram (i). The kinematical notation is then as shown in Fig. 1 where the two photons are 'almost real' i.e. q^2 = (virtual photon mass)$^2 \simeq 0$. We use the following notation:

E = incident beam energy

$E'_{1,2}$ = scattered e^+, e^- energy

$\nu_{1,2}$ = e^+, e^- energy loss

$\theta_{1,2}$ = e^+, e^- scattering angles

$S_{\gamma\gamma}$ = ($\gamma\gamma$ effective mass)^2

$q^2_{1,2}$ = (virtual photon mass)^2

$= -2E_{1,2}E'_{1,2}(1-\cos\theta_{1,2})$

$(E_{1,2}/m_e >> 1)$

In the case where $|q^2_{1,2}| << 4\nu_1\nu_2$, which will be true in the tagging region of kinematics

$$S_{\gamma\gamma} = 4\nu_1\nu_2$$

It is convenient to introduce the following dimensionless quantities:

$$y_{1,2} = \nu_{1,2}/E, \quad x_{1,2} = E_{1,2}/E$$

$$z = \sqrt{S_{\gamma\gamma}}/2E = \sqrt{y_1 y_2}$$

These all have the range $0 \to 1$.

It may be shown [5],[6] that the cross-section for the process illustrated in Fig. 1

$$e^+e^- \rightarrow e^+e^- X(z,\beta)$$

(where X is an arbitrary hadronic system of mass z and laboratory velocity βC) may be written as:

$$\frac{d^4\sigma(e^+e^-\rightarrow e^+e^-X)}{dy_1 dy_2 d(\cos\theta_1) d(\cos\theta_2)} = f_1 f_2 \sigma(\gamma\gamma\rightarrow X(z)) \qquad \text{-----} \quad (A1)$$

The factorisable form of the RHS of (A1) is a consequence of the Equivalent Photon Approximation.[2] f_1, f_2 are the flux factors of virtual photons from the e^+, e^- defined in terms of the kinematic variables by the expression[7]:

$$f(y,\theta) = \left(\frac{\alpha}{2\pi}\right) \frac{\left[1 + (1-y)^2\right]}{y\left[1-\cos\theta+\frac{m_e^2}{2E^2}\left(\frac{y}{1-y}\right)^2\right]} \qquad \text{----} \quad (A2)$$

$$f_1 = f(y_1,\theta_1), \quad f_2 = f(y_2,\theta_2)$$

$\sigma(\gamma\gamma \rightarrow X(z))$ is the cross-section for real unpolarised photons to produce the hadronic system X of mass z. The velocity in the lab, β, of the CM system of X is given by:

$$\beta = \frac{y_2 - y_1}{y_2 + y_1} \qquad \text{-----} \quad (A3)$$

As the γγ physics is contained essentially in $\sigma(\gamma\gamma \rightarrow X)$ which is a function only of $S_{\gamma\gamma}$ (or z) it is convenient to change variables from y_1, y_2 to $y_1 (\equiv y)$ and z. The cross-sections for a fixed value of z is then given by integrating the following expression over the variables y, θ_1, θ_2:

$$\left.\begin{aligned} \frac{1}{\sigma_{\gamma\gamma}(z)} \frac{d^4\sigma}{dz\, dy\, d(\cos\theta_1)\, d(\cos\theta_2)} &= \frac{(\alpha/\pi)^2}{2zy}\left[1+(1-y)^2\right]\left[1+(1-z^2/y)^2\right] \\ \times \frac{1}{1-\cos\theta_1+\frac{m_e^2}{2E^2}\left(\frac{y}{1-y}\right)^2} &\times \frac{1}{1-\cos\theta_2+\frac{m_e^2}{2E}\frac{1}{(y/z^2-1)^2}} \end{aligned}\right\} \quad (A4)$$

The integrations over θ_1, θ_2 are independant and can be done exactly, giving factors

$$\left[\ln\{1-\cos\theta_1 + \frac{m_e^2}{2E^2}\left(\frac{b}{1-y}\right)^2\}\right]_{\theta_1^L}^{\theta_1^U}, \qquad \left[\ln\{1-\cos\theta_2 + \frac{m_e^2}{2E^2}\frac{1}{(y/z^2-1)^2}\}\right]_{\theta_2^L}^{\theta_2^U} \tag{A5}$$

In the region $1>>\theta_{1,2}>>\frac{m_e^2}{E^2}$, which is true for the practical range of tagging angles 15 mrad$<\theta_{1,2}<$150 mrad discussed in the main text, these expressions simplify to:

$$2\ln(\theta_1^U/\theta_1^L), \quad 2\ln(\theta_2^U/\theta_2^L) \qquad (1>>\theta_{1,2}>>\frac{m_e^2}{E^2})$$

Alternatively, if the full range of integration is taken, the m_e^2/E^2 terms give the dominant contribution, and the expressions(A5) become:

$$\ln\left[\frac{4E^2}{m_e^2}\left(\frac{1-y}{y}\right)^2+1\right], \quad \ln\left[\frac{4E^2}{m_e^2}\left(\frac{y}{z^2}-1\right)^2+1\right]$$

$$\theta_{1,2}^L = 0, \quad \theta_{1,2}^U = \pi$$

As $E^2/m_e^2 \sim 4\times10^{10}$, when E = 100 GeV whereas the other factors are of order unity except very close to y = 0 or y = 1, the expressions further simplify to

$$2\ln(E/m_e), \quad 2\ln(E/m_e)$$

$$\theta_{1,2}^L = 0, \ \theta_{1,2}^U = \pi$$

$$y \neq 0, 1$$

The cross-section, integrated over the full range of θ_1, θ_2 then becomes:

$$\frac{1}{\sigma_{\gamma\gamma}(z)}\frac{d^2\sigma}{dzdy} = \left(\frac{\alpha}{\pi}\right)^2 2(\ln E/m_e)^2 \frac{\left[1-(1-y)^2\right]\left[1+(1-z^2/y)^2\right]}{zy} \quad \text{--- (A6)}$$

The y integration is again straightforward, leading to the result:

$$\frac{1}{\sigma_{\gamma\gamma}(z)}\frac{d\sigma}{dz} = \left(\frac{\alpha}{\pi}\right)^2 2(\ln E/m_e)^2 \frac{1}{z} \times \left[(2+z^2)^2 \ln y - 2(2+z^2)y + y^2 + 2z^2\frac{(2+z^2)}{y} - z^4/y^2\right]_{y_L}^{y_U} \quad \text{---(A7)}$$

where y_U, y_L are upper and lower limits of the y integration.

The photon flux curves $\frac{d\mathcal{L}_{\gamma\gamma}}{dz}$, (defined in Eqn(4) of the main text) presented in this report were infact calculated by numerical integration [8] of Eqn(A4) over the relevant ranges of θ_1, θ_2, y. When the full angular range was taken, expressions A5 for the θ_1, θ_2 integration were inserted into equation A4 and numerical integration [8] was carried over the remaining variable y. Good agreement with Eqn A7 was found.

Appendix B

Estimation of Single Particle Inclusive Cross-sections for Annihilation and 2γ Processes at LEP Energies

a) Annihilation Cross-section.

The form used for the invariant cross-section is that suggested by Gatto and Preparata[3]:

$$\frac{E_\pi}{\pi}\frac{d^2\sigma}{dp_L dp_T^2} = \frac{k}{S^2}(1+\cos^2\theta)\left(\frac{1-x}{x}\right)^2 \qquad \text{---- (B1)}$$

where $x = p/E$.

This function gives a good fit to the highest energy ($\sqrt{S}$ = 7.4GeV) SPEAR [9] single particle inclusive cross-section for x>0.1. For smaller values of x the SPEAR points lie below Eqn B1. The normalisation constant k is fixed by matching the SPEAR data for $\sqrt{S}$ = 7.4GeV and x>0.1.

b) 2γ Cross-section.

A Feynman scaling hypothesis is made for the single particle invariant cross-section in γγ collisions:

$$E^*\frac{d^3\sigma}{dp^{*3}} = \sigma_{\gamma\gamma}(S_{\gamma\gamma})\ f(x^*,p_T^*) \qquad \text{---- (B2)}$$

here $x^* = 2p_L^*/\sqrt{S_{\gamma\gamma}}$. Starred quantities are defined in the γγCM system (the barycentric frame of the hadronic system X in Fig. 1) . From the Lorentz invariance of dp^{*3}/E_π^*, and neglecting the angle between the virtual γ and beam directions,

$$E_\pi\frac{d^3\sigma}{dp^3} = \sigma_{\gamma\gamma}(S_{\gamma\gamma})\ f(x^*,p_T) \qquad \text{---- (B3)}$$

where unstarred quantities refer to the laboratory frame. By Lorenz transformation to the laboratory system

$$x^* = p_L/\nu$$

where ν is the energy of the virtual photon radiated by the electron moving in the $p_L > 0$ direction. So, integrating over the azimuthal angle of the transverse momentum vector:

$$E_\pi \frac{d^2\sigma(\nu, S_{\gamma\gamma})}{\pi dp_L dp_T^2} = \sigma_{\gamma\gamma}(S_{\gamma\gamma})\ f(\frac{p_L}{\nu}, p_T) \quad \text{---- (B4)}$$

The observed single particle invariant cross-section for a given range of ν (or $y = \nu/E$) and $S_{\gamma\gamma}$ (or $z = \sqrt{S_{\gamma\gamma}}/2E$) is then given by multiplying B3 by the photon flux factor on the RHS of Eqn A6 and integrating over the appropriate ranges of y and z. If restrictions on the electron angles are also to be applied (or for events where the electrons are tagged) Eqn A4 gives the relevant flux factor.

Almost nothing is known experimentally of the nature of the hadronic final states produced in $\gamma\gamma$ collisions, so extrapolations are not possible as in the annihilation reaction. The small angles and high energies of the photons involved in the collision however might lead to the expectation of strong leading particle effects.

Here we estimate only the 'pp' like or diffractive component of the hadron production. It is clearly of great physics interest to see if a 'quark annihilation' component also exists. If it does, the relatively clean separation between 1γ and 2γ events mentioned in the main text on the basis of p_T cuts, may be overly optimistic.

The assumptions made in the calculation of the single particle inclusive cross-sections using Eqn B3 and Eqns A4 or A6 are:

(1) $\sigma_{\gamma\gamma} = \text{const} = 2.5 \times 10^{-31} \text{cm}^2$ (3)

(2) Factorisation of $f(x^*, p_T^*)$:

$$f = \lambda(1-x^*)\ F(S_{\gamma\gamma}, p_T^*)$$

(3) The function $F(S_{\gamma\gamma}, p_T^*)$ is taken directly from a fit to π^0 production at the CERN ISR:

$p < 1.5$ GeV/c, $\sqrt{S} < 40$ GeV $\quad \alpha\ e^{-7.1p_T + p_T^2}$

$p < 1.5$ GeV/c, $\sqrt{S} > 40$ GeV $\quad \alpha\ e^{-7.3p_T + 1.3p_T^2}$

$p \gtrsim 1.5$ GeV/c $\quad \alpha\ p_T^{-7.5}\ e^{-\frac{30.8}{\sqrt{S}}\ p_T}$

(4) Normalisation constant λ given by

$$\int \frac{d^3\sigma}{dp^3}\, dp^3 = \sigma_{\gamma\gamma} \langle n_c \rangle = \sigma_{\gamma\gamma}\ \ln S_{\gamma\gamma} \qquad \left[S_{\gamma\gamma} \text{in (GeV)}^2\right]$$

The form chosen for f gives automatically an increase of the mean charged multiplicity $\langle n_c \rangle \alpha \ln S_{\gamma\gamma}$.

As in the case of the photon flux factor calculations described in Appendix A the necessary integrations over the angular or photon energy variables are done numerically.

Appendix C

Tagging Backgrounds from Beam-Beam Bremsstrahlung

The double differential cross-section for scattering an electron at an energy E' and angle θ from a two-photon interaction is:

$$\frac{d^2\sigma^{\gamma\gamma}}{dxdcos\theta} = \sigma_{\gamma\gamma} 7.72 \left(\frac{\alpha}{\pi}\right)^2 \ln\left(E/m_e\right) \frac{[1+x^2]}{(1-x)\theta^2} \quad \text{---- (C1)}$$

$$x = E'/E$$

This relation is obtained by integrating Eqn(A4). The numerical factor 7.72 corresponds to integration over the full angular range, and $0.01<x<0.99$ for the unobserved electron.

The corresponding cross-section for single beam-beam bremsstrahlung (σ_{BBB}) has been given by Altarelli and Stella.[10] The exact expression is lengthy, but may be approximated in the angular region where:

$$1 >> \theta >> \frac{m_e}{Ex}(1-x) \quad \text{---- (C2)}$$

by:

$$\frac{d^2\sigma^{BBB}}{dxdcos\theta} = 2\left(\frac{xE}{A}\right)^2 \frac{\alpha^3(1+x^2)}{1-x} \cdot \left\{ \ln\left(\frac{4xE^2}{m_e^2}\right) + \frac{1}{1-x}\left[x\ln x - \frac{1+x^2}{2(1-x)} + \frac{x}{(1-x)}\ln\left(\frac{2A}{m_e^2 x}\right)\right]\right\}$$

$$A = \frac{x^2E^2\theta^2}{2(1-x)} \quad \text{---- (C3)}$$

The agreement of Eqn C3 in the region C2 with the exact relation is within a few percent.

Fig. 8 shows the ratio of the beam-beam bremsstrahlung (BBB) and $\gamma\gamma$ cross-sections as a function of x and θ. For the BBB cross-section the exact expression from Ref (10) was used. $\frac{d^2\sigma}{dxdcos\theta}$ drops more rapidly with angle ($\alpha\frac{1}{\theta^4}$) for BBB than for $\gamma\gamma$ collisions ($\alpha\frac{1}{\theta^2}$). However for the angular region

of acceptance of the tagging system:

$$15\text{mrad} < \theta < 150\text{mrad}$$

(shaded in Fig. 8) the BBB cross-section is several orders of magnitude larger than the $\gamma\gamma$ one, except for the largest angles and $x \sim 1.0$.

Integrating Eqn(A4) over the full angular acceptance for double tagging and the range $0.05<x<0.95$ for both detected electrons, gives a total cross-section $\sigma^{D.T.}$ for double tagging of

$$\sigma^{D.T.} = 1.47 \times 10^{-34}\text{cm}^2$$

($\sigma_{\gamma\gamma}$=0.25μb is assumed). Integrating the BBB cross-section over the same angular and energy intervals leads to a cross-section σ^{BBB} of

$$\sigma^{BBB} = 1.16 \times 10^{-31}\text{cm}^2$$

Taking a bunch-bunch collision frequency of 188 kc/s[11] and a luminosity of $10^{32}\text{cm}^{-2}\text{sec}^{-1}$ the BBB singles rate in each half of the tagging system is:

$$R^{BBB} = 6.1 \times 10^{-5}/\text{b-b collision}$$

Another source of background comes from double beam-beam bremsstrahlung (DBBB). The double differential distribution in the photon energies has been given by Baier and Galitsky[12]

$$\frac{d^2\sigma}{dy_1 dy_2} = \frac{8\alpha^4}{m_e^2 \pi y_1 y_2}\left[(1-y_1)(1-y_2)\left[\frac{5}{4} + \frac{7}{8}\zeta(3)\right] + \left[(1-y_1)y_2^2 + (1-y_2)y_1^2\right]\left[\frac{1}{2} + \frac{7}{8}\zeta(3)\right] + y_1^2 y_2^2 \frac{7}{8}\zeta(3)\right] \quad \text{---- (C4)}$$

$y_{1,2} = \nu_{1,2}/E = \frac{\text{photon energy}}{E}$, $\frac{7}{8}\zeta(3) = 1.052.$

Integrating this expression over the range

$$0.01 < y_{1,2} < 0.99$$

gives a cross-section of $3.84 \times 10^{-28}\text{cm}^2$.

Integrating the single bremsstrahlung differential energy spectrum given in Ref (10).

$$\frac{d\sigma}{dy} = \frac{2\alpha^3}{m_e^2 y}\left[\frac{8}{3}(1-y) + 2y^2\right]\left[\ln\frac{4E^2}{m_e^2}\left(\frac{1-y}{y}\right) - \frac{1}{2}\right] \quad \text{---- (C5)}$$

over the same range of y yields a cross section of 3.42×10^{-25} cm^2. The ratio R^{BBB}/R^{DBBB} is then $\sim 10^3$.

References and Foot-notes

1) G. Barbiellini et al., PEP Summer Study 1975, (LBL-4800, SLAC-190, PEP-178) P159

2) E. Fermi, Z. Phys. 29 (1924) 315
C. Weizsäcker and E.J. Williams, Z. Phys 88 (1934) 612
R.H. Dalitz and D.R. Yennie, Phys. Rev. 105 (1957) 1598

3) R. Gatto and G. Preparata, Rivista del Nuovo Cimento 4 (1974) 445

4) E. Witten, Princeton University Report 1976

5) S.J. Brodsky, T. Kinoshita, H. Terazawa, Phys. Rev. D4 (1971) 1532

6) H. Terazawa, Rev. Mod. Phys. 45 (1973) 615

7) Here we consider only the leading term α $\log E/m_e$ in the photon flux factor. We also restrict ourselves throughout to small angles, where the approximation $\cos\theta \simeq 1-\theta^2/2$ is valid. It is also required that $\theta_{1,2} << y_{1,2}$.

8) This was done using the CERN 7600 Library Program RGAUSS written by B. Lautrup.

9) R.F. Schwitters, Proceedings at the 1975 International Symposium on Lepton and Photon Interactions at High Energies, Stanford 1975 P5, and B. Richter, private communication.

10) G. Altarelli and B. Stella, Lett. al N.C. 9 (1974) 416

11) E. Keil LEP Parameter List (Version 3)

12) V.N. Baier and V.M. Galitsky JETP Letts. 2 (1965) 165

Figure Captions

1) Kinematics of 2γ interaction. All quantities are defined in Appendix A.

2) y x virtual photon energy spectrum integrated from $\theta = 0$ to $\theta = \theta^{MAX}$. (y = photon energy/beam energy).

3) Single tagging efficiency $\frac{d\mathcal{L}_{\gamma\gamma}}{dz} \Big/ \left(\frac{d\mathcal{L}_{\gamma\gamma}}{dz}\right)^{TOTAL}$, for the angular range $0.1<\theta<100$mrad, $10<\theta<100$mrad, as a function of z, the normalised effective mass of the γγ system.

4) Double tagging efficiencies for the same angular ranges as shown in Fig. 3.

5) Photon flux factor $\frac{1}{\mathcal{L}_{ee}} \frac{d\mathcal{L}_{\gamma\gamma}}{dz} = \frac{1}{\sigma_{\gamma\gamma}(z)} \frac{d\sigma}{dz}$ for E = 100GeV, $0.1<\frac{E'}{E}<1.0$ integrated over the full angular range of both scattered electrons.

6) Single particle inclusive cross-sections $\frac{E\pi}{\pi} \frac{d^2\sigma}{dp_L dp_T^2}$ as a function of p_T for 1γ and 2γ processes, E = 100GeV, p_L = 2.0GeV/c. 2γ masses in the range $0.01<\frac{\sqrt{S_{\gamma\gamma}}}{E}<0.99$ are integrated over assuming $\sigma_{\gamma\gamma}$ = const = 250 nanob.

7) Single particle inclusive cross-sections $\frac{1}{2\pi p} \frac{d}{dpd(\cos\theta)}$ as a function of p for various values of θ, and for 1γ and 2γ processes. Assumptions as in Fig. 6.

8) Cross-section ratio of single electrons from γγ interactions and from beam-beam bremsstrahlung as a function of scattered electron energy for various electron scattering angles. E = 100GeV, $\sigma_{\gamma\gamma}$ = const = 250 nanob, x = E'/E. The angular acceptance of the proposed tagging system is shown shaded.

9) Proposed Detector System for Studying 2γ Physics on LEP.

10) z resolution of proposed tagging system.
Solid line ——— from Pb Glass detectors
Dashed line - - - - from magnetic analysis

11) Lowest order 2 photon graphs giving hadron production. X is a general hadron system. (i), (ii) have C = +1 for X, (iii) has C = -1.

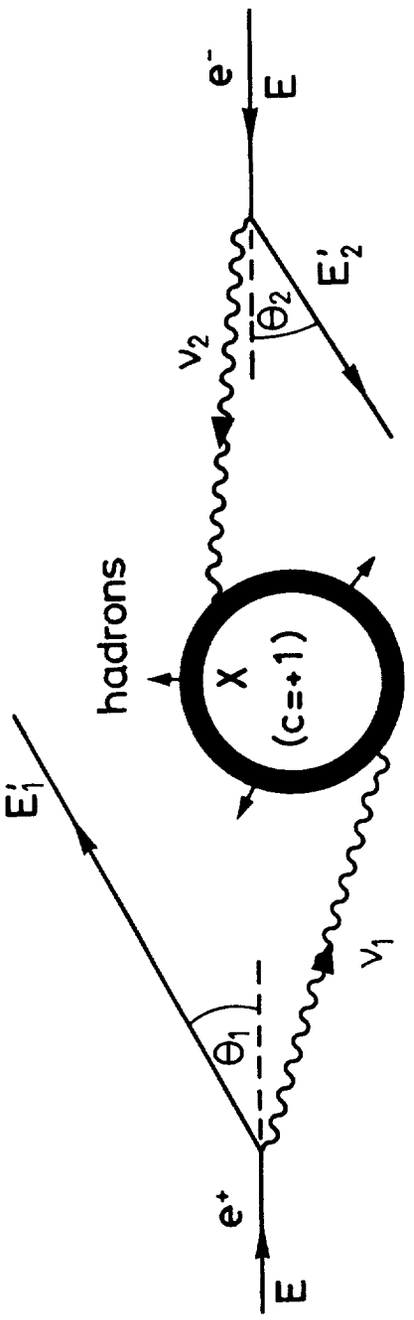

FIG. 1

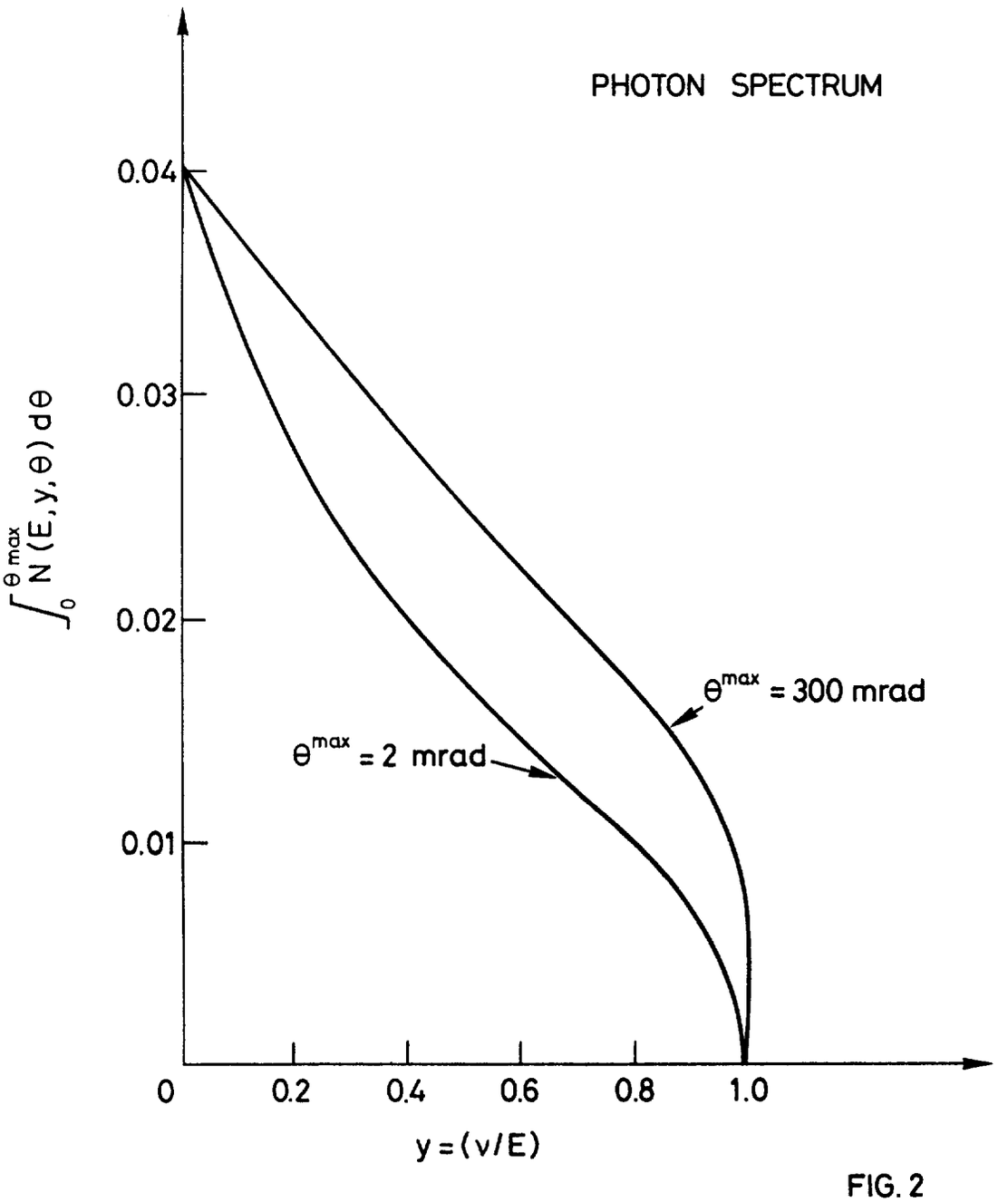
PHOTON SPECTRUM
0.04
0.03
0.02
0.01
$\int_0^{\theta\,max} N(E,y,\theta)\,d\theta$
θ^{max} = 300 mrad
θ^{max} = 2 mrad
0
0.2
0.4
0.6
0.8
1.0
y = (ν/E)

FIG. 2

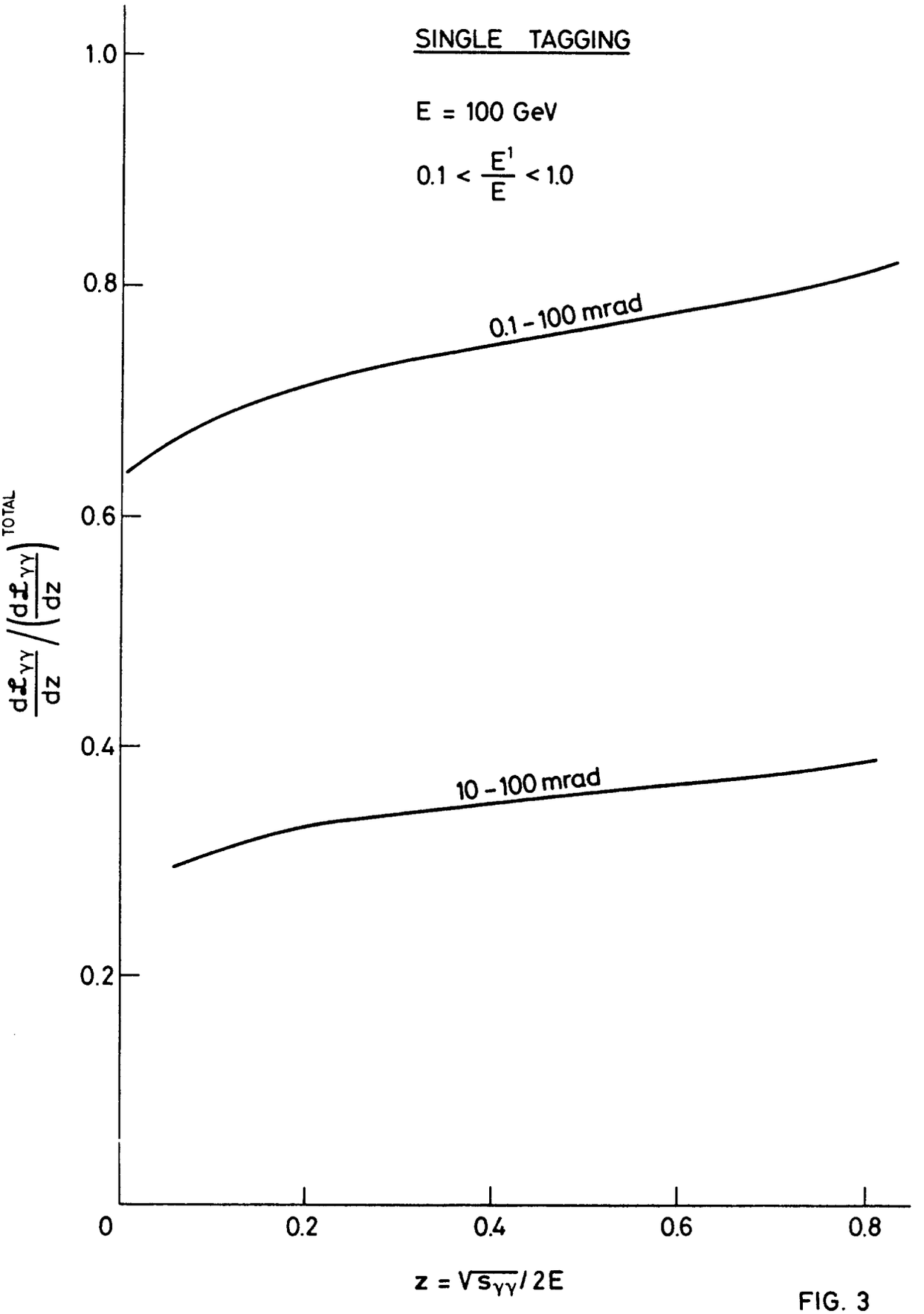
SINGLE TAGGING
E = 100 GeV
0.1 < E'/E < 1.0
0.1 - 100 mrad
10 - 100 mrad
1.0
0.8
0.6
0.4
0.2
0
0.2
0.4
0.6
0.8
dℒγγ/dz / (dℒγγ/dz)TOTAL
z = √sγγ / 2E

FIG. 3

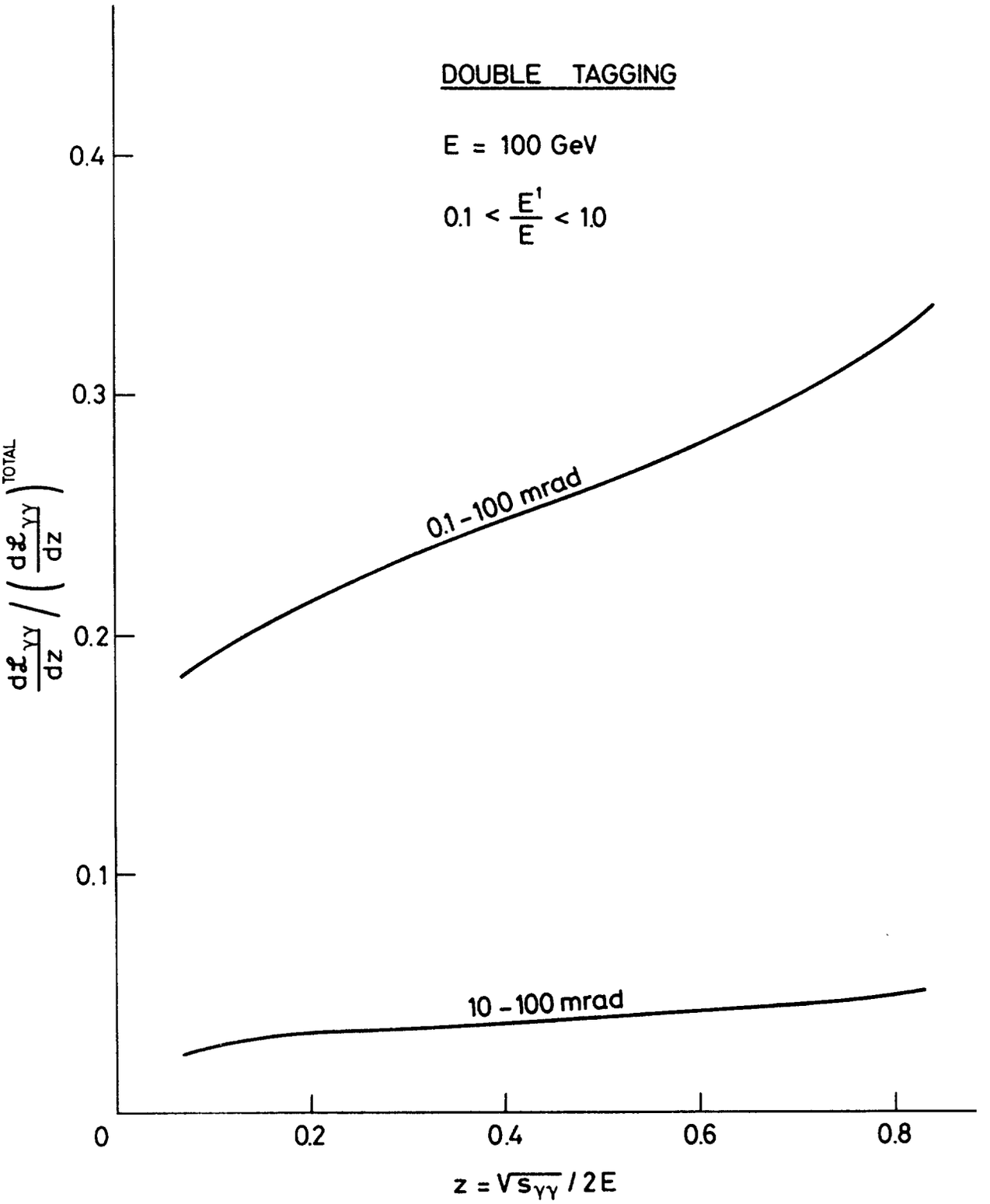
DOUBLE TAGGING
E = 100 GeV
0.1 < E'/E < 1.0
0.1 - 100 mrad
10 - 100 mrad
0.4
0.3
0.2
0.1
0
0.2
0.4
0.6
0.8
dℒγγ/dz / (dℒγγ/dz)TOTAL
z = √sγγ / 2E

FIG. 4

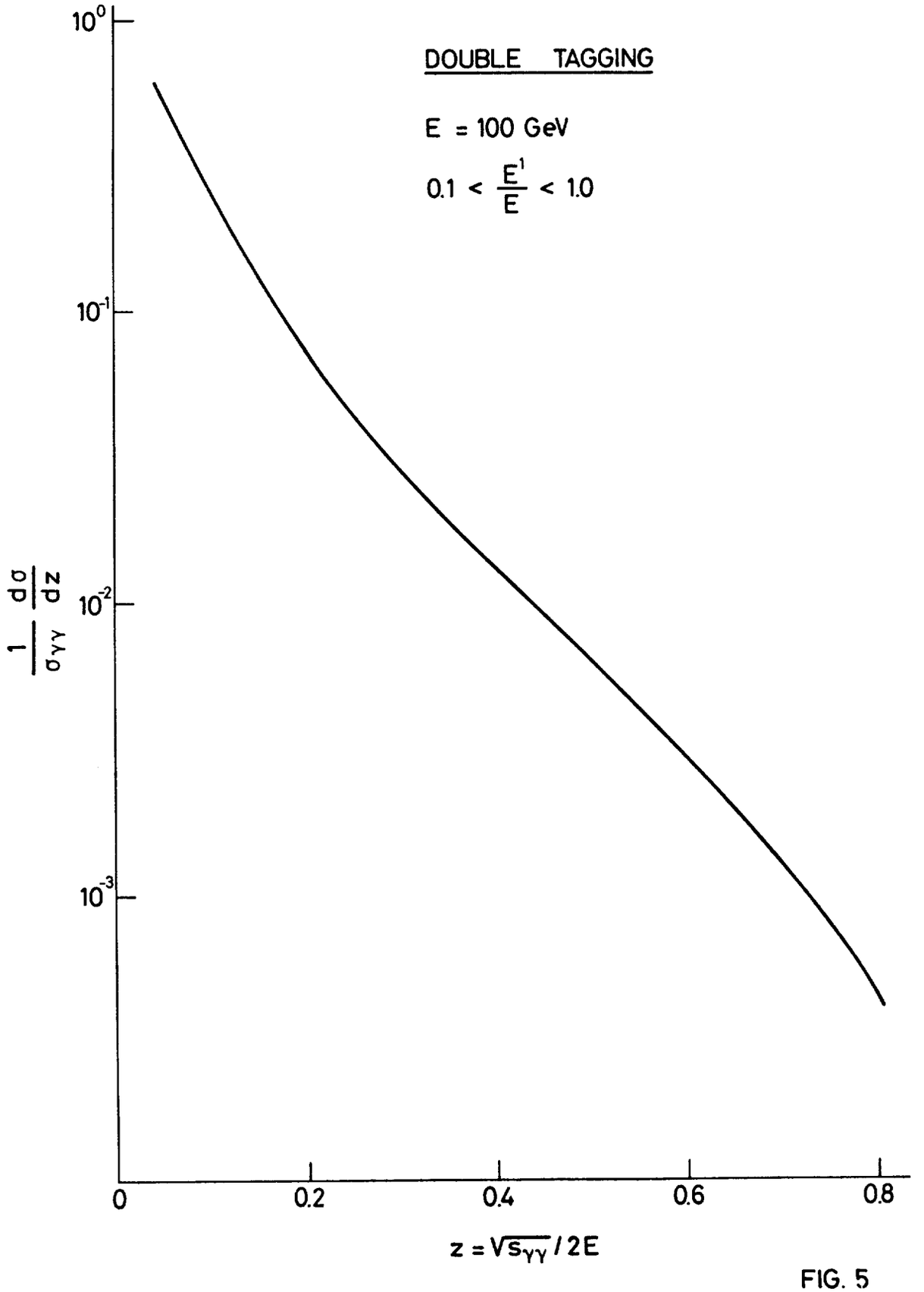
DOUBLE TAGGING
E = 100 GeV
0.1 < E'/E < 1.0
10^0
10^-1
10^-2
10^-3
1/σγγ dσ/dz
0
0.2
0.4
0.6
0.8
z = √sγγ / 2E

FIG. 5

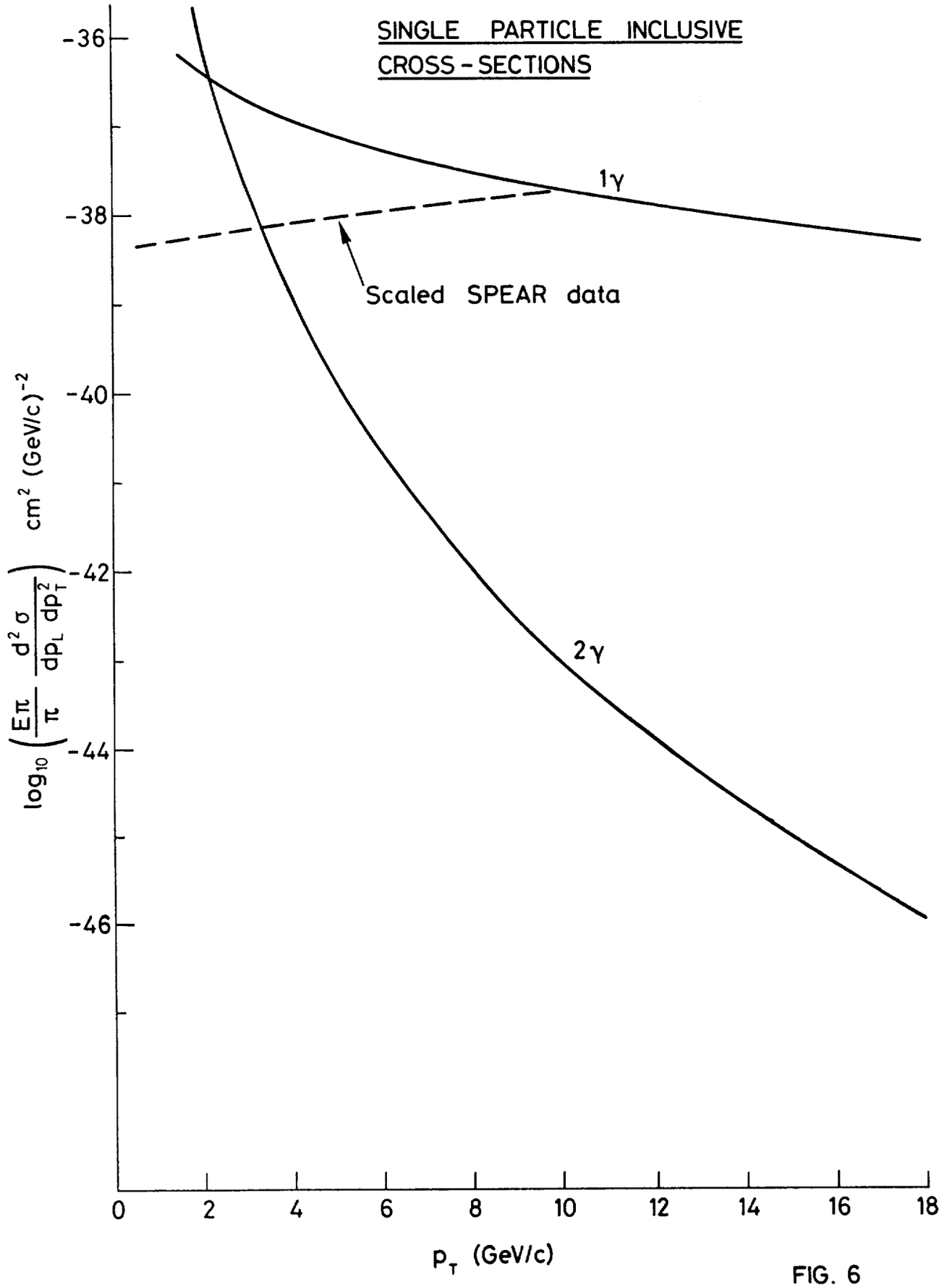
SINGLE PARTICLE INCLUSIVE
CROSS-SECTIONS
1γ
Scaled SPEAR data
2γ
-36
-38
-40
-42
-44
-46
$\log_{10}\left(\frac{E\pi}{\pi}\frac{d^2\sigma}{dp_L\,dp_T^2}\right)$ cm^2 (GeV/c)$^{-2}$
0
2
4
6
8
10
12
14
16
18
p_T (GeV/c)

FIG. 6

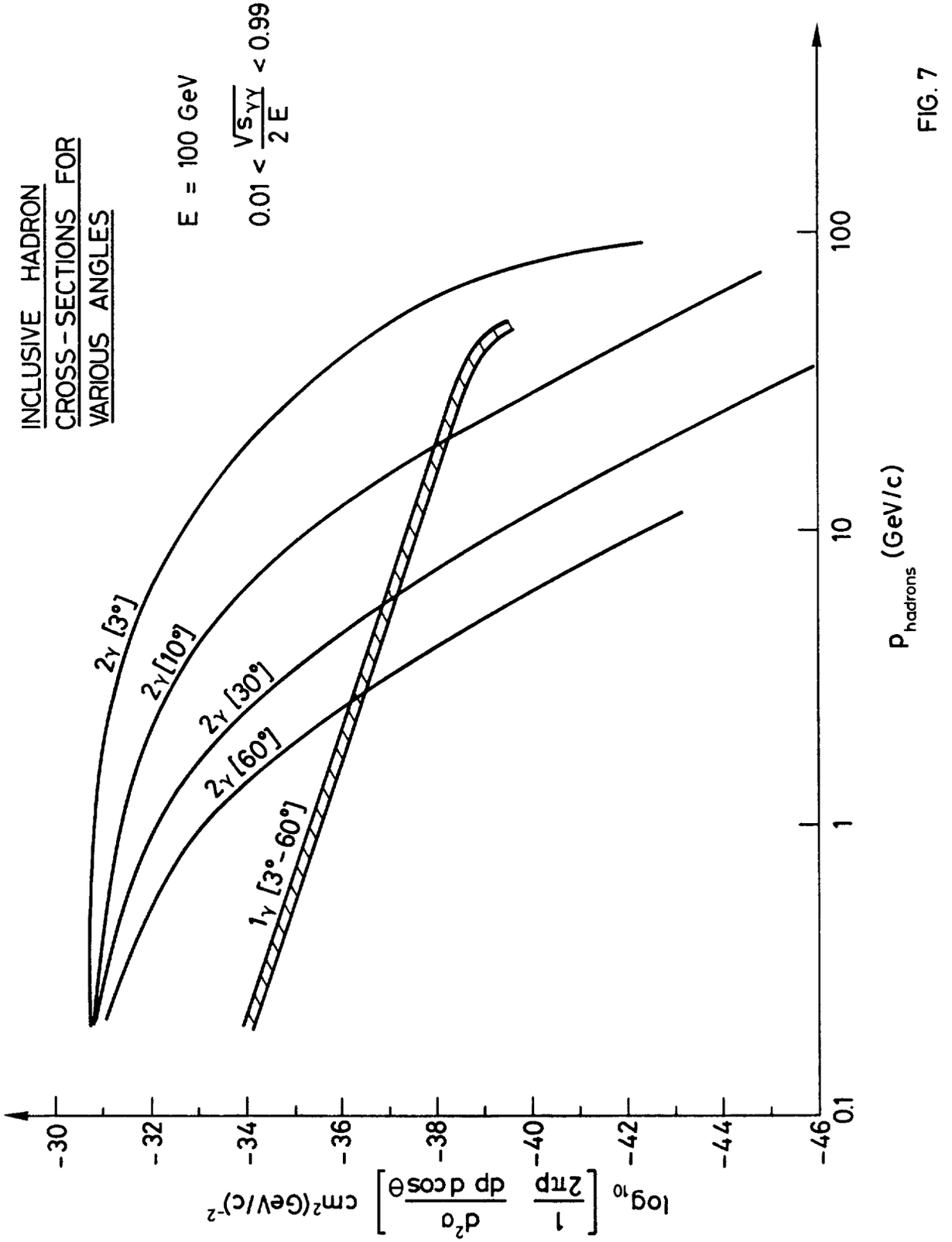
INCLUSIVE HADRON
CROSS-SECTIONS FOR
VARIOUS ANGLES
E = 100 GeV
$0.01 < \frac{\sqrt{s_{\gamma\gamma}}}{2E} < 0.99$
2γ [3°]
2γ [10°]
2γ [30°]
2γ [60°]
1γ [3°-60°]
$\log_{10}\left[\frac{1}{2\pi p}\frac{d^2\sigma}{dp\, d\cos\theta}\right]$ $cm^2(GeV/c)^{-2}$
$p_{hadrons}$ (GeV/c)
-30
-32
-34
-36
-38
-40
-42
-44
-46
0.1
1
10
100

FIG. 7

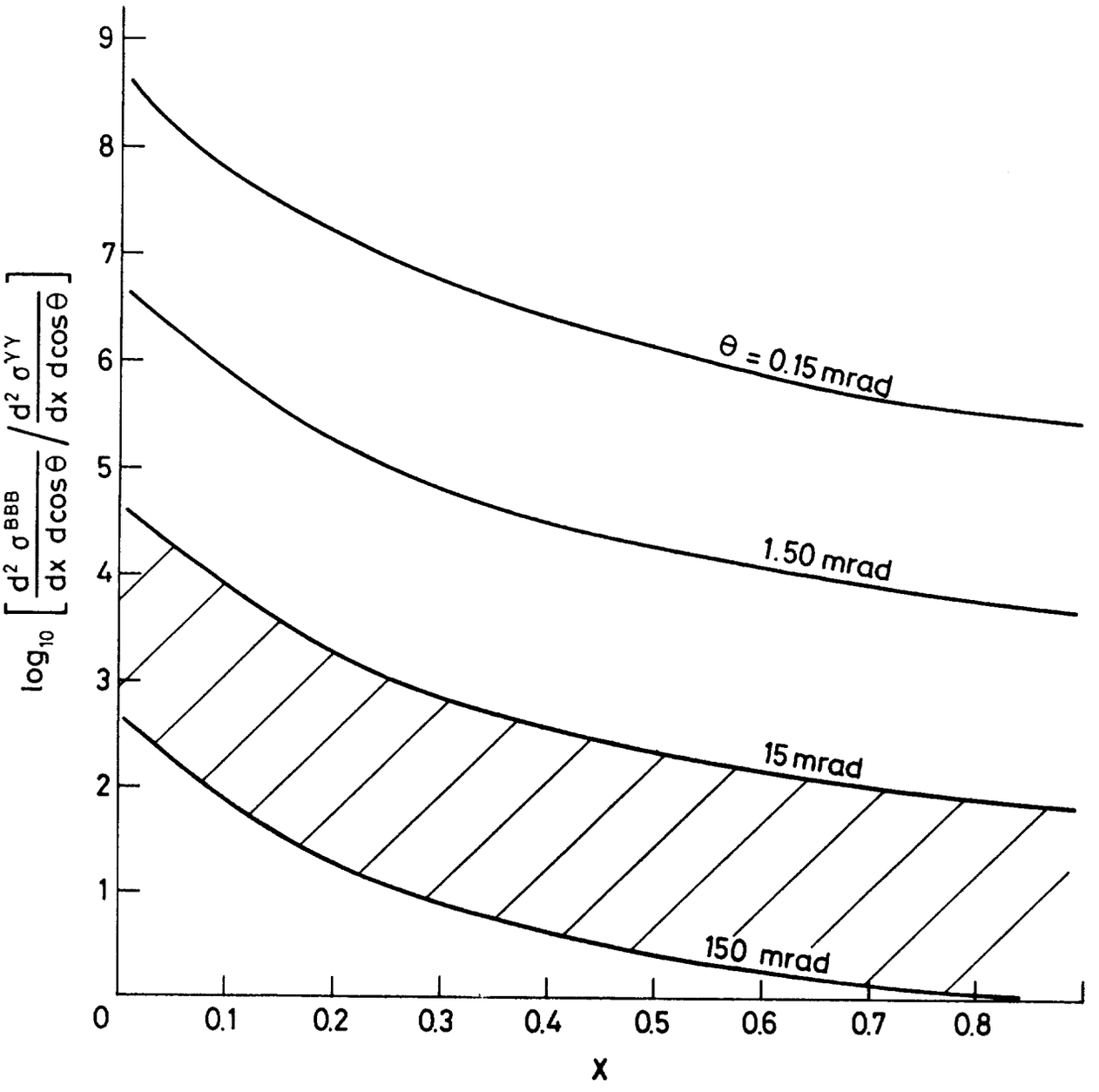
$\log_{10}\left[\frac{d^2\sigma^{BBB}}{dx\,d\cos\theta}\Big/\frac{d^2\sigma^{YY}}{dx\,d\cos\theta}\right]$
9
8
7
6
5
4
3
2
1
0
0.1
0.2
0.3
0.4
0.5
0.6
0.7
0.8
X
θ = 0.15 mrad
1.50 mrad
15 mrad
150 mrad

FIG. 8

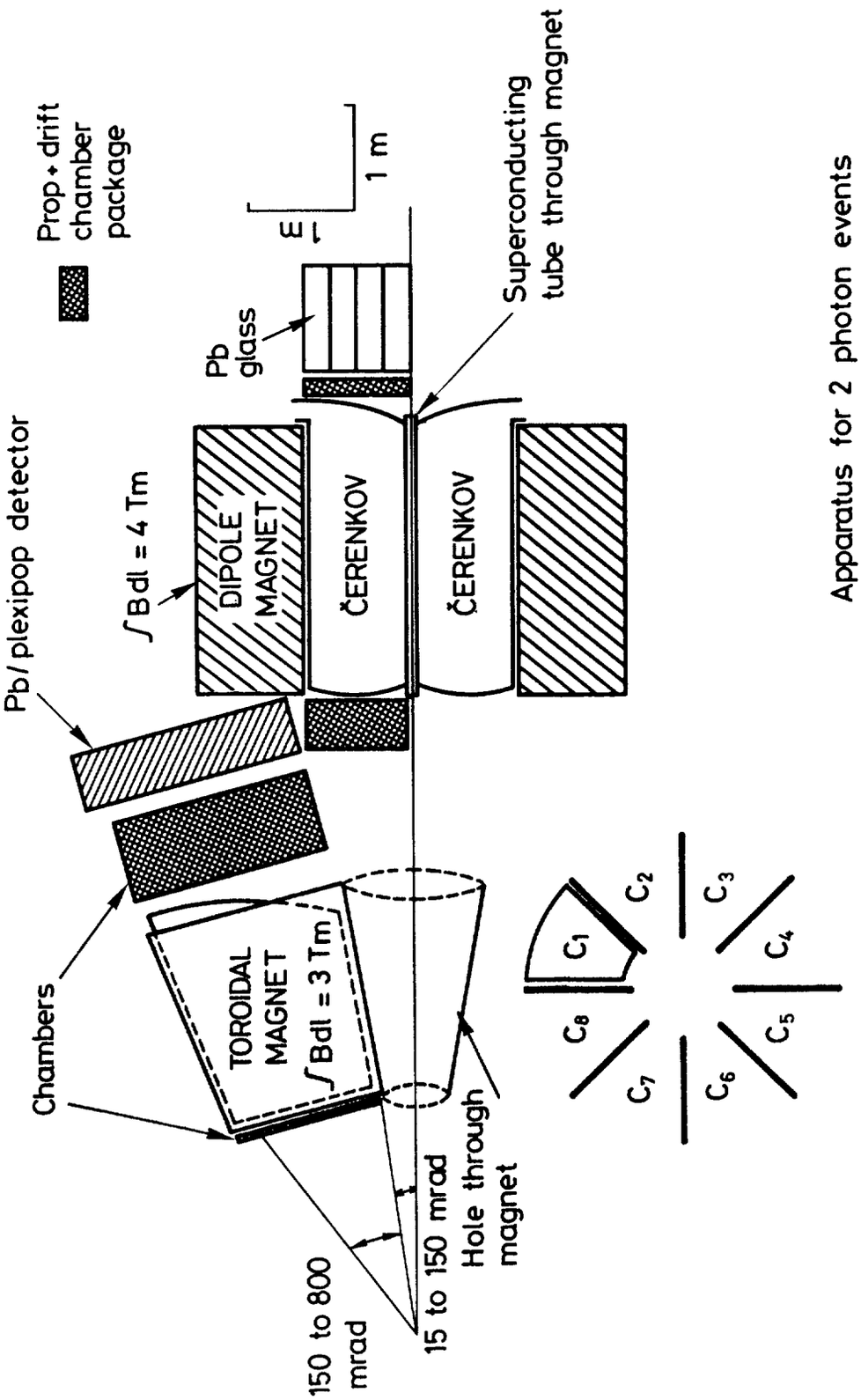

Apparatus for 2 photon events

FIG. 9

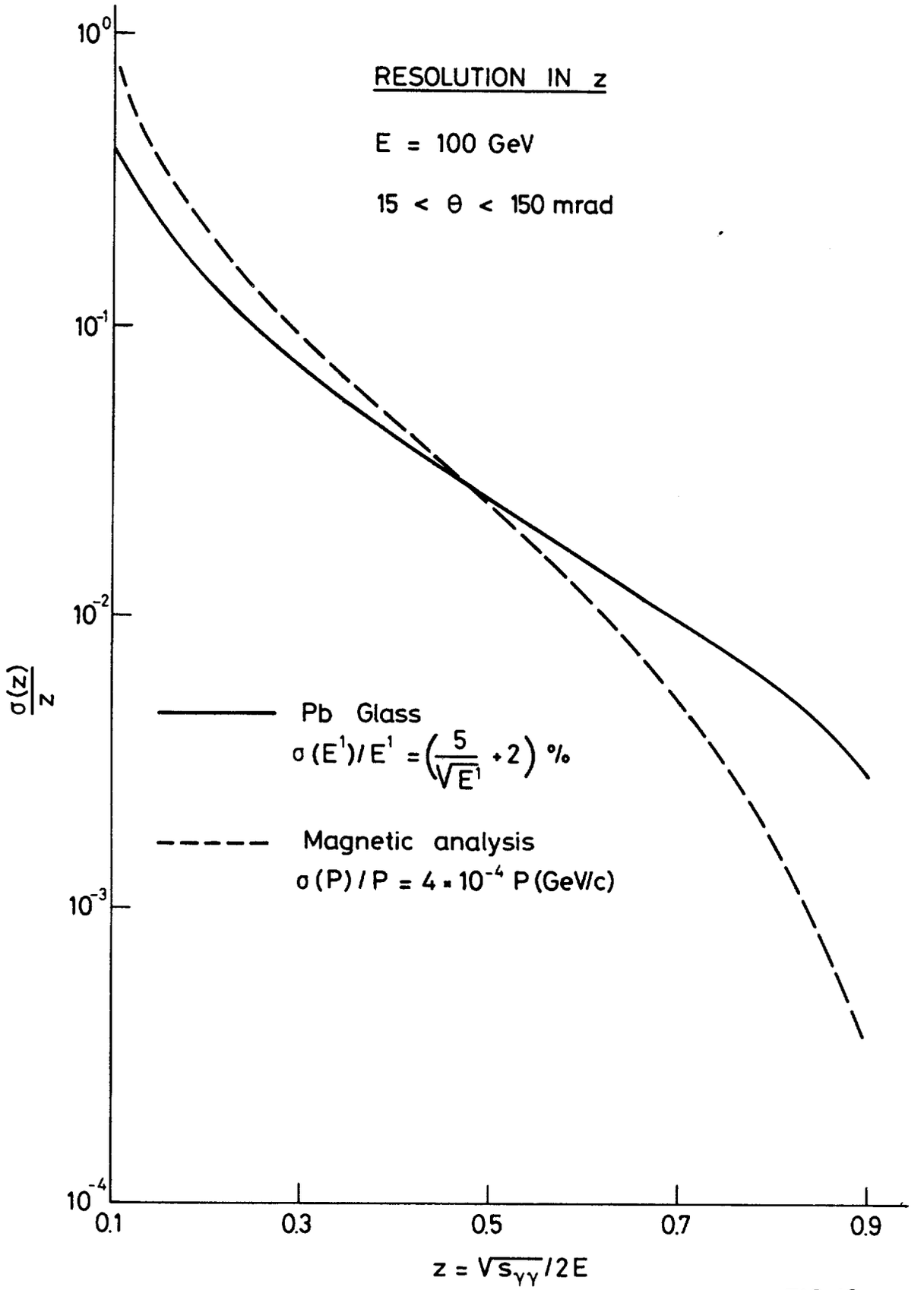
RESOLUTION IN z
E = 100 GeV
15 < θ < 150 mrad
Pb Glass
σ(E¹)/E¹ = (5/√E¹ + 2) %
Magnetic analysis
σ(P)/P = 4 • 10⁻⁴ P(GeV/c)
σ(z)/z
z = √s_γγ/2E
10⁰
10⁻¹
10⁻²
10⁻³
10⁻⁴
0.1
0.3
0.5
0.7
0.9

FIG. 10

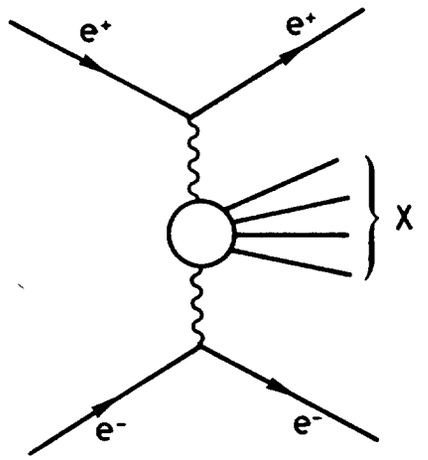

(i)

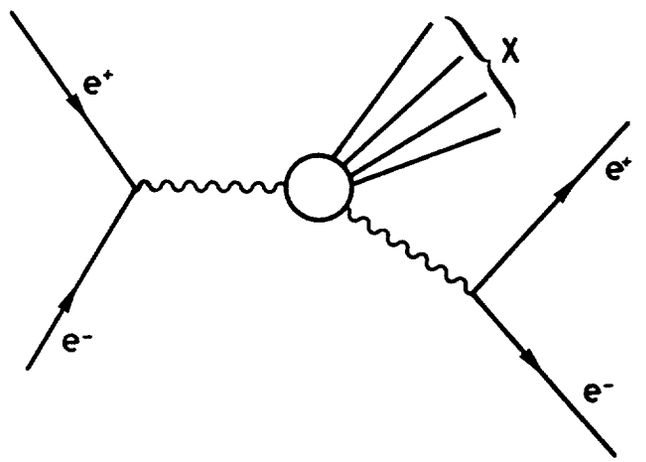

(ii)

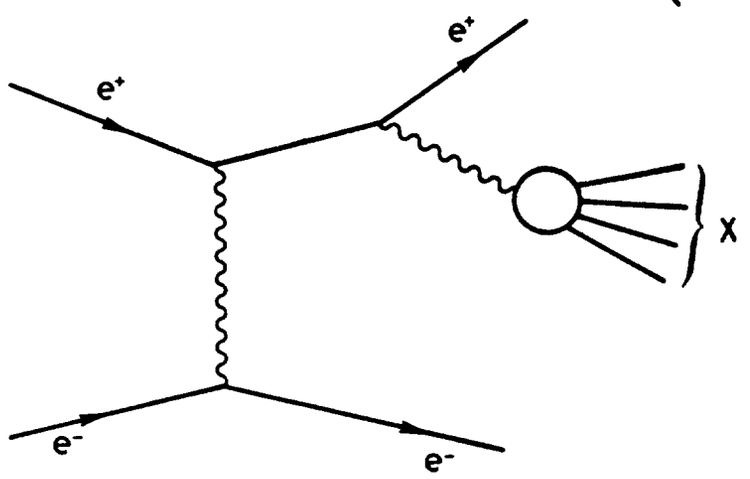

(iii)

FIG.11

VIII - SYNCHROTRON RADIATION AND BACKGROUND

H.F. Hoffmann and B. Wiik

1. INTRODUCTION

Synchrotron radiation emitted in the bending magnets and quadrupoles near or in the intersections of a large very high energy e^+e^- colliding beams machine is an important source of background to most experiments. From the experience with DORIS and SPEAR it is known that synchrotron radiation background becomes a limiting factor for experiments at higher beam energy ($\geq$ 3 GeV) and has to be overcome by masks, collimators, and weak magnets for the last bend to allow for acceptable conditions at higher energies.

In LEP we have to deal with critical energies of the synchrotron radiation, which are in the range of 300 to 400 keV and have a power line density owing to both beams of 900 watts per metre of magnetic field. Also the quadrupoles in the intersection straight section produce a similar amount of synchrotron radiation.

First of all in Section 2 we calculate the number of photons which can reach the detectors proposing a system of collimators and weak magnets, to keep this number down to tolerable levels for a realistic detector.

Owing to the high level of synchrotron radiation from the quadrupoles and the very high luminosity (100 μb^{-1} sec) envisaged in this machine, the direct interaction of the synchrotron radiation from one beam with the charged particles in the other beam via Compton scattering and pair production produces background which cannot be screened. The details are discussed in Section 3.

In Section 4 we mention briefly other sources of background, like beam gas bremsstrahlung, etc.

Thus the objective of this paper is to show that experiments can work in this environment and to give an idea of the amount of background to be envisaged. All numbers and estimates are subject to some change since the machine parameters are not yet frozen.

2. DIRECT SYNCHROTRON RADIATION FROM QUADRUPOLES AND BENDING MAGNETS

2.1 General remarks

In Fig. 1*) we show the layout of quadrupoles and bending magnets in the interaction region straight section. The $\sqrt{\beta_x}$, $\sqrt{\beta_y}$ and η-curves reflect the beam size and beam divergence.

There are nine quadrupoles between the crossing and the nearest bending magnet, which is about 300 m away. For this study a low field (10%) bending magnet is added, which is to be inserted between the Q8 and Q9 quadrupoles. The critical energy of the synchrotron radiation from this magnet is reduced from 356 keV for the 100% field magnet to 36 keV, and the radiated power per metre of magnetic field and per beam drops from 450 watts to 4.5 watts. The photon spectra of those magnets are given in Fig. 3*). Even in the case of the weak magnet there is still a very large number of "hard" photons.

In Fig. 2*) finally we show the photon spectrum emitted by the Q1 and Q2 quadrupoles integrated over the length of the quadrupoles.

2.2 Synchrotron radiation from the quadrupoles Q1, ..., Q8, Q9

In Table 1 the (1 σ) divergence[1] of the beam is noted in the Q1, ..., Q9 quadrupoles and, for completeness, in the bending magnet B1. Also shown in the table are the corresponding dimensions of the cone of synchrotron radiation in the crossing. From this it follows that, with a vacuum chamber in the intersection region of ±6.4 cm horizontal and ±3 cm vertical aperture (official aperture), only synchrotron radiation which corresponds to particles with more than (10 σ) divergence can hit the vacuum chamber in the crossing. Note that the emission angle of the synchrotron radiation with respect to the electron trajectory of $\langle\theta\rangle = m_e/E_{beam} = 1/\gamma = 5 \times 10^{-6}$ rad is negligible.

Since the photons emitted in the Q9 quadrupole are emitted at an angle of 0.56 mrad with respect to the axis of the straight section because of the 10% field magnet, they hit the vacuum chamber about 115 m downstream, 185 m upstream of the crossing point. In this place there is a collimator foreseen, which has to absorb the synchrotron radiation from the last 100% field magnet (see next section and Fig. 6). This collimator is sufficiently wide to stop the synchrotron radiation emitted in Q9.

---

*) Taken from Appendices 2 and 8.

Thus we conclude that the synchrotron radiation created in the Q1, ..., Q9 quadrupoles will not be seen by the experiments*).

2.3 Synchrotron radiation from the last bending magnet

In order to find out to what degree the synchrotron radiation must be collimated, a realistic detector is considered. Take it pessimistically to be only a gas volume (no walls) of 1 m radial dimension separated from the interaction point by a 0.02 cm thick iron sheet (thin vacuum chamber). Scaling from Fig. 4[2], where the mass attenuation coefficients for photons in copper are given, it follows that such a vacuum chamber starts to cut off below 20 keV (transmission at 20 keV: 0.3; at 15 keV: 4×10^{-4}; at 10 keV: 2×10^{-10}). Thus we rephrase the above question, asking: What is the tolerable rate of photons for energies above 15 keV? In Fig. 5 the absorption lengths for two limiting cases [argon (heavy) and methane (light)] are shown. Both gases are used in wire chambers.

Taking an average mixture between the two with λ = 2 m at 15 keV, λ = 10 m at 30 keV and λ = 50 m at 80 keV we have 50%, 10%, and 2% conversion respectively. The limit for detector d.c.-breakdown is about 10^7/sec or 2×10^7/sec incident photons at 15 keV; 10^8 photons/sec at 30 keV or 5×10^8 photons at 80 keV.

In terms of pattern recognition and reconstruction the limits are tighter. Here the question is how many conversions can be tolerated per bunch-bunch collision. The answer is somewhat arbitrary and depends on the amount of computer time available for reconstruction and on the type of event. Let us consider an event with $\sim$ 10 charged tracks giving rise to 50-100 digitizations. Pessimistically one would think that there would be a problem having more than $\sim$ 10 random conversions per bunch-bunch collision, corresponding to 4×10^6 photons/sec at 15 keV, 2×10^7 photons/sec at 30 keV and 1×10^8 photons/sec at 80 keV. Probably up to ten times more random digitizations can be accepted using the high resolution of drift chambers (off-line) or the time resolution of $\sim$ 100 nsec of proportional chambers (on-line gate). With the frequency of bunch-bunch collision of 2×10^5/sec this means, however, to work already in the d.c. breakdown limit.

---

*) The same is true for the synchrotron radiation owing to the magnetic field of the earth (critical energy: k_c = 132 eV for a vertical field component of 0.2 gauss).

The detector can be hardened by increasing the thickness of the vacuum chamber over most of the ±10 m length of the intersection region to, for example 1 mm. The transmission changes from 0.03 at 20 keV and 0.015 cm thickness to 2×10^{-10} at 0.1 cm and from 0.3 at 30 keV and 0.015 cm to 6×10^{-4} at 30 keV and 0.1 cm.

In the following one possible system of collimators is described (Fig. 6) which is somewhat optimized by trial and error. The basic idea is to keep the collimators, which screen the interaction region from the direct synchrotron radiation, as far as possible from the crossing. Then the number of photons at the detector is reduced by sheer solid angle and/or by the fact that photons only reach the experimental apparatus after several subsequent rescattering processes. This specific set of collimators imposes a constraint on the vacuum chamber within ±50 m of the crossing namely the "outer" horizontal aperture has to be $\geq$ 9 cm instead of the 6.4 cm nominal aperture in order to avoid having the direct unscattered synchrotron radiation from the 10% magnet hit the vacuum chamber downstream of the collimators at ±50 m (Fig. 6 collimators C2 and C5). A further condition is that the electron-positron beams can be adjusted horizontally with a precision of a few millimetres near the collimators to get a high efficiency in screening.

The collimators are assumed to be made of a high-Z material like tantalum or tungsten to be more effective and to correspond to a step of more than a centimetre in the vacuum chamber on the "far" side as seen from the crossing.

Back scattering from the collimators and leakage out of the inner edges were taken into account using information prepared for a similar study at DESY for PETRA[3]. There a computer program is being developed to investigate the propagation of photons in a vacuum chamber with collimators taking also multiple scattering processes on different materials and energy losses into account.

In this study photons which are scattered off the collimators into a direction not directly leading to the intersection region are neglected. These photons can reach the crossing after subsequent scatterings. The final numbers given below, however, should not change more than by a factor of two because of the distances involved. On the other hand the energy loss of about 30% photon energy per scattering was not taken into account, which shifts many photons into the energy range where the attenuation rises exponentially.

What happens at various collimators in detail is explained in Tables 2, 3 and 4.

The numbers correspond to two beams; the explanation follows Fig. 6 where only one beam entering from the right side is drawn. The set-up has to be symmetric with respect to the interaction point. Direct synchrotron radiation is drawn with full lines, scattered radiation with broken lines. About 15% of all the synchrotron radiation of the weak field magnet falls on the face towards the crossing of collimator C2. The amount of radiation back scattered through the opening at -10 m and hitting either the collimators or the vacuum chamber is given in Table 2 as well as that which is left after a second scattering. In Table 3 the leakage in the forward hemisphere out of collimator C5 is described. Of all synchrotron radiation of the weak magnet less than 7.5% hit collimator C5 in such a way that it can contribute to this effect. The number of photons which might reach the detectors is much lower than in the case described in Table 2. Finally the leakage in the forward hemisphere from collimator C6 is described in Table 4. Here about 3% of all synchrotron radiation of the full field magnet can contribute. The back scattered photons (Table 2) arrive in the crossing about 300 nsec after the bunch-bunch collision. The photons described in Table 3 and 4 arrive in coincidence with the real events.

It is beyond the precision obtained in this study to say whether or not conditions can be considered safe for all detectors after only one scattering from the collimator. In an insensitive experiment, perhaps with a "hardened" vacuum chamber, one scattering is certainly sufficient. Then a fairly small vacuum chamber with 18 to 20 cm diameter can be installed. (For circular chambers of that diameter wall-thickness can be as low as 0.2 mm of steel or titanium.)

With a second scattering, e.g. large "inside" collimators C7, C8, the situation seems to be safe for all experiments. Then the vacuum chamber would have to have a maximum diameter of 25 cm if installed slightly off-centre or 30 cm centred (corresponding minimum wall thickness for a circular chamber: 0.3 mm steel or titanium).

Another possibility to lower the amount of photons in the crossing is to split the 10% field magnet into two 5% field magnets, which should result in an improvement of another factor of five less photons compared to the 10% field magnet.

2.4 Conclusion concerning the direct synchrotron radiation

The interaction regions of LEP can be effectively screened against the synchrotron radiation from the bending magnets by means of collimators and a 10% field magnet for the last bend. This takes the properties of a sensitive detector into account.

The vacuum chamber in the intersection region has to have a horizontal aperture of +9 cm, -6.4 cm as a minimum, if photons may reach the detectors after only one scattering from collimators. In case photons have to scatter at least twice, the minimum dimensions are +9, -15 cm.

The synchrotron radiation from the quadrupoles passes easily through the standard aperture which corresponds in this case to a (10 σ) divergence of the radiation from the quadrupoles. Therefore no background is expected from this direct radiation created in the quadrupoles.

3. INTERACTION OF THE SYNCHROTRON RADIATION WITH THE OTHER BEAM

3.1 Introduction

The quadrupoles (Q1, Q2), which focus the electron and positron bunches on the intersection, also produce a large amount of synchrotron radiation. Since the synchrotron radiation is emitted nearly tangentially ($\langle\theta\rangle \approx m_e/E_{beam} = 1/\gamma \approx 5 \times 10^{-6}$) some of it is very effectively focused on the interaction point and on the other beam. So in practice, whenever two e^+e^- bunches collide, two more photon bunches also collide in coincidence. There are mainly two processes which occur with fairly large cross-sections namely:

$$\gamma e \rightarrow \gamma e \qquad \text{Compton scattering}$$

$$\gamma e \rightarrow e^+e^-e \qquad \text{pair production .}$$

The centre-of-mass energy of the photon-electron system is even high enough to allow for production of heavier particles [e.g. $\sqrt{s}$ = 1 GeV for a photon energy of 2.5 MeV which are still frequent in the photon spectrum of the quadrupoles (compare Fig. 2)]. The photon energy in the rest system of the electron rises up to 1000 GeV for laboratory energies up to $\sim$ 2.6 MeV.

3.2 Luminosity

The luminosity for the photon-electron collisions can be expressed in the following way[1]:

$$\frac{dL_{\gamma e}}{dk} = \frac{\partial N_\gamma}{\partial k \partial s} \frac{1}{f} \frac{N_e f l_Q}{4\pi n_b \sigma_x^* \sigma_y^*} F(Q)$$

with

$\frac{\partial^2 N_\gamma}{\partial k \partial s}$: synchrotron radiation spectrum of the contributing quadrupole per keV, sec and unit length of quadrupole $\left[\int_0^{l_Q} (\partial^2 N_\gamma)/\partial k \partial s)\, ds = \partial N_\gamma / \partial k \text{ of Fig. 2}\right]$

f : revolution frequency

l_Q : length of quadrupole = 3.5 m

N_e : number of electrons = 1.33×10^{13} per beam

n_b : number of circulating bunches per beam = 32

σ_x^* : horizontal r.m.s. beam radius = 0.08 mm

σ_y^* : vertical r.m.s. beam radius = 0.03 mm

$F(Q)$: geometrical correction factor describing the fraction of the total quadrupole length focusing synchrotron radiation on the other beam.

Not taking the divergence of the synchrotron light into account, we get $F(Q) = 0.03$ for Q1 and $F(Q) = 0.003$ [1] for Q2. Due to the divergence of the synchrotron light (emission angle with respect to the electron trajectory $\langle\theta\rangle = 1/\gamma_e$!) and the small vertical beam size, some of the synchrotron radiation misses the other beam. Therefore we take $F(Q) = 0.015$ for Q1 and $F(Q) = 0$ for Q2, Q3, etc. For convenience we express the luminosity in the following way:

$$\frac{dL_{\gamma e}}{dk} = \frac{\partial N_\gamma}{\partial k} \frac{1}{f N_e} F(Q) L_{e^+e^-}$$

with $L_{e^+e^-}$: luminosity of the electron positron collision = 100 μb^{-1} sec. Note that $\partial N_\gamma / \partial k$ as given in Fig. 2 is the photon spectrum for two beams.

Filling in the numbers we obtain:

$$\int_0^{10\ \mathrm{MeV}} \frac{2L_{\gamma e}}{dk}\, dk \lesssim 2\ \mu b^{-1}\ \mathrm{sec}^{-1} .$$

3.3 Compton scattering

In the rest frame of the electron, Compton scattering is described by the well-known Klein-Nishina formula (neglecting polarization):

$$\frac{d\sigma}{d\Omega} = \frac{1}{2}\left(\frac{\alpha}{m}\right)^2\left(\frac{k'}{k}\right)^2\left(\frac{k'}{k} + \frac{k}{k'} - \sin^2\theta_0\right)$$

with

$\frac{\alpha}{m}$: 2.82×10^{-13} cm

k : photon energy before the collision

k′: photon energy after the collision

θ_0: polar scattering angle of the photon in the rest frame of the electron.

The total cross-section is:

$$\sigma_{tot} = \frac{8}{3}\pi\left(\frac{\alpha}{m}\right)^2 = 665 \times 10^{-27}\ \text{cm}^2 \text{ per } \frac{k}{m_e} << 1$$

(Thomson scattering)

$$\sigma_{tot} = \pi\frac{\alpha^2}{km_e}\left[\ln\frac{2k}{m_e} + \frac{1}{2} + 0\left(\frac{m_e}{k}\ln\frac{k}{m_e}\right)\right] \text{ otherwise}$$

(Klein-Nishina)

This cross-section falls off roughly as 1/k.

3.4 Kinematics of the Compton scattering and rates

Denote variables in the laboratory frame before the collision with the index i, after the collision with the index f, and the rest frame of the electron with the index 0.

The initial states of photon and electron then are:

electron: $(e_i,\ p_i = p_{i1},\ p_{i2} = p_{i3} = 0)$

photon : $(k_i,\ k_i = k_{i1},\ k_{i2} = k_{i3} = 0)$.

and we obtain

$$k_0 = 2\gamma k_i$$

$$k_f = \frac{e_i k_0/m(1 - \beta\cos\theta_0)}{k_0/m(1 - \cos\theta_0) + 1}$$

and for $\theta_0 = 180°$

$$k_{f_{max}} = \frac{4\gamma^2 k_i}{4\gamma k_i/m + 1} \rightarrow e_i \text{ for } \frac{k_0}{m} >> 1 .$$

Remember that an electron is lost from the RF bucket in LEP having lost $\sim$ 0.5 GeV, which corresponds to $k_i \geq 3 \times 10^{-3}$ eV. Therefore Compton scattering of this type is also a beam-loss mechanism to be considered.

The relation between the scattering angle θ_0 and θ of the photon in the rest frame of the electron and the laboratory respectively is ($\theta = 0$ in the direction of the electron beam): $\tan\theta = 1/[\gamma \tan(\theta_0/2)]$.

With $\gamma = 2 \times 10^5$ we see that the photons are mostly focused in the direction of the electron beam.

In Fig. 7 the final photon energy k_f is shown versus the scattering angle θ. The curve-parameter is the initial photon energy k_i. In Fig. 8 the total photon rate integrated over the azimuth and the synchrotron radiation photon spectrum versus the scattering angle θ are given. The large photon energies and the high rates occur only at very small angles and should not present a problem. The scattered electrons however appear also at larger angles. The energy of the scattered electron versus its scattering angle for various initial photon energies is shown in Fig. 9. Finally in Fig. 10 the total electron rate versus the polar angle θ_e of the electron in the laboratory frame is given. The scattering angles θ_e correspond to two electron energies at a fixed photon energy.

The total rate due to Compton scattering is below 30 kHz.

3.5 Pair production*)

The total cross-section for pair production in an electron field is shown in Fig. 11[4]. Above $k_0 \geq 20$ MeV photon energy the cross-section rises as $\ln k_0$ and can be described approximately:
$\sigma_{tot}(k_0) = (1.8 \ln k_0 - 2.22)$ [5] mbarn for $k_0 \gtrsim 20$ MeV and k_0 in MeV.

The angular distribution of the electrons[6] with respect to the incident γ-ray in the relativistic case ($k_0 >> m_e$) in the rest frame of the electron is

$$\frac{d\Omega}{d\Omega_0} = A \frac{\theta_0}{\left[\theta_0^2 + (m_e/k_0)^2\right]^2} \left[\ln\left(1 + \frac{\theta_0^2 m_e^2}{k_0^2}\right) + B\right] .$$

---

*) Notation as for Compton scattering.

Since we are only interested in very general features, we shall only assume symmetrical pair production and not consider momentum transfer to the electron. The real dependence of the cross-section on the momentum transfer is given in Fig. 12[4]. These considerable simplifications do not play an important role for the final result since we integrate over many different initial photon energies. Therefore, we simply write a differential cross-section integrated over the azimuthal angles as follows (rest frame of the electron)

$$\frac{d\sigma}{d\theta_0} = \sigma_{tot}(k_0)g(k_0) \frac{\theta_0}{\left[\theta_0^2 + (m_e/k_0)^2\right]^2}$$

with $g(k_0)$ defined by $\int_0^\pi d\sigma/d\theta_0 \, d\theta_0 = \sigma_{tot}(k_0)$.

3.6 Kinematics and rates

Let the direction $\theta = 0$ of the scattering angle θ in the laboratory frame be the direction of the incident electron and let the direction $\theta_0 = 0$ in the rest frame of the electron be the direction of the incident photon. Then the relation between θ and θ_0 is

$$\tan \theta = \frac{\sin \theta_0}{\gamma(\beta/\beta_0 - \cos \theta_0)} \, .$$

γ and β refer to the "beam" electron and β_0 is the velocity of the produced electron in the rest frame of the "beam" electron. For $\beta_0 < \beta$ the angle θ is limited to values below 90° and to each angle θ correspond two angles θ_0 and two electron energies. For $\beta_0 > \beta$ the electrons can appear in the full range from 0° to 180° degrees. Thus in practice the electron pairs, even produced into a direction opposite to the direction of the electron beam, are turned around by the Lorentz-transformation and focused into the beam direction up to rather high photon energies. This is also the reason why even a very crude model of pair production already gives a realistic idea of the background condition.

For an energy e_0 of the produced electron of $e_0 = \frac{1}{2} k_0$ in Fig. 13 the laboratory energy of the produced electrons is plotted versus its laboratory angle. The curve-parameters are the initial photon energies.

Finally in Fig. 14 the rate of electrons integrated over the azimuthal angle and the photon spectrum versus the polar angle of the electrons is

indicated. The total rate remains below 20 kHz. Mostly the energy loss of the beam electron is small and it is not lost from the beam. Those which are lost appear in the same way as electrons which have undergone beam-gas bremsstrahlung (see Section 4).

3.7 Summary of Section 3

In Table 5 the synchrotron radiation spectrum is transformed into the rest frame of the electron and into the c.m. frame. The corresponding luminosities $L_{\gamma e}(k_i)$, the cross-sections and rates are noted.

Most of the Compton-scattered electrons and photons occur at very small angles and will be invisible to experiments. The pair-produced electrons appear with a higher rate at larger angles.

These processes fortunately do not limit the lifetime of the beams in LEP. They present some problems to the $\gamma\gamma$-type of experiments.

4. OTHER BACKGROUND IN THE INTERSECTION

4.1 Beam gas bremsstrahlung[7)]

The mechanism of beam gas bremsstrahlung loss is that an electron looses enough energy in a collision with the gas to be lost from the energy acceptance of the RF system. It will drift away from the bunch over probably several orbital periods until it strikes a physical aperture. The loss rate is given by

$$\frac{dn}{ndx} = \frac{\rho}{x_0} \ln \frac{E}{\Delta E} = \frac{\ln E/\Delta E}{x_0} \frac{MP}{RT}$$

in which

$\Delta E/E$: energy acceptance of LEP = 5×10^{-3}

x_0 : radiation length of the most dangerous gas species thought to be present, namely CO = 38.5 g/cm^2

M : molecular weight = 28 g/mole

P : partial pressure of CO = 5×10^{-9} Torr.

Then we have:

$$\frac{-dn}{ndx} = 2.25 \times 10^{-14} \text{ p (in } 10^{-9} \text{ Torr)/metre}$$

and with the number of particles circulating (2 beams) we get

$$n = N(\text{number of beam particles}) \times f \text{ (revolution frequency)}$$

$$= 2.6 \times 10^{13} \times 6.7 \times 10^{7} \approx 2 \times 10^{17}$$

and

$$\frac{dn}{dx} = 2 \times 10^{4}/\text{m}\cdot\text{sec} \ .$$

These electrons nearly carry 100 GeV energy and effective collimators of high-Z material and $\sim$ 20 radiation lengths thickness should be foreseen in places where they are going to hit the aperture. This can be calculated once more details are known about LEP. It would certainly be interesting to stop them far away from the intersections. The bremsstrahlung photons produced near the interaction region are, except for their energy, comparable to the synchrotron radiation photons. They will be stopped in a similar way in the collimators described in Section 2.

4.2 Background related to pressure in the interactions and near-by

In order to avoid Compton scattering of the about 10^{17} photons from the quadrupoles in the energy range of 10 to 100 keV which traverse the intersection, the pressure there and in the environs should be lower than in the rest of the machine.

The same applies to electro-production by electrons on the rest gas which might fake events with missing leptons.

A pressure below 10^{-10} Torr would be desirable.

We wish to thank our colleagues D. Coward (SLAC/CERN), H. Fischer (CERN) and D. Trines (DESY) for many discussions and their advice.

REFERENCES

1) E. Keil (CERN), private communication.

2) R.D. Evans, Handbuch der Physik, 34, 218 (1958).

3) D. Trines (DESY), private communication. The report on synchrotron radiation problems at PETRA will be published soon.

4) J.W. Motz, H.A. Olsen, H.W. Koch, Revs. Mod. Phys. 41, 581 (1969).

5) T.M. Knasel, The total pair production cross-section in hydrogen and helium (Parts I and II), DESY 70-2 and 70-3 (1970).

6) W. Heitler, The quantum theory of radiation (3rd edition) (Clarendon Press, Oxford, 1954).

7) e-p Working Group, Some preliminary remarks about LSR e-p interaction regions, internal report CERN ISR-GS/75-33 (1975).

Table 1

Beam divergence in machine elements near the crossing

Machine component	(1 σ) divergence (mrad)		Size in crossing (cm)	
	Horiz.	Vert.	Horiz.	Vert.
Q1	7×10^{-2}	2×10^{-1}	0.1	0.2
Q2	2×10^{-1}	2×10^{-1}	0.3	0.3
⋮	⋮	⋮	⋮	⋮
Q9	2×10^{-2}	1×10^{-2}	0.6	0.3
B1	2×10^{-2}	1×10^{-2}	0.7	0.3

Table 2

Reduction of the number of photons*) by collimator C2 (Fig. 6)

Energy range	$k_{average}$	Number of photons (15% of total weak field magnet)	back scattered into $90° \leq \theta \leq 180°$	reaching the interaction region at ±10 m		remaining after second back scattering from C3, C4, C7, C8	
in keV	in keV	per sec	per sec	per sec	per bunch-bunch collision	per sec	per bunch-bunch collision
1-20	10	2×10^{16}	0	0	0	0	0
20-60	40	8×10^{15}	2×10^{13}	5×10^{7}	250	2×10^{5}	0.5
60-140	100	2×10^{15}	9×10^{12}	3×10^{7}	100	1×10^{5}	0.5
140-260	200	2×10^{14}	1×10^{14}	2×10^{6}	20	2×10^{4}	0.1
260-340	300	3×10^{13}	3×10^{13}	1×10^{6}	10	1×10^{4}	0.1
340-660	500	1×10^{11}	2×10^{9}	3×10^{3}	2×10^{-2}	10^{2}	10^{-3}

*) These photons arrive 300 nsec after the bunch-bunch collision.

Table 3

Forward leakage of photons*) out of collimator C5

Energy range	$k_{average}$	Number of photons (7.5% of total weak field magnet)	leaking out in the forward direction	reaching the interaction region at ± 10 m	
in keV	in keV	per sec	per sec	per sec	per bunch-bunch collision
1-20	10	1×10^{16}	0	0	0
20-60	40	4×10^{15}	$< 10^{7}$	10^{2}	0
60-140	100	1×10^{15}	7×10^{9}	4×10^{4}	0.2
140-260	200	1×10^{14}	3×10^{11}	2×10^{6}	5
260-340	300	2×10^{13}	2×10^{11}	1×10^{6}	3
340-660	500	5×10^{10}	7×10^{9}	4×10^{4}	0.2

*) These photons arrive in coincidence with the bunch-bunch collision.

Table 4

Forward leakage of photons out of collimator C6

Energy range	$k_{average}$	Number of photons (3% of total full field magnet)	leaking out in the forward direction	reaching the interaction region at ±10 m	
in keV	in keV	per sec	per sec	per sec	per bunch-bunch collision
20-60	40	2×10^{15}	0	0	0
60-140	100	2×10^{15}	$< 2 \times 10^{7}$	5	0
140-260	200	2×10^{15}	$< 2 \times 10^{9}$	400	2×10^{-3}
260-340	300	1×10^{15}	4×10^{10}	8×10^{3}	4×10^{-2}
340-660	500	8×10^{14}	1×10^{13}	2×10^{6}	10
660-1340	1000	4×10^{14}	1×10^{13}	2×10^{6}	10
1340-2660	2000	5×10^{13}	2×10^{12}	4×10^{5}	2

Table 5

Summary of the interactions of synchrotron radiation with the other beam

Initial photon energy: k_i (keV)	Photon energy in the rest frame of the electron: k_0 (GeV)	c.m. energy (MeV)	$L_{\gamma e}$ (cm^{-2} sec^{-1})	$\sigma_{Compton}$ (mb)	Compton rate (sec^{-1})	σ_{pair} (mb)	Pair rate (sec^{-1})
$(0\text{-}1) \times 10^{-3}$	$(0\text{-}0.2) \times 10^{-3}$	0-0.8	4×10^{28}	400	15000	-	-
$(1\text{-}10) \times 10^{-3}$	$(0.2\text{-}2) \times 10^{-3}$	0.8-2.2	4×10^{28}	100	4000	< 0.5	10
$(10\text{-}100) \times 10^{-3}$	$(2\text{-}20) \times 10^{-3}$	2.2-6.4	9×10^{28}	100-20	5200	0.5-2.4	100
$(100\text{-}1000) \times 10^{-3}$	0.02-0.2	6.4-20	1.9×10^{29}	20-4	2000	2.4-7.3	900
1-10	0.2-2	20-63	4×10^{29}	4-1	1000	7.4-11.5	3200
10-30	2-6	63-110	2.8×10^{29}	2×10^{-1}	150	11.5-13	3400
30-100	6-20	110-200	3.2×10^{29}	8×10^{-2}	90	13-16	4500
100-300	20-60	200-350	2.2×10^{29}	$(8 \times 10^{-2})\text{-}(3 \times 10^{-2})$	10	16-17.6	3700
300-1000	60-200	350-630	3×10^{28}	$(3 \times 10^{-2})\text{-}10^{-2}$	1	17.6-19.7	600
$(1\text{-}3) \times 10^{3}$	200-600	630-1100	3×10^{27}	$10^{-2}\text{-}(3 \times 10^{-3})$	2×10^{-2}	19.7-21.7	60
$(3\text{-}10) \times 10^{3}$	600-2000	1100-2000	5×10^{24}	$(3 \times 10^{-2})\text{-}10^{-3}$	10^{-5}	21.7-24	0.1
Integrated rates:			1.6×10^{30}		< 30000		< 20000

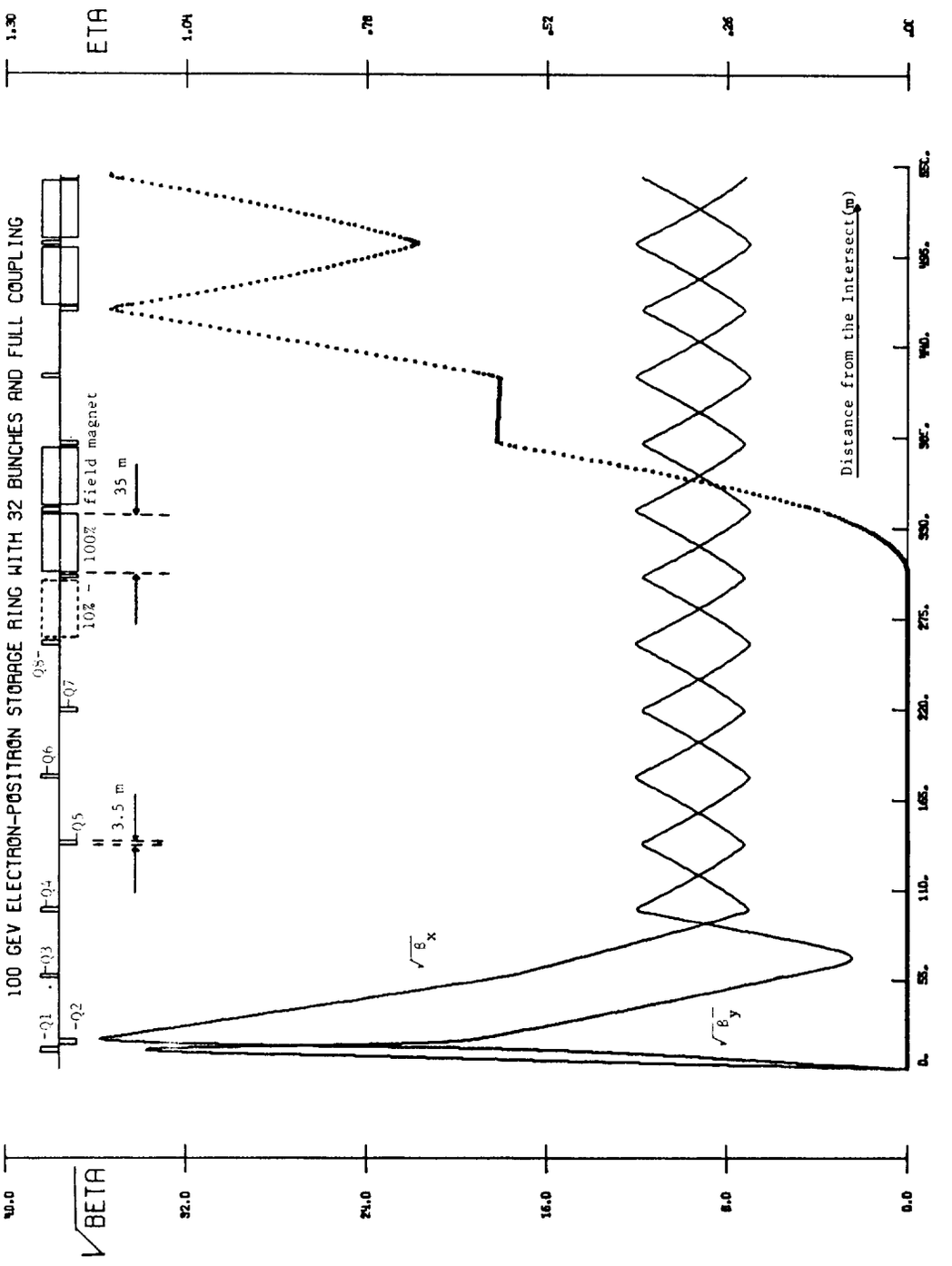
100 GEV ELECTRON-POSITRON STORAGE RING WITH 32 BUNCHES AND FULL COUPLING
ETA
BETA
Q1
Q2
Q3
Q4
Q5
Q6
Q7
Q8
3.5 m
35 m
100% field magnet
10%
Distance from the Intersect(m)

Fig. 1

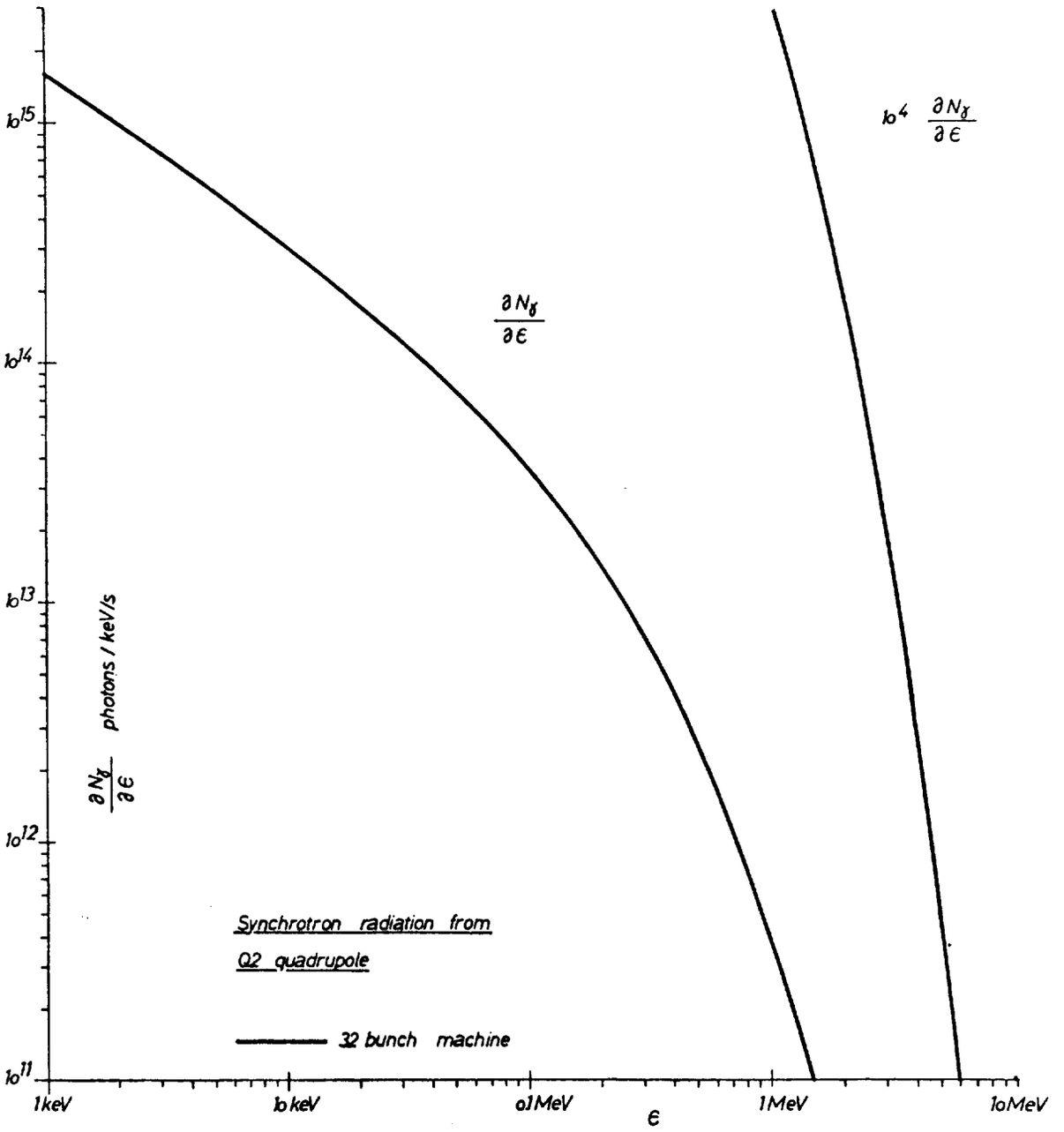
10^{15}
10^{14}
10^{13}
10^{12}
10^{11}
$\frac{\partial N_\gamma}{\partial \epsilon}$ photons / keV/s
$10^4 \frac{\partial N_\gamma}{\partial \epsilon}$
$\frac{\partial N_\gamma}{\partial \epsilon}$
Synchrotron radiation from
Q2 quadrupole
32 bunch machine
1keV
10keV
0.1MeV
1MeV
10MeV
ϵ

Fig. 2

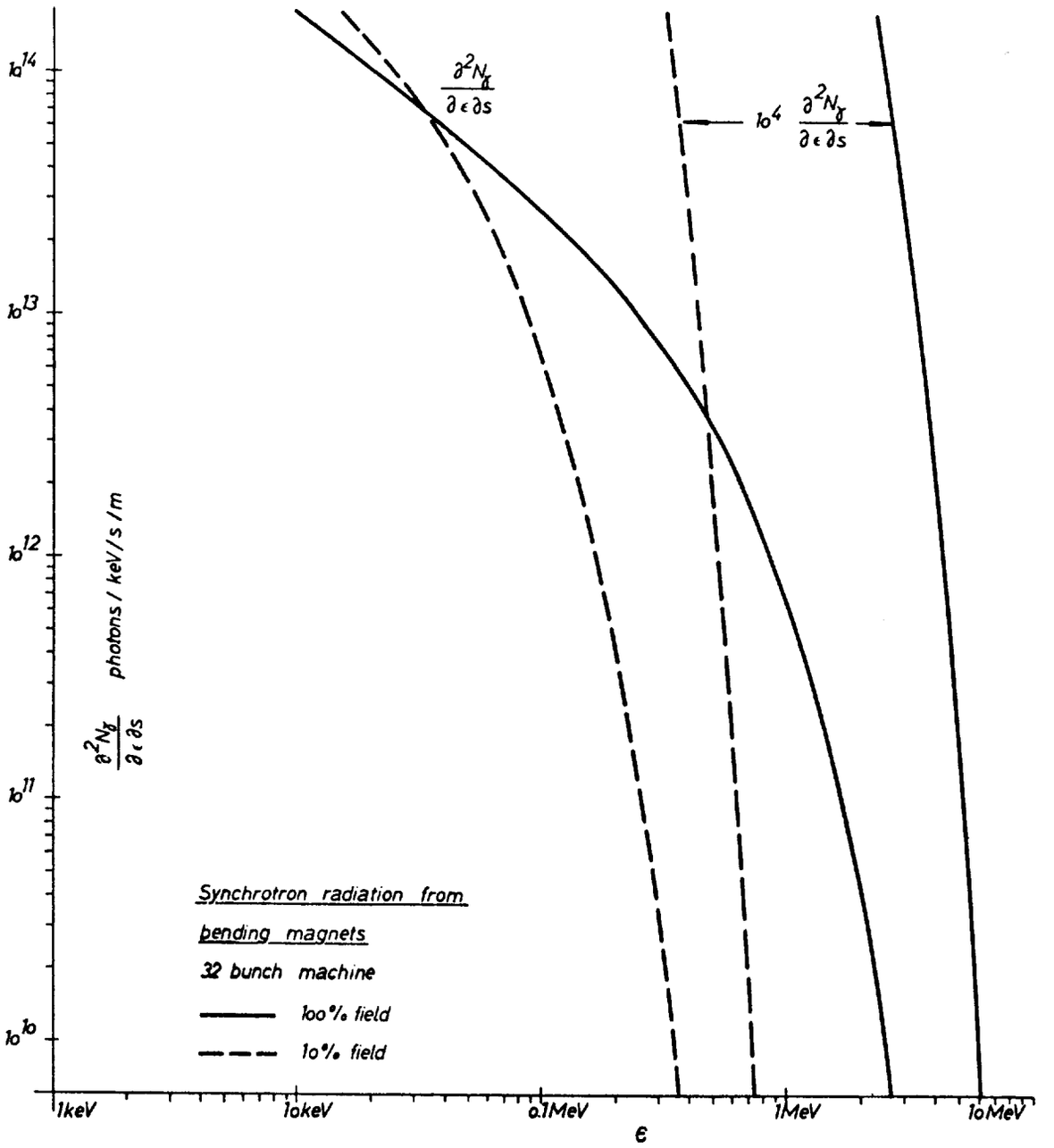
10^{14}
10^{13}
10^{12}
10^{11}
10^{10}
$\frac{\partial^2 N_\gamma}{\partial \epsilon \partial s}$ photons / keV / s / m
$\frac{\partial^2 N_\gamma}{\partial \epsilon \partial s}$
$10^4 \frac{\partial^2 N_\gamma}{\partial \epsilon \partial s}$
Synchrotron radiation from
bending magnets
32 bunch machine
100% field
10% field
1keV
10keV
0.1MeV
1MeV
10MeV
ϵ

Fig. 3

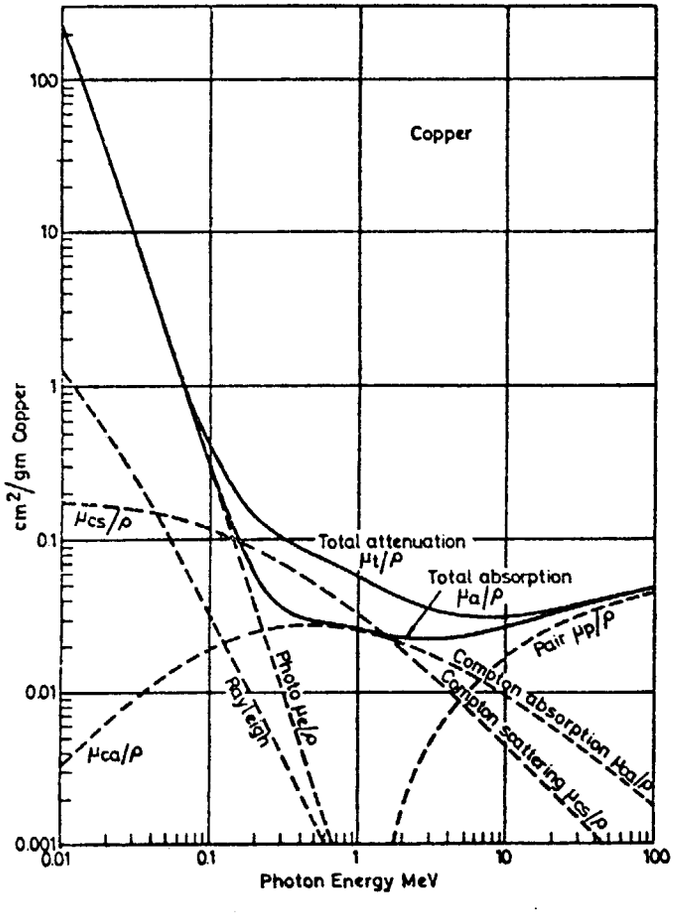

Mass attenuation coefficients for photons in copper. $\rho = 8.92$ gm/cm^3.

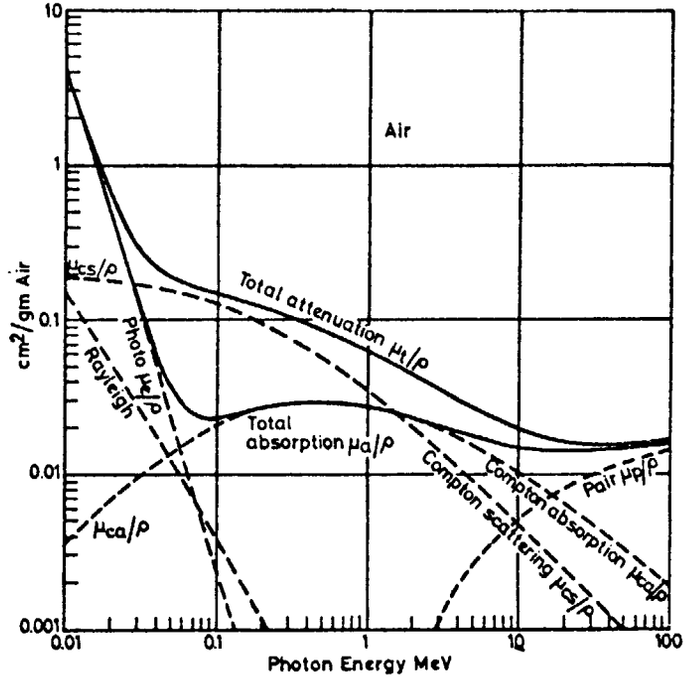

Mass attenuation coefficients for photons in air. At NTP the density of air $\rho = 0.001293$ gm/cm^3.

Fig. 4

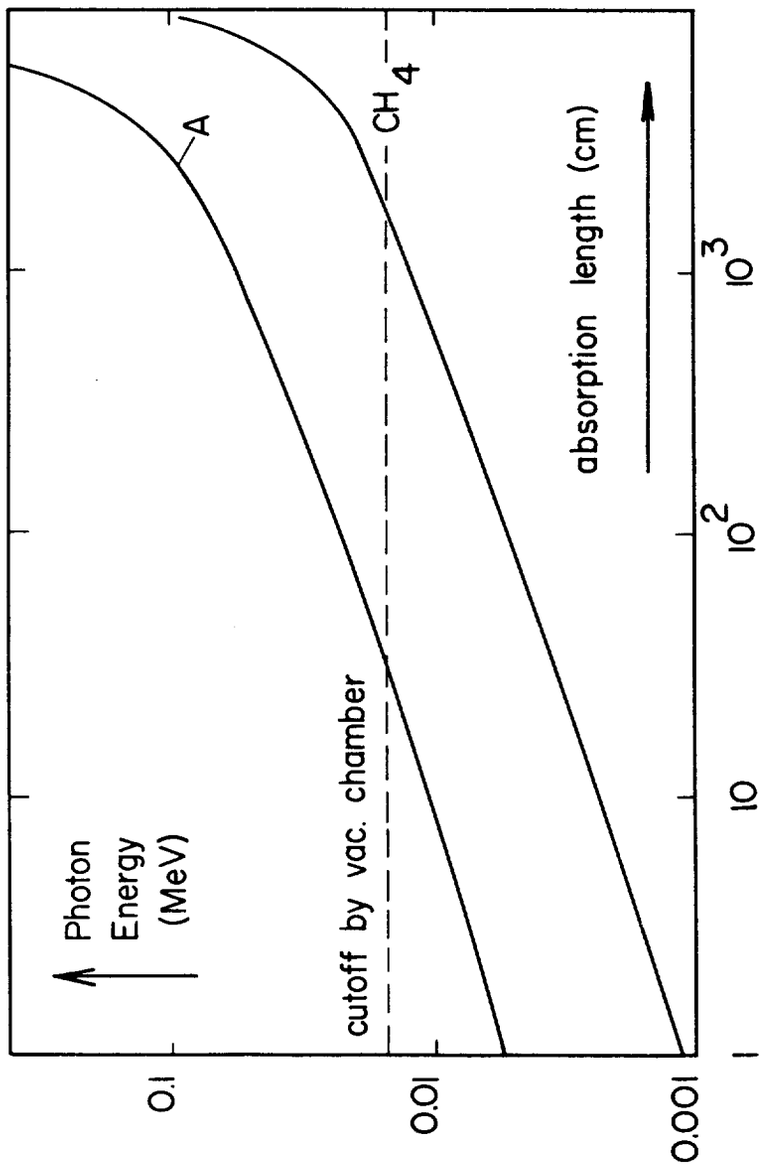

Absorption Lengths in a Detector Gas

Fig. 5

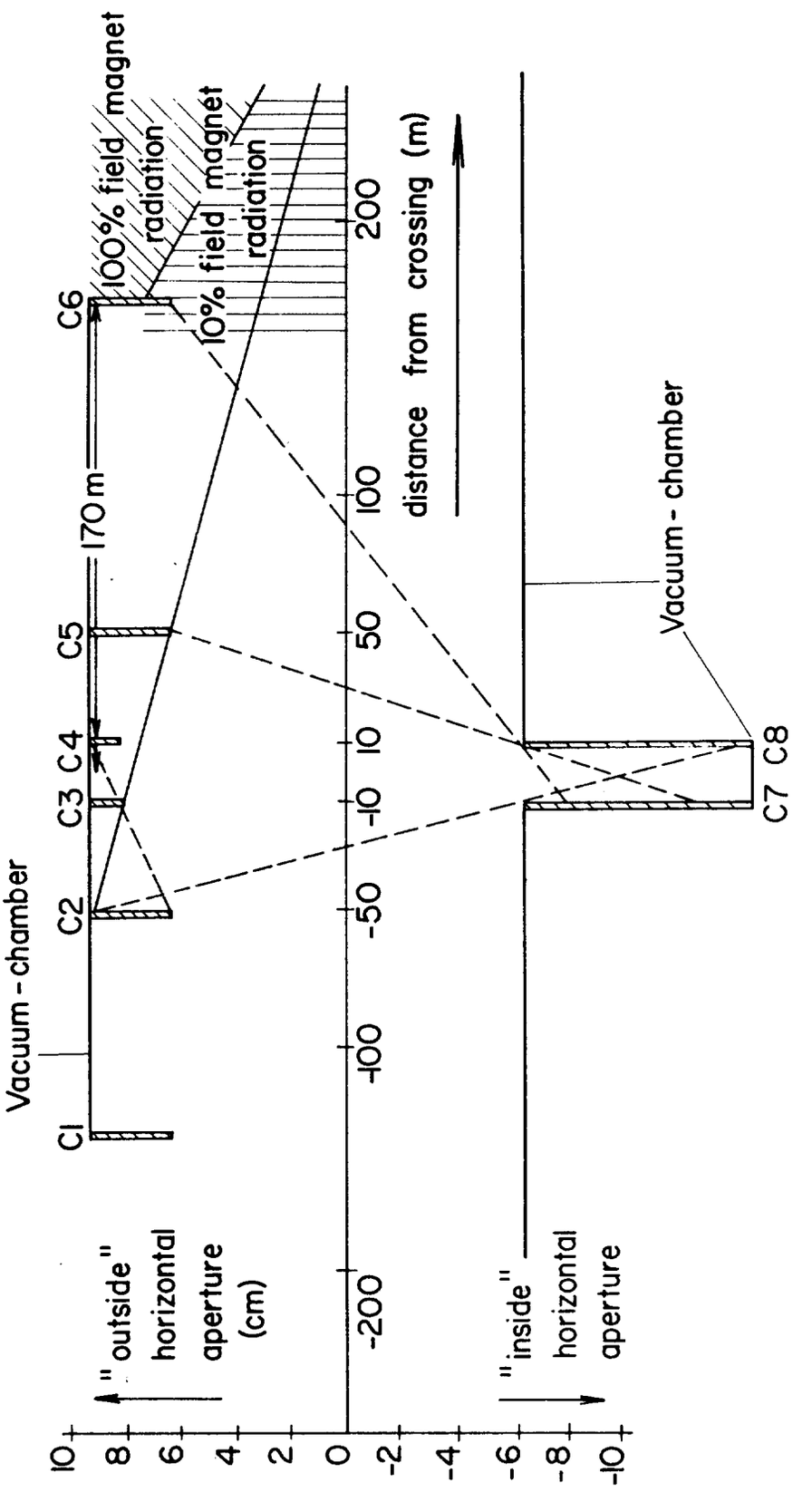

Layout of Collimators in the horizontal Plane

Fig. 6

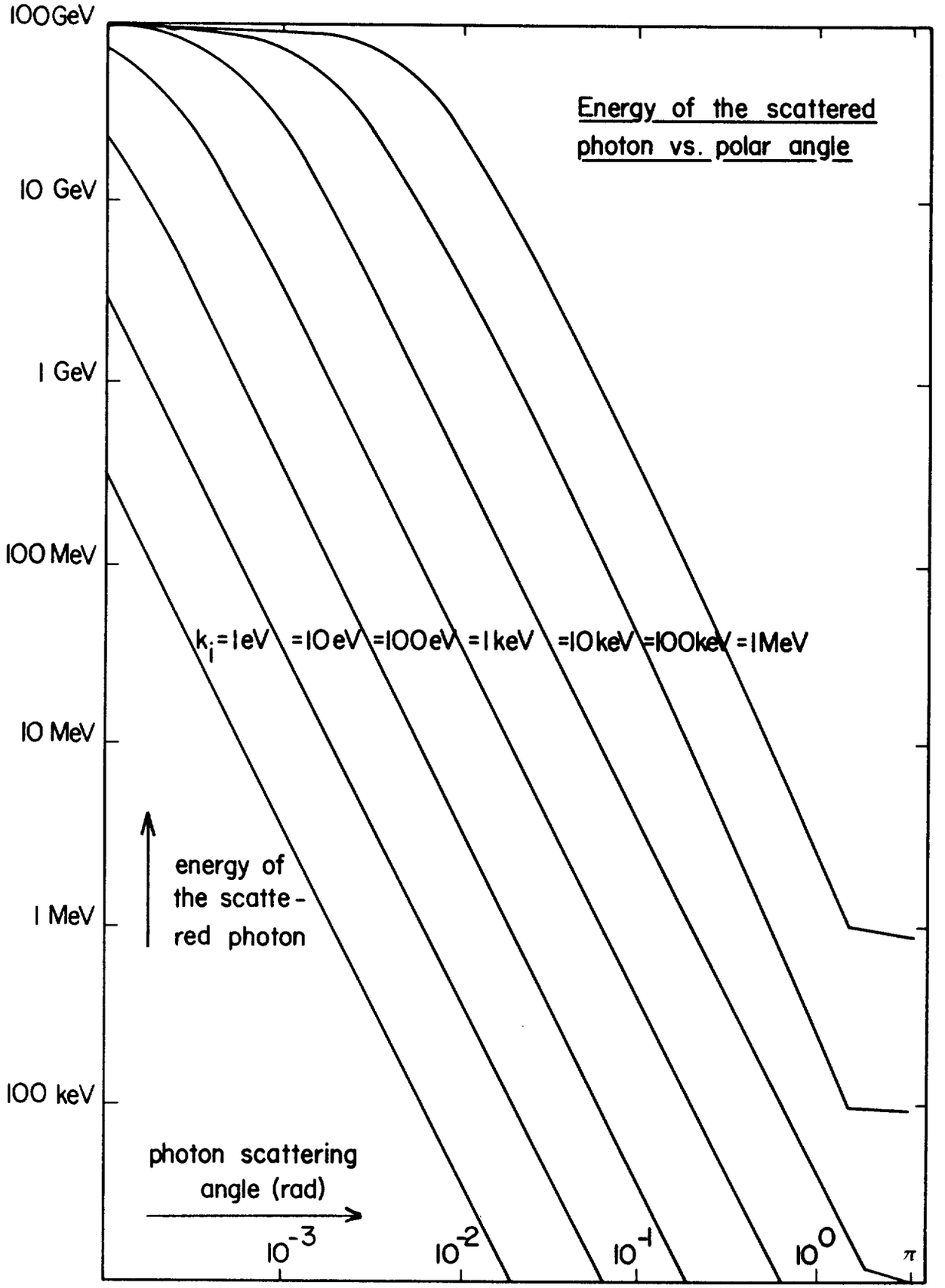
100 GeV
10 GeV
1 GeV
100 MeV
10 MeV
1 MeV
100 keV
Energy of the scattered photon vs. polar angle
k_i = 1eV = 10eV = 100eV = 1keV = 10keV = 100keV = 1MeV
energy of the scatte-red photon
photon scattering angle (rad)
10^{-3}
10^{-2}
10^{-1}
10^{0}
π

Fig. 7

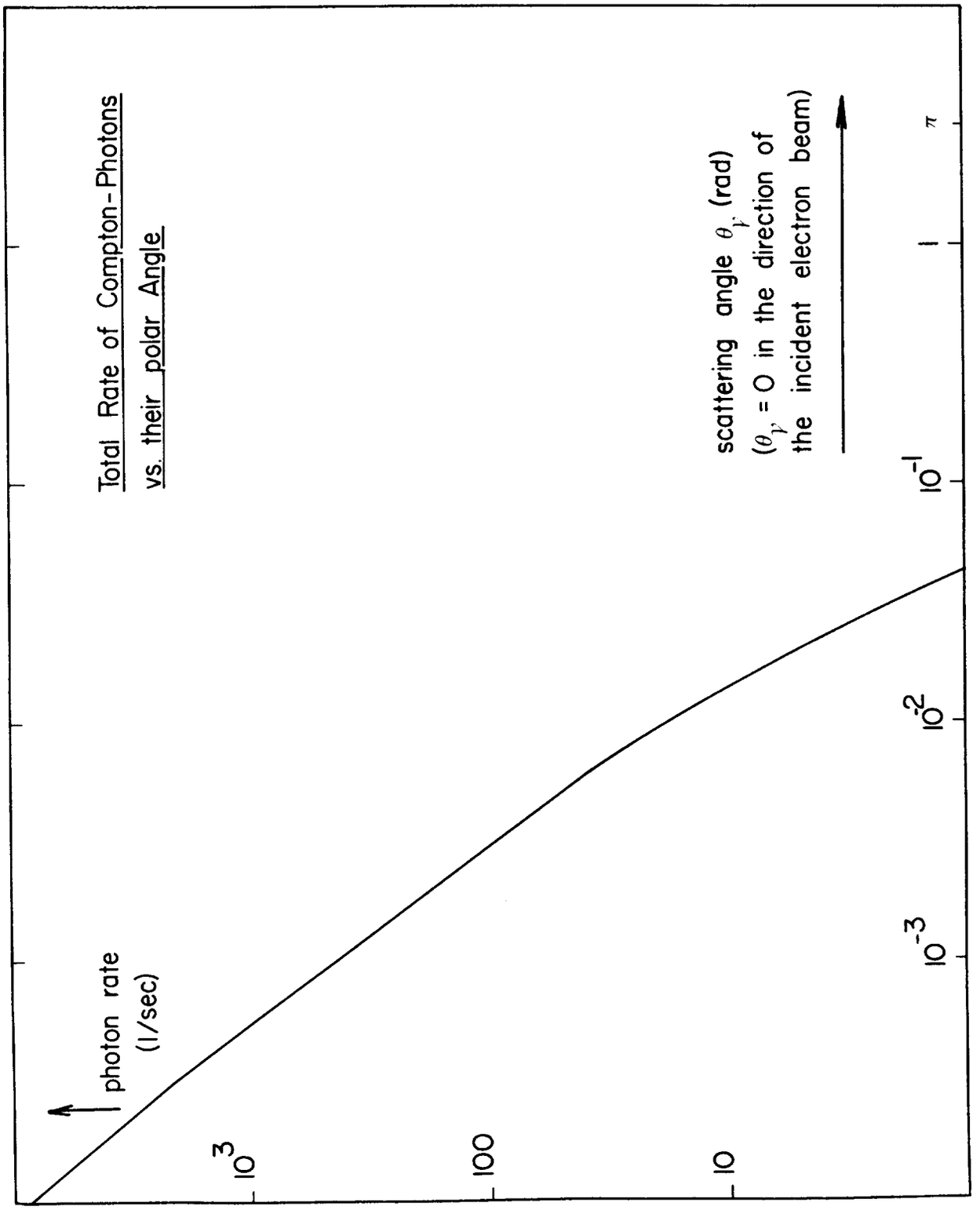
Total Rate of Compton-Photons
vs. their polar Angle
photon rate
(1/sec)
10^3
100
10
10^{-3}
10^{-2}
10^{-1}
1
π
scattering angle θ_γ (rad)
(θ_γ = 0 in the direction of
the incident electron beam)

Fig. 8

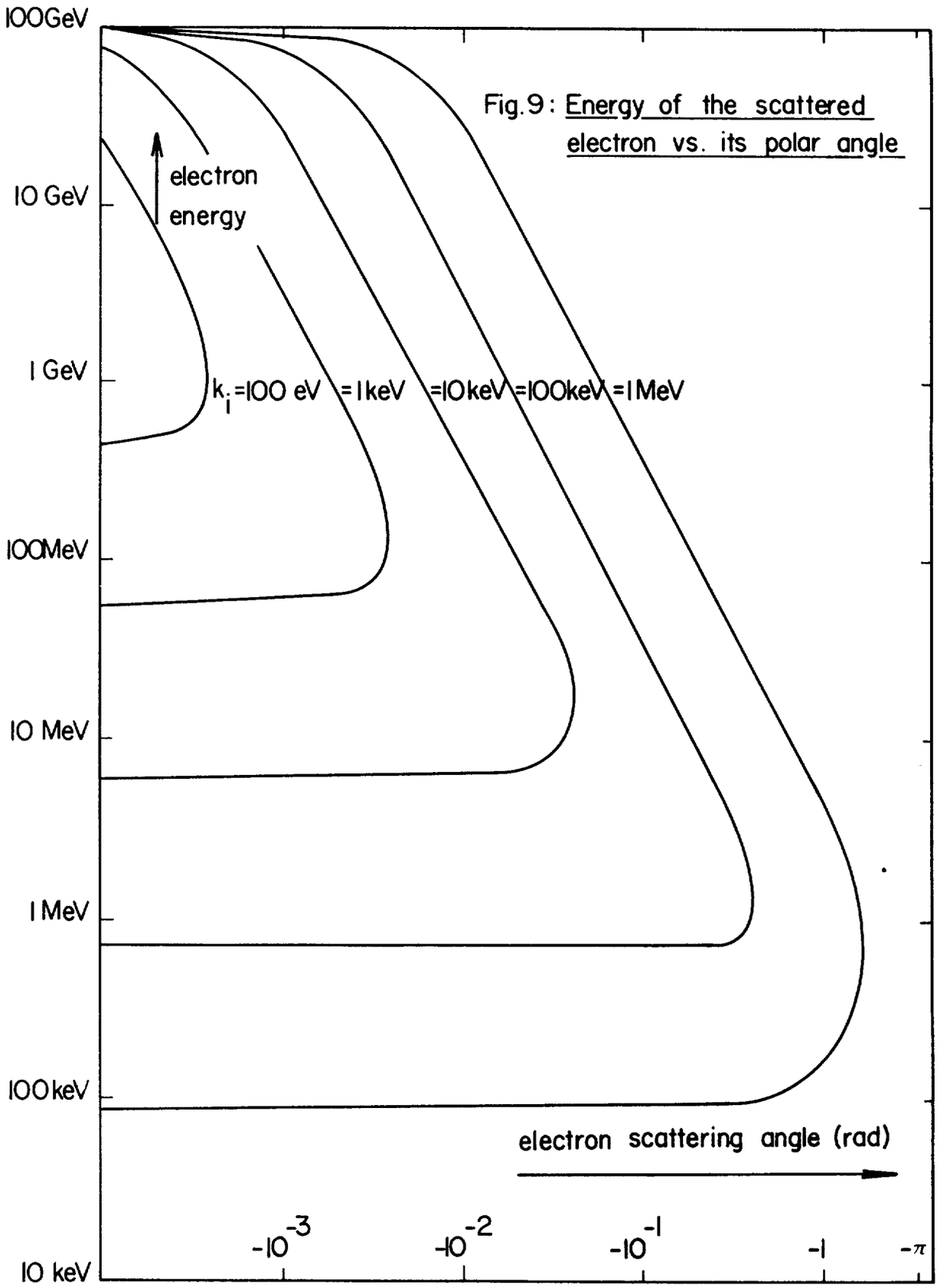

Fig.9: Energy of the scattered electron vs. its polar angle

Fig. 9

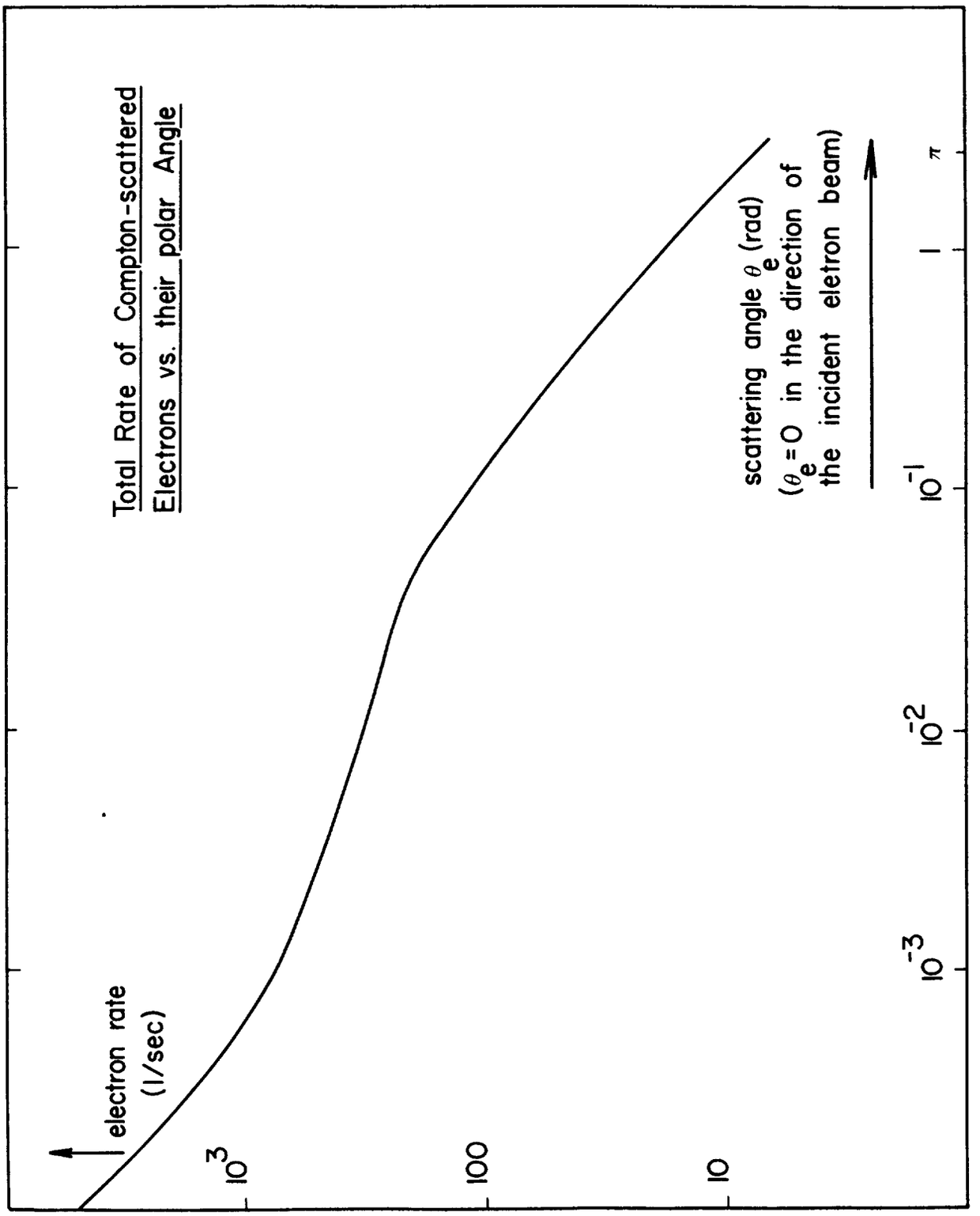
Total Rate of Compton-scattered Electrons vs. their polar Angle
electron rate (1/sec)
10^3
100
10
10^{-3}
10^{-2}
10^{-1}
1
π
scattering angle θ_e (rad)
(θ_e=0 in the direction of the incident eletron beam)

Fig. 10

Cross section for pair production in an electron field (solid line) and proton field (dashed line). Note that the photon energy is given in MeV and is equal to 0.511 k.

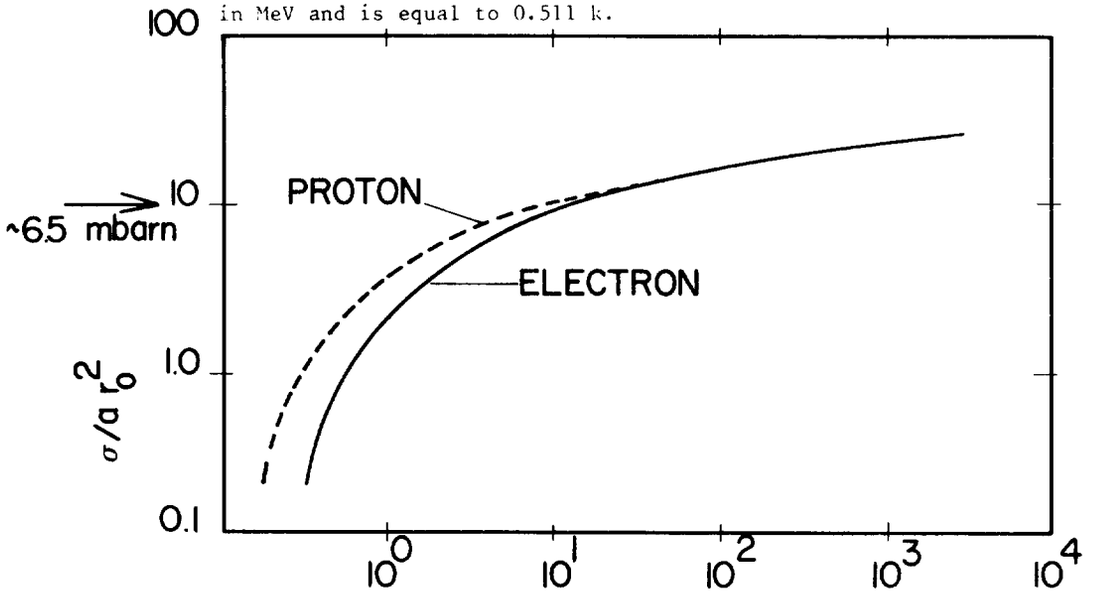

Fig. 11

Dependence of the triplet differential cross section dσ/dq on the momentum q of the recoiling electron for values of the photon energy k equal to 1000, 100, 50 and 20.

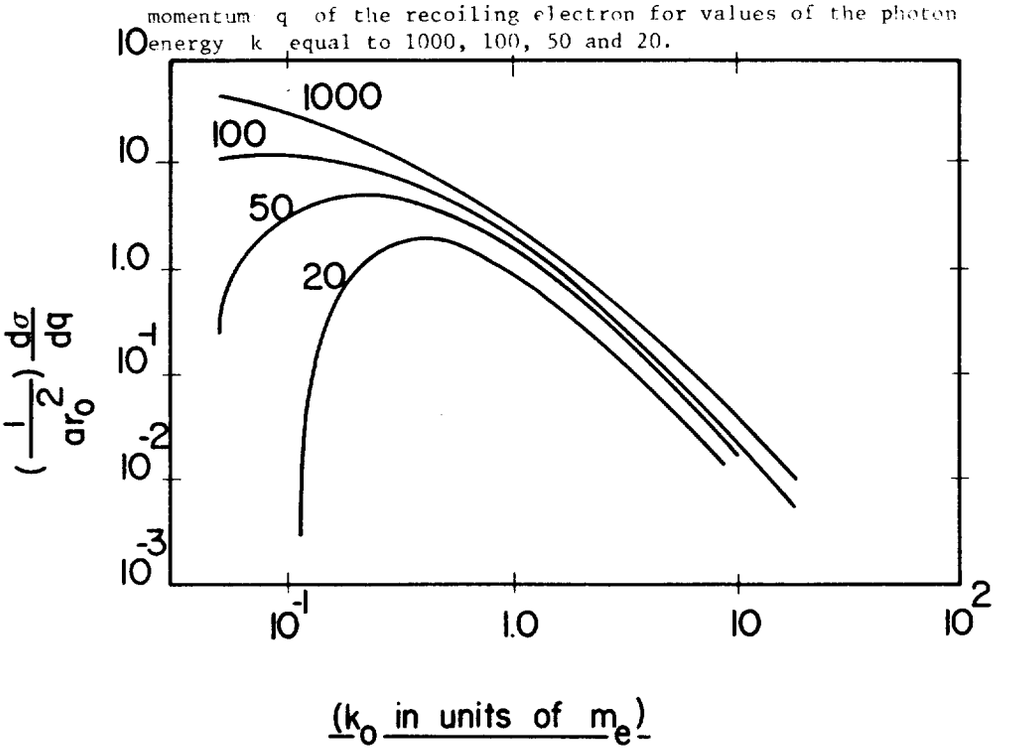

Fig. 12

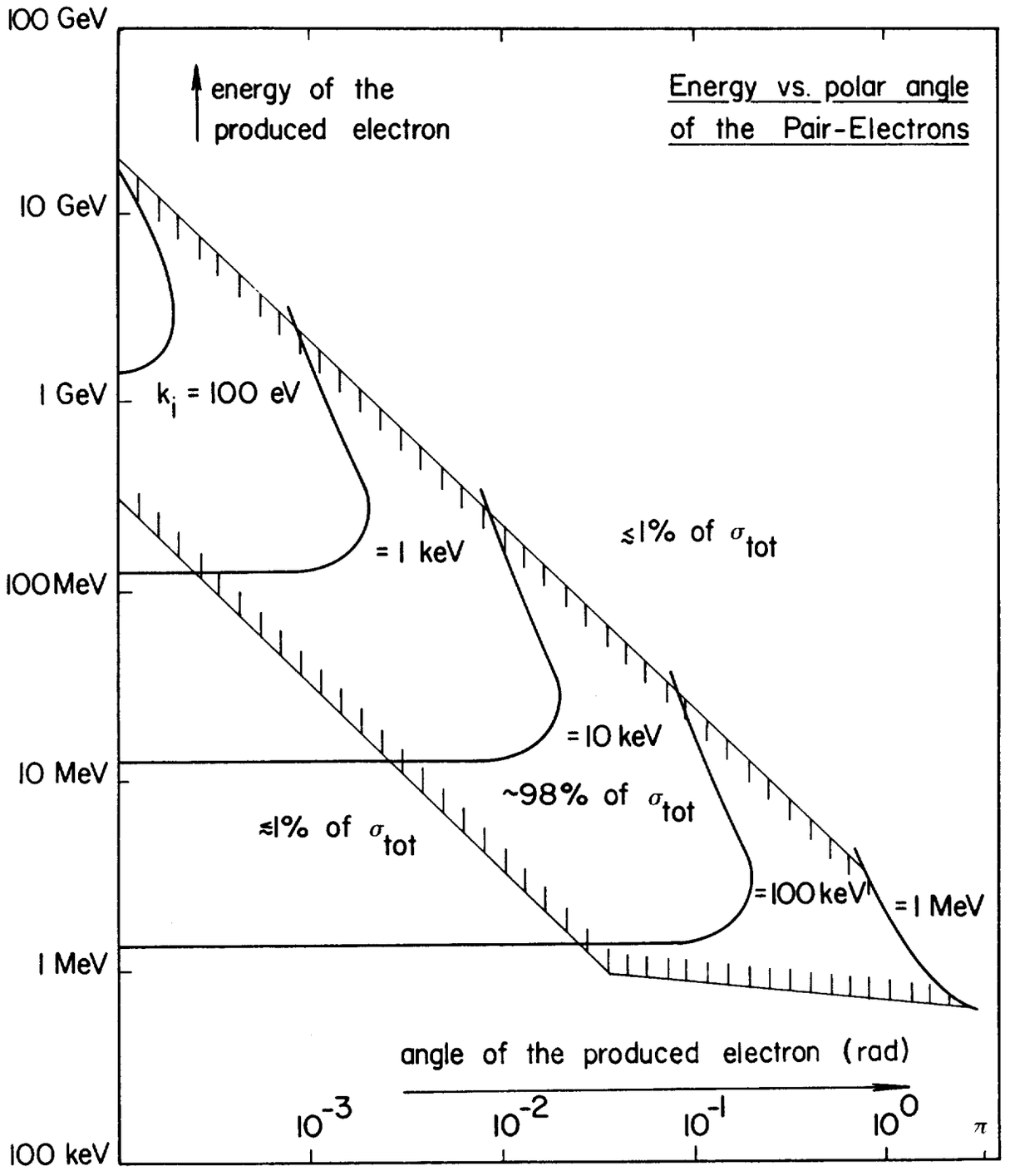
100 GeV
10 GeV
1 GeV
100MeV
10 MeV
1 MeV
100 keV
energy of the produced electron
Energy vs. polar angle of the Pair-Electrons
k_i = 100 eV
= 1 keV
≲1% of σ_{tot}
= 10 keV
~98% of σ_{tot}
≲1% of σ_{tot}
= 100 keV
= 1 MeV
angle of the produced electron (rad)
10^{-3}
10^{-2}
10^{-1}
10^{0}
π

Fig. 13

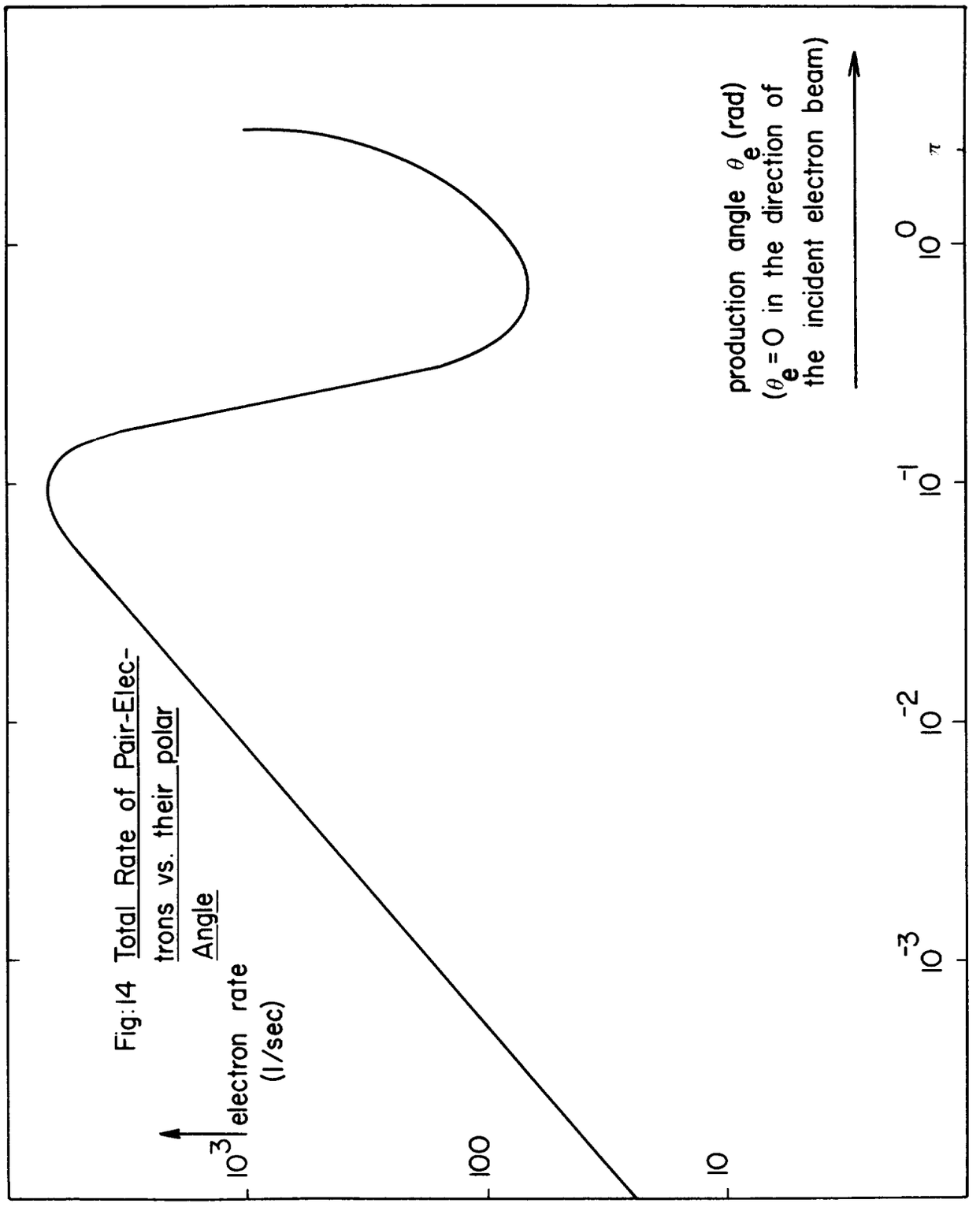
Fig:14 Total Rate of Pair-Electrons vs. their polar Angle
electron rate (1/sec)
10^3
100
10
10^{-3}
10^{-2}
10^{-1}
10^0
π
production angle θ_e (rad)
(θ_e=0 in the direction of the incident electron beam)

Fig. 14

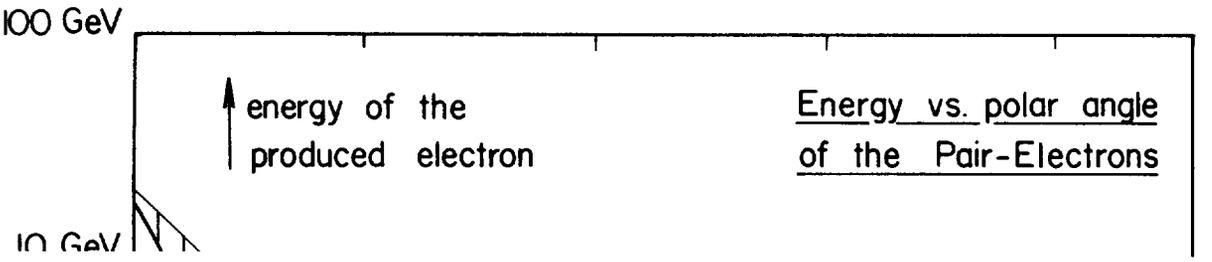
100 GeV
energy of the
produced electron
Energy vs. polar angle
of the Pair-Electrons
10 GeV

APPENDIX 1

EUROPEAN ORGANIZATION FOR NUCLEAR RESEARCH

CERN/ISR-LTD/76-9

VERY HIGH ENERGY ELECTRON-POSITRON COLLIDING BEAMS FOR THE STUDY OF THE WEAK INTERACTIONS

B. Richter*)

CERN

ABSTRACT

We consider the design of very high energy electron-positron colliding-beam storage rings for use primarily as a tool for investigating the weak interactions. These devices appear to be a very powerful tool for determining the properties of these interactions. Experimental possibilities are described, a cost minimization technique is developed, and a model machine is designed to operate at centre-of-mass energies of up to 200 GeV. Costs are discussed, and problems delineated that must be solved before such a machine can be finally designed.

Geneva - 19 March 1976

---

*) Visitor from Stanford Linear Accelerator Center, Stanford, California.

1. INTRODUCTION

In the last two to three years, the pace of discovery in high-energy physics has been extraordinary. Experimenters have seen the birth of a new class of particles -- the ψ and other related heavy particles; found a new interaction -- the weak neutral current interaction; found familiar particles in unexpected situations -- the large transverse momentum leptons found in p-p collisions; found familiar particles in strange combinations -- the electron-muon events observed in e^+-e^- annihilation reactions, and neutrino interactions as well as the dimuon events observed in neutrino interactions, etc. The larger part of the most exciting work of the last few years has centred on studies involving reactions with electrons, muons, or neutrinos in either the initial or final state.

Indeed, the centre of interest of high-energy physics at the present moment is on the experimental results pouring from the e^+-e^- colliding-beam machines SPEAR at SLAC and DORIS at DESY, and from the high-energy neutrino reactions being studied at FNAL and soon to be studied with higher intensity and more refined apparatus at CERN with the start-up of the SPS. Lepton reactions are illuminating the structure of the hadrons, the weak interaction, and possible relations between particles and classes of interactions. The importance of this work is indicated by the funding of construction of two new e^+-e^- colliding-beam machines with c.m. energies of 30-35 GeV in both Europe and the U.S. These machines are primarily being built for the contribution they can make to our understanding of hadrons and quantum electrodynamics. They should begin to see the effects of weak interactions but these weak effects are expected to make only a small contribution to the processes that can be studied at the maximum energies of these machines.

The weak interaction can at present be studied directly only by neutrino-induced reactions with c.m. energies (E^*) of at best 10-20 GeV. There is intense interest in the weak interactions, which is manifested both by the effort going into studies of these interactions with presently and soon to be available machines, and by the justifications given for new generations of very high c.m. energy proton machines. The weak interactions are thought possibly to hold the clue to a unified picture of the elementary particles, their structure and dynamics. It is our belief that a study of these interactions through processes where one can hope to understand them and at energies where their strength has become comparable to that of the other interactions, is of great importance to high-energy physics, and *that the weak interactions can best be understood through a study of very high energy* e^+-e^- *collisions.*

This paper is concerned with the possibility of building e^+-e^- colliding beam machines with energies of several hundred GeV in the c.m. system. With such a machine one can hope to understand the structure of the weak force itself by a

study of reactions that involve only leptons in the initial and final states in an energy region where the weak interactions dominate. Relations between different classes of particles can be studied by comparing the production of such particles through the weak interactions, and the relation between the weak and electromagnetic interaction (and possibly even the strong interaction) can be studied by investigating various kinds of particle production in the energy region where the weak and electromagnetic forces are comparable in strength.

There is little argument about the desirability of studying the weak interactions via e^+-e^- interactions, but there is considerable uncertainty about the feasibility of the necessary machines and the costs of such machines compared to other approaches. These other approaches include very high energy conventional proton accelerators, high-energy p-p colliding-beam machines, or e-p colliding-beam machines; they have been studied and their properties are known. We believe that given costs for e^+-e^- tools comparable to those of the other machines mentioned above for the same effective centre-of-mass energy[1], the e^+-e^- is the most desirable tool for the light it can cast on the important questions.

In this paper, we consider the possibility of designing such e^+-e^- machines. We first briefly consider the physics, for a guide is required to specify the necessary interaction rate for such a machine. An optimization procedure is developed to determine the two critical parameters, radius and total power consumption, which, together with the interaction rate and energy, determine the rest of the machine design and the costs. A specific model machine with a c.m. energy of 200 GeV is designed with the aim of identifying questions which need to be answered before such a machine could be built with confidence. Some problems do turn up, and suggestions for solutions are presented.

Our conclusions are as follows:

i) e^+-e^- machines with $E^* \approx 200$ GeV can be built with conventional technology with sufficient interaction rate to study the weak interactions.

ii) Such machines have very large radii and uncertain costs. Using unit costs derived from much smaller machines, the cost of a machine with $E^* = 200$ GeV and luminosity $\mathscr{L} = 10^{32}$ cm^{-2} sec^{-1} appears to be about one to three times the cost of the CERN SPS.

iii) The cost uncertainties are primarily related to the large extrapolation from much smaller machines where unit costs are likely to be larger than those in a very big machine. Engineering studies can resolve many of these uncertainties, and give a reasonable idea of the costs of such a project.

iv) There are some questions of machine design that must be answered, the most critical involving the amount of free space required at the collision points for experimental physics. Work by both experimental physicists and accelerator physicists will be required to resolve this.

v) New technology, such as superconducting RF systems, will make a significant contribution only if the costs of such systems can be greatly reduced from present amounts. Since no working large-scale superconducting system exists, an investigation of the possibilities of superconductivity will require an extensive research and development effort. Superconducting magnets have no application in the structure of the machine itself, for the magnetic fields involved are extremely low and the power consumption in the magnets is negligible compared to the RF system.

vi) There appear to be significant opportunities for re-cycling the energy used in such a project.

2. PHYSICS

In this section we consider the rates for some processes of interest in very high energy e^+-e^- interactions. Our aim is to indicate qualitatively the kinds of reactions that can be studied, and to make some rough calculations of expected counting rates. These counting rate estimates must be approximate, for there is no established weak-interaction theory with which to make predictions in the energy region of interest, and different models differ by large amounts in their predicted cross-sections. This is in contrast to the situation at the energies of present experiments, where the differences between models are small. In spite of the uncertainties, rate calculations must be made to establish the required luminosity (reaction rate per unit cross-section).

We will begin by calculating the cross-section for the simple process

$$e^+ - e^- \rightarrow \mu^+ - \mu^- \qquad (1)$$

and consider both the electromagnetic and the weak contributions to reaction (1). The lowest-order Feynman diagrams that contribute to (1) are shown in Fig. 1. Since we are interested here in rates for reactions so that we can determine the required luminosity $\mathscr{L}$ for a high-energy machine, only total cross-sections are given. There are interference effects between the weak and electromagnetic contributions to (1) that affect the total cross-section as well as the angular distribution. What we will give here are the cross-sections for one type of interaction in the absence of the other. This will be a good approximation in those energy regions where one or the other interaction dominates, but there can be significant errors in the regions where they are comparable.

The cross-section for (1) via one-photon annihilation is

$$\sigma(\gamma) = \frac{4\pi\ \alpha^2}{3s} \tag{2}$$

where α is the fine-structure constant, and s is the square of the c.m. energy. We consider two models. One is what might be called the "Fermi" model, and the other the Weinberg-Salam model. By the "Fermi" model, we mean the usual V - A interaction with a coupling constant for both V and A each equal to $G/\sqrt{2}$, and an infinite Z^0 mass. The cross-section in this case is

$$\sigma_F = G^2 s/6\pi\ . \tag{3}$$

This cross-section increases linearly with s and will eventually overtake the electromagnetic cross-section. The ratio of this lowest-order weak cross-section to the electromagnetic cross-section is

$$\varepsilon_F = \frac{G^2 s^2}{8\pi^2\ \alpha^2} = 2.7 \times 10^{-8}\ s^2\ (\text{GeV})\ , \tag{4}$$

where G has been taken to be $10^{-5}/m_p^2$. The c.m. energy where $\varepsilon_F = 1$ is $\sim$ 80 GeV. Above this energy the weak interaction dominates, and below it the electromagnetic dominates.

This kind of calculation gives a weak cross-section that will eventually exceed the unitarity bound that for a given angular momentum state is

$$\sigma_{max} \leq \frac{(2J + 1)\ 4\pi}{s}\ . \tag{5}$$

For J = 1 which is appropriate for the V and A interactions, the value of s at which the cross-section of Eq. (3) passes this bound is $(1500\ \text{GeV})^2$. We could modify Eq. (3) by the addition of an *ad hoc* form factor

$$F^2 = \left[1 + (s/s_0)\right]^{-2}$$

which with $s_0 = (1500\ \text{GeV})^2$ would assure that (3) never exceeded the unitarity bound. Such a form factor would reduce the weak cross-section by $\sim$ 25% at a c.m. energy of 200 GeV.

Most interest is now centred on gauge theories of weak interactions that handle the divergences of the old weak theories in a natural way and that might give a unified description of the weak and electromagnetic interactions. The by now classical gauge theory is the Weinberg-Salam model which predicted the existence of neutral currents and which gives the carrier of the neutral current, Z^0, a mass of $\approx$ 100 GeV. In the Weinberg-Salam model, the cross-section for reaction (1) is given by

$$\sigma_W = \frac{\sigma_F}{16\left[1 - (s/m_{Z^0}^2)\right]^2} , \tag{7}$$

where we have included only the term due to the axial-vector coupling. The vector coupling strength depends on the Weinberg angle, and although the present determinations of this angle are crude, they indicate that the vector coupling would be smaller than the axial-vector coupling.

The yield versus c.m. energy for the μ-pair production reaction from Eqs. (2), (3), and (7), is given in Fig. 2 for $\mathscr{L} = 10^{32}$ cm^{-2} sec^{-1}. In this plot we have assumed a Z^0 mass of 100 GeV for the Weinberg model. The combined yield of the electromagnetic and weak interactions at $E^* = 200$ GeV ranges from 1/h in the Weinberg model to 35/h in the Fermi model. These yields are adequate for experiments, although the yield in the Weinberg model is not comfortable. However, σ_W increases rapidly as E^* decreases toward the Z^0 mass of 100 GeV.

If the Z^0 were larger, σ_W at $E^* = 200$ GeV would increase. Any model with a finite mass neutral current carrier will have the form of Eq. (7). We can find the maximum Z^0 mass to which we are sensitive in μ-pair production by requiring

$$\eta = \frac{\sigma_W(m_{Z^0})}{\sigma_W(\infty)} \tag{8}$$

to be greater than some minimum value that will allow experiments to make statistically significant measurements. For $s = (200\ \text{GeV})^2$, the Z^0 mass which makes $\eta = 1.25$ is about 600 GeV, while for $\eta = 1.05$ it is 1200 GeV. These experiments appear to be sensitive to the existence of finite-mass neutral current carriers of higher mass than experiments suggested for other proposed machines.

In addition to μ-pair processes, there is elastic electron scattering which in lowest order goes through the four diagrams of Fig. 3. We know of no complete calculation of this process, but weak effects should be comparable to or possibly greater than those in μ-pair production for the same momentum transfer.

The high-energy e^+-e^- machine is a new-particle factory of unparalleled versatility. Hypothesized particles such as the charged weak-current carrier ($W^\pm$), Higgs particles, leptons (sequential or gauge), point bosons, gluons, etc., all can be produced directly if their masses are less than 100 GeV for those which can be produced only in pairs, or less than 200 GeV for those that can be produced singly or in association with light particles such as electrons or muons. There is *no* way to produce most of these particles in an environment free from very large backgrounds other than by the use of e^+-e^- colliding beams.

Hadron production can take place in lowest order through the diagrams of Fig. 4. The usual conserved current arguments would lead us to expect the ratio of hadron production to μ-pair production via the weak interaction (R_W) to be about the same as the ratio of hadron production to μ-pair production via the electromagnetic interaction (R_γ). We know R_γ only to $E^* \approx 8$ GeV from the SPEAR experiments, where it is found to be ~ 5. Making a large extrapolation, we expect that hadron production by both the weak and electromagnetic interactions can be studied with these machines, the yield being about five times that shown in Fig. 2.

So far, the discussion has centred on the physics that can be done with neutral-current weak interactions in lowest order. Both the charged and neutral currents contribute to the production of all kinds of particles in the next higher order. Two of the multitude of diagrams in second order that result in lepton production are shown in Fig. 5. These diagrams individually are infinite in the case of infinite Z^0 and W masses. One of the most interesting possibilities of high-energy e^+-e^- colliding beams is the study of the effect of such higher-order processes. The effective coupling constant of the weak interactions -- the analogue of α in the electromagnetic interactions -- is $Gs/\sqrt{2}$, which, at $E^* = 200$ GeV, is about 1/4. With such a large coupling the effect of higher-order weak interactions should be observable. Some calculations are required to see what effect these higher-order terms might be expected to have in a variety of models.

We shall not discuss further the physics that could be done with these e^+-e^- machines, for our object in this section has been to give rough cross-sections to use in order to determine the required luminosity. It seems that a luminosity of 10^{32} cm^{-2} sec^{-1} is reasonable to use in our first look at the design of high-energy machines, and we shall use that value throughout the rest of this study. A more thorough calculation of many kinds of cross-sections is important, for such calculations might indicate that a different luminosity is required.

3. A FISRT LOOK AT MACHINE PARAMETERS

The design of a high-energy e^+-e^- colliding-beams machine is governed by a set of equations linking the luminosity, interaction region tune shift, RF power, beam energy, and radius[2]. For a large class of lattices, these equations together with the betatron phase change per cell of the lattice, determine nearly all the properties of the machine. The basic equation is that linking the luminosity ($\mathscr{L}$), maximum tune shift ($\Delta\nu_y$), RF power delivered to both beams (P_B) to make up for radiation loss, the bending radius (ρ), the interaction region vertical β-function (β_y^*), and beam energy (E)

$$\mathscr{L} = 1.23 \times 10^{33} \frac{\Delta\nu_y \; P_B(\mathrm{MW}) \; \rho(\mathrm{m})}{E^3(\mathrm{GeV}) \; \beta_y^*(\mathrm{m})} , \qquad (9)$$

where the units of the various quantities are indicated in the equation. The luminosity and beam energy are the input parameters determined by the physics that one wants to do. The parameter $\Delta\nu_y$ is related to the non-linear electromagnetic interaction between the two beams at the collision point. Experiments with many e^+-e^- storage rings have indicated that there is a maximum value of $\Delta\nu_y$ above which the beam lifetime decreases sharply. This maximum value is about 0.06, and we shall use this in Eq. (9).

The parameter β_y^* should apparently be as small as possible. As we shall see later, the cost of a very large machine does not seem to depend strongly on β_y^*. There is, however, a lower bound to β_y^* arising from two sources. The first is practical: a very low β at one point in the machine means a much larger value at another point. These very large values of β impose tight tolerances on the elements of the machine at the point where β is large, and also generate serious problems with the momentum dependence of the machine parameters. This momentum dependence in extreme cases can be sufficiently severe to make difficulties in injection, and even in containing the natural energy spread in the circulating beams. The second source is related to the maximum luminosity at the two-beam instability limit. Equation (9) is derived under the assumption that $\beta_y^* > \sigma_\ell$, the beam bunch length. For $\beta_y^* < \sigma_\ell$ the maximum luminosity decreases for a given RF power and machine radius. The natural bunch length in an electron storage ring is easily calculable and is expected to be about a centimetre. However, there is a phenomenon known in the machine trade as "bunch-lengthening", which arises from the interaction of the beam with the vacuum chamber and results in significant increases in the bunch length. This bunch-lengthening is understood well enough now to make a rough calculation of the size of the effect, and it is reasonable to expect that the maximum bunch length in a machine with high luminosity and a beam energy of $\sim$ 100 GeV will be < 5 cm. We will use 5 cm for β_y^* in Eq. (9), which now becomes

$$\mathscr{L} = 1.47 \times 10^{33} \frac{P_B \rho}{E^3} . \qquad (10)$$

We can use Eq. (10) to get a 0^{th}-order idea of the beam power and radius required for a very large electron machine. We can also get some idea of special problems that might turn up in the design. To begin, we shall simply scale ρ and P_B from the values used in the LBL-SLAC PEP storage-ring design. We will let P and ρ each vary as $E^{3/2}$, while we hold $\mathscr{L}$ constant at 10^{32} cm^{-2} sec^{-1}. As we shall see in the next section, the machine we get with this kind of scaling is very far from optimal in cost, but this exercise is useful to give some feeling for the machine parameters.

Table 1 gives a few of the gross parameters of a machine scaled in this way. One thing immediately apparent about this table is the relatively low values of

RF beam power required for even the highest machine energies. The 100 GeV c.m. example has a beam power which is only about 60% greater than the beam power in the PEP design, although the energy is a factor of 3 higher. This is a consequence of the value of β^* of 5 cm used here, compared to the β^* of 20 cm used in the PEP design.

The radii of these machines are large and the magnetic fields are correspondingly low. The 200 GeV c.m. machine of Table 1 has a bending field of only 1.1 kG. Even with this low value of B, however, the energy loss per turn of the circulating beams from synchrotron radiation is very large, and reaches in the 2 × 100 GeV machine about 3% of the beam energy per turn. This large fractional energy loss per turn is unprecedented in circular accelerators and may give rise to special beam dynamics problems associated with the distribution around the ring of the RF system.

The magnitude of the energy loss per turn also poses special problems for a CW RF system. While conventional electron linacs would have no trouble with the required energy gain (360 m of the SLAC accelerator would be sufficient), they are pulsed devices and not CW. In a CW device we must supply power to make up for the normal cavity dissipation, which depends only on the voltage per unit length on the cavity and the shunt impedance (Z). The power dissipated in cavity walls is given by

$$P_D = V^2/Z\ L \qquad (11)$$

where V is the total voltage on the cavity system, and L is the total length of RF cavities. The voltage V will be greater than the radiation loss U_0 given in Table 1 by a factor of about 15% in this size machine because of the overvoltage required to get a sufficiently long lifetime against quantum fluctuations in the synchrotron radiation. For our first look at a machine design, we will use the value Z = 19 MΩ per metre, which is the shunt impedance of the SPEAR and PEP cavities at an RF frequency of 350 MHz. We can get a rough idea of the total length of RF cavity required in these machines by simply setting the power dissipated in the cavities equal to the power supplied to make up for synchrotron radiation in the beams. If we do so, we get the values for cavity length given in Table 2. It is the large length of RF cavity required, coupled with the high cost per metre of RF cavities, that makes this entire scaling procedure impractical. We have, for example, arrived at a 200 GeV c.m. energy machine, which has a total circumference of bending magnets of roughly 20 km and a total length of RF cavity of 25 km. If we use the cost per unit length of PEP RF cavities, we find that the RF cavities alone would cost considerably more than $2000 million. We have arrived at this position by using a scaling which did not take into account the relative costs of different kinds of components. In the next section we develop a more realistic scaling to arrive at a more appropriate set of parameters for a very large electron storage ring.

4. MACHINE PARAMETERS, VIA A COST OPTIMIZATION

The scaling in power and energy used in the previous section was an arbitrary guess that resulted in a machine with an anomalously long RF system. In this section we sketch a more reasonable scaling procedure which uses some rough component cost figures, and include these costs in choosing a radius and RF system length for a high-energy e^+-e^- machine which minimize the total cost of the machine for a given energy and luminosity. Specifically, we shall use as an example a 200 GeV c.m. machine, and base the component costs on those in the PEP cost estimate[3]. This optimization will be crude because cost per unit length of components of a real machine will depend on the detailed design of the machine and on its location. Hopefully the size of a 200 GeV c.m. ring will introduce economies of scale not possible in as "small" a machine as PEP. All costs used here include an allowance over fabrication costs of 20% for engineering and design and a further 20% for contingencies.

The model machine whose costs we minimize consists of a housing of radius R (we ignore the difference between bending radius ρ and R; in practice, these differ by 10-15%), containing the bending components plus a long straight section containing the RF cavity system. We will not include in the minimization costs of experimental areas, laboratory buildings, shops, etc., for these are fixed costs that depend on the scale of the planned experimental programme and are not affected significantly by changes in circumference.

The unit costs we use are given in Table 3 [4].

The cost equation is

$$C = 2\pi k_1 R + (P_B + P_D)k_2 + L k_3 + (k_4/\varepsilon)(P_B + P_D) + F , \qquad (12)$$

where k_1, k_2, and k_3 are the unit costs of the ring, RF power, and cavities, respectively; R is the machine radius; P_B is the power supplied to both beams to make up for synchrotron radiation; P_D is the power dissipated as cavity losses; L is the RF cavity total length. The next-to-last term represents the 10-year power costs of the total RF system; k_4 is the 10-year cost of a megawatt of power (counting only machine on-time), and ε is the RF system efficiency. Finally, F is the fixed cost for such things as roads, experimental areas, workshops, offices, etc. The cost minimum is found by setting the partial derivative of C with respect to R and $P_D = 0$.

P_B and L can be written in terms of R and P_D. Defining $\delta \equiv E_{beam}/100$ GeV and $\gamma \equiv \beta_y^*/5$ cm,

$$P_B = \frac{68\ \delta^3 \gamma}{R} \quad \text{(MW)} \qquad (13a)$$

$$L = \frac{1.02 \times 10^5\ \delta^8}{P_D\ R^2\ Z} \quad \text{(km)} , \qquad (13b)$$

where Z is the cavity shunt impedance in MΩ/m. Substituting (13) into (12), we get

$$C = 2\pi k_1 R + \frac{68\,\delta^3\gamma\left[k_2 + (k_4/\varepsilon)\right]}{R} + \frac{1.02\times 10^5\,\delta^8}{P_D R^2 Z} k_3 + \frac{k_4}{\varepsilon} P_D + F \,. \qquad (14)$$

We now work out several examples of machines with $\mathscr{L} = 10^{32}$ cm^{-2} sec^{-1}. In all these examples, δ is set to unity (200 GeV c.m.), ε is assumed to be 75%, and Z is taken as 19 MΩ/m from the SPEAR and PEP designs.

A) PEP costs, $\beta_y^* = 5$ cm. Power at \$0.03/kWh

At the cost mininum, we find

$$R = 5.5 \text{ km}$$
$$P_D = 69 \text{ MW}$$
$$P_B = 12.3 \text{ MW}$$
$$L = 2.6 \text{ km.}$$

The cost for the ring, klystron system, cavities, and 10 years of operating power are \$440. \$50, \$210, and \$190 million, respectively. To find the total cost of the facility, we must guess at F in Eq. (12). Taking F = \$200 million, the total construction cost of this version of a 200 GeV c.m. e^+-e^- ring is about \$900 million, about 1.8 times the cost of the CERN SPS in 1975 dollars.

B) PEP costs, $\beta_y^* = 5$ cm. Power at \$0.05/kWh

Power costs have inflated relative to other costs by a large amount in the past few years. Whether it will continue to increase is uncertain, and so in this example we assume a 70% relative increase in those costs. At the cost minimum we find

$$R = 6.2 \text{ km}$$
$$P_D = 50 \text{ MW}$$
$$P_B = 11 \text{ MW}$$
$$L = 2.8 \text{ km.}$$

The cost for the ring, the klystrons, the cavities, and 10-years operating power are \$500, \$35, \$225, and \$235 million, respectively. The total construction cost of this version of the 200 GeV c.m. ring will be about \$1000 million -- about twice the cost of the CERN SPS in 1975 dollars.

C) PEP costs and $\beta_y^* = 10$ cm. Power at \$0.05/kWh

Increasing β_y^* has only a small effect on costs. The change occurs through a change in the (P_B R) product derived from the luminosity equation (9). The result of the minimization is

$$R = 6.5 \text{ km}$$
$$P_D = 47 \text{ MW}$$
$$P_B = 21 \text{ MW}$$
$$L = 2.7 \text{ km.}$$

The total cost in this case is increased by about \$20 million over case (A).

D) $\beta_y^* = 5$ cm and lower component costs. Power at \$0.05/kWh

PEP costs are for a relatively small machine, installed in a tunnel bored in sandstone on the SLAC site. We can examine the changes in machine parameters that would occur if we reduced various component costs to take account of different fabrication techniques or a different kind of site. To give an extreme example, we will reduce the ring costs per unit length by a factor of 2 and the cavity costs per unit length by a factor of 4 [5] over those used in case (B). The low ring cost might be realized by sitting the machine on flat terrain where the housing could be very inexpensive, and by using different techniques to fabricate the very small cross-section, very long magnets used. Cavity costs might be reduced by using a cavity of higher shunt impedance per unit length or possibly by mass-production fabrication techniques. These cost reduction factors are only intended to give some idea of the sensitivity of the machine parameters and total cost to the cost assumptions. The parameters found for this case are

$$R = 6.5 \text{ km}$$
$$P_D = 24 \text{ MW}$$
$$P_B = 10 \text{ MW}$$
$$L = 5.3 \text{ km.}$$

The costs are \$260, \$20, \$106, and \$132 million for the ring, klystrons, cavity, and 10-year operating costs. This gives a machine costing about a factor of 2 less than that in case (A).

This optimization procedure can easily be carried out for any centre-of-mass energy. When this is done for a constant luminosity of 10^{32} cm^{-2} sec^{-1}, we find we are in a region where the machine radius and costs scale like the square of the c.m. energy. Figure 6 gives the radius for a machine of any energy, optimized as described above. The curve is for our case (B). For case (D), that of reduced unit costs, the radii are 10% larger, and the costs are a factor of 2 smaller at a given energy.

The E^2 scaling is an unexpected result. It is like that expected of stationary-target machines which scale roughly linearly in machine energy but quadratically as a function of c.m. energy.

The optimization procedure used here is certainly crude, for it does not include the cost of capital, the effect of the choice of radius on the cost of machine components, etc. With the excursion made in power costs, β_y^*, and component costs, the radius of the resulting ring has only changed from 5.5 to 6.5 km, while the cost of the machine has changed by over a factor of 2. It seems reasonable to assume after these exercises that the radius of a 200 GeV c.m. machine will be about 6 km, and in the next section a detailed design of a model ring is made.

5. A 200 GeV c.m. DESIGN

5.1 General design

We use the methods of Ref. 2, with some modifications, to design a machine for 200 GeV in the centre of mass. The basic design equations link the beam size, the number of particles in each bunch, the machine energy, the interaction region β-function, the RF power, the bending radius, and the two-beam interaction tune shift. They are

$$\mathscr{L} = \frac{N^2 f}{4\pi b \sigma_x^* \sigma_y^*} \tag{15}$$

$$\Delta\nu_y = \frac{N \beta_y^* r_e m_e}{2\pi b E(\sigma_x^* + \sigma_y^*) \sigma_y^*} \tag{16}$$

$$\Delta\nu_y = \frac{N \beta_x^* r_e m_e}{2\pi b E(\sigma_x^* + \sigma_y^*) \sigma_x^*} \tag{17}$$

$$P_B(\mathrm{MW}) = 2.83 \times 10^{-20} N f \frac{E^4(\mathrm{GeV})}{\rho(\mathrm{m})} , \tag{18}$$

where N is the total number of particles in one beam; f is the orbit frequency; b is the number of bunches into which each beam is divided; σ_x^* and σ_y^* are the horizontal and vertical standard deviations of the beam size at the interaction point, respectively; β_x^* is the horizontal β-function at the interaction region; and r_e and m_e are the classical electron radius and electron rest mass, respectively. Following Ref. 2, we rewrite these as

$$\mathscr{L} = 1.23 \times 10^{33} \frac{\Delta\nu_y P_B(\mathrm{MW}) \rho(\mathrm{m})}{E^3(\mathrm{GeV}) \beta_y^*(\mathrm{m})} \quad (\mathrm{cm}^{-2}\ \mathrm{sec}^{-1}) \tag{9}$$

$$\frac{\sigma_x^* \sigma_y^*}{\beta_y^*} = \frac{8.08 \times 10^2 P_B(\mathrm{MW}) \rho(\mathrm{m})}{b \Delta\nu_y E^5(\mathrm{GeV}) f(\mathrm{Hz})} \quad (\mathrm{cm}) \tag{19}$$

$$\frac{\sigma_x^{*2}}{\beta_x^*} = \frac{8.08 \times 10^2 \; P_B(\mathrm{MW}) \; \rho(\mathrm{m})}{b \; \Delta\nu_x \; E^5(\mathrm{GeV}) \; f(\mathrm{Hz})} \quad (\mathrm{cm}) \tag{20}$$

$$N = \frac{3.53 \times 10^{19} \; P_B(\mathrm{MW}) \; \rho(\mathrm{m})}{E^4(\mathrm{GeV}) \; f(\mathrm{Hz})} \; . \tag{21}$$

We have assumed $\sigma_x^* >> \sigma_y^*$, and set $\sigma_x^* + \sigma_y^* = \sigma_x^*$. This is always true in practical e^+-e^- machines.

As indicated earlier, there is a bound on $\Delta\nu_y$. Not so much is known about $\Delta\nu_x$, but theory indicates there should be a bound on it also, and we will assume both $\Delta\nu_x$ and $\Delta\nu_y$ are limited to ≤ 0.06 and use the limiting value of 0.06 in the following discussion.

Equations (9), (18), (19), and (20) relate the properties of the beams to the lattice parameters at the interaction point. In order to specify a machine design, these parameters must be related to the arcs of the machine that connect the interaction regions. To do this, we adopt a procedure different from that in Ref. 2 and assume that the magnet systems that bring the beams from the ends of the arcs to the collision points are such that the dispersion of the lattice is zero at the collision points. There are good reasons for the choice of zero-dispersion interaction regions for machines with large fractional energy losses per turn. These have to do with the excitation of synchro-betatron resonances and with the horizontal separation of the electron and positron beams at the interaction regions. The two machines now under construction (PEP and PETRA) have made different choices. PEP has interaction regions with finite dispersion, while the PETRA interaction regions have zero dispersion. The reasons for these different choices relate to the detailed design of each machine and to the placement of their respective RF systems. At their c.m. energies of 15-20 GeV per beam, either choice is satisfactory if the RF placement matches that choice. The effect of our choice of dispersion-free interaction region is to increase the required horizontal aperture of the magnets in the arcs, and in the sense that one gets a larger value of the machine aperture, this choice might be called conservative.

We will make the arcs of the machine from simple doublet cells. The entire machine will then consist of a series of doublet cells connecting long straight sections composed of quadrupoles that match the machine functions at the ends of the arcs to those at the interaction points. The straight sections are assumed to be sufficiently long to contain the RF, injection, beam-separation equipment, etc. We do not consider the design of these straight sections, for it is a straightforward process. A summary of the properties of doublet cells is given in Ref. 2.

In this kind of machine, the horizontal beam emittance at the interaction points and in the arcs is given by

$$\frac{\sigma_x^{*2}}{\beta_x^*} = \frac{\sigma_{x\beta}^{\ 2}}{\beta_x} = \frac{2R}{\nu^3}\left(\frac{\sigma_E}{E}\right)^2 \tag{22a}$$

$$= 1.48 \times 10^{-4}\ \frac{E^2(\text{GeV})\ R}{\nu^3\ \rho}\ , \tag{22b}$$

where σ_E is the energy spread in the beam, $\sigma_{x\beta}$ is the betatron contribution to the beam size in the arcs, β_x is the β-function in the arc, R is the average radius of the arc, ν is the contribution to the tune of the arcs only, and σ and β on the left side of Eq. (22b) are in centimetres. Equation (22) gives the maximum value of the tune of the machine allowable if the horizontal incoherent two-beam limit is not to be exceeded. This maximum tune in turn gives the minimum horizontal aperture in the vacuum chamber of the arcs as well as the smallest allowed momentum compaction. Combining (22b) and (19), and using the maximum value of $\Delta\nu_x$, we find

$$\nu_{max}^{\ 3} = 1.10 \times 10^{-8}\ \frac{E^7(\text{GeV})\ R(\text{m})\ b\ f(\text{Hz})}{\rho^2(\text{m})\ P_B(\text{MW})}\ . \tag{23}$$

5.2 Lattice parameters

We can now set down most of the properties of the 200 GeV c.m. machine, and will use a bending radius and beam power consistent with those found in the previous section. The design parameters are as follows:

$\mathscr{L}$	=	10^{32}	(cm^{-2} sec^{-1})
E	=	100	(GeV each beam)
ρ	=	6.2	(km)
R	=	6.8	(km)
P_B	=	11	(MW, both beams)
$\Delta\nu_x$	=	$\Delta\nu_y$ = 0.06	
b	=	4	(eight interaction regions)
f	=	6.4	(kHz)
β_y^*	=	5	(cm)
N	=	3.8×10^{12}	(particles, each beam)
U_0	=	1.43	(GeV/turn synchrotron loss)
B	=	540	(gauss in bending magnets)
σ_E/E	=	1.1×10^{-3}	
ν_{max}	=	88	(in arcs)
ν_x	=	80	(in arcs).

Fixing the betatron phase shift per cell determines the horizontal beam size and the cell parameters. We give two examples:

μ	90	45	(degrees/cell)
n	320	640	(cells)
cell length	134	67	(m)
β_{max}	228	130	(m)
β_{min}	39	59	(m)
σ_x(max)	0.34	0.26	(cm)
σ_y(max)	0.20	0.15	(cm) (full coupling)
quadrupole focal length	49	44	(m)
η_{max}	1.78	1.34	(m) / $\Delta p/p$.

In these examples, σ_x(max) is taken at the centre of the horizontal-focusing quadrupoles and includes both synchrotron and betatron contributions to the beam size; σ_y(max) is measured at the centre of the vertical-focusing quadrupoles and is the value for *full* horizontal-vertical betatron coupling. This full coupling is not required in normal operation of such a machine, but might be accidentally reached, for example, during energy changes after injection.

To complete the design, we need the aperture and β_x^*. We take the minimum full aperture (A) required in the cells to be 20σ + 1 cm. Of this, 1 cm is allowed for residual orbit distributions, $\pm 6\sigma$ is required to achieve sufficient lifetime for Gaussian beams, and $\pm 4\sigma$ is assumed to be needed for the mismatch and consequent increase in β_{max} coming from the strong beam-beam interaction. The horizontal apertures given below are for zero horizontal-vertical coupling, while the vertical apertures are for 100% coupling.

β_x^* is determined from β_y^*, ν, and ν_{max}, by the choice of coupling during normal colliding-beam operations. This coupling is much less than the full coupling assumed to derive the vertical aperture. The colliding-beam configuration coupling constant k need be only larger than the natural coupling in the machine. The coupling coefficient k is defined by

$$\frac{\sigma_y}{\beta_y^{\frac{1}{2}}} = k \frac{\sigma_x}{\beta_x^{\frac{1}{2}}} . \qquad (24)$$

We take k to be 17%, a value much larger than the natural coupling in typical colliding-beam machines, where it ranges from 5% to 10%. The rest of the lattice parameters are then

μ	90	45	(degrees/cell)
A_x	7.8	6.2	(cm)

A_y	5.0	4.0	(cm) (full coupling)
k	0.17	0.17	
β_x^*	1	1	(m)

5.3 Operation below peak energy

This model machine has been designed for a luminosity of 10^{32} cm^{-2} sec^{-1} at a c.m. energy of 200 GeV. With this machine one should be able to conduct physics experiments over a broad band of energies, and the machine's potential depends on both the energy dependence of the luminosity and the expected energy dependence of the cross-section of interest. The energy dependence of the cross-sections illustrated in Fig. 2 are very different. The one-photon process is proportional to E^{-2}, the Fermi weak process to E^2, and the Weinberg weak process depends on whether one is above or below the Z^0 mass. There are many other cross-sections of interest, and the energy dependence of a good fraction of them is not in the literature. Some work is required by the theoretical community.

We can, however, discuss the expected energy dependence of the machine's luminosity. For a fixed aperture in the arcs, the luminosity $\mathscr{L}$ of an e^+-e^- machine can be made to be

$$\mathscr{L} \propto E^2 \tag{25}$$

for operation below the design maximum energy. Several procedures are available to achieve this $\mathscr{L}$ *versus* E dependence. A variable tune scheme is described in Ref. 2, and a scheme which uses "wiggler" magnets is described in the PEP Design Report[3]. To achieve a flatter E dependence than that given in Eq. (25), *the machine aperture must be increased.* This, of course, wastes space for high-energy operation. To give some idea of how much additional space is required in the aperture, we can take, as an example, 100 GeV c.m. operation with $\mathscr{L} = 10^{32}$ cm^{-2} sec^{-1}. For this lower-energy operation, the horizontal full aperture increases from the 7.8 cm found for 90° phase shift per cell at 200 GeV c.m. to a value of 14 cm. The magnet configuration is of course identical, and the quadrupoles are excited to give a tune of 34 in the arcs.

We shall not go here into the general question of aperture *versus* E for specified $\mathscr{L}$ *versus* E dependences, but we do want to make the point that the desired $\mathscr{L}$ *versus* E curve is what will actually determine the aperture of the machine. It is important to study both the physics needs for high $\mathscr{L}$ at low energy and the economic consequences of increased aperture.

Here, then, is a model machine that realizes our goal of a design for an e^+-e^- colliding-beam device that operates at c.m. energies of up to 200 GeV. In the process of designing this machine, we have not found anything obviously impossible, but there are some problem areas. In the next section, we discuss some of

these areas and indicate where we believe further work is required before the physics community can proceed confidently with the construction of such a device. There are also significant opportunities for cost savings, and a few of these are mentioned in the discussion.

6. PROBLEMS AND OPPORTUNITIES

In this section we shall discuss some of the things omitted from the previous analysis, including a re-examination of the one parameter that might seem at first glance somewhat radical, β_y^*.

6.1 Low β_y^*

The value of β_y^* of 5 cm used in the model machine poses problems both to the designers of the machine and to its users. The β-function will increase as we move from the collision point in the long straight section required for experiments toward the position of the first of the focusing elements in the machine. The value of β_y in this straight section is given by

$$\beta_y(D) = \beta_y^* + (D^2/\beta_y^*) \ , \tag{26}$$

where D is the position in the straight section measured with respect to the interaction point. If, for example, the first magnetic element of the lattice is located at a distance of 20 m from the collision point, the β-function at 20 m will be 8 km. This very large β implies extremely stringent tolerances on the magnetic field quality of the first quadrupoles and, in addition, gives large chromatic aberrations in the focusing structure that must be corrected elsewhere in the lattice. The tolerances on the magnetic field quality are probably not a problem, for with only eight interaction regions there exist 16 sets of lenses, and if necessary these can be equipped with multiple-harmonic correcting coils.

The problem of chromatic aberrations is much more serious. The aberrations cause a variation in the tune of the machine over the natural momentum spread in the beam that must not become so large as to move the tune for any particle within the beam to a resonance. In addition, the chromaticity (C ≡ the change in tune with momentum) is of the wrong sign for stability of the beams with respect to certain coherent oscillations. The sign of C must be reversed with a system of sextupoles distributed in the arcs, and the fact that C cannot be corrected where it is generated leads to restrictions on the momentum aperture of the machine. C depends on the ratio of the β-function of the quadrupoles to their focal length. The focal length of the interaction region quadrupoles is almost equal to their distance from the collision point D_0, and we find

$$C \approx k(D_0/\beta_y^*) \ , \tag{27}$$

where D_0 has been assumed to be very much greater than β_y^*, and k is approximately independent of machine design. In the PEP design, where chromaticity effects have been investigated in detail, $D_0 \approx 10$ m, and $\beta_y^* = 0.2$ m, giving C = 50 k. This value seems safe, but not by a large amount.

We must guess at D_0 for our model machine with 100 GeV beams. Existing machines from which we might scale are SPEAR (D_0 = 2.5 m, for 4 GeV/c beams), PEP (D_0 = 10 m for 18 GeV/c beams), and the ISR (D_0 = 8 m for 26 GeV/c beams). It is unquestionably convenient to the experimenters to have long free spaces clear at the interaction region, and we might guess, given no other considerations, that a D_0 of 20 m might be suitable for 100 GeV beams. With this choice and our value of β_y^* = 5 cm, C is 8 times that of the PEP lattice. It is not at all clear that a workable compensation system can be designed with such a large value of C, and this is one of the areas that needs further study.

An alternative possibility is to use very small diameter quadrupoles close to the interaction region, as indicated in Fig. 7. Such quadrupoles might be buildable with cos 2θ current distribution[6]. A quadrupole with an outer radius of 10 cm beginning at 2.5 m from the interaction region can greatly reduce C at the cost of allowing only a short free space for the study of particles produced in the interaction at an angle less than 40 mrad. Since the e^+-e^- reactions of interest are in low angular momentum states, there will be no very strong forward-peaking of the secondary particles, and this loss of long free space at very small angles might not be a serious problem. This is a subject that needs study by experimental physicists.

6.2 Tolerances

The standard tolerance calculations compute the effect of a randomly distributed set of field, position, and gradient errors on energy distributions and tune errors. These calculations compute the probability that the orbit or tune will lie within some allowed deviation with some specified probability. These calculations are extremely conservative in that they take no account of the difference between short- and long-range tolerances. They indicate that for a tune error of 0.01, the quadrupole gradients in the arcs must be as specified to a few parts in 10^4. For orbit distortions of the order of 0.5 cm, the bending magnet fields must be accurate to a few parts in 10^4, and the quadrupole positions must be accurate to about 0.1 mm. The bending field and gradient tolerances can be met with some difficulty, but the quadrupole position tolerances cannot be met in a machine of 40-50 km circumference. Good position tolerances can be achieved, however, over short sections of the circumference, and these coupled with steering coils appropriately distributed, can keep the beam centred in the machine aperture. The probability of the beam's making the first tune on the first try will be negligibly

small, and the machine will have to be equipped with sensors to allow the measurement of the position and angle of the first injected pulse at many points on the azimuth so that the necessary initial set-up ot the steering coils can be made.

6.3 Injection and site

Injection into a storage ring with a maximum beam energy of 100 GeV will probably have to be done at an energy no lower than about 20 GeV. Single-beam and coupled-beam instabilities are much more serious at low than at high energies, and low-energy injection schemes have given trouble at the existing high-luminosity storage rings, SPEAR and DORIS.

There is at present only one electron accelerator that can serve as an injector at these kinds of energies, the SLAC linac, but the SLAC site cannot accommodate a ring of the size required for 100 GeV beams. However, a 20 GeV synchrotron can be built at a very small fraction of the cost estimated for this project, and thus the availability of an injector should not be a determining influence on the choice of site. The design of a 20 GeV synchrotron is not a difficult problem, and will not be discussed further.

Since electron storage rings require considerably less shielding than proton machines, a flat site that does not require either tunnels or deep cuts may be advantage. It might be possible to reduce housing costs greatly by building on a flat terrain and covering the machine with about one metre of concrete or slightly more earth.

6.4 More on RF

There are many questions here that need further analysis. A few are listed.

6.4.1 Azimuthal distribution of RF

The synchrotron radiation losses around the arcs of the machine are continuous but the number of RF stations is finite. Thus the central energy of the circulating beam fluctuates coherently about the design energy and is larger than design on leaving an accelerating station and less than design on entering one. The electron and positron beams will coincide at the collision points in spite of this effect, for we have designed a lattice with zero dispersion in the interaction regions.

If the RF accelerating sections are placed in long straight sections equally spaced around the machine, the distance of the beam from the central orbit (Δx) between accelerating stations is given by

$$\Delta x \approx \pm \frac{\eta\, U_0}{2\, n_A\, E_0} \left(1 - \frac{2\, D_0}{\Delta}\right), \tag{28}$$

where η is the momentum dispersion, D is the position along the orbit measured between accelerating stations, and Δ is the separation between accelerating stations. The + (-) sign is for the e^- (e^+) beam for example, and n_A is the number of accelerating stations. For our model machine at 100 GeV, Δx in the arcs immediately before or after an accelerating station is

$$\Delta x = \pm 1.3/n_A \text{ cm} \tag{29}$$

for the machine with 90° phase shift per cell. With eight symmetrically placed interaction regions, it is probably desirable to have at least four accelerating sections, implying Δx of about ±3 mm maximum in the arcs. For comparison, in the PEP design, Δx is about ±0.5 mm. The effect of these systematic deviations of the orbit from the central orbit needs further investigation: they might excite synchro-betatron resonances.

6.4.2 Higher-mode losses

A beam with very large beam currents, as in this design, can lose energy by exciting various high-frequency electromagnetic modes in the vacuum chamber and in the guide field, in addition to the normal synchrotron radiation. These higher-mode losses require larger RF voltages and more RF power. These effects have not been estimated here, and do need calculation.

6.4.3 Exotic RF

The prototype machine uses a great deal of power to heat the walls of its conventional RF cavities. Two techniques might save power or money or both: superconducting RF cavities and pulsed RF systems. The costs for cavity systems plus 10-year cavity power for cases (A) and (C) of Section 4 are about $400 million and $200 million, respectively. If using superconducting or pulsed techniques can save a significant percentage of these funds, they would be of great benefit.

Superconducting RF systems have been discussed and worked on for many years, but there is to date no reliably operating system of any significant size. What is clear from the work done so far, is that at the frequencies of greatest interest to the circular-accelerator builders (100 to 1000 MHz), the maximum voltage gradient attainable in a superconducting structure seems to be limited by some fundamental surface phenomena in the cavities. The maximum voltage gradient attained reliably at HEPL is about 1.5 to 2 MeV/m at a frequency of about 1000 MHz [7]. While large voltage gradients have been obtained at higher frequencies, the aperture allowed in higher frequency cavities is generally too small for circular machines. Even if a voltage gradient can be made as large at a few hundred MHz as has been obtained at 1 GHz, 1-2 km of cavity will be required. If a complete cryogenic RF system -- cavities, dewars, tuners, refrigeration, He distribution, etc. -- can be produced at a cost of the order of a few $\times 10^7$ dollars per km, it would be of great interest.

Besides costs, there are several beam dynamics questions that must be answered in connection with superconducting RF systems. The cavities will have natural Q's of the order of 10^9 for unwanted modes as well as for their designed fundamental mode. These modes can be excited by the beam, which is capable of driving all harmonics of the orbit frequency up to something around 100 GHz. The effect on beam stability needs investigation, and a method will probably be required to lower the Q for these modes while preserving the high Q for the accelerating frequency. Both beam dynamics and engineering considerations need investigation before such a system can be constructed. A vigorous programme of hardware research and development and theoretical investigation must be pursued to decide the feasibility of such systems and to get some idea of the costs. Such a programme will require many years of effort.

Pulsed RF systems are a possibility that might be worth some work. The orbit frequency of the machine design in this paper is only 6 kHz, and with four equally spaced bunches in the machine, the bunch frequency near the interaction regions is only $\sim$ 24 kHz. It might be possible to design a lower-duty cycle RF system that significantly cuts total power demand.

6.5 Energy use

The energy consumption of our machine is very large. With conventional RF systems, the total energy input for RF alone ranges from 45 to 90 MW. We have tried to treat energy as an economic entity by including the 10-years operating costs for energy in the optimization of the machine parameters. We have used prices higher than those currently charged for energy, but even with this price, energy costs might not be a true reflection of its value to society. The high-energy physics community would do well to consider ways to minimize energy consumption or to re-use the energy consumed in machine operations.

If our e^+-e^- machine is considered as an energy converter, it produces two products: i) the degraded energy that comes out as heat in the cavity walls, magnets, etc.; ii) a more ordered form of energy, the 10 MW of X-rays with an energy of about 0.25 MeV emitted by the beam. Both of these products are valuable resources, both can be used, and we should consider these possible uses in the design and sitting of the machine.

The use of degraded heat energy is the simplest and most obvious. In most accelerators, the maximum temperature of the cooling water at the outlet is usually designed to be about 50°C. This is low for effective secondary use of the heat, but there is no reason why cooling water outlet temperatures cannot be raised to the 85°- 95°C region with ease, or even higher with difficulty. At temperatures of 85°-95°C, there are many uses for this thermal energy. Three of the most obvious are: i) heating and cooling of residential, industrial, and commercial

buildings; ii) drying of grain after harvest; and iii) heating of greenhouses. Many others will undoubtedly occur to the reader. Since the machine energy input is electrical, we can in principle recover a fraction of the primary fuel used to generate the electricity we consume that depends on the ratio of electrical generating efficiency to the efficiency of conversion of primary fuel to low-grade heat.

The second form of energy, the synchrotron X-rays, might be of even more value as a resource when used as X-rays rather than as another source of low-grade heat. Two examples of applications that require large amounts of X-rays are sterilization and materials modification. For example, there has been discussion in the past year of the creation of a world-wide "grain bank". Such a project *might* be economically more attractive if the grain can first be sterilized by X-ray bombardment.

There has been some work recently on greatly strengthening plastics by X-ray bombardment during polymerization. If such a material is useful, the high-energy e^+-e^- machine might be an ideal source of X-rays.

In either case (both of which might be wishful thinking), our "product", X-rays, is worth far more than the energy consumed in producing it. There might be other such uses, and such applications should be considered before making a final design and before choosing a site.

7. CONCLUSIONS

An e^+-e^- storage ring in the range of a few hundred GeV in the centre of mass can be built with present technology. There are a few questions of accelerator physics to be resolved, and a very important question of the free space required for experiments. With more detailed work on unit costs, the total cost of e^+-e^- rings can be defined well enough to allow a comparison with other projects that have been discussed as the next step in high-energy physics machines. It is likely that the e^+-e^- costs will be at the low end of the range found in this paper, and in that case the e^+-e^- machine at 200 GeV c.m. would seem to be the most useful project on the horizon.

Acknowledgements

The valuable comments and criticisms of J. Allaby, J. Ellis, A. Hofman, E. Keil, K. Johnsen and B. Zotter are gratefully acknowledged.

REFERENCES AND FOOTNOTES

1) The other machines involve the collision of an electron, neutrino, or proton with another proton (in e-p colliding beams, stationary-target machines, or p-p colliding beams). In our present picture of proton structure, the proton is composed of constituents, and the basic collisions occur between these constituents and the electrons, neutrinos, or other proton constituents. This gives an effective c.m. energy for the basic collisions considerably lower than that calculated considering the proton as a whole.

2) J. Rees and B. Richter, SLAC Report No. PEP-69 or SPEAR-167, October 1973.

3) PEP Design Report, SLAC, 1976.

4) Certain items in the budget of Ref. 3 have been combined to arrive at the unit costs used here. The responsibility for any omissions or misinterpretation is the author's.

5) C. Zettler (private communication) reports the complete cost per unit length for the CERN SPS RF-cavity system to be about $\$30 \times 10^6$/km.

6) The possibility of using small-diameter distributed-coil quadrupoles was suggested by A. Hofman, CERN.

7) M.S. McAshan et al., Proc. 9^{th} Internat. Conf. on High-Energy Accelerators, Stanford, 1974.

Table 1

Parameters for the zero-order high-energy e^+-e^- machines

E^*	ρ (m)	P_B (2 beams) (MW)	U_0 (MeV)
100	1030	4.1 × 2	507
150	1900	7.5 × 2	1400
200	2930	11.6 × 2	2870

Table 2

Cavity length for cavity power dissipation equal to synchrotron power required by the beams

c.m. energy (GeV)	L (m)
100	2260
150	9410
200	25600

Table 3

Unit cost in 1975 dollars of systems derived from the PEP cost estimates. Engineering and design, and contingency are included at 20% each

System	Cost ($ million)
Main Ring	
* Magnets, supports, installation, cooling	2.9 per km
Housing	4.6
Vacuum system	2.2
Instrumentation and control (excluding computer)	1.7
Misc.	1.4
	12.8 per km
RF Power	
Klystrons, waveguide, control	0.43 per MW
Cooling water, a.c. connections, misc.	0.15
	0.58 per MW
RF cavity	81 per km
a.c. Power (at $0.03/kWh)**	0.18 per MW-year

*) This item is lower by a factor of 2 than the PEP cost, since magnets for this machine are much lower-field than PEP's.

**) The power cost used is typical of CERN and Brookhaven, not of SLAC. I have also assumed a system on time of 6000 hours/year.

Figure captions

Fig. 1 : Feynman diagrams for μ-pair production by one-photon exchange and by the weak neutral current.

Fig. 2 : μ-pair production counting rate *versus* c.m. energy for a machine with $\mathscr{L} = 10^{32}$ cm^{-2} sec^{-1}. The curves are explained in the text.

Fig. 3 : Feynman diagrams for Bhabha scattering via one-photon exchange and via the weak neutral current.

Fig. 4 : Feynman diagrams for hadron production via one-photon exchange and via the weak neutral current.

Fig. 5 : Two of the many higher-order diagrams for lepton production by the weak interactions.

Fig. 6 : The radius *versus* c.m. energy for an optimized machine using the costs of Case B.

Fig. 7 : Schematic diagram of a distributed quadrupole to reduce the peak value of β_y.

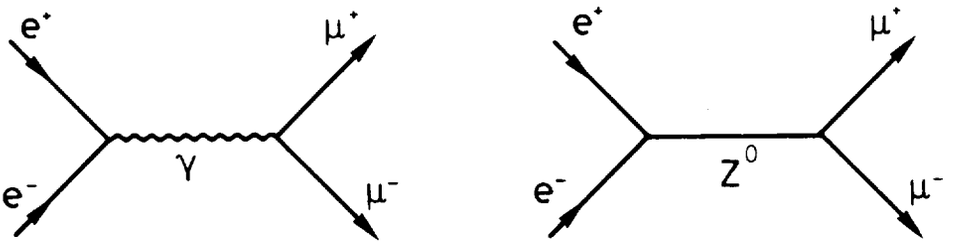

Fig. 1

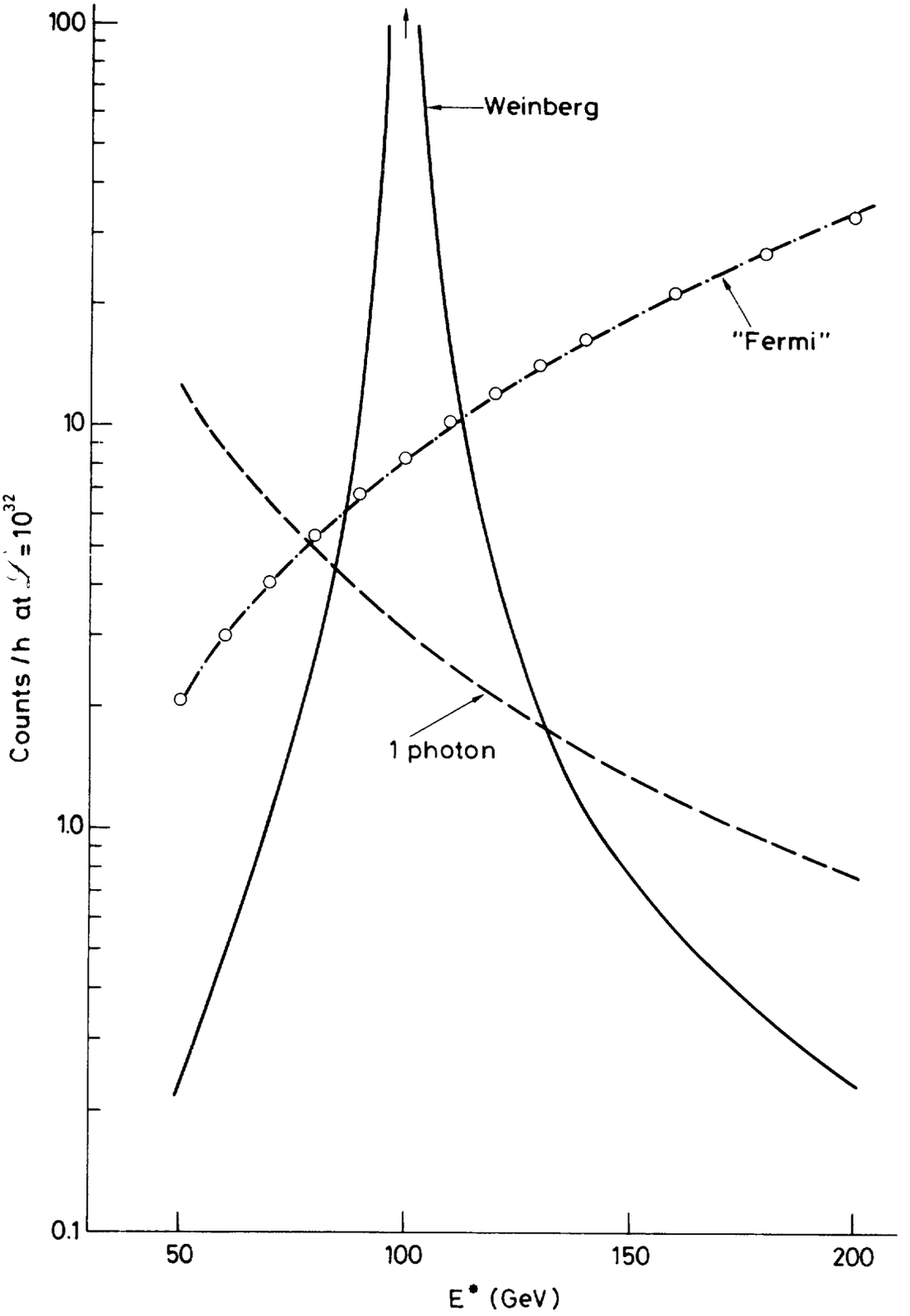
100
10
1.0
0.1
Counts /h at $\mathcal{L}=10^{32}$
Weinberg
"Fermi"
1 photon
50
100
150
200
E* (GeV)

Fig. 2

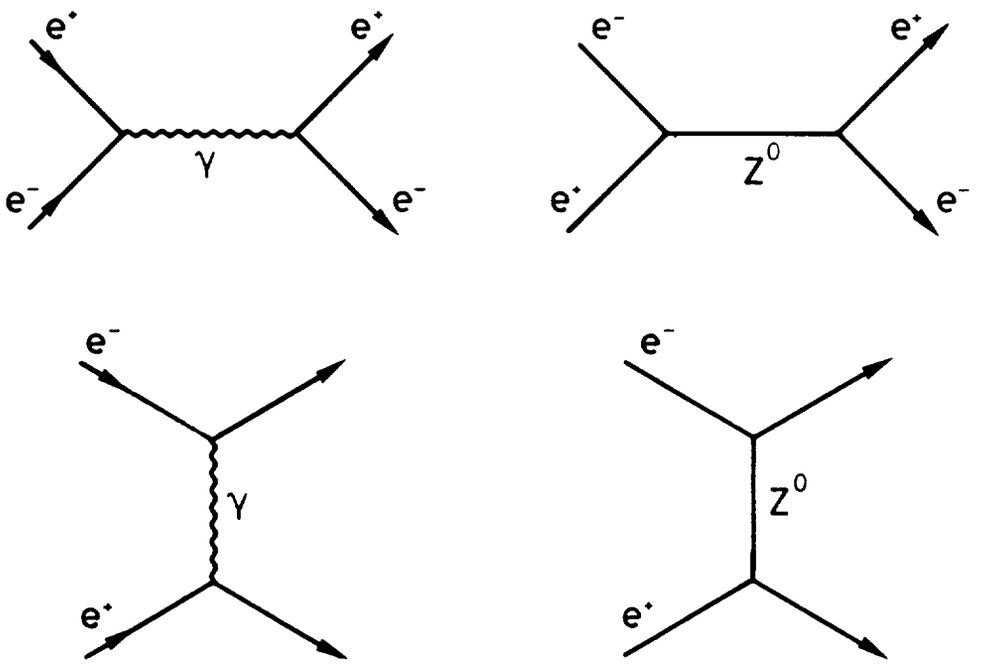

Fig. 3

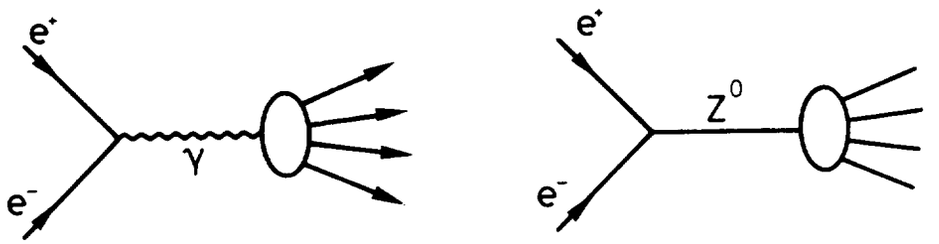

Fig. 4

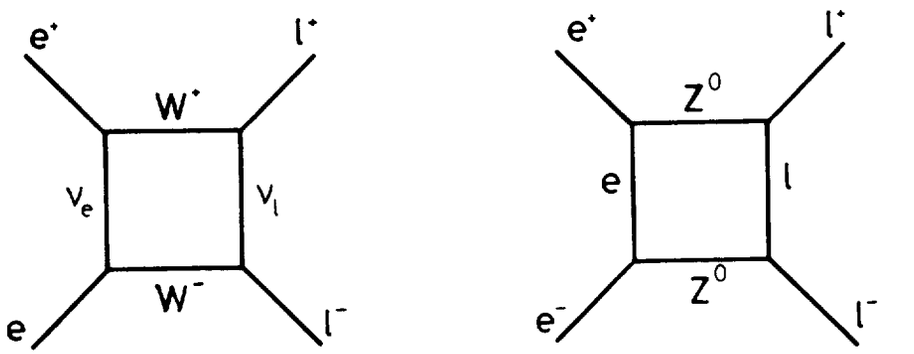

Fig. 5

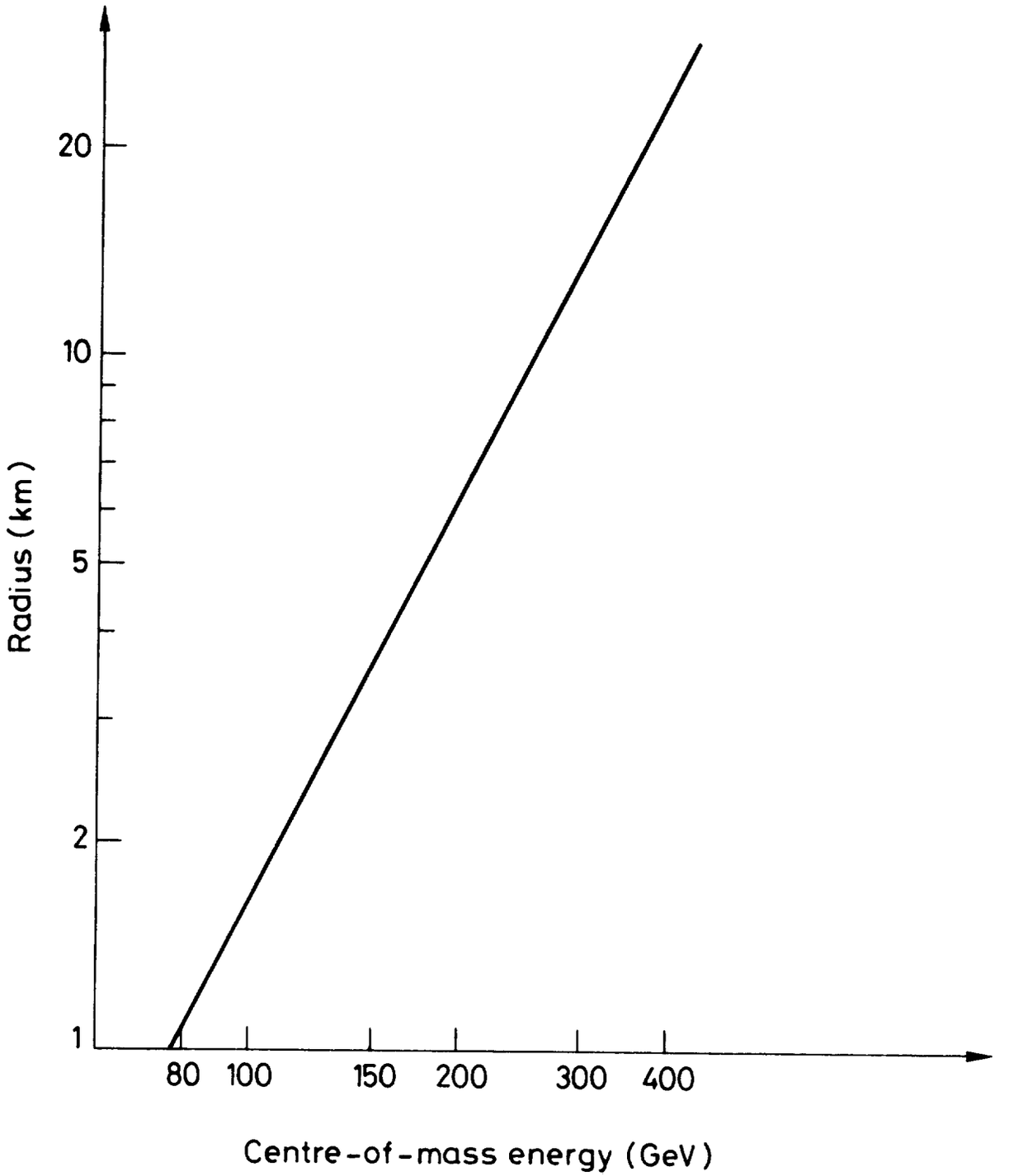
20
10
5
2
1
Radius (km)
80
100
150
200
300
400
Centre-of-mass energy (GeV)

Fig. 6

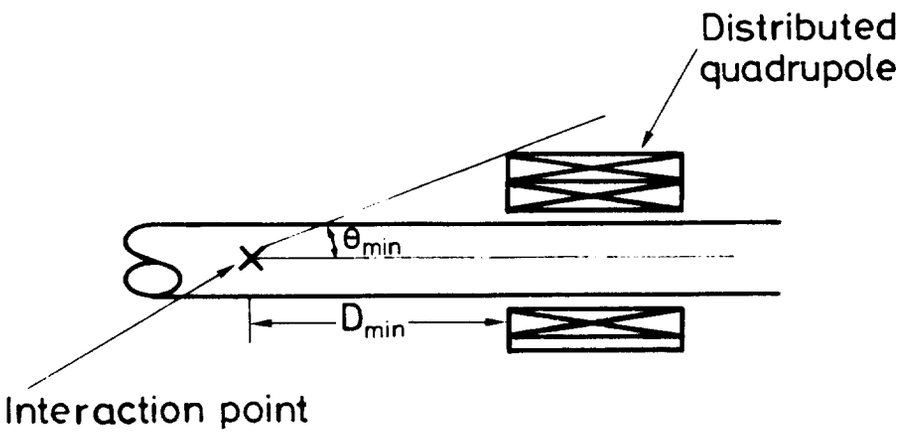

Fig. 7

APPENDIX 2

EUROPEAN ORGANIZATION FOR NUCLEAR RESEARCH

CERN/ISR-LTD/76-17 Rev. 2
Closed distribution

LEP Parameter List

(Version 3)

Compiled by E. Keil

This parameter list is issued at a moment when many machine parameters are still under discussion. It is subject to modifications in the near future. Parameters changed with respect to the previous list are marked by *.

Geneva - 4 August, 1976

1. Overall machine parameters at maximum energy

1.01	Maximum energy per beam	$E = 100$ GeV
* 1.02	Luminosity	$\mathcal{L} = 0.906\text{E}32\ \text{cm}^{-2}\ \text{s}^{-1}$
1.03	Number of intersections	$n_{int} = 8$
1.04	Number of bunches	$k_b = 32$
* 1.05	Machine circumference	$C = 51.460$ km
* 1.06	Average machine radius	$C/2\pi = 8.190$ km
* 1.07	Betatron wave-number	$Q_x = Q_y = 106.24$
* 1.08	Momentum compaction factor	$\alpha = 1.08\text{E}-4$
* 1.09	Circulating current/beam	$I = 12.45$ mA
* 1.10	Number of particles/beam	$N = 1.333\text{E}13$
* 1.11	Transverse damping time	$\tau_x = \tau_y = 24.2$ ms
* 1.12	Uncorrected chromaticities	$\xi_x = -248.1$
*		$\xi_y = -307.5$
* 1.13	Energy variation of damping partition number	$\partial J/\partial p/p = -476$

2. Intersection region parameters

* 2.01	Horizontal amplitude function	$\beta_x^* = 0.625$ m
2.02	Vertical amplitude function	$\beta_y^* = 0.1$ m
2.03	Dispersion	$\eta_x^* = 0$
* 2.04	Horizontal rms beam radius	$\sigma_x^* = 0.08430$ mm
* 2.05	Vertical rms beam radius	$\sigma_y^* = 0.03372$ mm
* 2.06	Natural rms energy spread	$\sigma_e = 1.08\text{E}-3$
* 2.07	Natural rms bunch length at I = 0	$\sigma_{z0} = 11.5$ mm
2.08	Actual rms bunch length at nominal current	$\sigma_z = 25$ mm
* 2.09	Coupling	$\kappa = 1.0$
* 2.10	Maximum beam-beam tune shift	$\Delta Q_x = 0.06$
2.11	Crossing angle	$\chi = 0$
* 2.12	Beam-beam bremsstrahlung lifetime	$\tau_{bb} = 13.84$ h
2.13	Quantum lifetime	$\tau_q = 10$ h
* 2.14	Polarization time	$\tau_{pol} = 0.873$ h
2.15	Free space around crossing points	$\ell_{int} = \pm 10$ m

3. Cell parameters

	3.01	Cell layout			$\frac{1}{2}$QF - B - QD - B - $\frac{1}{2}$QF
*	3.02	Length of cell			L_p = 81 m
*	3.03	Length of bending magnets (B)			L_B = 35 m
*	3.04	Length of quadrupoles (QF, QD)			L_Q = 2.5 m
*	3.05	Bending field			B_M = 0.05347 T
*	3.06	Bending angle per period			θ_p = 11.220 mrad
*	3.07	Bending radius			ρ = 6.239 km
*	3.08	Horizontal phase advance			μ_x = 59.2°
*	3.09	Vertical phase advance			μ_y = 55.5°
*	3.10	Horizontally focusing quadrupole gradient			$(\partial B/\partial x)_F$ = - 3.28 T/m
*					(or K_F = - 9.8203E-3 m^{-2}
*	3.11	Vertically focusing quadrupole gradient			$(\partial B/\partial x)_D$ = 3.18 T/m
					(or K_D = 9.5474E-3 m^{-2}
*	3.12	Average radius of normal cells			R = 7.219 km
			β_x	β_y	η_x
*	3.13	Orbit parameters in F quadrupoles	138.16	52.05	1.149 m
*	3.14	Orbit parameters in D quadrupoles	49.37	143.32	0.712 m
*	3.15	Horizontal rms beam radius in F quadrupoles			σ_x = 2.167 mm
*	3.16	Vertical rms beam radius in D quadrupoles			σ_y = 1.277 mm
*	3.17	Horizontal aperture			A_x = ± 64 mm
*	3.18	Vertical aperture			A_y = ± 36 mm

4. RF system parameters

*	4.01	Synchrotron energy loss/turn	U_0 = 1.42 GeV
*	4.02	Synchrotron power/beam	P_b = 17.7 MW
	4.03	Frequency	f_{RF} = 350 MHz
*	4.04	Peak RF voltage/turn	V_{RF} = 1.68 GV
*	4.05	RF bucket height	σ_b = 6.602E-3
*	4.06	Stable phase angle	ϕ_s = 115°
*	4.07	Number of synchrotron oscillations/turn	Q_s = 0.08532
*	4.08	Shunt impedance	Z_s = 20 MΩ/m

4.09	Length of active RF structure	ℓ_{RF} = 2.8 km
* 4.10	Fundamental mode RF structure dissipation	P_c = 50.6 MW
* 4.11	Total RF generator power	P_{tot} = 89.9 MW
* 4.12	Higher mode energy loss/turn	U_{hm} = 110 MeV
* 4.13	Power loss to higher modes	P_{hm} = 1.3 MW

5. Energy variation of machine and beam parameters for E $\leqslant$ 100 GeV

5.10 Constant beam size using wiggler magnets

5.11 $\mathcal{L} = (E/100\ \text{GeV})^2\ 10^{32}\ \text{cm}^{-2}\ \text{s}^{-1}$

5.12 $\sigma_x^*,\ \sigma_y^*,\ \sigma_e \sim E^0$

5.13 I, N $\sim E$

5.20 Variable beam size using wiggler magnets and/or variable tune

5.21 $\mathcal{L} = 10^{32}\ \text{cm}^{-2}\ \text{s}^{-1}$ for 50 GeV $\leqslant$ E $\leqslant$ 100 GeV

5.22 $\sigma_x^*,\ \sigma_y^*,$ I, N $\sim E^{-1}$ for 50 GeV $<$ E $\leqslant$ 100 GeV

5.23 $\mathcal{L} = (E/50\ \text{GeV})^2 \times 10^{32}\ \text{cm}^{-2}\ \text{s}^{-1}$ for E $\leqslant$ 50 GeV

5.24 $\sigma_x^*,\ \sigma_y^*,\ \sigma_e \sim E^0$ for E $\leqslant$ 50 GeV

5.25 I,N $\sim E$ for E $\leqslant$ 50 GeV

6. Synchrotron radiation

			normal cell magnet	10% field magnet
* 6.01	Synchrotron power line density	W	900	9.0 W/m
* 6.02	Critical energy	E_c	356	36 keV

7. Comments

The numbers below refer to the line numbers in the parameter list.

2.02: β_y^* has been fixed by imposing a lower limit on τ_{bb}. At constant $\mathcal{L}$, $\tau_{bb} \sim \beta_y^*$.

2.08: Estimated bunch lengthening factor: 2.5.

2.10: The vertical tune shift is smaller than the horizontal one, $\Delta Q_y = \Delta Q_x \beta_y^*/\beta_x^*$.

2.14: τ_{pol} is calculated ignoring the existence of depolarizing resonances which may prevent polarization of the beam as discussed by D. Möhl and B.W. Montague in CERN/ISR-LTD/76-21.

3.17: The horizontal aperture corresponds to ± ($20\sigma_{x\ max}$ + 20 mm for c.o.)

3.18: The vertical aperture corresponds to ± ($20\sigma_{y\ max}$ + 10 mm for c.o.) $\sigma_{y\ max}$ is taken for a fully coupled beam. The apertures are chosen large enough to allow $\mathcal{L} = 10^{32}$ cm^{-2} s^{-1} at 50 GeV.

4: Some parameters of the RF system are fixed by beam dynamics, others are best guesses for an actual RF system.

4.08: The definition of shunt impedance is $Z_s = V_{RF}^2/P_c$.

4.11: P_{tot} is calculated according to P.B. Wilson, IXth Int. Conf. High Energy Accelerators, Stanford 1974, p. 57 (1974).

4.12, 4.13: Estimated for σ_z = 25 mm and a higher mode loss impedance of 9 GΩ. These figures are included in the figures for V_{RF} and P_{tot}.

5: The luminosity variation shown under 5.1, is "guaranteed". The one shown under 5.2 is the design aim. It is not yet clear that it can actually be reached.

6: It is envisaged that the synchrotron radiation falling into the interaction regions is softened by a magnet with 10% of the nominal magnetic field. This magnet is not yet included in the lattice design.

6.02: The critical energy E_c describes the spectrum of synchrotron radiation. Half the power is in photons with energies less than E_c.

6.02: The mean photon energy is $(8/15\sqrt{3})E_c$.

The machine layout and the orbit functions $\sqrt{\beta_x}$, $\sqrt{\beta_y}$, η in the vicinity of the crossing point are shown in Figs. 1 and 2.

8. Revision history

Version 1: E, $\mathcal{L}$, n_{int}, k_b, β_x^*, β_y^*, η_x^*, ΔQ, C are input parameters. Their choice is discussed by B. Richter in CERN/ISR-LTD/76-9.

Version 2: Because of beam loading problems in Version 1, k_b was increased to 32. The beams are assumed to be separated where they would cross outside the intersection regions. The lattice was modified to obtained the smaller beam size required, and the aperture was increased.

Version 3: Vertical closed orbit distortions make it unlikely that the small value of σ_y^* required in Version 2 can actually be obtained. This problem is solved by assuming full coupling. In order to limit the increase in current, β_x^* was reduced. The lattice was modified to obtain the beam size required.

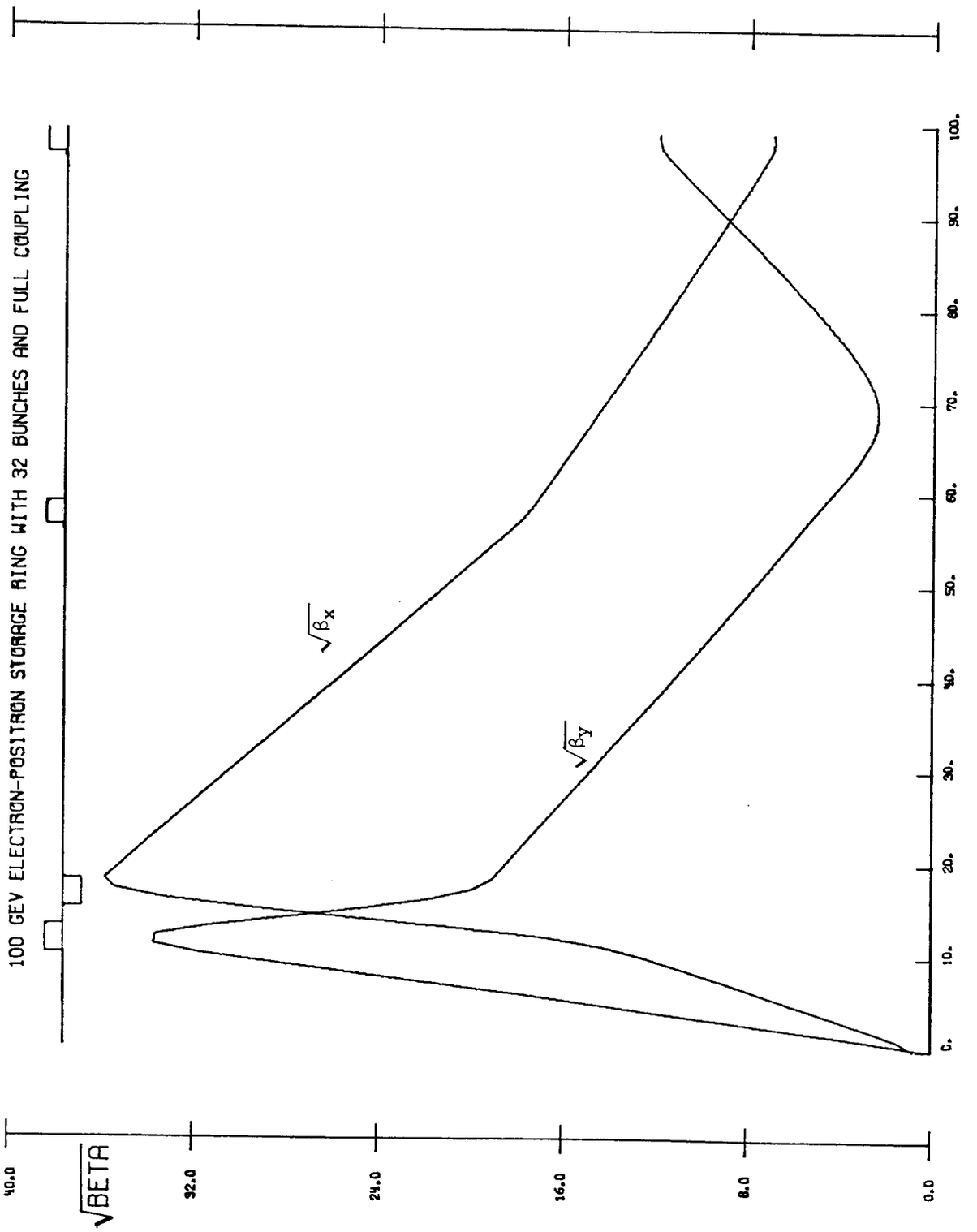
100 GEV ELECTRON-POSITRON STORAGE RING WITH 32 BUNCHES AND FULL COUPLING
√BETA
40.0
32.0
24.0
16.0
8.0
0.0
0.
10.
20.
30.
40.
50.
60.
70.
80.
90.
100.
$\sqrt{\beta_x}$
$\sqrt{\beta_y}$

FIG. 1

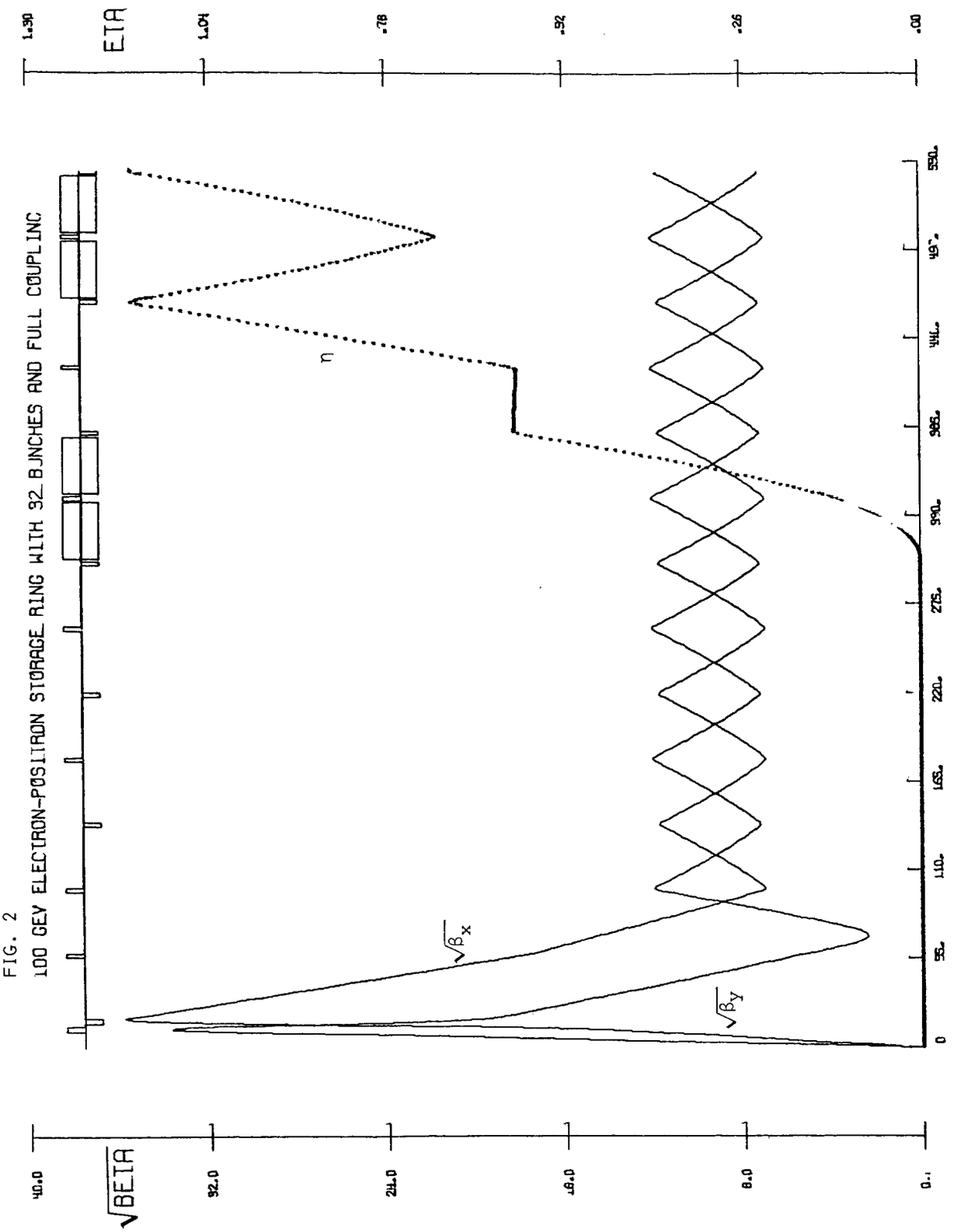

FIG. 2
100 GEV ELECTRON-POSITRON STORAGE RING WITH 32 BUNCHES AND FULL COUPLING

APPENDIX 3

EUROPEAN ORGANIZATION FOR NUCLEAR RESEARCH

CERN ISR-LTD/76-37
Closed Distribution

SEXTUPOLE AND OCTUPOLE SCHEMES IN VERY HIGH ENERGY ELECTRON RINGS

by

B. Autin

Abstract

Sextupole and octupole schemes which correct the chromatic aberration of 100 GeV electron rings are described. Residual tune fluctuations lie within the synchrotron frequency. The β-function variations are controlled at the crossing points and in the lattice.

Geneva, Switzerland
August 1976

TABLE OF CONTENTS

1. INTRODUCTION

The interest arisen by the recent discoveries made with electron-positron collision rings leads to envisage the possibility of building very large machines of this type in which the centre of mass energies and the luminosity would be as high as 200 GeV and 10^{32} $cm^{-2}s^{-1}$ respectively[1,2]. A first approach in designing such a machine is guided by the basic relation[3] which links the luminosity L, the energy E, the non-linear vertical beam-beam tune shift $\Delta\nu_y$, the power P_B delivered to the beam to compensate for the energy losses due to synchrotron radiation, the radius of curvature ρ and the value of the vertical β function β_y^* at the intersection :

$$L(cm^{-2}s^{-1}) = 1.23 \times 10^{33} \frac{\Delta\nu_y \; P_B(MW)\rho(m)}{E^3(GeV) \quad \beta_y^*(m)} \quad .$$

L and E are fixed by physics. $\Delta\nu_y$ is a constant, estimated to be 0.06. The product $P_B\rho$ influences the cost of the machine considerably; it is kept at its minimum value if β_y^* is as small as possible. The lower limit of β_y^* is determined by the length of a bunch of particles and the first studies concerned a machine for which β_y^* was equal to 5 cm. Further considerations, like the limitation in life time due to beam-beam Bremsstrahlung[4], tend to raise β_y^* and the reference machine which is dealt with here has a β_y^* value equal to 10 cm. Such small values are necessarily associated with very high ones in the adjacent quadrupoles because of the quadratic dependence of β with the distance D in a straight section :

$$\beta_y = \beta_y^* + \frac{D^2}{\beta_y^*} \quad .$$

As the proposed experimental set-ups require at least 10 metre completely free on each side of the crossing point, one has to admit a β function which is greater than 1 km. Whether the effects on aperture and alignment tolerances can be accepted is an important question which will not be treated here. Moreover, the focusing defects due to the errors of momentum $\Delta p/p$ of the particles ("chromaticity") are directly proportional to β_y and may be a severe limitation for the performances of a machine. Usually, the correction of chromaticity consists of calculating the various multipole components of the main magnetic field which eliminate the influence of the momentum errors. This method requires a non-zero dispersion of the orbits at the location of the correcting elements. In the present case, this dispersion does not exist for reasons of high luminosity and decoupling of synchrotron and betatron

oscillations in the region where the defects are the strongest. So, a scheme of non-linear magnetic lenses has to be designed outside the neighbourhood of the intersections. It must provide a satisfactory distribution of the betatron frequencies within a given momentum spread without perturbing the closed orbits and the amplitudes of the betatron oscillation. In addition, it is desirable for luminosity reasons that the variations of β_y^* with $\Delta p/p$ be controlled.

In section 2, the "linear" machine is described and the variations of the tunes and of the β function are evaluated as functions of $\Delta p/p$. The principles of the sextupole grouping are recalled in section 3. The procedure of correction is described by successive steps in the three following sections : a trial of compensation of the natural chromaticity of the machine with two families of sextupoles (§4), an additional control of the β fluctuations by a matching of the insertion to the lattice on the off-momentum orbits (§5), and finally an independent control of betatron frequencies and amplitudes in the insertion and in the periods (§6). A sextupole scheme is defined for nominal operating conditions :

$$E = 100 \text{ GeV} \qquad \beta_y^* = 10 \text{ cm} \qquad -0.005 \leqslant \frac{\Delta p}{p} \leqslant 0.005$$

How this can be adapted to take into account larger momentum spread or reduced β values is discussed in section 7.

2. RING STRUCTURE ON THE CENTRAL ORBIT

This structure was designed by E. Keil[2] and is recalled here for comparison with the structure on the off-momentum orbits.

The ring has a quasi-circular shape. It is almost fifty kilometre long and is divided into eight superperiods (Figure 1).

Since each superperiod is symmetric, it is sufficient to describe one sixteenth of the total machine. A diagram and the variations of the functions β_x, β_y and η (or α_p), the orbit dispersion function, are plotted in Figure 2. The cell has a FODO structure ; its phase advance was chosen equal to $\pi/3$ in order to make an independent grouping of the sextupoles as will be explained in the next section. This phase is also very convenient for designing the dispersion suppressor which consists simply of two normal cells, one having no dipoles and the other having special bending magnets. The RF section occupies two normal cells without bending magnets in a region of zero dispersion. The values of the β functions at the intersection,

$$\beta_x^* = 2.5 \text{ m} \qquad \beta_y^* = 0.1 \text{ m}$$

are achieved with the low-β section which matches the betatron oscillations of this special region to those of the cells.

The tunes are equal in both planes to 138.24. Their derivatives with respect to Δp/p are :

$$Q'_x = \frac{dQ_x}{d(\Delta p/p)} = -185.41 \qquad Q'_y = \frac{dQ_y}{d(\Delta p/p)} = -334.39 \ .$$

The difference between these two values is due to the low-β sections which are much more focusing in the vertical plane than in the horizontal plane. The contribution of the insertions to Q'_y is 56.7 % while it amounts only to 23 % for Q'_x.

The variations of β with Δp/p can be calculated rigorously to the first order by using the expressions derived in reference 5. As the insertion is matched to the regular cells on the central orbit only, the focusing perturbations produced by momentum errors open gradient stopbands which result in an overwiggling of the β function. The principle of the calculation is the following. Let a superperiod be composed of a special section inserted into a regular lattice :

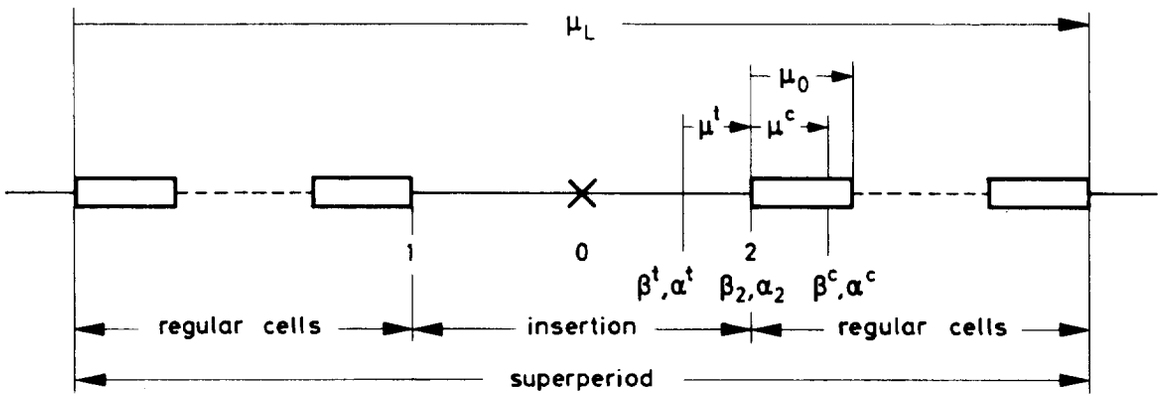

The β and α ($= -\frac{1}{2}\frac{d\beta}{ds}$) functions can be traced from 1 to 2 with the formulae

$$\left.\frac{\Delta\beta_2}{\beta_2}\right|_q^t = \frac{\Delta p}{p}\int_1^2 K\,\beta^t \sin 2\mu^t ds$$

$$\left.\Delta\alpha_2\right|_q^t = \alpha_2 \left.\frac{\Delta\beta_2}{\beta_2}\right|_q^t - \frac{\Delta p}{p}\int_1^2 K\,\beta^t \cos 2\mu^t ds$$

where β and α are the unperturbed functions known on the central orbit and K ($= G/B\rho$) is the focusing parameter of the quadrupoles defined as the ratio of the gradient G to the magnetic rigidity ($B\rho$). Letters t and q refer to insertion and quadrupole respectively.

In the cell (superscript "c"), the variations of β and α at point 2 are given by

$$\left.\frac{\Delta\beta_2}{\beta_2}\right|_q^c = \frac{1}{2 \sin \mu_0} \frac{\Delta p}{p} \int_c K \beta^c \cos (\mu_0 - 2\mu^c) ds$$

$$\left.\Delta\alpha_2\right|_q^c = \alpha_2 \left.\frac{\Delta\beta_2}{\beta_2}\right|_q^c + \frac{1}{2 \sin \mu_0} \frac{\Delta p}{p} \int_c K \beta^c \sin (\mu_0 - 2\mu^c) ds$$

The discontinuity of the variations of β and α at point 2 are defined by

$$\frac{\delta\beta}{\beta} = \left.\frac{\Delta\beta_2}{\beta_2}\right|_q^t - \left.\frac{\Delta\beta_2}{\beta_2}\right|_q^c$$

$$\delta\alpha = \left.\Delta\alpha_2\right|_q^t - \left.\Delta\alpha_2\right|_q^c$$

and the maximum fractional change of β in the superperiod is

$$\frac{\Delta\beta}{\beta} = \frac{1}{2 \sin \mu_L} \sqrt{\left(\frac{\delta\beta}{\beta}\right)^2 + \left(\delta\alpha - \alpha \frac{\delta\beta}{\beta}\right)^2} \quad .$$

In the case of a symmetric superperiod, the previous formula becomes :

$$\frac{\Delta\beta}{\beta} = \frac{\delta\alpha}{\sin \mu_L}$$

where $\delta\alpha$ is obtained by tracing α through the insertion from the symmetry point O. This expression is formally the same as the one given in Ref. 6) which was established for a model of low-β section where the triplets adjacent to the crossing point are replaced by single lenses which cause the slope of β to change by $-2\Delta\alpha$. In the present case

$$\frac{\Delta\beta_x}{\beta_x} = 40.67 \qquad \frac{\Delta\beta_y}{\beta_y} = 131.27 \quad .$$

In order to stabilize the beam against the head-tail effect, Q' must be made positive and sextupoles which have a focusing field proportional to $\Delta p/p$ are to be embodied in the machine. The order of magnitude of Q'_y and $\Delta\beta_y/\beta_y$ must be expected to become noticeably non-linear functions of $\Delta p/p$ even for $\Delta p/p$ as small as a few per mille. These non-linearities are especially dangerous in the sextupoles. Hence their arrangement has to be chosen such as to maintain the fluctuations of Q and β within a reasonable range.

3. GROUPING OF NON-LINEAR LENSES

The idea of combining sextupoles into sets which have specific functions was first proposed by Edwards and Teng[7]. It has already been applied to proton machines[8,9]. The effects which will be taken into account here are the orbit distortion, the chromaticity, the β function perturbation and the excitation of non-linear resonances.

In a 2n-pole magnetic lens, the field obeys the law

$$B = \frac{1}{(n-1)!} \frac{\partial^{n-1} B}{\partial x^{n-1}} x^{n-1} \quad ,$$

the primary effect is a distortion of the off-momentum orbit

$$x_p = \eta \frac{\Delta p}{p}$$

and this orbit distortion oscillates around the machine with a phase μ.

The tune Q and the betatron function β are determined by the parameter

$$K = \frac{1}{(B\rho)} \left.\frac{d\beta}{dx}\right|_{x=x_p} = K^{(n-2)} \frac{x_p^{n-2}}{(n-2)!}$$

where :

$$K^{(n-2)} = \frac{1}{(B\rho)} \frac{\partial^{n-1} B}{\partial x^{n-1}} \quad .$$

We note that β fluctuates with the phase 2μ while Q is simply scalar, and hence that the variations of Q and β can be made independent.

For non-linear resonances, the tunes are such that

$$m_x Q_x + m_y Q_y = q \ ,$$

where m_x, m_y and q are integer, m_y is even and m_x and m_y satisfy the relation

$$m_x + m_y = n \ ,$$

n being the order of the resonances. They are excited by the term $K^{(n-2)}$ and the relevant phases are $m_x \mu_x + m_y \mu_y$.

In the following, sextupoles and octupoles only are considered. They are located in regular cells whose phase advance is assumed to be equal to $\pi/3$ in both planes, which, in reality, is only an approximation. They can be of F- or D-types according to their location near an F- or a D-quadrupole. In a group of a given type of lenses, the β and η functions on the central orbit are the same in the lenses. Due to the decoupling of β_x and β_y, the F- and D-lenses have their main effect in the horizontal and vertical plane respectively.

Four kinds of grouping will be described. In scheme (A), all the sextupoles of the same type (F or D) are connected in series and act essentially upon Q' since the orbit and β perturbations remain confined within the region occupied by the lenses and the non-linear resonances are not affected. Schemes B and C provide an additional control of the β function, they influence also Q' and this point will be discussed in more detail in section 5. A, B and C are one-variable schemes ; a linear combination D of A and B or A and C has the same properties, but Q' and $\Delta\beta/\beta$ can be independently adjusted with the two variables. The vector diagrams of each scheme are summed up in Table 1.

4. CONTROL OF THE BETATRON FREQUENCIES

To control the variations of the betatron frequencies with $\Delta p/p$ requires two variables only : K'_F and K'_D. In order to incorporate the principle outlined in the previous section, two families of sextupoles are distributed in 84 regular cells or 14 A-groups. The structure of the superperiod is

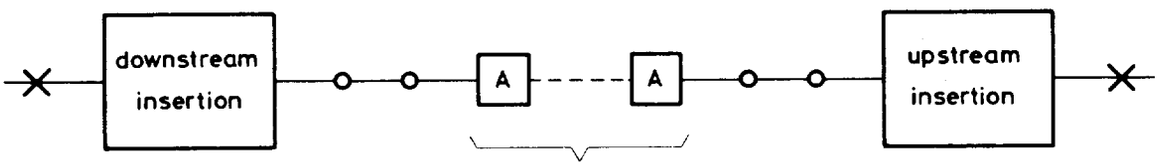

The symbol -O- denotes a cell without sextupoles. The superperiod is no longer symmetric because the cell is asymmetric since the sextupoles are placed on one side of their corresponding quadrupole. The system of correction equations can be written

$$S\,\overline{k'} = \overline{q}\ ,$$

where S is a matrix of sextupole coefficients,

$$\overline{k'} = \begin{pmatrix} K'_F \\ K'_D \end{pmatrix}$$

and

$$\overline{q} = \begin{pmatrix} Q'_x \\ Q'_y \end{pmatrix}$$

is the sum of the quadrupole contributions and of the wanted chromaticity. In the case where the residual chromaticity is zero in both planes,

$$K'_F = -0.219726\ m^{-3} \qquad K'_D = 0.470953\ m^{-3}$$

for a sextupole length of 0.5 m. The variations of

$$DQ = Q(\Delta p/p) - Q(0)$$

and

$$\frac{D\beta}{\beta} = \frac{\beta(\Delta p/p) - \beta(0)}{\beta(0)}$$

are plotted in Figures 3, 4 and 5. The high order terms in $\Delta p/p$ are very important and must be attenuated. Octupoles and decapoles could be added in order to cancel the terms in $(\Delta p/p)^2$ and $(\Delta p/p)^3$; that measure would be appropriate if these terms had their origin in the defect of focusing strength of the quadrupoles. However, the observed variations are considerably stronger and are generated by the sextupoles. It is preferable to optimize the sextupole scheme to take this effect into account rather than to correct the initial scheme.

5. ADDITIONAL CONTROL OF THE BETATRON AMPLITUDE

The previous scheme was simple but rigid. An efficient way of making it more flexible consists of controlling the β function. A harmonic method[8,9] of correction of $\Delta\beta/\beta$ is possible but not well adapted because the perturbation is very localized, essentially in the D-quadrupoles adjacent to the crossing point, and has an associated spectrum too rich in harmonics. It is more drastic and simpler to cancel all the widths of the gradient stopbands by prolonging the insertion into the normal lattice and matching it to regular cells. This method had already been sketched in reference 9. The structure of the superperiod is then

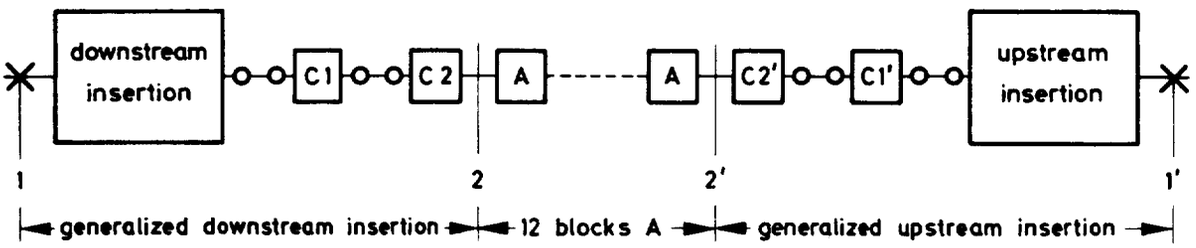

Since the β function perturbation is vector-like, two blocks C are required in a generalized insertion ; they are independent since their relative phase shift is $4\pi/3$ for the β fluctuation. The upstream generalized insertion is geometrically symmetric with respect to the downstream one but the sextupole strengths are not necessarily the same because α ($= -\frac{1}{2}\, d\beta/ds$) at the points 2 and 2' is fixed by the cell and may be different from zero. The matching of each insertion to the cells requires four equations per plane. The equations express the continuity of β and α at points 2 and 2' ; they can be written :

$$\left.\frac{\Delta\beta_2}{\beta_2}\right|_s^t + \left.\frac{\Delta\beta_2}{\beta_2}\right|_q^t = \left.\frac{\Delta\beta_2}{\beta_2}\right|_s^c + \left.\frac{\Delta\beta_2}{\beta_2}\right|_q^c$$

$$\left.\Delta\alpha_2\right|_s^t + \left.\Delta\alpha_2\right|_q^t = \left.\Delta\alpha_2\right|_s^c + \left.\Delta\alpha_2\right|_q^c \quad ,$$

where q, s, t and c stand for quadrupole, sextupole, downstream insertion and cell. A similar set is to be repeated for the upstream insertion ; t and 2 are then replaced by t' and 2'. The two variables which are available in blocks A are used to control the chromaticity. The matrix S of the sextupole coefficients has now ten rows and ten columns. The detailed calculation of the various perturbations relies upon the formulae derived in reference 5. The α and β tracking is performed from the crossing point ; the starting values of $d\alpha/d(\Delta p/p)$ and $d\beta/d(\Delta p/p)$ are set to zero and the linear variation of β^* vanishes.

This scheme represents an improvement with respect to the previous one from the point of view of β variations. However, the most interesting point may be the behaviour of the Q variations which was first observed with a machine whose β_y^* was 5 cm. In section 3, it was seen that $D\beta/\beta$ could be controlled with either B- or C-blocks. The two schemes were tested. The results are shown in Figure 6 ; the source of so considerable a difference between the two schemes can be found by comparing the structure of the two blocks.

If the reference sign of the sextupole strength is this of the sextupole located in the second cell, it must be the same in both cases since the defect to be corrected is always the mismatch of the insertion due to quadrupole focusing errors. The combination of the sextupoles in groupings of type C is twice as efficient as the B combination ; so, if the reference sextupole strength is expected to be K' for C, it will be 2K' for B ; the associated chromaticity is then $-4\Delta Q'$ for C and $4\Delta Q'$ for B. It is therefore natural to think of a correlation between the variations of ΔQ and the chromaticity of the sextupoles located in the insertion. This hypothesis will be checked in the next section.

6. INDEPENDENT CONTROL OF Q AND β IN THE INSERTION AND IN THE CELL

In this last scheme, Q' is controlled separately in the generalized insertion and in the periodic part of the machine. In order to complete its flexibility, $d(\Delta\beta/\beta)/d(\Delta p/p)$ and $d\alpha/d(\Delta p/p)$ are assigned to fixed values at points 2 and 2'. The system of correction has 2 × 9 equations :

$$\text{downstream insertion} \begin{cases} \Delta Q\big|_s^t + \Delta Q\big|_q^t = aQ' \\ \dfrac{\Delta\beta_2}{\beta_2}\Big|_s^t + \dfrac{\Delta\beta_2}{\beta_2}\Big|_q^t = \dfrac{\Delta\beta_2}{\beta_2} \\ \Delta\alpha_2\big|_s^t + \Delta\alpha_2\big|_q^t = \Delta\alpha_2 \end{cases}$$

$$\text{period} \begin{cases} \Delta Q\big|_s^c + \Delta Q\big|_q^c = (1 - a - b)Q'/N \\ \dfrac{\Delta\beta_2}{\beta_2}\Big|_s^c + \dfrac{\Delta\beta_2}{\beta_2}\Big|_q^c = \dfrac{\Delta\beta_2}{\beta_2} \\ \Delta\alpha_2\big|_s^c + \Delta\alpha_2\big|_q^c = \Delta\alpha_2 \end{cases}$$

$$\text{upstream insertion} \quad \begin{cases} \Delta Q\big|_s^{t'} + \Delta Q\big|_q^{t'} = bQ' \\ \dfrac{\Delta\beta_2}{\beta_2}\Big|_s^{t'} + \dfrac{\Delta\beta_2}{\beta_2}\Big|_q^{t'} = \dfrac{\Delta\beta_2}{\beta_2} \\ \Delta\alpha_2\big|_s^{t'} + \Delta\alpha_2\big|_q^{t'} = \Delta\alpha_2 \end{cases}$$

N is the number of periods. The constants a, b, $\Delta\beta_2/\beta_2$ and $\Delta\alpha_2$ are determined by trial and error until the optimum Q distribution is found. Three variables are required in each region. They are provided by superimposing two blocks A and two blocks B separated by two cells without sextupoles.

(A)	1	1	1	1	1	1	0	0	1	1	1	1	1	1
(B)	0	1	0	0	1	0	0	0	0	2	0	0	2	0
				(B1)							(B2)			
(D) = (A) + (B)	1	2	1	1	2	1	0	0	1	3	1	1	3	1

Sextupoles of the same index are connected in series. The superperiod has the following structure :

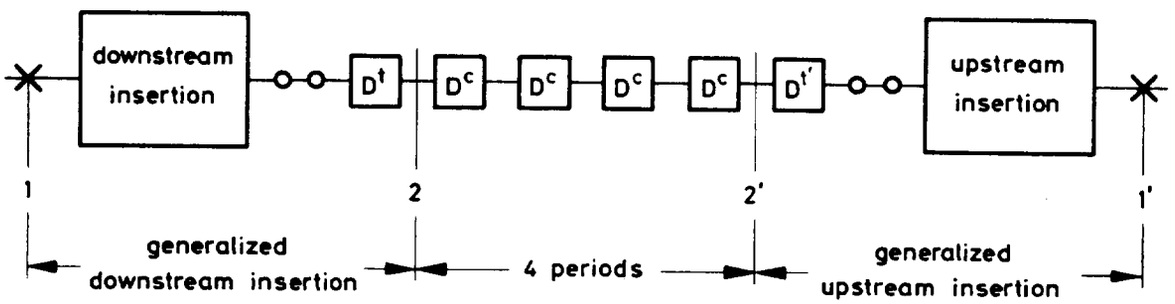

For a momentum spread of ±5 o/oo, an optimum Q distribution was found for

$$a_x = b_x = 0.379 \qquad \frac{\Delta\beta_2}{\beta_2}\Big|_x = 0 \qquad \Delta\alpha_{2_x} = -2.82\,\frac{\Delta p}{p}$$

$$a_y = b_y = 0.0527 \qquad \frac{\Delta\beta_2}{\beta_2}\Big|_y = 36\,\frac{\Delta p}{p} \qquad \Delta\alpha_{2_y} = 0 \ .$$

The exact location of the sextupoles in half a superperiod is represented in Figure 11. They are 0.5 m long. The values of $K'_y(m^{-3})$ are given in the following table.

Type	Number p super-period	K'_y	Type	Number p super-period	K'_y	Type	Number p super-period	K'_y
SF1	8	-0.374797	SF4	32	-0.203121	SF1'	8	-0.410757
SD1	2	0.500476	SD4	32	0.761692	SD1'	8	0.510187
SF2	2	-0.058069	SF5	8	-0.142142	SF2'	2	0.007997
SD2	2	1.994508	SD5	8	0.234010	SD2'	2	2.034118
SF3	2	0.090052	SF6	8	-0.289198	SF3'	2	0.167825
SD3	2	-2.539304	SD6	8	0.229185	SD3'	2	2.617755

The variations of DQ and $D\beta/\beta$ at the intersection and in the period are represented in Figures 7, 8 and 9. The tune spread is less than 0.015. At the crossing point, the beam is thinner on the off-momentum orbits than on the central orbit, the luminosity is accordingly a little enhanced with respect to the figure deduced from central orbit parameters. In the optimisation process, it was found that the cubic component of DQ was cancelled by adjusting the parameter a ; the quadratic component was simultaneously reduced but was definitely eliminated by varying $\Delta\beta_2/\beta_2$. The linear variation of $\Delta\beta_2/\beta_2$ with $\Delta p/p$ has an adverse effect on some of the tolerances to be imposed to the magnets but remains quite acceptable. It could be removed but an octupole field would then be needed to correct the remanent quadratic component.

In the following, this scheme will be referred to as the reference scheme.

7. OPERATION AT ENERGIES BELOW 100 GeV

An electron-positron ring must be continuously adjustable in a wide range of energy and the natural loss of luminosity when the energy is decreased must be compensated.

One way of overcoming the luminosity loss consists of using a system of wiggler magnets[10], which may increase the momentum spread. Although this effect is rather weak (10 %) in the present machine, it was tried to see what maximum momentum spread could be compatible with the chromaticity requirements and a new optimisation was performed for

$$-0.008 \leqslant \frac{\Delta p}{p} \leqslant +0.008 \quad .$$

The DQ variations are plotted in Figure 10. The uniformity of DQ_x is obtained by superimposing octupoles on the sextupoles. The octupoles are connected according to the scheme described in section 4 for the sextupoles. Their strength K''_y expressed in m^{-4} is

$$K''_F = 1.23789 \qquad K''_D = -1.13308 \ .$$

$|DQ_{max}|$ is just below 0.06 ; this is precisely the value of the synchrotron frequency which is considered as a measure of the maximum permissible fluctuations of the betatron frequencies. Figure 11 represents the azimuthal variations of β_x, β_y and η on the orbit corresponding to $\Delta p/p = -0.008$. The graph is limited to the downstream insertion and the first of the four periods of a superperiod. It illustrates the damping of the β_y perturbation which is really considerable since it reaches 330 % in the insertion and is more than three times higher than that predicted by the first order perturbation theory (§3).

An alternative or a complement to the wiggler system is an adjustable low-β insertion. It was mentioned in the introduction that the value of β^*_y had been augmented with respect to its optimum value for luminosity in order to have a longer lifetime τ. However, when limited by the beam-beam Bremsstrahlung, τ increases when the energy decreases[11,12]. So, at constant τ, β^*_y can be diminished to counteract the luminosity loss. Figure 12 shows the DQ variations of a machine for which

$$\beta^*_x = 1.25 \text{ m} \qquad \beta^*_y = 0.05 \text{ m} \ .$$

They are quite comparable to those of the reference scheme. The same statement applies to the β variations.

Here also, an octupole field is added to the sextupole field and the strengths $K''_y(m^{-4})$ are

$$K''_F = 2.65209 \qquad K''_D = -8.53142 \ .$$

8. CONCLUSION

A scheme of sextupoles has been determined to correct the chromaticity of very high energy $e^+ - e^-$ rings. In special circumstances, octupoles may have to be employed. The procedure followed could be applied to other types of machine. Special attention, however, has to be given to the betatron phase advance per

cell, μ, which plays a permanent underlying role in the method. An appropriate grouping of the sextupoles can easily be found each time μ is a simple fraction of π. A difficulty arises where μ is equal to $\pi/2$ because the control of β by the matching of the insertion to the period of the machine is no longer possible. Unfortunately, $\pi/2$ is a usual choice for the new projects of proton machines. The perturbations, however, are less violent in proton machines than in electron machines, and it may be sufficient to use the first two steps of the method by taking advantage of the fact that, within an insertion, one can generally find a few places where the dispersion is finite and the phase shift adequate.

REFERENCES

1) B. RICHTER, Very high energy electron-positron colliding beams for the study of the weak interactions, Divisional Report CERN ISR-LTD/76-9 (1976).

2) E. KEIL, LEP parameter list, Divisional Report CERN ISR-LTD/76-17 (1976).

3) J. REES and B. RICHTER, SLAC Report No. PEP-69 or SPEAR-167 (October 1973).

4) E. KEIL, Private communication.

5) B. AUTIN and A. VERDIER, Focusing perturbations in alternating gradient structures, Divisional Report CERN ISR-LTD/76-14 (1976).

6) R.W. CHASMAN, E.D. COURANT and M. MONTH, Effects in low periodicity lattices resulting from low β insertions, 1975 Particle Accelerator Conference, Washington D.C., March 12-14 (1975).

7) L. DI LELLA et al., Performance Study on Proton-Proton Storage Rings at several hundred GeV/c, Divisional Report CERN ISR-AS/74-64 (1974).

8) D. EDWARDS, S. OHNUMA and L.C. TENG, Compensation of chromatic aberrations in a single period lattice, IEEE Trans. on Nucl. Sci. NS-22, 1426 (1975).

9) B. AUTIN and A.A. GARREN, Chromaticity corrections for large Proton Storage Rings at CERN, Divisional Report CERN ISR-GS-MA/75-32 (1975).

10) A. HUTTON, Maintaining constant luminosity in Electron Storage Rings using wiggler magnets, Divisional Report CERN ISR-LTD/76-20 (1976).

11) H. MEYER and A. WRULICH, Lifetime due to the beam-beam Bremsstrahlung effect, PET/75-2 (January 1975).

12) PEP Design Report, SLAC (1976).

Type	Connection	Orbit	β-perturbation	3rd-order resonances	4th-order resonances (octupoles)
A	1 1 1 1 1 1	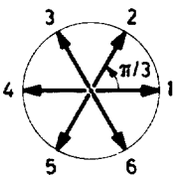	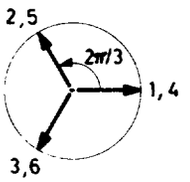		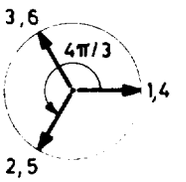
B	0 1 0 0 1 0			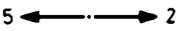	
C	-1 1 -1 -1 1 -1	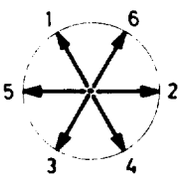	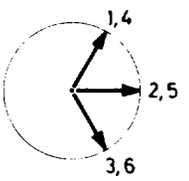		
D	1 2 1 1 2 1	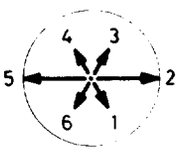	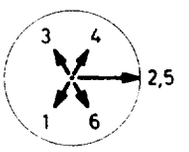	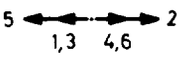	

Table 1 - Vector diagrams of the perturbations caused by various blocks of sextupoles (or octupoles). Within a block, all the lenses of same index are connected in series ; the sign - means reversed polarity. The figure at the end of each arrow denotes the number of the cell.

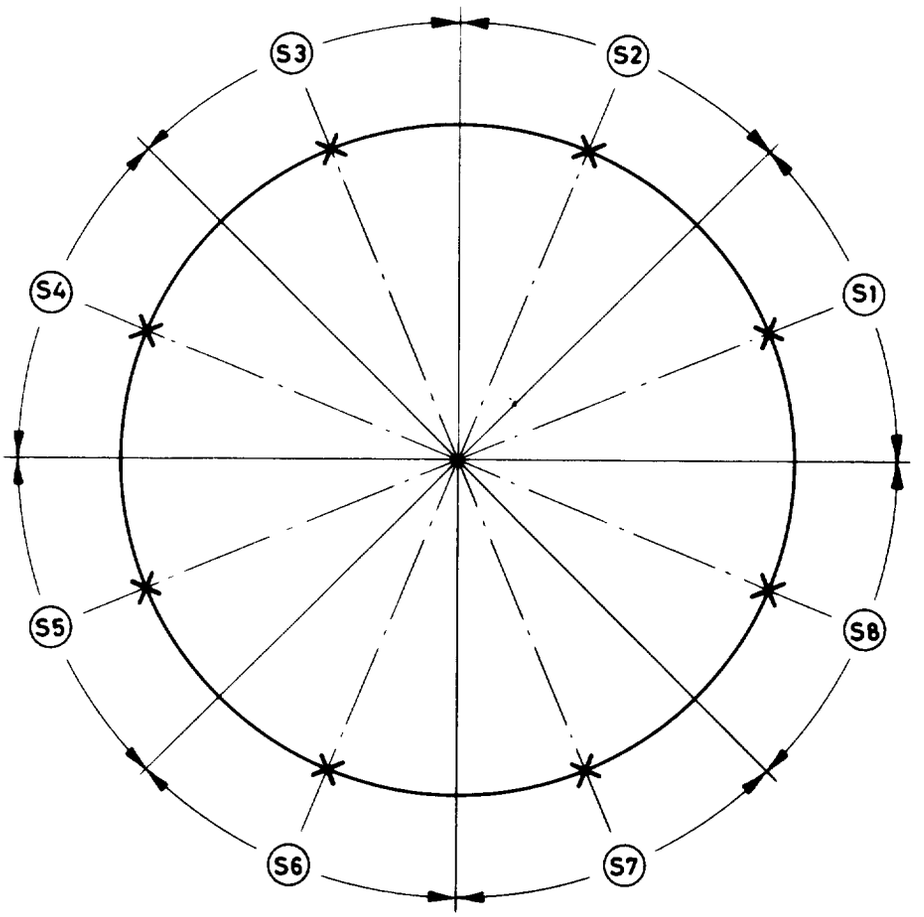

S : superperiod

X : crossing point

Figure 1 - Symmetry of the machine

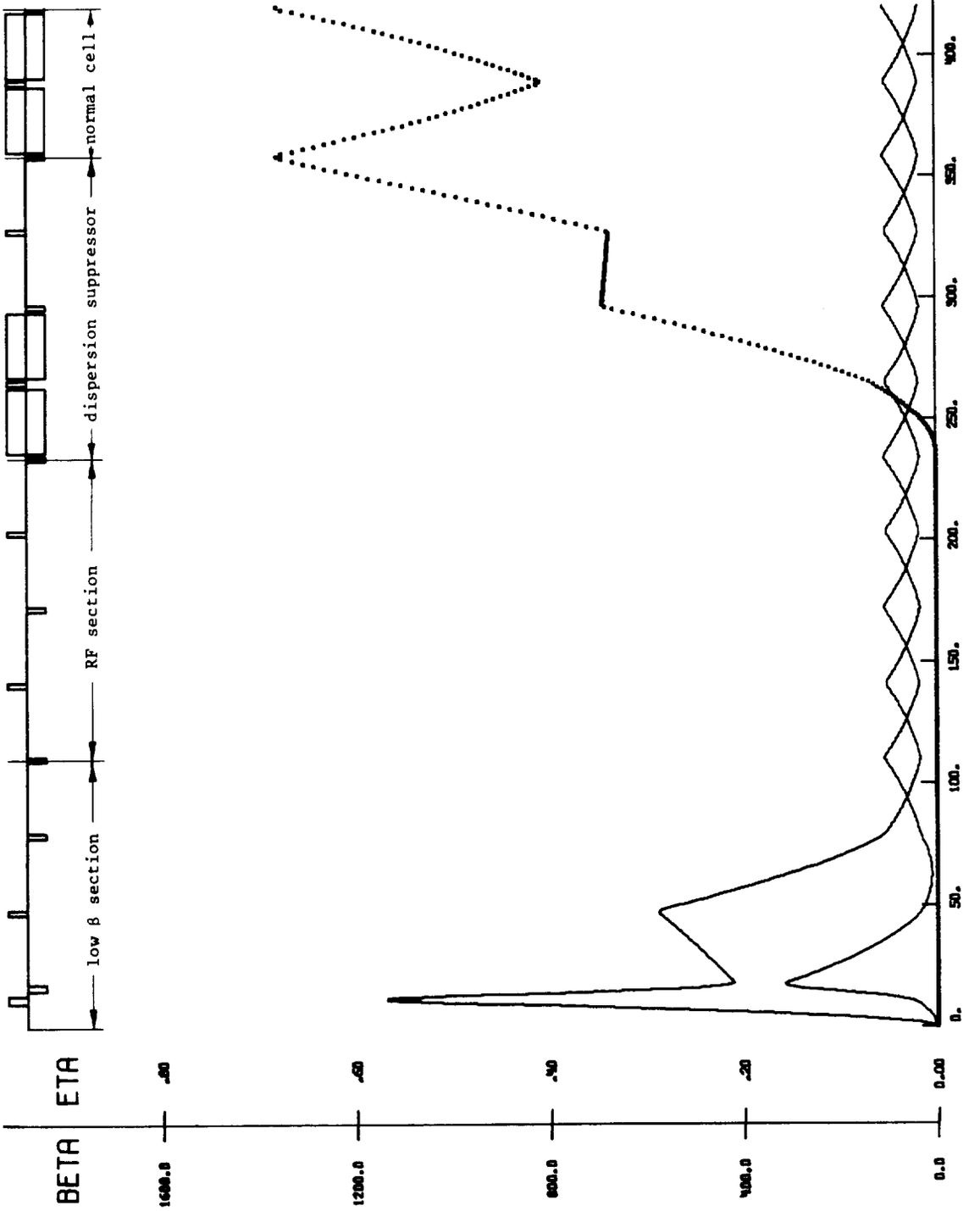

Figure 2 - Structure functions on the central orbit

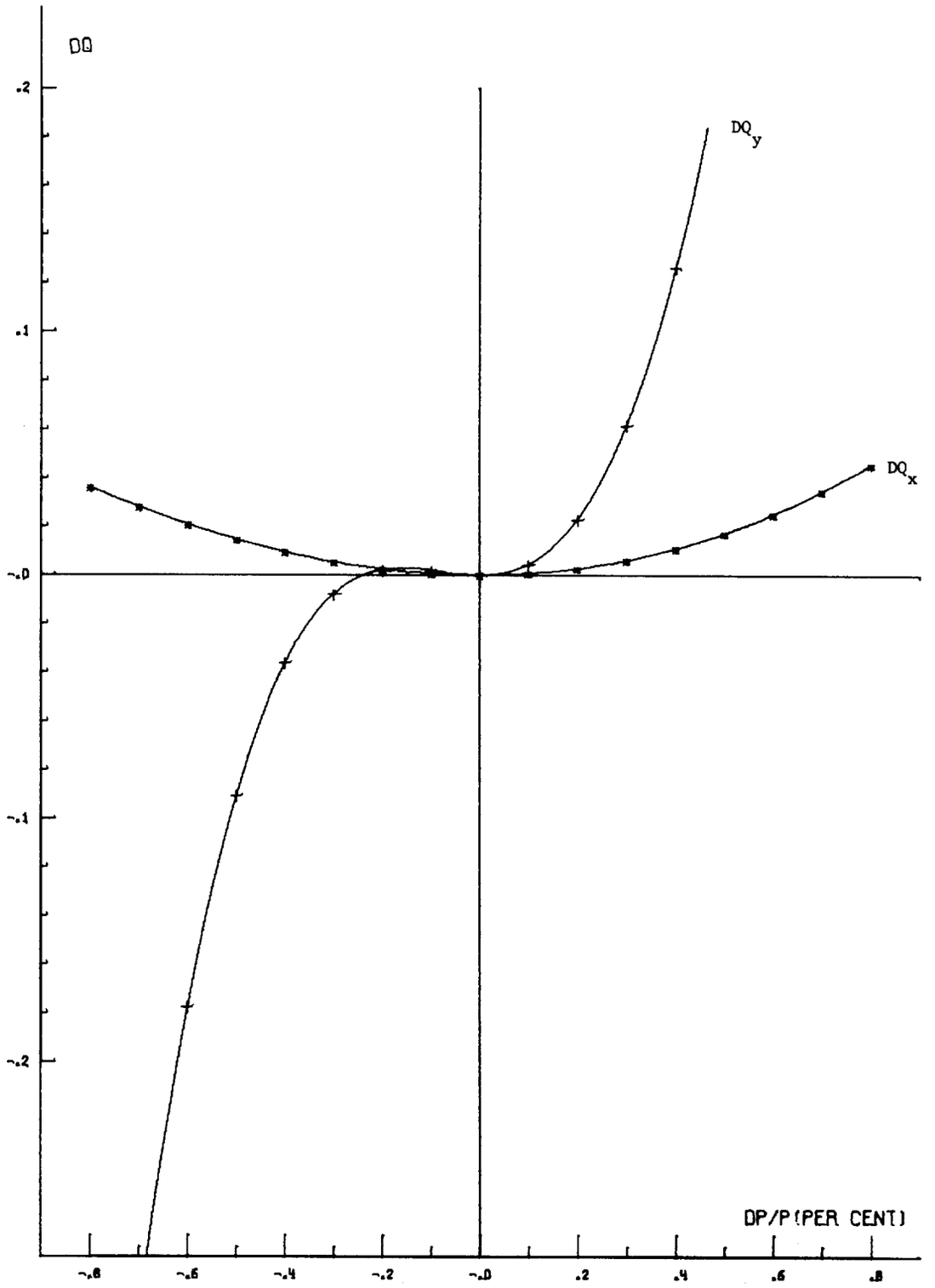

Figure 3 - DQ = f(Δp/p) for the scheme 1 (§4)

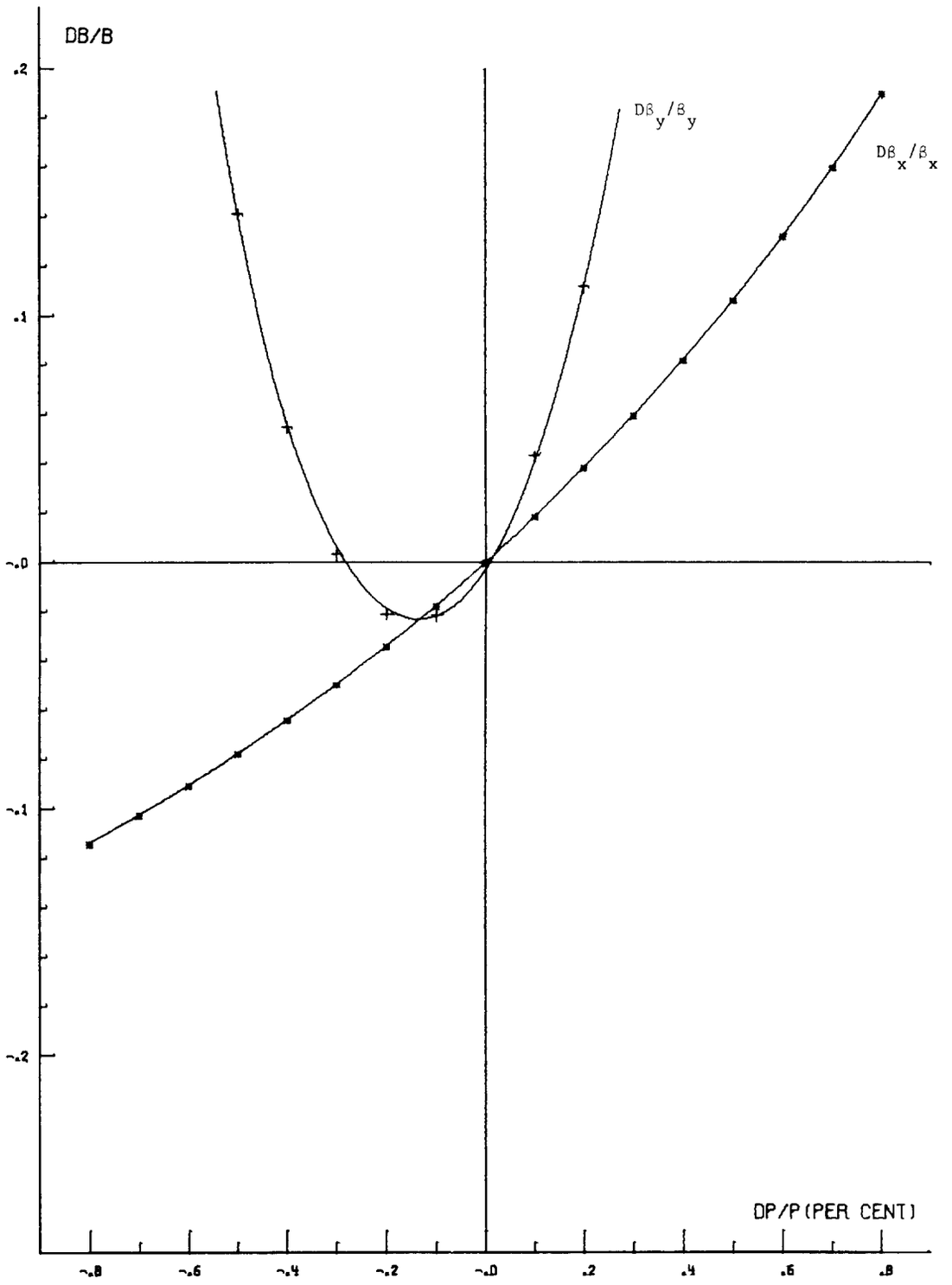

Figure 4 - $D\beta/\beta = f(\Delta p/p)$ at the crossing point for the scheme 1 (§4)

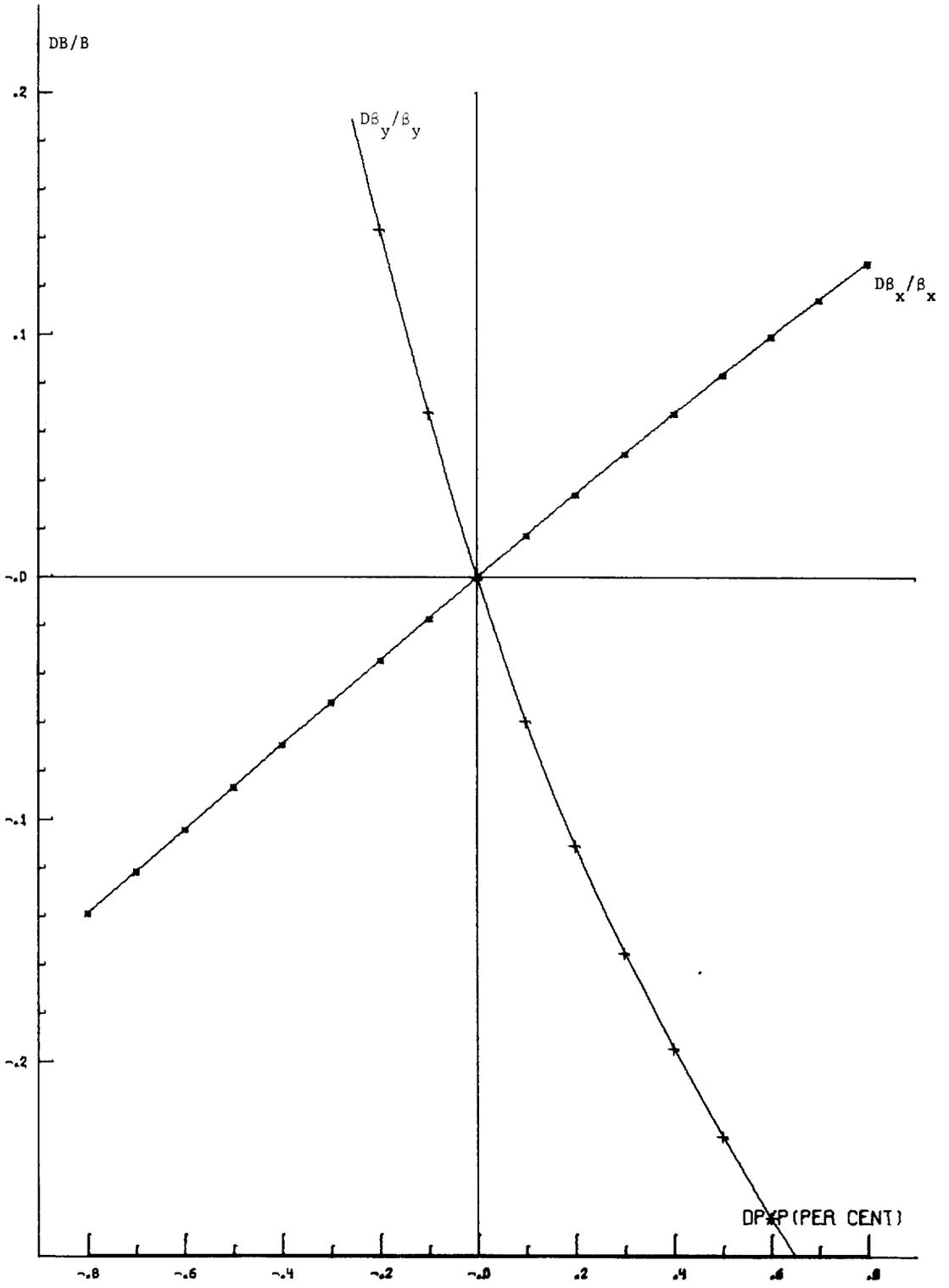

Figure 5 - $D\beta/\beta = f(\Delta p/p)$ in the F quadrupole of a normal cell for the scheme 1 (§4)

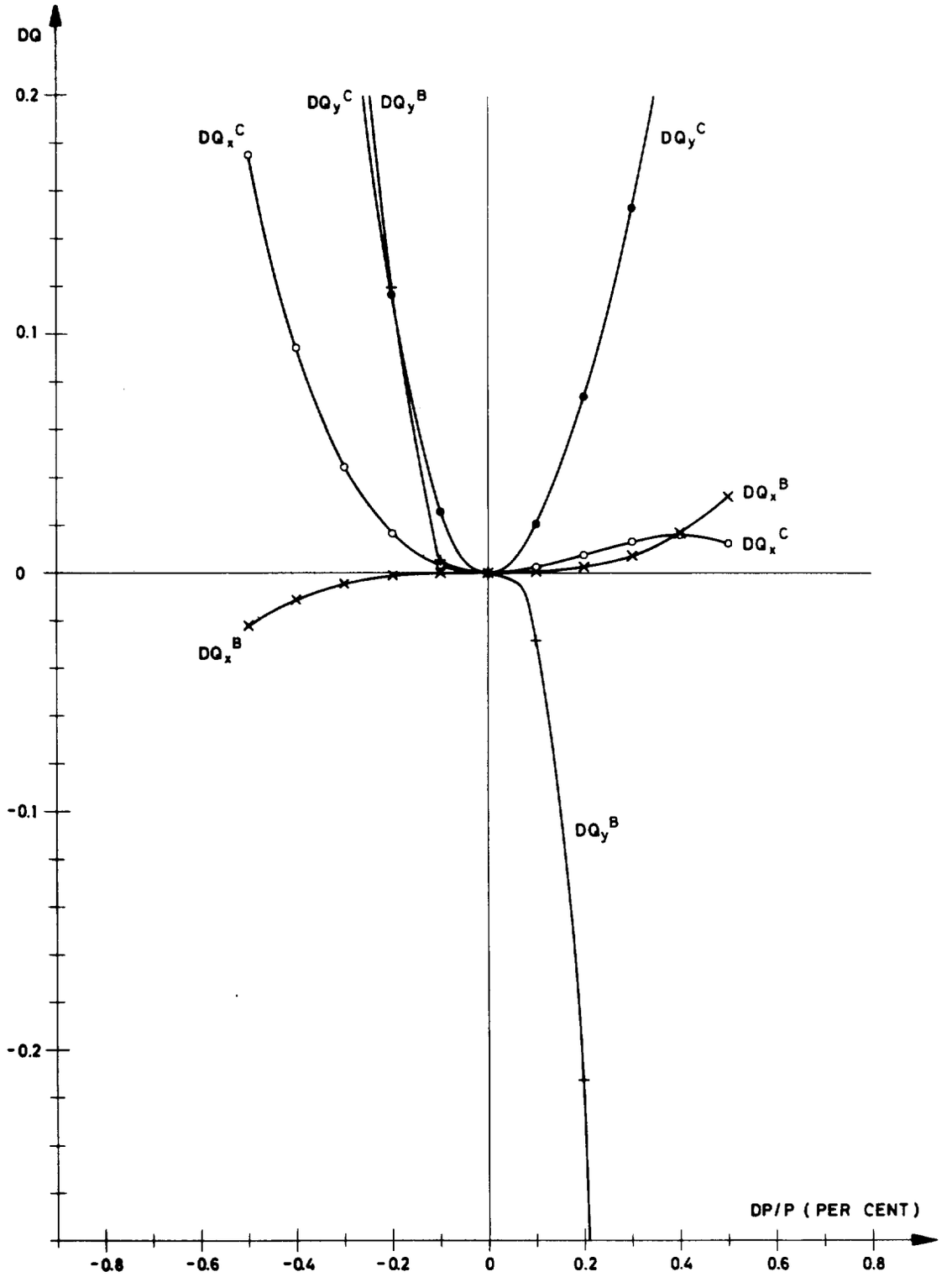

Figure 6 - DQ = f(Δp/p) for the scheme 2 (§5). Superscripts B and C refer to the type of sextupole groupings used in this scheme.

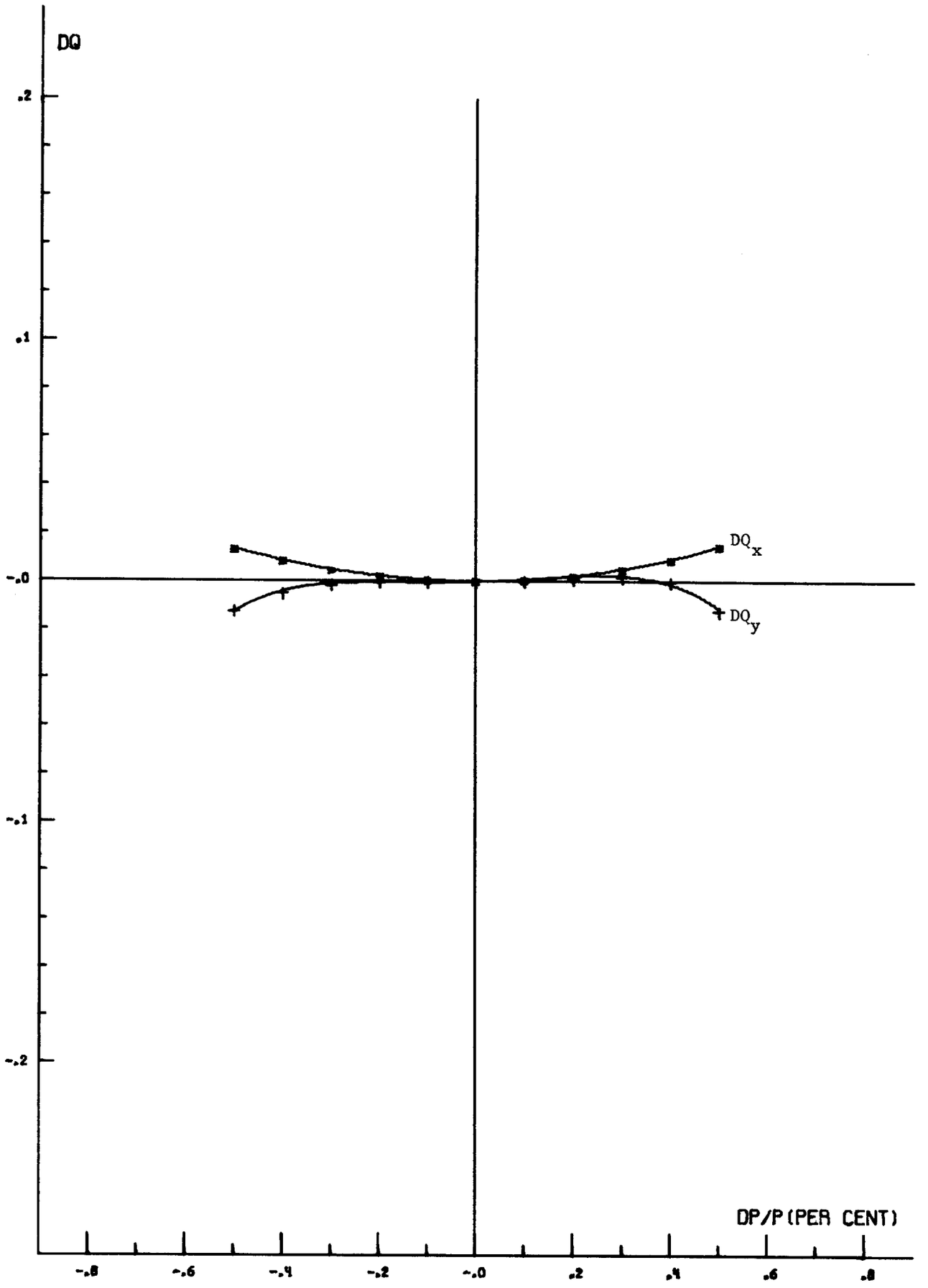

Figure 7 - DQ = f(Δp/p) for the reference scheme (§6)

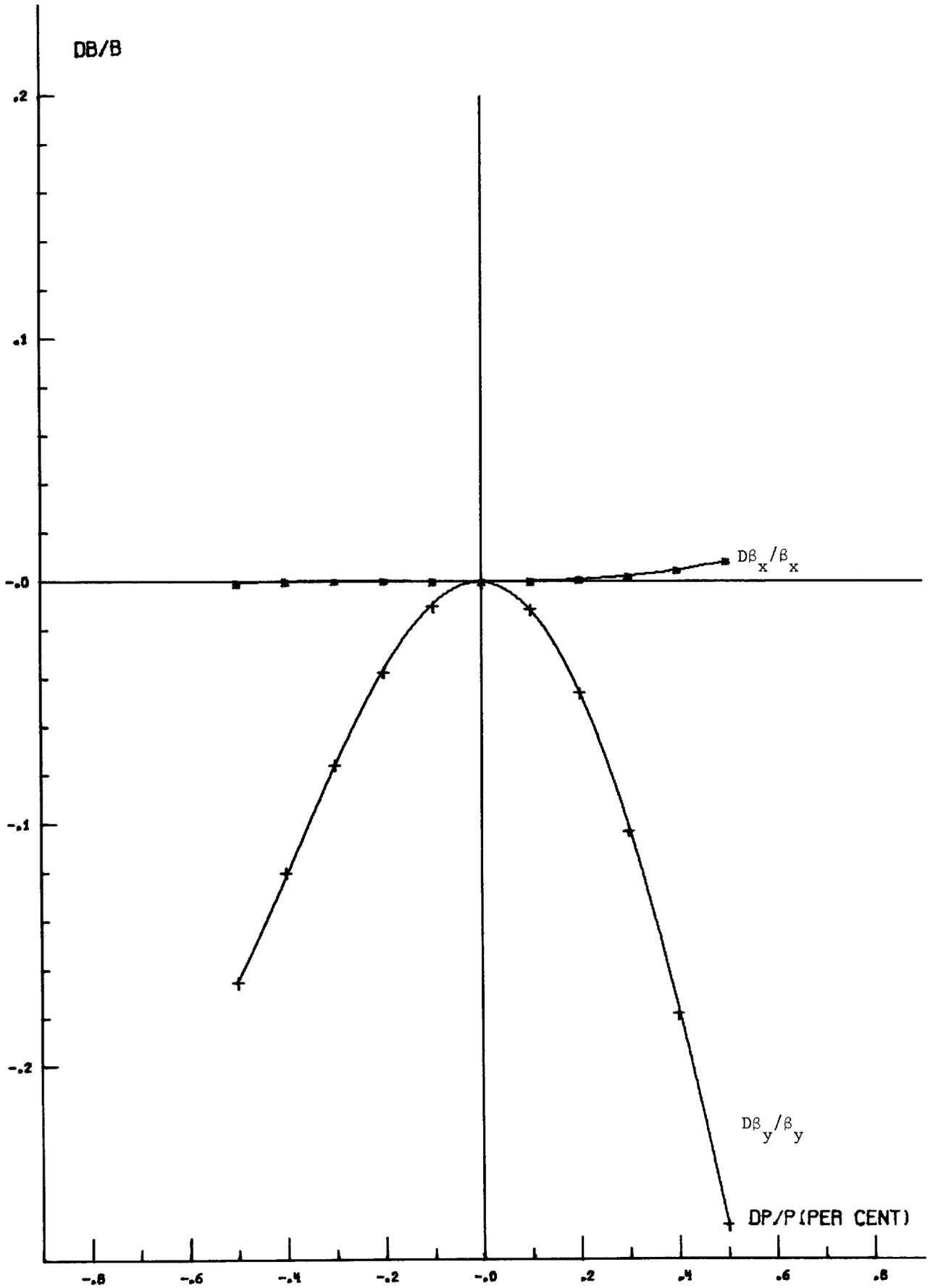

Figure 8 - $D\beta/\beta = f(\Delta p/p)$ at the crossing point for the reference scheme (§6)

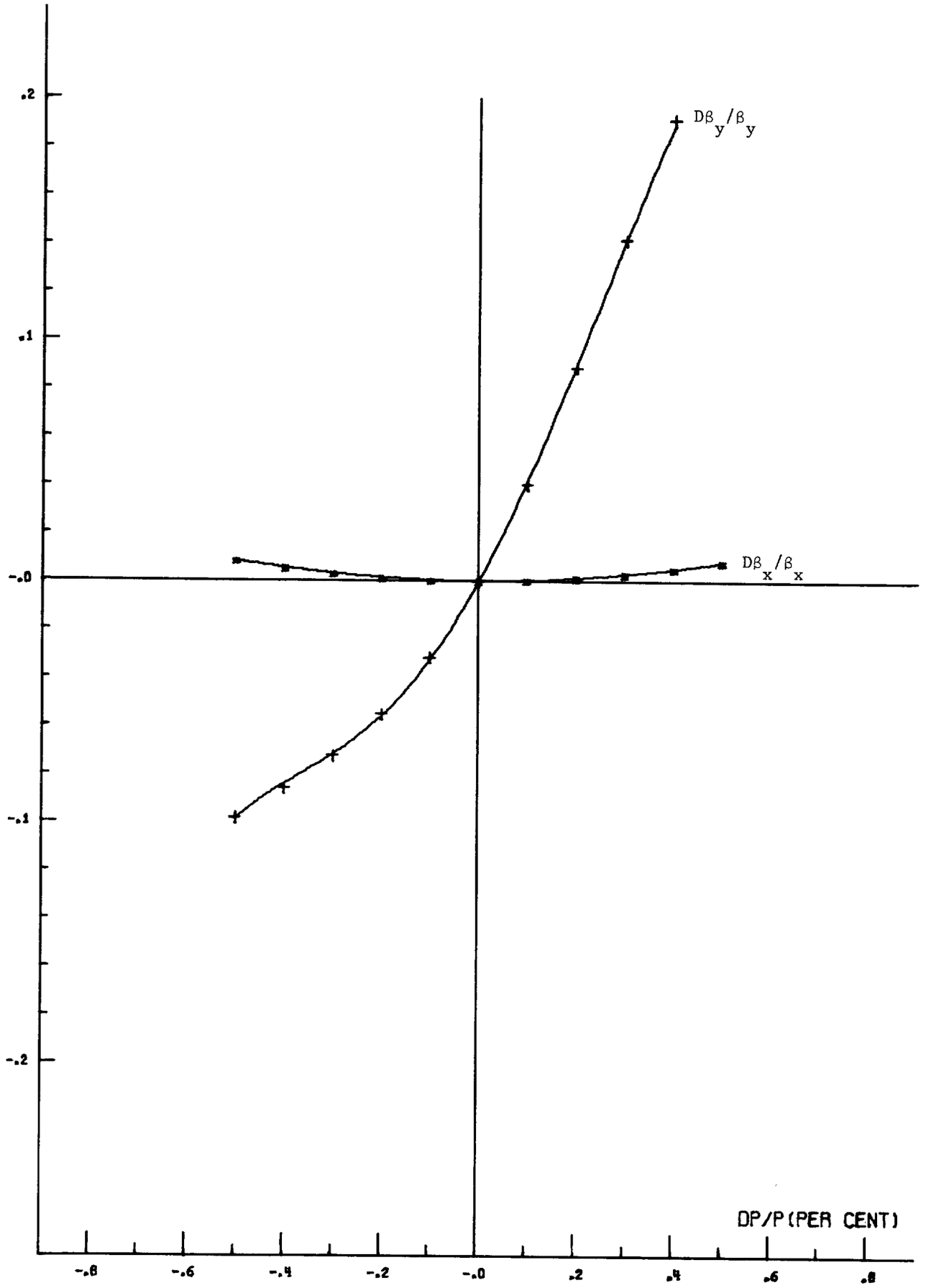

Figure 9 - $D\beta/\beta = f(\Delta p/p)$ at the end of a period for the reference scheme (§6)

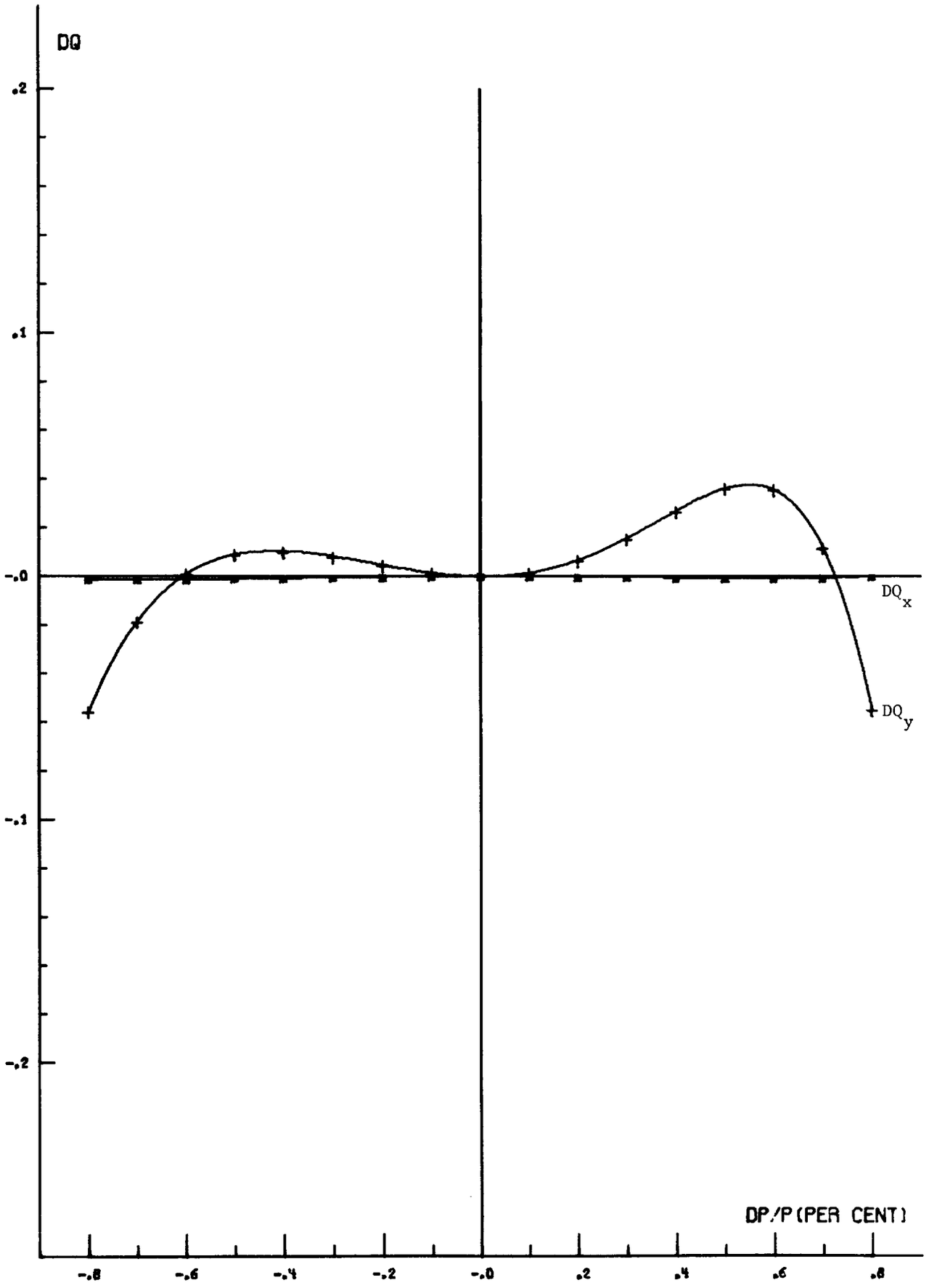

Figure 10 - DQ = f(Δp/p). The sextupole scheme is optimized for a momentum range : $-0.008 \leqslant \Delta p/p \leqslant +0.008$ (§7)

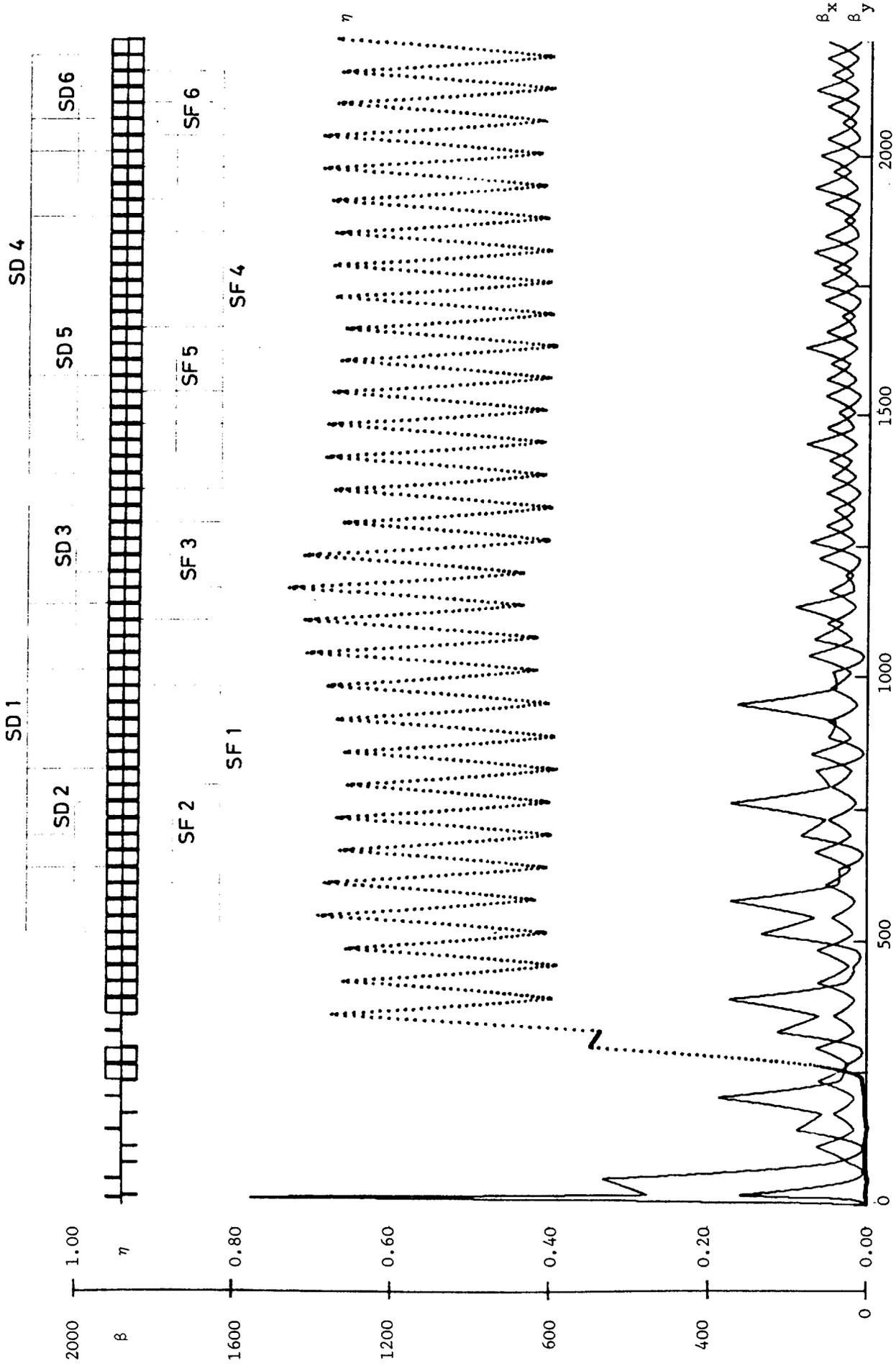

Figure 11 - Structure functions on an off-momentum orbit ($\Delta p/p = -0.008$) (§7)

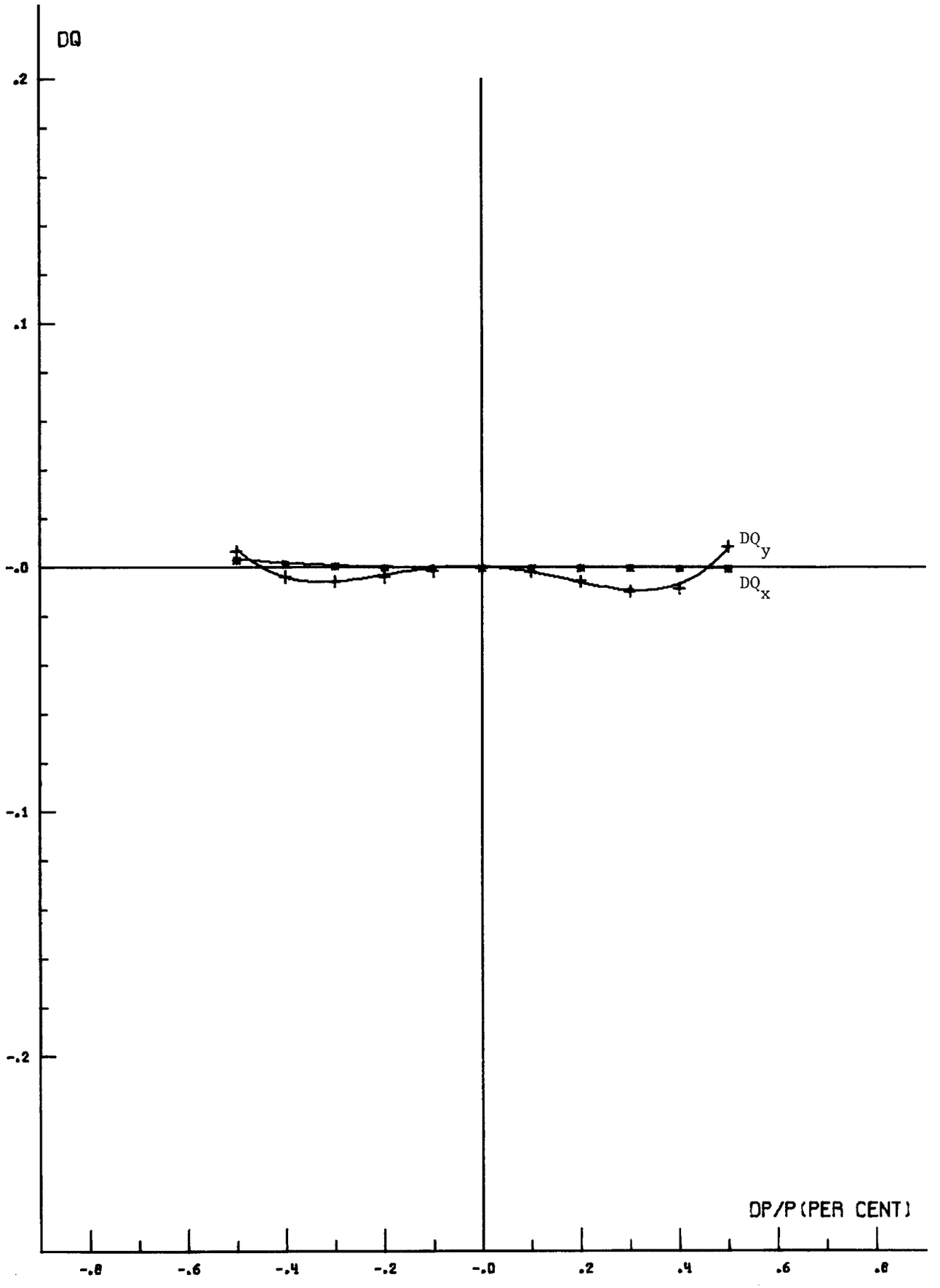

Figure 12 - DQ = f(Δp/p) for β_y^* = 5 cm and β_x^* = 1.25 m (§7)

APPENDIX 4

EUROPEAN ORGANIZATION FOR NUCLEAR RESEARCH

CERN/ISR-LTD/76-20

MAINTAINING CONSTANT LUMINOSITY IN ELECTRON STORAGE RINGS USING WIGGLER MAGNETS

by

A. Hutton

Geneva - June, 1976

1. INTRODUCTION

In e^+-e^- storage rings the luminosity decreases as the fourth power of the energy if the lattice configuration remains constant. Various ways of modifying the lattice have been suggested in order to improve this situation [1,2], usually with the aim of keeping the beam size constant which means that the luminosity decreases as the square of the energy. In this paper the possibility of maintaining the luminosity constant using wiggler magnets is examined and the consequences on the emittance, the energy spread of the beam and the beam current are examined. It is assumed that the intersection region is dispersion free so that the beam size at the intersection is only due to betatron oscillations.

2. LUMINOSITY EQUATIONS

The luminosity in e^+-e^- storage rings is given by [3]

$$L = \frac{N^2 f}{4\pi k \sigma_x^* \sigma_y^*} \tag{1}$$

where N is the total number of particles per beam (assumed equal), f is the revolution frequency, σ_x^* and σ_y^* are the rms horizontal and vertical beam radii at the interaction point and k is the number of bunches in one beam.

The beam-beam tune shift is given by [3]

$$\Delta Q_x = \frac{N r_e \beta_y^*}{2\pi k(\sigma_x^* + \sigma_y^*) \sigma_y^* \gamma} \tag{2}$$

$$\Delta Q_y = \frac{N r_e \beta_y^*}{2\pi k(\sigma_x^* + \sigma_y^*) \sigma_x^* \gamma} \tag{3}$$

where r_e is the classical radius of the electron and γ is the ratio of the electron energy to the rest mass of the electron. In general $\sigma_x^* >> \sigma_y^*$ and if we define the horizontal emittance ε_x as

$$\varepsilon_x = \frac{\sigma_x^2}{\beta_x} \tag{4}$$

equation (2) reduces to

$$\Delta Q_x = \frac{r_e}{2\pi k} \quad \frac{N}{\varepsilon_x \gamma} \tag{5}$$

and combining Eqs. (1) and (3) gives

$$\Delta Q_y = \frac{2\beta_y^*}{f} \frac{L}{N\gamma} \tag{6}$$

It is assumed that the electron storage ring is operated at the maximum allowable beam tune shift in both planes. Then Eqs. (5) and (6) give the relevant energy scaling laws for constant luminosity,

$$N \propto \frac{1}{\gamma} \qquad \varepsilon_x \propto \frac{1}{\gamma^2} \tag{7}$$

Thus the beam current should increase with decreasing energy (i.e. the stored energy of the beam will be constant) and the beam dimensions will increase as the inverse of the energy. Together, this implies that the current density decreases proportionally to the energy.

As is well known, wiggler magnets provide an effective means of increasing the emittance, however, there is one inherent difficulty. It is clear from Eq. (6) that the beam tune shift is reduced if β_y^* is minimized, and all electron storage rings follow this principle. This produces a very large value of β_y in the adjacent quadrupoles introducing a large achromaticity which is very difficult to correct. In general, correction is only possible over a small range of energy errors and the energy spread of the beam must be within these limits. Unfortunately use of wiggler magnets to increase the emittance has the necessary side effect of increasing the energy spread of the beam. The relative size of these effects depends on the precise location of the wiggler magnets and it is possible to obtain constant luminosity whilst maintaining the relative energy spread within reasonable limits.

3. EQUATIONS GOVERNING THE ENERGY SPREAD AND EMITTANCE

The equation for the relative energy spread is given by [3]

$$\delta = \frac{\sigma_\varepsilon}{E} = \left[\frac{55}{32\sqrt{3}} \frac{\hbar}{mc} \frac{\gamma^2}{J_\varepsilon} \frac{\langle|1/\rho^3|\rangle}{\langle 1/\rho^2\rangle}\right]^{\frac{1}{2}} \tag{8}$$

where J_ε is the energy damping partition coefficient (≈ 2 in an isomagnetic guide field), ρ is the radius of curvature ($< >$ indicates an average round the ring), m is the mass of the electron and $\hbar$ and c have their usual significance. In the case of an isomagnetic guide field of radius of curvature ρ_0 of total

length $L_0 = 2\pi\ \rho_0$ with an equal field wiggler of radius of curvature ρ_w and length L_w, the energy spread δ at energy E can be related to the energy spread δ_0 at the maximum energy E_0 where the wiggler is not excited by

$$\frac{\delta}{\delta_0} = \frac{E}{E_0}\left[\frac{1 + \frac{L_w}{L_0}\left(\frac{\rho_0}{\rho_w}\right)^3}{1 + \frac{L_w}{L_0}\left(\frac{\rho_0}{\rho_w}\right)^2}\right]^{\frac{1}{2}} \tag{9}$$

The equation for the horizontal emittance ε_x is given by [3]

$$\varepsilon_x = \frac{55}{32\sqrt{3}}\ \frac{\hbar}{mc}\ \frac{\gamma^2}{J_x}\ \frac{\langle |1/\rho|^3\ W\rangle}{\langle 1/\rho^2\rangle} \tag{10}$$

where W is the Courant and Snyder Invariant (also denoted by $\mathcal{H}$) given by

$$W = \frac{\alpha_p^2 + (\alpha\ \alpha_p + \beta\ \alpha_p')^2}{\beta} \tag{11}$$

where α, β, α_p and α_p' are the standard betatron functions. Comparing the emittance ε_x to the emittance ε_{x0} at E_0 gives

$$\frac{\varepsilon_x}{\varepsilon_{x0}} = \frac{E^2}{{E_0}^2}\ \frac{1 + \frac{L_w}{L_0}\left(\frac{\rho_0}{\rho_w}\right)^3 \frac{W_w}{W_0}}{1 + \frac{L_w}{L_0}\left(\frac{\rho_0}{\rho_w}\right)^2} \tag{12}$$

where $\frac{W_w}{W_0}$ is the ratio of the invariant in the wiggler to the average lattice value. It is clear that the relative changes of emittance and relative energy spread with energy can only be affected by the value of $\frac{W_w}{W_0}$.

4. RELATIONSHIP BETWEEN EMITTANCE AND RELATIVE ENERGY SPREAD

We will now examine in detail the behaviour of Eqs. (9) and (12) as a function of $\frac{W_w}{W_0}$ and particularly the behaviour of the emittance at constant relative energy spread and vice versa. It turns out that the relative effect is independent of wiggler length for values of less than a few per cent of the lattice bending length. A value of 1% is used in the following graphs and values of the W ratio of 1, 2, 3 and 4 will be considered. In Fig. 1 the emittance ratio for constant relative energy spread is shown and in Fig. 2 the luminosity variation under these conditions. It is clear that a considerable gain in

luminosity may be achieved, even exceeding the value at top energy without violating the restriction of constant relative energy spread. It is possible to examine the effect on the relative energy spread at constant luminosity. This appears impractical at very low energies so a compromise of constant luminosity down to half the maximum energy and constant emittance at lower energies is shown in Fig. 3. It can be seen that such a luminosity variation is possible with a W ratio of about 4 and in this case the relative energy spread is within ± 10% of the value at maximum energy. Such a variation of luminosity with energy is in fact one of the design aims of LEP [5] (a 100 GeV e^+-e^- electron ring project).

5. WIGGLER POSITION

There is therefore considerable advantage to be gained from siting the wiggler in a high W zone and a value of about 4 times the average lattice value would meet the luminosity and energy spread requirements. This value, corresponding to an α_p value about twice the normal lattice value, is modest compared to the values routinely employed in injection regions of proton accelerators. One simple way of obtaining it is to put one wavelength of normal lattice next to a dispersion free zone with no matching section. An overshoot occurs and an α_p value of twice the lattice value is obtained after half a wavelength. After one wavelength α_p is again zero and a normal dispersion suppressor can be used to match into the lattice. Such a scheme is shown in Fig. 4 taking the LEP lattice as a starting point and using a missing magnet dispersion suppressor. A W ratio of 3.73 is obtained in this particular case which is almost exactly the required value.

6. APERTURE REQUIREMENT

Since the beam size is now increasing at low energies, a larger aperture must be provided all around the ring and assuming constant luminosity down to half energy implies that the beam dimensions will be approximately doubled. A more exact calculation may be performed assuming constant luminosity and constant energy spread down to half energy.

Then the width due to betatron oscillations is given by

$$\varepsilon_\beta = \frac{\sigma_\beta^2}{\beta} = \frac{\varepsilon_{\beta 0}}{\gamma^2} = \frac{\sigma_{\beta 0}^2}{\gamma^2 \beta}$$

i.e.

$$\sigma_\beta = \frac{\sigma_{\beta 0}}{\gamma}$$

Thus, vertically, the aperture requirement is exactly doubled.

Horizontally, there is also a contribution due to the energy spread and, since the energy spread is constant

$$\sigma_\varepsilon = \sigma_{\varepsilon 0}$$

now approximately [3]

$$\frac{\sigma_{\varepsilon 0}{}^2}{\sigma_{\beta 0}{}^2} = \frac{J_x}{J_\varepsilon} = \frac{1}{2}$$

so

$$\frac{\sigma_x}{\sigma_{x0}} = \left(\frac{4 + 1/2}{1 + 1/2}\right)^{1/2} = \sqrt{3}$$

Thus horizontally the aperture requirement is increased by a factor $\sqrt{3} = 1.73$.

7. CONCLUSION

By the simple expedient of placing the wiggler magnets in a high dispersion zone of a storage ring, it is possible to obtain constant luminosity over a wide energy range without increasing the relative energy spread. The only disadvantage is that the aperture requirement is about doubled, which in a high energy electron storage ring where the magnet fields are necessarily low, may not be a major drawback.

ACKNOWLEDGEMENT

I should like to thank E. Keil for many helpful discussions in the course of this study.

REFERENCES

1) J. Rees and B. Richter; Preliminary Design of a 15-GeV Electron-Positron Variable-Tune Storage Ring. SPEAR-167, PEP-69 (1973).

2) J.M. Paterson, J. Rees and H. Wiedemann; Control of Beam Size and Polarization Time in PEP. SPEAR-186, PEP-125 (1975).

3) M. Sands; The Physics of Electron Storage Rings - An Introduction. SLAC-121 (1970).

4) E.D. Courant and H.S. Snyder; Theory of the Alternating-Gradient Synchrotron, Annals of Physics 3, 1-48 (1958).

5) E. Keil; LEP Parameter List (Version 2). CERN/ISR-LTD/76-17 Rev. (1976).

FIGURE CAPTIONS

Figure 1 - Emittance as a function of energy with constant relative energy spread. Also shown is the natural variation in a constant guide field and that required for constant luminosity.

Figure 2 - Luminosity as a function of energy with constant relative energy spread. Also shown is the natural variation and the variation with constant emittance.

Figure 3 - Relative energy spread as a function of energy with constant luminosity for energy ratio 0.5 - 1.0 and constant emittance for energy ratio 0.2 - 0.5. Also shown is the natural variation in a constant guide field.

Figure 4 - Section of LEP lattice showing from the left, the intersection region, a dispersion-free region for installation of RF cavities, the dispersion enhancer, dispersion suppressor and finally a normal cell. The quantities plotted are the horizontal beta function β_x, the dispersion function α_p and the Courant and Snyder Invariant W. Maximum value of W is 3.73 times the average lattice value.

EMITTANCE AS A FUNCTION OF ENERGY WITH CONSTANT RELATIVE ENERGY SPREAD

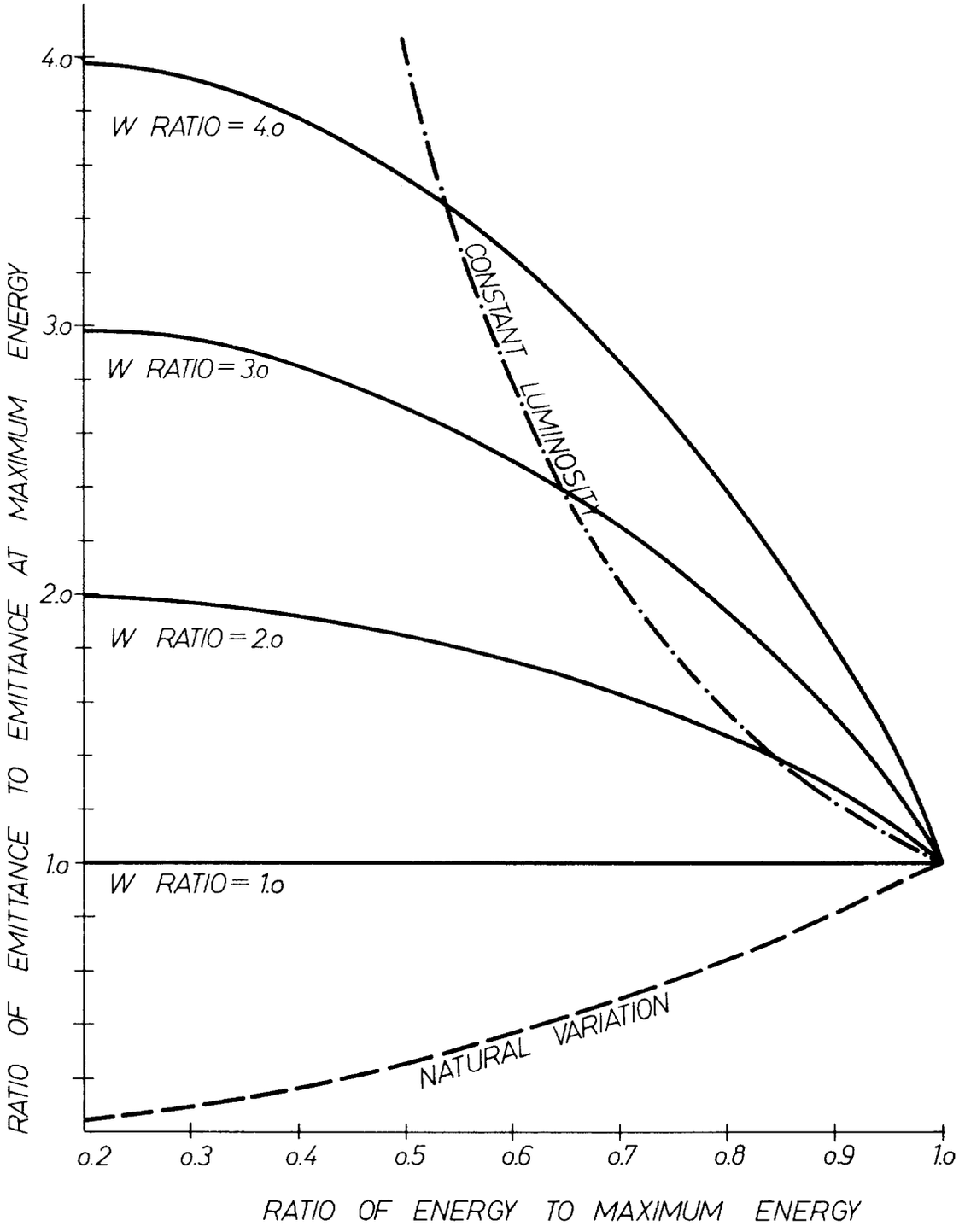

Figure 1

LUMINOSITY AS A FUNCTION OF ENERGY WITH CONSTANT RELATIVE ENERGY SPREAD

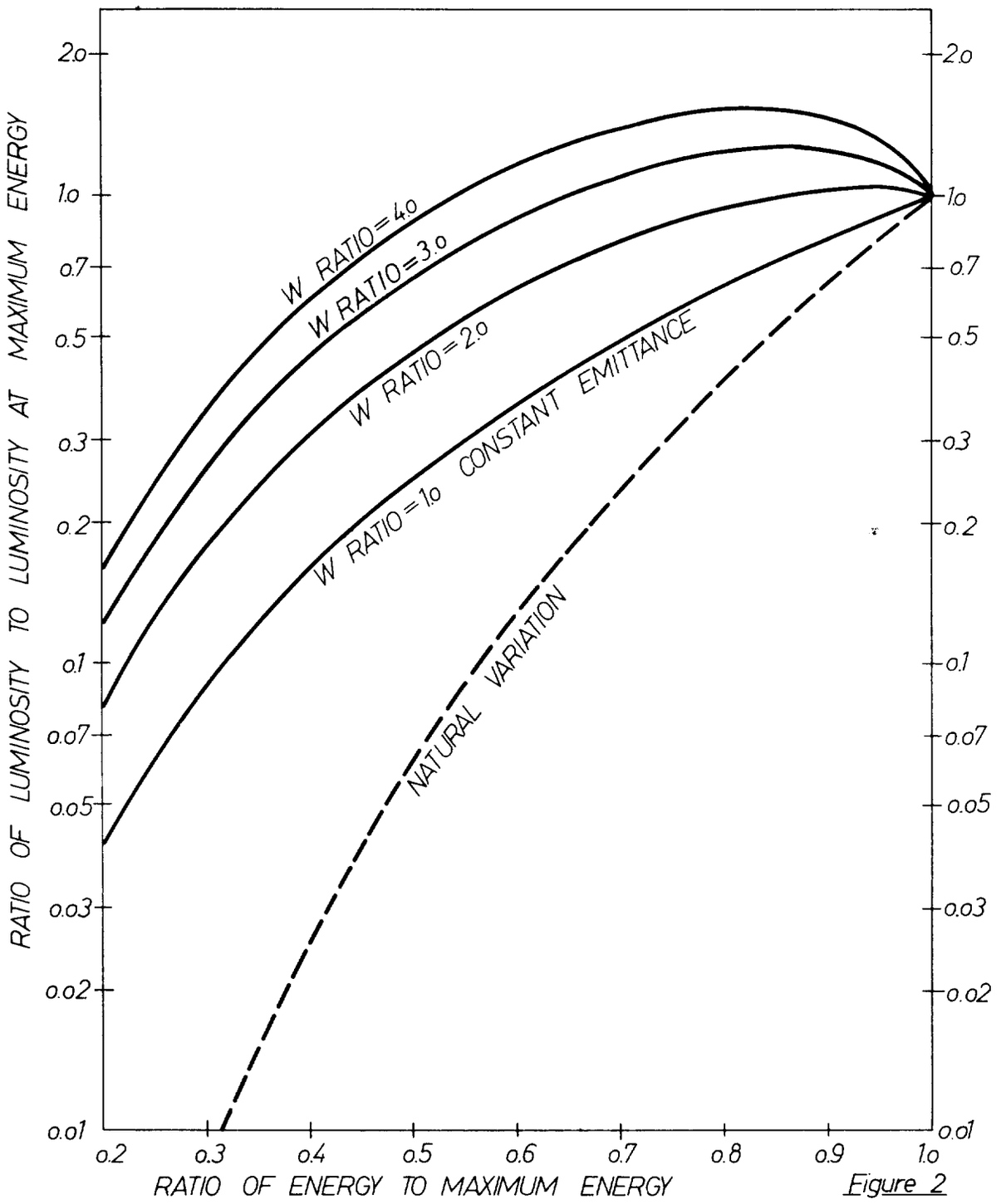

Figure 2

RELATIVE ENERGY SPREAD AS A FUNCTION OF ENERGY

CONSTANT LUMINOSITY FOR ENERGY RATIO 0.5 - 1.0
CONSTANT EMITTANCE FOR ENERGY RATIO 0.2 — 0.5

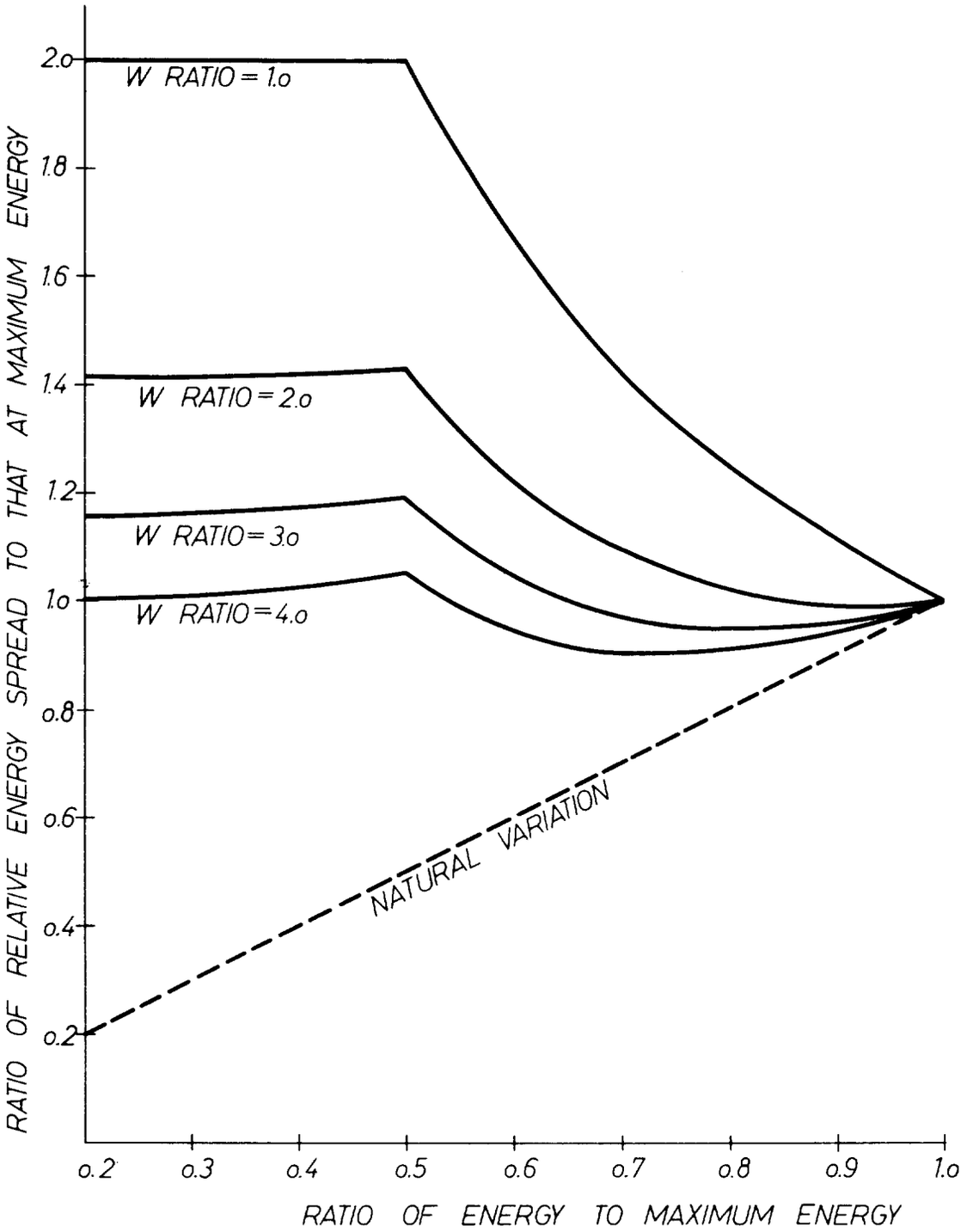

Figure 3

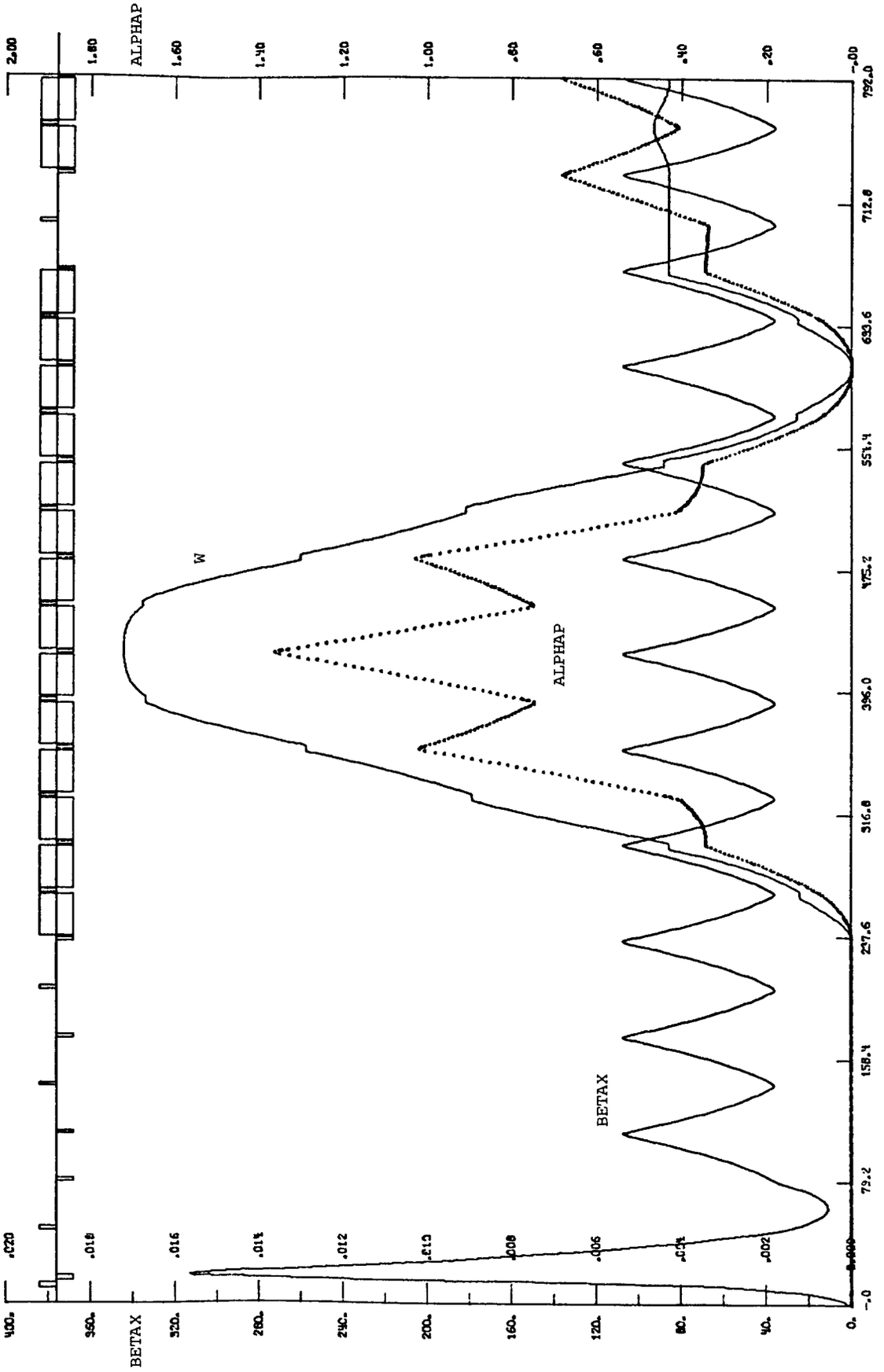

FIGURE 4

APPENDIX 5

EUROPEAN ORGANIZATION FOR NUCLEAR RESEARCH

CERN/PS-DL 76-6

CERN/ISR-LTD/76-21

DEPOLARISATION IN LARGE ELECTRON STORAGE RINGS

by

D. Möhl and B.W. Montague

Abstract

It is shown from elementary considerations that polarised beams of electrons or positrons are unlikely to be obtained in storage rings much above about 30 GeV in top energy.

Normal design criteria in such machines result in large energy spreads which straddle depolarising resonances. The requirement that such resonances be weak enough as not to cause substantial depolarisation, imposes control of vertical closed-orbit errors and beam size beyond what is currently believed to be feasible.

Geneva - June, 1976

Submitted to Nuclear Instruments and Methods

1. INTRODUCTION

Radiative polarisation of electrons and positrons, predicted by Sokolov and Ternov [1] and observed in ACO [2], VEPP-2 [3] and SPEAR [4], is in competition with various depolarising effects. To obtain, and maintain, a high degree of polarisation in the beam requires that the depolarisation time τ_{dep} be much greater than the polarisation time τ_{pol}, given by

$$\tau_{pol} = \frac{8\, m_0\, R\, \rho^2}{5\sqrt{3}\, \hbar\, r_0\, \gamma^5} \qquad (1)$$

where R is the average radius and ρ the bending radius of the machine, r_0 the classical radius of the electron, $\hbar$ the normalised Planck's constant, m_0 the electron rest mass and γ the Lorentz factor.

Typical polarisation times at top energy range from a few tens of minutes to several hours. The Large Electron Positron storage ring [5] (LEP), currently under study at CERN, has $\tau_{pol} \simeq 50$ minutes at 100 GeV. At lower energy in a given machine τ_{pol} would increase rapidly unless wigglers were used to prevent this [6].

Depolarisation can occur if particles spend an appreciable fraction of their time in the neighbourhood of spin resonances. Such resonances occur for

$$\gamma a = k \pm k_x Q_x \pm k_z Q_z \pm k_s Q_s$$

where $a = \frac{g - 2}{2} \approx \frac{\alpha}{2\pi} \approx 1.16 \times 10^{-3}$, g is the gyromagnetic ratio, α the fine-structure constant, k, k_x, k_z, k_s are positive integers (or zero), Q_x, Q_z the betatron wave numbers and Q_s the synchrotron oscillation wave number.

Strong resonances, known as imperfection resonances, are those given by $\gamma a = k$, and correspond to an integral number of spin-precessions per revolution of the machine. They are driven mainly by radial fields

associated with the k'th harmonic of the vertical closed-orbit distortion through imperfections and focusing forces, which produce resonant precession perturbations. In addition, longitudinal fields at magnet ends can influence the resonance strength; however, we consider here only the radial field effects, which are likely to be the dominant ones in high energy machines.

2. SPACING OF RESONANCES

The condition $\gamma a = k$ gives immediately the energy spacing of adjacent resonances

$$\Delta E = \frac{m_0 c^2}{a} \approx 440 \text{ MeV} \qquad (2)$$

which is determined only by fundamental constants. (A similar relation was used by Hereward [7] for protons.) This is the maximum space available to accommodate the natural energy spread of the electron bunches, but the presence of other resonance families may reduce this further. The standard deviation σ_E of the energy spread in an electron storage ring is given approximately by

$$\sigma_E = \left(\frac{55\hbar c\, m_0 c^2}{32\sqrt{3}}\right)^{\frac{1}{2}} \frac{\gamma^2}{\sqrt{\rho}} \qquad (3)$$

In the lower energy range σ_E is sufficiently small to be accommodated comfortably between two adjacent spin resonances. For example, in the electron-proton option of the CERN Large Storage Ring design (LSR) [8] the 20 GeV electrons have $\sigma_E \approx 15$ MeV, which provides about $\pm 14\sigma_E$ between the $\gamma a = k$ resonances. In contrast, LEP at 100 GeV has $\sigma_E \approx 110$ MeV, leaving only $\pm 2\sigma_E$ spacing. Thus, with the nominal energy centred between two such resonances, the fraction of the beam outside $2\sigma_E$ crosses these resonances four times in each period of synchrotron oscillation, and rapid depolarisation might occur.

3. LOWER LIMIT OF τ_{dep}

This can be obtained by analogy with the quantum lifetime $\tau_{2\sigma}$ for an energy-aperture limitation at $\pm 2\sigma_E$, which is a measure of the diffusion rate at this part of the Gaussian distribution. If the particles outside $2\sigma_E$ were fully depolarised within a time $\tau_{2\sigma}$ due to the repeated resonance crossing, then $\tau_{dep} \approx \tau_{2\sigma}$. Since $\tau_{2\sigma}$ is about one radiation damping time, $\sim$ 12 msec for LEP, the beam would never develop any measurable polarisation if this situation were to occur in practice. To examine this further we consider in more detail the crossing of the resonances.

4. RESONANCE WIDTH

We assume that the spin perturbation arises from the radial magnetic field $B_r(t)$ associated with the k'th Fourier component of a vertical closed-orbit imperfection

$$z = z_k \sin k \Omega_r t$$

where $\Omega_r = \frac{c}{R}$ is the orbit revolution frequency, R being the average radius. The corresponding field component is

$$B_r(t) = - \frac{m_0 c \gamma k^2 z_k}{e R^2} \sin k \Omega_r t = B_k \sin k \Omega_r t \qquad (4)$$

and the precession perturbation frequency [9] is (for $\gamma a >> 1$)

$$\omega_k(t) = - \frac{e a}{m_0} B_r(t) = \frac{c \gamma a k^2 z_k}{R^2} \sin k \Omega_r t$$

The resonance width $\hat{\omega}$ is obtained by averaging the product of $\omega_k(t)$ and a phase term which is modulated with the superperiodicity of the machine. However, apart from certain systematic resonances we can write to within a factor of order unity

$$\hat{\omega} \approx \frac{c \gamma a k^2 z_k}{R^2} \qquad (5)$$

We express this resonance width in terms of the corresponding energy width

$$[\Delta\gamma]_{res} = \frac{\hat{\omega}}{a\,\Omega_r} = \frac{\gamma\ k^2\ z_k}{R} = \frac{(\gamma a)^3}{a}\ \frac{z_k}{R} \tag{6}$$

(since we are considering the resonance $\gamma a = k$).

In order that the k'th and (k + 1)'th resonances be distinct and well separated, we must have the condition

$$m_0c^2[\Delta\gamma]_{res} << \frac{m_0c^2}{a} \quad \text{(from (2))}$$

so, from (6),

$$z_k << \frac{R}{(\gamma a)^3} \tag{7}$$

Now for LEP at 100 GeV, $\gamma \approx 2 \times 10^5$, R = 8.1 km, B_0 = 546 gauss and ρ = 6.1 km. Then γa = 232 and the criterion (7) for distinct, separated resonances is

$$z_k << 0.65 \text{ mm}, \quad \text{or} \quad B_k << 2 \text{ gauss} \tag{7a}$$

If this is not satisfied, a large fraction of the particles will be living permanently inside the resonances and no polarisation is possible. Note that (7) is a necessary but not a sufficient condition for polarisation to be possible.

5. RESONANCE CROSSING SPEED

Particles may cross a spin resonance either smoothly, as a result of synchrotron (energy) oscillations, or stochastically as a consequence of quantum jumps in energy. For the smooth motion two limiting regimes can be distinguished, "fast" crossing and "slow" crossing [9,10]. In a fast crossing, the perturbation of the spin precession is very small during the particles' passage through the resonance and the polarisation of the beam is only slightly reduced by each traversal. Slow crossings are characterised by the perturbed precession

motion varying very slowly and adiabatically on the scale of the unperturbed precession frequency. If the resonance traversal takes place strictly symmetrically either side, almost the whole population undergoes a spin flip and the polarisation of the beam is reversed [9].

A parameter characterising the crossing speed is [3]

$$\kappa = \left[\frac{\pi\,\hat{\omega}^2}{2a\;\Omega_r\;\frac{d\gamma}{dt}}\right] = \frac{(\gamma a)^3\;z_k}{R}\left[\frac{\pi\;c}{2a\;R\;\frac{d\gamma}{dt}}\right]^{\frac{1}{2}} = \frac{\gamma a\;B_k}{B_0}\left[\frac{\pi\;c}{2a\;R\;\frac{d\gamma}{dt}}\right]^{\frac{1}{2}} \tag{8}$$

where we have expressed κ also in terms of the k'th harmonic of the radial field from Eq. (4) and of the bending field B_0. The criteria are

$$\kappa \ll 1 \quad \text{for fast crossing}$$
$$\kappa \gg 1 \quad \text{for slow crossing}$$

If we take as reference those particles executing synchrotron oscillations at frequency Ω_s and amplitude σ_E, the maximum value of $\frac{d\gamma}{dt}$ is

$$\left(\frac{d\gamma}{dt}\right)_{max} = \frac{\Omega_s\;\sigma_E}{m_0 c^2} \tag{9}$$

which, for LEP, is $\sim 0.85 \times 10^6\ s^{-1}$. This value in (8) makes the criterion for a fast crossing

$$z_k \ll 0.08\ \text{mm} \quad (B_k \ll 0.3\ \text{gauss}) \tag{8a}$$

For constant $\frac{d\gamma}{dt}$, the polarisation before (P_0) and after (P) traversal of a resonance (in the absence of stochastic motion), were shown by Froissart and Stora [9] to be related by

$$P = P_0\,(2e^{-\frac{\kappa^2}{4}} - 1) \tag{10}$$

We assume that the effect of repetitive crossing is mainly additive because of randomisation due to quantum energy fluctuations. For a fast crossing, the depolarisation D per resonance traversal is then

$$D = \frac{P_0 - P}{P_0} \approx \frac{\kappa^2}{2}$$

Taking account of the number of phase oscillations in the polarisation time, Eq. (1), one can readily estimate that the inequality (8a) must be satisfied by several orders of magnitude for appreciable polarisation to develop. Quadrupole alignment to 0.1 mm rms might reduce z_k to a few microns, but this still falls short by a considerable amount.

The slow crossing regime is only of academic interest for high energy electron rings, since it implies broad resonances and a varying distribution of precession angles across the resonance, according to initial phases. Thus, the part of the beam inside a resonance is largely depolarised, even in the idealised situation of coherent adiabatic motion.

Consideration of the energy fluctuations due to quantum emission of photons results in an even more unfavourable situation. The critical photon energy may be expressed as a fraction of the beam energy by

$$\frac{[\Delta\gamma]_c}{\gamma} = \frac{\hbar\,\omega_c}{m_0c^2\,\gamma} = \frac{3\hbar\,c}{2m_0c^2}\,\frac{\gamma^2}{\rho} \qquad (11)$$

For high energy electron rings this quantity is of order 10^{-6}, i.e. about 10^{-3} of a standard deviation in bunch energy spread. Since the mean number of quanta emitted per electron in each machine revolution

$$\langle N \rangle = \frac{5\pi}{\sqrt{3}}\,\alpha\,\gamma$$

is around 10^4 for these large machines, the diffusion rate is fast on the scale of synchrotron oscillation period, and coherence of spin

motion will be rapidly destroyed for particles crossing a resonance in the "slow" regime. Even in a low energy storage ring like ACO, depolarisation takes place in a few seconds when the beam is brought on to the resonance $\gamma a = 1$ at 440 MeV [2].

6. CONCLUSIONS

In very high energy electron storage rings optimised according to normal criteria, the energy spread in the bunches is so large that a substantial fraction of the beam sweeps through depolarising resonances due to synchrotron (energy) oscillations.

Broad resonances and slow crossings create strong depolarising effects due to phase mixing and quantum fluctuations of energy. Narrow resonances and fast crossings, sufficient to reduce the depolarisation rate to an acceptable level, require, at 100 GeV, vertical closed orbit errors considerably smaller than the best we can envisage. Furthermore, depolarisation effects, which we have not considered in detail, arising from free vertical betatron oscillations and the proximity of resonances of type $\gamma a = k \pm k_z Q_z$, could impose impracticable constraints on vertical beam size. Recent results at SPEAR [11] suggest that this can be a serious problem even in the lower range of energies.

We conclude that, at 100 GeV, polarised electron or positron beams are practically excluded. The maximum energy at which polarised beams may be feasible is unlikely to be much above 30 GeV, at which energy the depolarisation time might be comparable to the quantum lifetime for a 6σ aperture. The energy may even be lower when all the potential sources of depolarisation are taken into account.

REFERENCES

1) A.A. Sokolov and I.M. Ternov; Sov. Phys. Doklady, 8, 1203 (1964).

2) The Orsay Storage Ring Group; Proc. VIIIth Int. Conf. on High Energy Accelerators, CERN (1971) p. 127.

3) V.N. Baier; Sov. Phys. Uspekhi, 14, 695 (1972).

4) U. Camerini, D. Cline, J. Learned, A.K. Mann, L.K. Resvanis; Univ. of Pennsylvania preprint (July 1975).

5) B. Richter; Report CERN/ISR-LTD/76-9 (March 1976). (Talk delivered at the Meeting on e^+e^- Physics, Flaine, Haute-Savoie, February 22 - 28, 1976).

6) A. Hutton; Report CERN/ISR-LTD/76-18 (May 1976). (Submitted to Particle Accelerators).

7) H.G. Hereward; Proc. Summer Studies on High Energy Physics with Polarised Beams, Argonne Nat. Lab. Rpt. ANL/HEP 75-02, p XVII, 1 (1975).

8) B.W. Montague; Report CERN/ISR-LTD/76-16 (April 1976). (Talk delivered at the Meeting on e^+e^- Physics, Flaine, Haute-Savoie, February 22 - 28, 1976).

9) M. Froissart and R. Stora; Nucl. Inst. and Methods, 7, 297 (1960).

10) Ya.S. Derbenev, A.M. Kondratenko and A.N. Skrinsky; Sov. Phys. JETP, 33, 658 (1971).

11) A.W. Chao and R.F. Schwitters; private communication (May 1976).

APPENDIX 6

EUROPEAN ORGANIZATION FOR NUCLEAR RESEARCH

CERN-ISR-LTD/76-22

ABOUT TRANSIENT BEAM LOADING AND ENERGY CONSERVATION

by

by E. Keil, W. Schnell and B. Zotter

Geneva, June 1976

1. Introduction

In large electron storage rings the energy extracted by one bunch at every passage through the RF cavities has become a concern. The following formulae contain, in substance, no new information and are based on nothing but energy conservation. They do, however, express the situation in terms of few, generally known quantities and show how little one has to choose.

2. Required energy extraction

The definition of the quality factor, Q, of a cavity resonator is given by

$$Q = W \frac{\omega}{P_\ell} \tag{1}$$

where W is the total stored electromagnetic energy, $\omega/2\pi$ the cavity frequency and P_ℓ the power loss to the cavity walls. If, on the other hand, P_b is the average power to be delivered to the beam in order to make up for synchrotron radiation and all higher-mode losses, the energy, U, to be delivered to each bunch at each passage through the cavities is given by

$$U = \frac{P_b}{k_b f_{rev}} \tag{2}$$

where k_b is the number of bunches and f_{rev} the revolution frequency. Introducing the harmonic number

$$h = \frac{\omega}{2\pi f_{rev}}$$

one obtains, from (1) and (2)

$$\eta = \frac{U}{W} = \frac{P_b}{P_\ell} \frac{2\pi h}{k_b Q} \tag{3}$$

for the fraction of stored energy that must be extracted at each passage (cf. ref. [1]).

---

1) P.B. Wilson, Proc. IXth Intern. Conf. on High Energy Acc., p. 58 (1975).

If W is interpreted as the stored energy at the arrival of a bunch then, clearly, η cannot be larger than one. But then P_ℓ is the power loss at that moment, not necessarily the average loss.

3. Maximum possible energy extraction

The energy conservation arguments presented above only give an upper bound for the energy gain of a bunch. In the following, we shall calculate a tighter upper bound by considering the beam-cavity interaction in a little more detail.

A particularly simple model applies to the case where the bunch spacing is large enough that all the higher modes excited by the passage of the bunches decay between successive bunch passages. In this case, we only have to consider two types of field, the field in the lowest cavity mode driven by the RF transmitter and left behind by previous bunch passages, and the field induced by the passage of the bunch to which all modes contribute. The energy gained by a bunch on passing through an RF cavity can then be written as follows[2]:

$$U = 2(W_{oi}\, W_{or})^{\frac{1}{2}} \sin\phi - \sum_{\lambda=o}^{\infty} W_{\lambda r} \tag{4}$$

Here W_{oi} is the stored energy in the lowest cavity mode just before the passage of the bunch, and the $W_{\lambda r}$ are the energies radiated into the λ-th mode. In particular, W_{or} is the energy which the bunch would radiate into the lowest cavity mode if the cavity was not driven by the RF transmitter. ϕ is the phase angle of the RF measured from zero crossing. Again, (4) expresses nothing but energy conservation. If we introduce

$$W_{or} = n\, W_{oi} \tag{5}$$

and

$$\sum_{\lambda=o}^{\infty} W_{\lambda r} = B\, W_{or} \tag{6}$$

---

2) P.L. Morton and V.K. Neil, UCRL-18103, p. 365.

we can put (4) into the following form:

$$\frac{U}{W_{oi}} = 2\sqrt{n}\sin\phi - Bn \tag{7}$$

Here, (5) says only that W_{or} is some unspecified multiple or fraction of W_{oi}. B describes the effect of the higher-order modes excited by the bunch passage. It has been called the beam loading enhancement factor[1].

We may look for the maximum of (7) with respect to n. It occurs at

$$n_{opt} = \left(\frac{\sin\phi}{B}\right)^2 \tag{8}$$

and has a value

$$\left.\frac{U}{W_{oi}}\right|_{opt} = \frac{\sin^2\phi}{B} \tag{9}$$

It is quite clear that W_{or} - and hence n - is proportional to the square of the bunch charge. B is only a function of the bunch and cavity geometry and is always bigger than one. It can be obtained by standard energy loss calculations[2)3)]. Therefore, there is just one bunch charge which fulfills (8) and hence is able to extract the fraction (9) of the stored energy from the cavity. For all other bunch charges, the energy extraction by the bunch will be smaller.

For e^+e^- storage rings up to energies of about 15 GeV, such as PEP or PETRA, $\sin\phi \ll 1$, and hence only a small fraction of the stored energy can be extracted. In higher energy machines, such as LEP, B is more important in limiting the energy extracted, since $\sin\phi \approx 1$.

4. Numerical examples

The table below shows the parameters of several machines and the energy extraction efficiency η calculated by using (3).

---

3) E. Keil, Nucl. Instr. Methods 100, 419 (1972).

	PEP[4]	PETRA[5]	LEP I[6]	LEP II[7]	
h	2592	3840	59452	57645	
k_b	3	4	4	32	
Q	30000	30000	30000	30000	
P_b	5.0	3.6	20.2	24.3	MW
P_ℓ	3.3	1.2	55.5	44.8	MW
η	0.27	0.60	1.13	0.20	

It may be seen from this table that in all machines a very substantial fraction of the stored energy must be extracted by the beam in order to make up for the synchrotron radiation losses. In LEP I, the fraction is actually greater than one. This was the reason for abandoning this machine in favour of LEP II.

---

4) LBL-4288/SLAC-189 (1976).

5) Updated version of the PETRA proposal, Hamburg 1976.

6) E. Keil, CERN/ISR-LTD/76-17.

7) E. Keil, CERN/ISR-LTD/76-17 Rev.

APPENDIX 7

EUROPEAN ORGANIZATION FOR NUCLEAR RESEARCH

CERN-ISR-LTD/76-8

MODULATED CAVITIES

by

W. Schnell

Abstract

In electron storage rings containing only a small number of bunches modulation of the radio frequency could save power. A scheme for modulating the RF with the bunch-repetition frequency is proposed. It makes use of one or several low-loss storage cavities coupled to the accelerating cavity.

Geneva, February 1976

Introduction

Modern electron-positron storage rings are designed to contain only a few bunches but to operate at RF harmonic numbers of several thousand. As the time between the passage of consecutive bunches is still short compared with the natural fill time of the cavities one applies a continuous wave. Hence, for a very large fraction of time RF fields are generated and power is dissipated whilst the cavities do not interact with any beam. Ideally one should replace the resonant cavity by a loss-free storage system (e.g. the capacitance of a charged delay line) and a switch transferring energy to the accelerating gap and back during the passage of a bunch only. This still seems beyond present day technology. As a compromise, one might keep resonant cavities but modulate their stored energy - by forced energy exchange with a low-loss storage device - with rise and fall times faster than the natural decay time, but slow compared with an RF cycle.

This paper deals with the simplest form of such a scheme, i.e. a sinusoidal modulation by the bunch repetition frequency, f_b, or a harmonically related frequency. The reduction in power loss is modest but the system proposed is rather simple also. It is described below.

One storage cavity

To the accelerating cavity - which can have any of the customary shapes - a second cavity is being coupled. It does not directly interact with the beam and will be called the storage cavity. Both cavities have their unperturbed resonance tuned to the same frequency. The coupling is adjusted in such a way that the two resonant modes of the coupled system are - in the simplest case - at

$$f_1 = f_{RF} + f_b$$

$$f_2 = f_{RF} - f_b$$

where f_{RF} is the main RF frequency. The power source is made to supply a driving current proportional to

$$\cos \omega_b t \quad \sin \omega_{RF} t$$

which means that both modes f_1 and f_2, are driven with equal amplitudes. Fig. 1a shows the resulting RF envelopes in the two cavities. The bunches are made to coincide with the upward peak of the RF wave in the accelerating cavity. The energy oscillates between the two cavities at a rate $2f_b$. The dissipation in the accelerating cavity is reduced by a factor of two. Obviously, the storage cavity adds its own share to the total dissipation. But since this cavity does not need to contain an accelerating gap its field configuration can be of the

$$H_{omn}$$

type, which is associated with low losses.

If Q_1 and Q_2 are the quality factors of the accelerating and the storage cavities respectively, the total power dissipation for a given peak accelerating voltage is reduced by a factor

$$q = \frac{Q_1 + Q_2}{2Q_2}$$

with respect to CW operation of the accelerating cavity alone.

The scheme favours such types of accelerating cavities which derive a high shunt impedance from a low stored energy (e.g. a high R/Q) rather than a high quality factor, but we take, as an example, the usual circular re-entrant cavity of about half a wavelength length. At 350 MHz we assume a practical value of $Q_1 = 3.5 \times 10^4$ for copper walls (cf. ref[1]). In the SLED scheme[2) 3)] a system of storage cavities is used for a pulsed RF application. A Q-factor of 10^5 at 2856 MHz is quoted for the

H_{015}-mode. Scaling to 350 MHz yields $Q_2 = 2.9 \times 10^5$, but also the very large diameter of 1.7 m. For an H_{011} cavity whose length equals its diameter the theoretical value[4) 5)] (always for c_u) is

$$Q_2 = 1.6 \times 10^5$$

The diameter is 1.12 m which is still embarrassingly large. This would yield

$$q = 0.61$$

for the reduction in power loss.

Fig. 2 shows a sketch. The table below shows the required degree of coupling in terms of the relative bandwidth

$$k = \frac{f_2 - f_1}{f_{RF}} = \frac{2f_b}{f_{RF}}$$

for a few "typical" [6) 7) 8)] (?) cases.

Table 1

Degree of coupling, k, in units of 10^{-3}, for different machine circumferences and numbers of bunches, and for 350 MHz RF.

Machine circumference		2.304	6.911	50	km
Number of bunches:	1	0.744			
	2	1.49			
	3		0.744		
	4	2.98		0.14	

The first column pertains to the PETRA project. For four bunches $k = 3 \times 10^{-3}$. In reality PETRA works at 500 MHz, which would lead to 2×10^{-3}.

For even numbers of bunches one may consider modulating with $f_b/2$ and using the downwards half-wave of the RF envelope as shown in Fig. 1b. The required coupling is halved in this case, but every second bunch has to be shifted by half an RF wavelength.

Two storage cavities

By adding a second storage cavity one can obtain a system of three coupled cavities with resonant modes at $f_{RF} \pm f_b$ and f_{RF}, capable of supporting a modulated wave proportional to

$$\sin^2 \frac{\omega_b}{2} t \quad \sin \omega_{RF} t \ .$$

The dissipation in the accelerating cavity is reduced by a factor

$$\frac{\int_0^{\frac{\pi}{2}} \sin^4\phi \ d\phi}{\frac{\pi}{2}} = \frac{3}{8}$$

and the total dissipation by

$$q = \frac{6Q_1 + 3Q_2}{8Q_2} \ .$$

With the values used above one finds

$$q = 0.54.$$

The gain with respect to the previous case seems hardly worth while.

Miscellaneous problems

Mechanical tolerances and stability of the storage cavity have to

be studied. The absence of beam-loading gives one some hope that - like in the SLED scheme - one might do without servo-tuners. One might also copy the needle tuners of that scheme for tuning the storage cavity off, and reverting to CW operation, at low electron energies.

Clearly the excitation of unwanted modes in the storage cavity must be avoided. At least the separation of the theoretically degenerate E_{1nm} mode does seem possible[2) 5)].

Figure 2 suggests some obvious constructional difficulties for direct slot coupling. One may couple to the flat face of the H_{onm} cavity, brazing only its cover plate (or a concentrically circular part) to the side of the accelerating cavity. If even this should turn out too expensive, loop couplers have to be considered. A comparison of the relative bandwidths of Table 1 with the inverse quality factors suggests that one might, perhaps, be able to avoid adjustable coupling.

The necessity to add RF modulators to the power sources clearly reduces the potential saving in capital cost. Alternatively one may consider two separate CW power sources for f_1 and f_2 (in the two-cavity scheme) whose outputs are added in a hybrid junction.

Coupled accelerating cavities

Normally an odd number (five in practice) of accelerating cavities are coupled and powered from one central feedpoint. It would be very advantageous to use only one storage cavity - also coupled to the central accelerating cell - to modulate the whole string. In fact, the modulation scheme may never become economically attractive without that feature. This, clearly, has to be studied. The following semi-qualitative consideration may give an indication. A five-cell structure is assumed. Instead of the two outermost cells of lengths $c/2f_{RF}$ each, which have to be filled by an outgoing and reflected wave, one may consider a travelling-wave structure of two wavelength total length. To fill this in a quarter, say, of f_b^{-1} one needs a group velocity, c_g, given by

$$c_g = 8 \frac{f_b}{f_{RF}} c = 4kc .$$

For the worst (and most realistic) case of Table 1 one needs 1.2% of the velocity of light, c.

The group velocity is the rate of change of frequency with inverse guide wavelength. Hence, if $\Delta f/\Delta\phi$ is the slope of the usual dispersion diagram of frequency shift versus change of phase shift per cell, and if $c/2f_{RF}$ is the cell length, one has

$$c_g = \pi \frac{\Delta f}{\Delta\phi f_{RF}} c .$$

Figure 5 of reference [1] yields $c_g/c = 1.1\%$ for the SPEAR II RF structure - but only in the middle of the pass band, not near the π-mode where the structure is used. Thus, one is once again led to consider structures operating at mid-band such as biperiodic or sidecoupled structures. On the other hand, reducing the bunch number, reverting to the scheme of Fig. 1b, and increasing the machine radius all tend to facilitate the combination of one storage cell with many accelerating cells.

Acknowledgement

I am grateful to A. Hofmann who suggested making use of H_o waves in some way, and to F. Sacherer who proposed applying sinusoidal modulation by some method.

References

1) M.A. Allen, P.B. Wilson. Proc. IXth Inter. Conf. on High Energy Accelerators, p. 92, 1974.

2) Z.D. Farkas, H.A. Hogg, G.A. Loew, P.W. Wilson. Proc. IXth Inter. Conf. on High Energy Accelerators, p. 576, 1974.

3) Z.D. Farkas, H.A. Hogg, G.A. Loew, P.W. Wilson. IEEE Trans. Nucl. Sci. NS 22, No. 3, p. 1299, 1975.

4) H.R.L. Lamont. "Wave Guides", Methuen and Co. Ltd., p. 86, 1949.

5) "Taschenbuch der Hochfrequenztechnik", H. Meinke, F.W. Gundlach, edit., p. 473.

6) "PETRA Ein Vorschlag zur Erweiterung der Speicherringanlagen by DESY zu hohen Energien", 1974.

7) E. Keil, ISR Divisional Report in preparation.

8) B. Richter, private communication. Report in preparation.

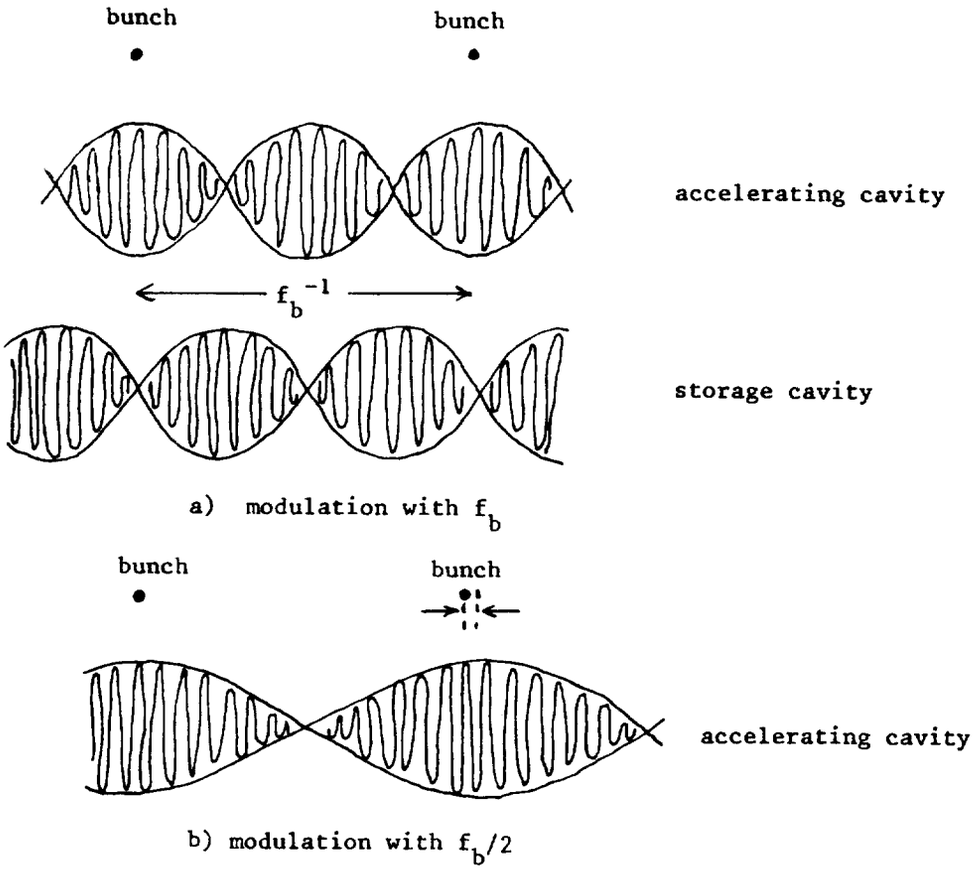

Fig. 1. RF waveforms

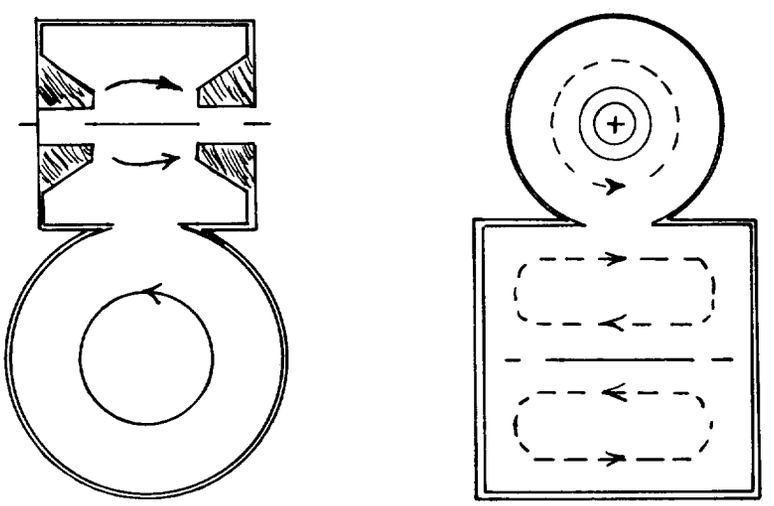

Fig. 2. One H_{011} storage cavity

APPENDIX 8

EUROPEAN ORGANIZATION FOR NUCLEAR RESEARCH

CERN/ISR-LTD/76-23

SYNCHROTRON RADIATION FROM A LARGE ELECTRON-POSITRON STORAGE RING

by

E. Keil

Abstract

General expressions are compiled for the synchrotron radiation produced in bending magnets and quadrupoles. Numerical examples are given for an e^+-e^- storage ring at 100 GeV.

Geneva - June 1976

1. INTRODUCTION

The well known formulae for synchrotron radiation [1,2] are first compiled for the case of bending magnets. They are then generalized to the case of synchrotron radiation produced in quadrupoles. Finally, numerical examples are shown for the case of an e^+-e^- storage ring at an energy of 100 GeV.

2. SYNCHROTRON RADIATION FROM BENDING MAGNETS

In an isomagnetic machine where the bending radius ρ is constant or zero, the energy loss per turn is given by

$$U_0 = \frac{C_\gamma E^4}{\rho} \tag{1}$$

Here E is the electron energy, and

$$C_\gamma = \frac{4\pi}{3} \frac{r_e}{E_0^3} \tag{2}$$

where r_e is the classical electron radius and E_0 is the electron rest energy. Combining (1) and (2) yields

$$U_0 = \frac{4\pi}{3} \frac{r_e E_0 \gamma^4}{\rho} \tag{3}$$

The total power loss of a circulating electron current I in a machine with bending radius ρ becomes

$$P_\gamma = \frac{4\pi}{3} \frac{r_e E_0 \gamma^4 I}{e \rho} \tag{4}$$

The critical energy ε_c is defined as follows

$$\varepsilon_c = \frac{3}{2} \hbar c \gamma^3/\rho \tag{5}$$

The power spectrum $\partial P_\gamma/\partial \varepsilon$ is given by

$$\frac{\partial P_\gamma}{\partial \varepsilon} = \frac{P_\gamma}{\varepsilon_c} S_b(\varepsilon/\varepsilon_c) \tag{6}$$

where $S_b(x)$ is the universal function shown in Fig. 1.

$$S_b(x) = \frac{9\sqrt{3}}{8\pi} \; x \int_x^\infty K_{5/3}(s) \; ds \tag{7}$$

$S_b(x)$ is identical to the spectral function $S(\xi)$ defined on p. 115 of ref. 1.

The quantum spectrum $\partial N_\gamma / \partial \varepsilon$ is

$$\frac{\partial N_\gamma}{\partial \varepsilon} = \frac{P_\gamma}{\varepsilon_c^{\,2}} \; N_b(\varepsilon/\varepsilon_c) \tag{8}$$

where $N_b(x)$ is another universal function defined by

$$N_b(x) = x^{-1} \; S_b(x) \tag{9}$$

We also define the quantities (4), (6) and (8) per unit length of bending magnet

$$\frac{\partial P_\gamma}{\partial s} = \frac{2}{3} \; \frac{r_e \; E_0 \; \gamma^4 \; I}{e \; \rho^2} \tag{10}$$

$$\frac{\partial^2 P_\gamma}{\partial \varepsilon \partial s} = \frac{P_\gamma}{2\pi\rho \; \varepsilon_c} \; S_b(\varepsilon/\varepsilon_c) = \frac{\partial P_\gamma}{\partial s} \; \frac{S_b(\varepsilon/\varepsilon_c)}{\varepsilon_c} \tag{11}$$

$$\frac{\partial^2 N_\gamma}{\partial \varepsilon \partial s} = \frac{P_\gamma}{2\pi\rho \; \varepsilon_c^{\,2}} \; N_b(\varepsilon/\varepsilon_c) \tag{12}$$

3. SYNCHROTRON RADIATION FROM QUADRUPOLES

A quadrupole differs from a bending magnet by the fact that the bending radius is a function of the electron excursion from the axis of the quadrupole. In order to obtain the synchrotron radiation formulae, the contributions of all electrons have to be superimposed.

Let the distribution of the excursion x be normalized such that

$$I = \int_{-\infty}^{+\infty} i(x) \; dx \tag{13}$$

and let the distribution i(x) be a Gaussian of rms width σ. Then i(x) is given by the following expression

$$i(x) = \frac{I}{\sigma\sqrt{2\pi}} \; e^{-x^2/2\sigma^2} \tag{14}$$

It is known that in a quadrupole the bending radius $\rho(x)$ varies as follows

$$\rho(x) = \rho(\sigma) \; \frac{\sigma}{x} = \rho_0 \; \sigma/x \tag{15}$$

where ρ_0 is the bending radius at one standard deviation σ. In the following, the variation of the excursion x inside a quadrupole is neglected, i.e. x is considered constant through the quadrupole.

When studying the synchrotron radiation from quadrupoles it is best to consider only quantities per unit length of quadrupole. Generalizing (10), using (14) and (15) yields

$$\frac{\partial P_\gamma}{\partial s} = \frac{2}{3} \; \frac{r_e \; E_0 \; \gamma^4}{e} \; \frac{I}{\sigma\sqrt{2\pi}} \int_{-\infty}^{+\infty} e^{-x^2/2\sigma^2} \; \frac{x^2 \; dx}{\rho_0^{\,2} \; \sigma^2} \tag{16}$$

The integration is straightforward

$$\frac{\partial P_\gamma}{\partial s} = \frac{2}{3} \; \frac{r_e \; E_0 \; \gamma^4 \; I}{e \; \rho_0^{\,2}} \tag{17}$$

It may be seen that the correct result for a quadrupole is obtained by evaluating the bending magnet formula (10) at a distance σ from the quadrupole axis. (This result was quoted to me by A. Hofmann.)

The power spectrum per unit length is obtained by generalizing (11)

$$\frac{\partial^2 P_\gamma}{\partial\varepsilon\partial s} = \frac{I}{\sigma\sqrt{2\pi}} \int_{-\infty}^{+\infty} \frac{P_\gamma(x) \; e^{-x^2/2\sigma^2}}{2\pi\rho(x) \; \varepsilon_c(x)} \; S_p(\varepsilon/\varepsilon_c(x)) \; dx \tag{18}$$

By making the appropriate substitutions for $P_\gamma(x)$, $\rho(x)$, $\varepsilon_c(x)$, and some arithmetic, (18) may be written in the following form

$$\frac{\partial^2 P_\gamma}{\partial\varepsilon\partial s} = \frac{2}{3} \; \frac{r_e \; E_0 \; \gamma^4 \; I}{e \; \rho_0^{\,2} \; \varepsilon_{c0}} \; S_q(\varepsilon/\varepsilon_{c0}) = \left.\frac{\partial P_\gamma}{\partial s}\right|_0 \; \frac{S_q(\varepsilon/\varepsilon_{c0})}{\varepsilon_{c0}} \tag{19}$$

Here ε_{c0} is the critical energy at a distance σ from the quadrupole axis, and $S_q(x)$ is a new universal function, also shown in Fig. 1

$$S_q(x) = \frac{9\sqrt{3}}{8\pi} \; x \int_0^\infty K_{5/3}(s) \; [1 - \mathrm{erf}(x/s\sqrt{2})] \; ds \tag{20}$$

Apart from the spectral function S_q, (20) is identical to (11) if the quantities involved are all evaluated at a distance σ from the quadrupole axis.

The quantum spectrum from a quadrupole is given by

$$\frac{\partial^2 N_\gamma}{\partial \varepsilon \partial s} = \frac{1}{\varepsilon} \frac{\partial^2 P_\gamma}{\partial \varepsilon \partial s} = \frac{\partial P_\gamma}{\partial s} \Bigg|_0 \frac{N_q(\varepsilon/\varepsilon_{c0})}{{\varepsilon_{c0}}^2} \tag{21}$$

where the function $N_q(x)$ is defined by

$$N_q(x) = x^{-1} \; S_q(x) \tag{22}$$

A comparison of the spectral functions $S_b(x)$ and $S_q(x)$ shown in Fig. 1 shows that quadrupoles produce more synchrotron radiation at energies above the critical energy than bending magnets.

4. SYNCHROTRON RADIATION SPECTRA IN LEP

As a practical application of the preceding analysis we calculate below the synchrotron radiation spectra for LEP. We consider two machines

- the 4 bunch machine summarized in ref. 3;
- the 32 bunch machine presently considered as an alternative.

For each machine, photon spectra are shown produced by:

- the normal cell bending magnets;
- special bending magnets with 10% of the nominal field [4];
- the horizontally focusing quadrupole Q2. (Since the beam size is largest in this quadrupole, it is likely to be the dominant source of quadrupole synchrotron radiation.)

The parameters entering the calculation are shown in the two tables below.

Table I: Bending magnet parameters

	4 bunches	32 bunches
P_γ (2 beams)	20.2	24.4 MW
ε_c	363	358 keV

Table II: Quadrupole parameters

		4 bunches	32 bunches	
Strength of Q2	K	0.02525	0.05122	m^{-2}
rms beam radius	σ	6.2229	1.807	mm
Bending radius	ρ	6364	10804	m
Quadrupole length	ℓ_Q	3.5	3	m
Current	I	6.96	8.50	mA
$(\partial P_\gamma/\partial s)_0$		1.512×10^{21}	6.41×10^{20}	eV/s
ε_{c0}		349	205	keV

5. CONCLUSIONS

Formulae have been derived for various quantities related to synchrotron radiation, both for bending magnets and quadrupoles. The spectral distribution of synchrotron radiation from quadrupoles has been shown to contain more power above the critical energy than the spectrum from bending magnets. The photon flux at about one MeV from bending magnets can be reduced by installing reduced field bending magnets near the crossing points. When this has been done, most of the synchrotron radiation in that energy range comes from the interaction region quadrupoles.

REFERENCES

1) M. Sands; SLAC-121 (1970).

2) R.A. Mack; CEAL-1027 (1966).
This paper uses a different normalization of the spectral function $S_b(x)$.

3) E. Keil; CERN/ISR-LTD/76-17 (1976).

4) LBL-4288, SLAC-189 (1976).

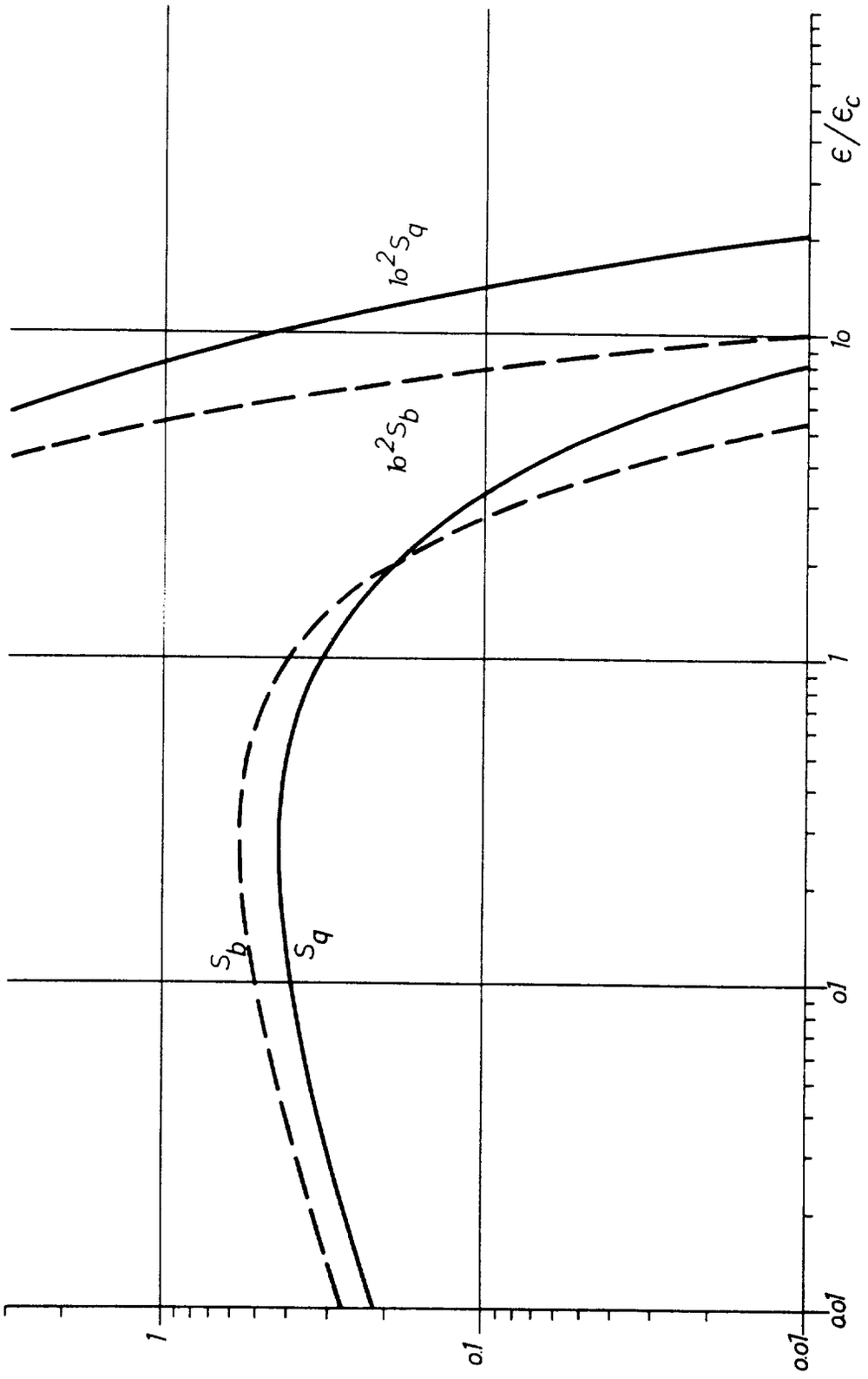

Fig. 1

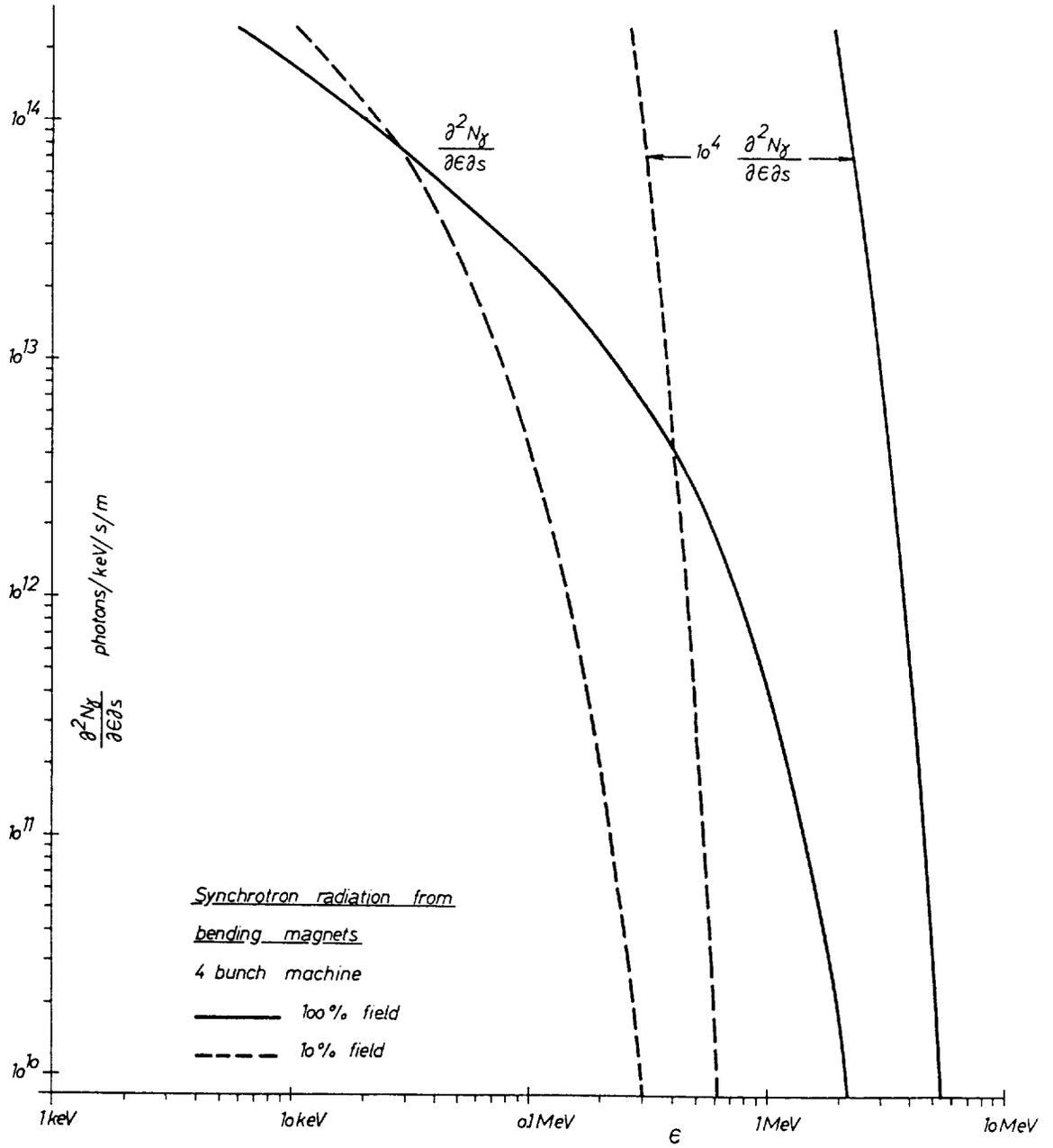
10^{14}
10^{13}
10^{12}
10^{11}
10^{10}
$\frac{\partial^2 N_\gamma}{\partial \epsilon \partial s}$ photons/keV/s/m
$\frac{\partial^2 N_\gamma}{\partial \epsilon \partial s}$
10^4 $\frac{\partial^2 N_\gamma}{\partial \epsilon \partial s}$
Synchrotron radiation from
bending magnets
4 bunch machine
100 % field
10 % field
1keV
10keV
0.1MeV
1MeV
10MeV
ϵ

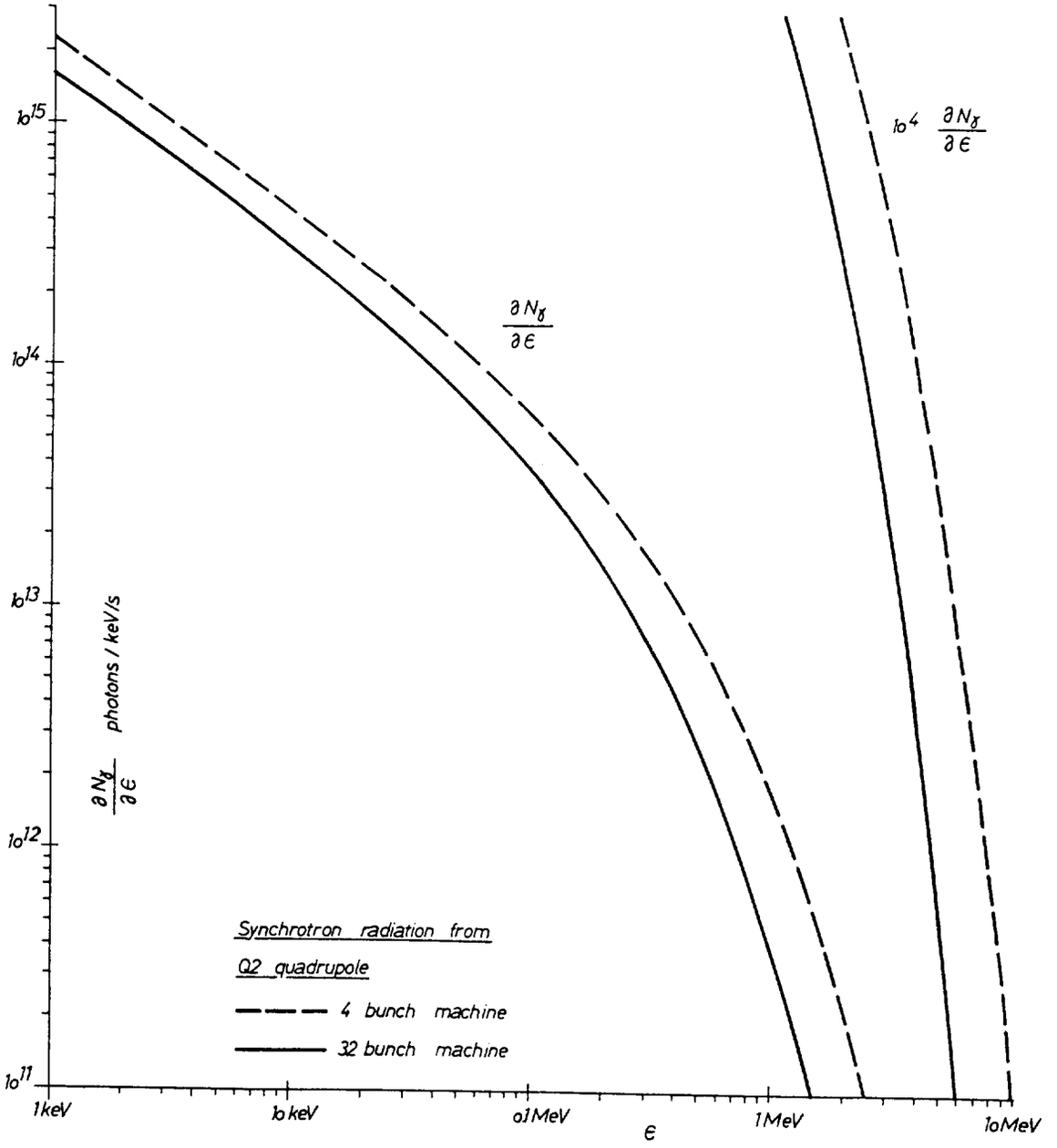
10^{15}
10^{14}
10^{13}
10^{12}
10^{11}
$\frac{\partial N_\gamma}{\partial \epsilon}$ photons / keV/s
$\frac{\partial N_\gamma}{\partial \epsilon}$
10^4 $\frac{\partial N_\gamma}{\partial \epsilon}$
Synchrotron radiation from
Q2 quadrupole
4 bunch machine
32 bunch machine
1keV
10keV
01MeV
1MeV
10MeV
ϵ

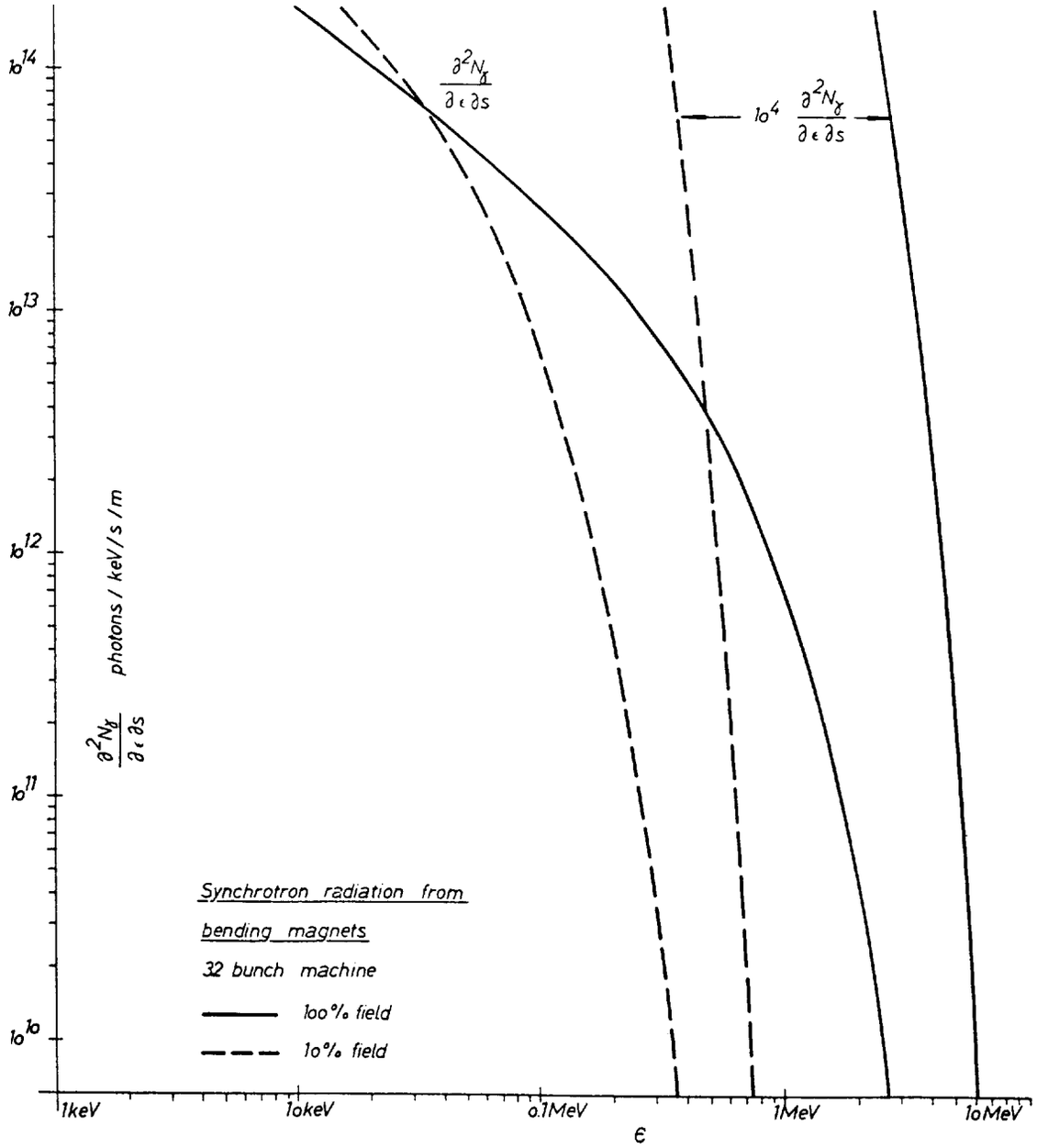
10^{14}
10^{13}
10^{12}
10^{11}
10^{10}
$\frac{\partial^2 N_\gamma}{\partial \epsilon\, \partial s}$ photons / keV / s / m
$\frac{\partial^2 N_\gamma}{\partial \epsilon\, \partial s}$
10^4 $\frac{\partial^2 N_\gamma}{\partial \epsilon\, \partial s}$
Synchrotron radiation from
bending magnets
32 bunch machine
100% field
10% field
1keV
10keV
0.1MeV
1MeV
10MeV
ϵ